Atomic and Electronic Properties of 2D Moiré Interfaces

A thesis submitted to The University of Manchester for the degree of Doctor of Philosophy in the Faculty of Science and Engineering.

2022

Astrid Marie Weston

School of Physics and Astronomy

Contents

Word count: 37,986

List of Figures

List of Tables

List of Abbreviations

2D 2-Dimensional

ADF Annular dark field

AFM Atomic force microscopy

AP Anti-parallel

BSE Back-scattered electrons

C-AFM Conductive atomic force microscopy

C-TEM Conventional transmission electron microscope

DFT Density functional theory

DIC Differential interference contrast

DOS Density of states

EFM Electrostatic force microscopy

EsB Energy selective back-scattered

FET Field effect transistor

HAADF High angle annular dark field

hBN Hexagonal boron nitride

HOPG Highly oriented pyrolytic graphite

IPA Isopropyl alcohol

KPFM Kelvin probe force microscopy

LAADF Low angle annular dark field

LL Landau levels

LUT Look-up table

MoS_2 Molybdenum disulphide

$MoSe_2$ Molybdenum diselenide

P Parallel

PCA Principal component analysis

PFM Piezo-response force microscopy

PL Photo luminescence

PMMA Polymethyl methacrylate

PPC Polypropylene carbonate

PVA Polyvinyl alcohol

QHE Quantum Hall effect

RIE Reactive ion etching

SdH Shubnikov-de Haas

SE Secondary electrons

SHG Second harmonic generation

SEM Scanning electron microscopy

SiN Silicon nitride

SiO_2 Silicon dioxide

SPM Scanning probe microscopy

STEM Scanning transmission electron microscopy

STM Scanning tunnellling microscopy

STS Scanning tunnelling spectroscopy

TEM Transmission electron microscopy

TMDs Transition metal dichalcogenides

vdWs Van der Waals

vHs Van Hove singularities

WD Working distance

WS_2 Tungsten disulphide

WS_2 Tungsten diselenide

Abstract

With a wide variety of 2-Dimensional (2D) metals, semiconductors and insulators available there has been significant interest in creating novel optoelectronic devices that can surpass the performance of traditional state-of-the-art electronics. More recently, a new degree of freedom in the meta-material design has been achieved by vertically stacking 2D crystals with a slight rotational misalignment.

The work presented in this thesis details the fabrication of twisted bilayers of transition metal dichalcogenides (TMDs), with rotational alignment close to $\sim 0^\circ$ or 180° depending on the desired polytype (3R and 2H, respectively), to study the effects of lattice reconstruction on their electronic properties. The two main projects in this thesis focus firstly on lattice reconstruction at the atomic scale and secondly on the electrical properties induced by lattice reconstruction.

To demonstrate lattice reconstruction at the atomic scale, scanning transmission electron microscopy (STEM) was employed. Our observations were combined with density functional theory (DFT) and multiscale calculations to determine the angle at which the transition from rigid to reconstructed lattices occurs and describe the atomic structure of the reconstructed lattices.

The electronic properties of reconstructed TMDs were studied using scanning probe microscopy (SPM) techniques such as conductive atomic force microscopy (C-AFM) and Kelvin probe force microscopy (KPFM), the latter of which revealed out-of-plane ferroelectricity where the oppositely polarised states were spatially confined to the triangular domains observed in 3R-polytypes but not in the 2H-polytype. Then, scanning electron microscopy (SEM) was used to study domain boundary dynamics as a function of an out-of-plane displacement to elucidate the ferroelectric switching phenomena. Finally, electrical transport measurements were performed to demonstrate such behaviour in prototype ferroelectric devices with a tunnelling junction geometry. Electronic SPM imaging techniques were employed prior to electrically contacting them.

Declaration

No portion of the work referred to in the thesis has been submitted in support of an application for another degree or qualification of this or any other university or other institute of learning.

Copyright Statement

(i) The author of this thesis (including any appendices and/or schedules to this thesis) owns certain copyright or related rights in it (the "Copyright") and s/he has given The University of Manchester certain rights to use such Copyright, including for administrative purposes.

(ii) Copies of this thesis, either in full or in extracts and whether in hard or electronic copy, may be made only in accordance with the Copyright, Designs and Patents Act 1988 (as amended) and regulations issued under it or, where appropriate, in accordance with licensing agreements which the University has from time to time. This page must form part of any such copies made.

(iii) The ownership of certain Copyright, patents, designs, trademarks and other intellectual property (the "Intellectual Property") and any reproductions of copyright works in the thesis, for example graphs and tables ("Reproductions"), which may be described in this thesis, may not be owned by the author and may be owned by third parties. Such Intellectual Property and Reproductions cannot and must not be made available for use without the prior written permission of the owner(s) of the relevant Intellectual Property and/or Reproductions.

(iv) Further information on the conditions under which disclosure, publication and commercialisation of this thesis, the Copyright and any Intellectual Property and/or Reproductions described in it may take place is available in the University IP Policy (see http://documents.manchester.ac.uk/DocuInfo.aspx?DocID=24420), in any relevant Thesis restriction declarations deposited in the University Library, The University Library's regulations (see http://www.library.manchester.ac.uk/about/regulations/) and in The University's policy on Presentation of Theses.

Acknowledgements

During the course of this PhD I have been helped by an endless number of my peers and I would like to take this opportunity to express my gratitude. I firstly thank my supervisor Prof. Roman Gorbachev for providing me with great opportunities, for his exceptional kindness and endless support during the course of this PhD. I also want to thank my masters supervisor Dr Andrey Kretinin for advising me to pursue this PhD project.

The pandemic has undoubtedly thrown some obstacles during this PhD and I have luckily come out the other side relatively unscathed thanks to the support of my peers and all the technical staff working here at the National Graphene Institute who kept the cleanroom running smoothly. I also want to thank the graphene NOWNANO CDT, the EPSRC and the Lloyds Register Foundation for funding this PhD project. A special thanks goes to Dr Alex Summerfield, Dr Nick Clark, Dr James Howarth, Dr Daniel Terry and Dr Johanna Zultak and particularly Dr Matthew Hamer (the graphene whisperer) for passing on their knowledge and providing me with endless advice and support.

I also want to thank all of the collaborators whose work is included in this thesis. A special thanks to Dr Yi-Chao Zou, Dr Nick Clark and Prof Sarah Haigh for your expertise and providing the STEM data and analysis. Thank you to Dr Vladimir Enaldiev and Prof Vladimir Fal'ko who provided all of the theoretical models, our collaborators at the National Physical Laboratory and to Dr Teruo Hashimoto for sharing his SEM expertise.

Finally, a special thanks to my friends and family who have supported me over the years and have kept me smiling. A particular thanks to my late grandparents, Evelyn and Raymond Weston, who taught me the importance in pursuing knowledge and always encouraged me to work hard.

Chapter1

Introduction

Graphene was the first of the 2-dimensional (2D) materials family to be studied. In 2004 [1] researchers described the Dirac physics that leads to the exotic electrical properties of graphene. This came much to the surprise of the scientific community as it was widely speculated that a single monolayer could not exist due to thermal instabilities at such atomic length scales [2, 3]. It was later found that monolayers of graphene could be stabilised with the support of a bulk substrate or by nano scale rippling [4]. Not only does graphene have exceptional electrical properties, but it's simple structure is an excellent model system for studying quantum electrodynamic theories that date back to the early 20th Century [5, 6].

Soon after, a whole library of materials with the same definitive layered structure were also studied; now with a variety of 2D semiconductors, metals, insulators and various correlated states there is great opportunity to build electronics at the nano-metre scale. One particularly interesting 2D material group is transition metal dichalcogenides (TMDs) that, in recent years, have attracted considerable attention owing to their excellent optoelectronic properties [7–11].

The main objective of this thesis was to fabricate twisted bilayers of TMDs with a minimal angle of rotational alignment (<1°) to study the atomic and electronic structure induced by a mechanism known as lattice reconstruction. A similar study of minimally twisted bilayer graphene experimentally observed such a phenomena but atomic resolution imaging was not achieved [12]. The motivation to study lattice reconstruction in TMDs stems from their wide range of band-gap energies and their excellent optical [7, 8, 10] and electronic properties [9, 13, 14]. These properties can be manipulated with small rotational twist angles thus providing a plethora of possible optoelectronic applications (discussed in **Chapter 2**). To achieve this, devices were prepared for electron microscopy and electrical scanning probe microscopy studies.

Then, electrical scanning probe microscopy techniques were used to aid the design and fabrication of electron tunnelling junction devices for electrical transport studies (discussed in **Chapters 3 and 4**) to demonstrate the viability of this system for applications such as ferroelectric memory storage devices. A brief description of each of the chapters are detailed below;

Chapter 2 introduces 2-dimensional materials such as graphene hexagonal boron nitride and transition metal dichalcogenides that have been studied in this project. The atomic and electronic structure of their monolayer crystals as well as their potential applications are discussed in detail. The concept of moiré superlattices is then introduced followed by a detailed literature review of the research that has been achieved so far.

Chapter 3 describes the experimental techniques needed to exfoliate, identify and transfer 2-dimensional crystals to fabricate van der Waals heterostructures. Further detail is given on the techniques required for precise rotational alignment of vertically stacked crystals, essential to the success of this project. The procedure for fabricating electrical contacts for electronic-based characterisation is also outlined.

Chapter 4 describes the characterisation tools used to study the atomic and electronic structure of lattice reconstruction in twisted bilayer transition metal dichalcogenides. The theory and principles of scanning transmission electron microscopy, used to study the atomic structure, is introduced. Electrical scanning probe microscopy techniques as well as scanning electron microscopy, used to study electronic properties, are also discussed. Finally, details of the techniques used for microscopy image processing are introduced.

Chapter 5 describes the atomic structure of reconstructed superlattices of twisted bilayer TMDs. There are two different reconstructed superlattices that can be fabricated owing to the two different polytypes (2H and 3R) that can form in a bilayer of TMDs, both of which are experimentally observed and discussed in detail.

Chapter 6 describes the electronic properties of reconstructed superlattices of bilayer TMDs. Conductive atomic force microscopy (C-AFM) was used to demonstrate the key differences in electronic structure of the 2H- and 3R- polytypes, however, the rest of the chapter focuses on the electronic properties of 3R-type superlattices. This further characterisation was acquired using Kelvin probe force microscopy, scanning electron microscopy and electrical transport measurements to demonstrate out-of-plane ferroelectric polarisation and to elucidate the ferroelectric switching mechanism.

Chapter 7 is the final chapter and discusses the future outlooks that stem from this project. As this project aimed to reveal the fundamental properties of lattice reconstruction in transition metal dichalcogenides, there is now scope to apply this knowledge and to explore the possible optoelectronic applications.

Chapter2

Background and Theory of 2-Dimensional Materials and Moiré Superlattices

In this chapter 2D materials such as graphene, hexagonal boron nitride (hBN) and transition metal dichalcogenides (TMDs) and their heterostructures will be introduced with a discussion of their atomic and electronic structures. The concept of moiré superlattices will also be discussed including a detailed literature review on the current state of research in systems such as graphene/hexagonal boron nitride, twisted bilayer graphene and twisted bilayer transition metal dichalcogenides.

2.1 2-Dimensional Materials

2D materials are a class of materials that consist of atomically thin sheets (spatially confined in the z-direction) that originate from bulk crystals with a layered structure. The layered structure is a consequence of strong intra-planar (covalent) bonding and weak inter-planar van der Waals (vdWs) forces. The term collectively describes three main long-range interactions occurring when atoms are in relatively close proximity including electrostatic, polarisation/induction and dispersion forces [15]. Graphene can be isolated by the method of mechanical exfoliation i.e. cleaving/peeling with adhesive tape (originally with scotch tape). The adhesive forces of the tape are stronger than the vdWs forces and therefore are able to separate the individual layers from one another. In this section, the atomic and electronic structure of graphene, hBN and TMDs are discussed in detail.

2.1.1 Graphene

Graphene is an atomically thin layer of the bulk crystalline material graphite. Each layer of graphite consists of an in-plane hexagonal array of carbon atoms. The carbon atoms are covalently bonded in-plane and weakly held together by vdWs forces out-of-plane. The anisotropy between these forces is the archetypal structure for most layered materials.

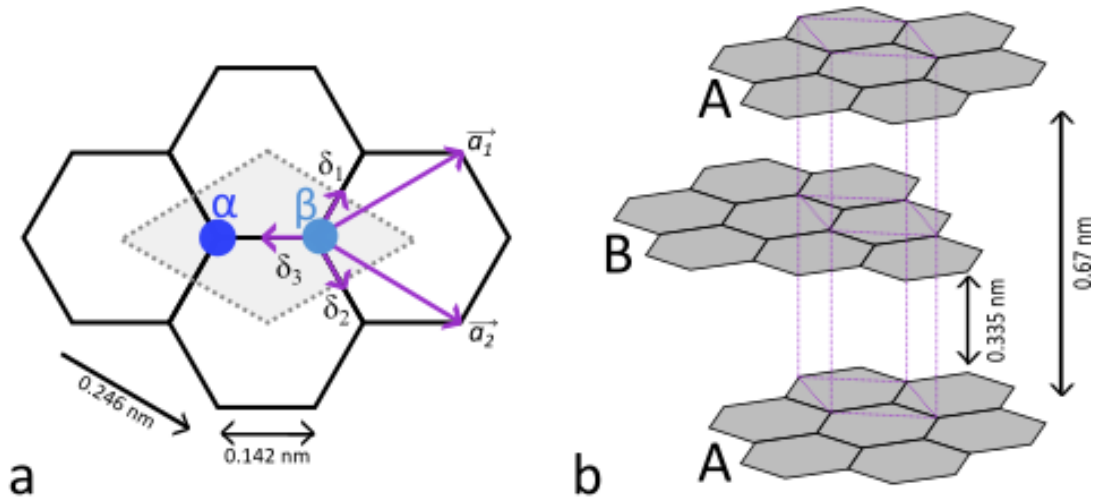

Fig. 2.1: **Graphene crystal structure.** **a** Schematic illustration of the hexagonal crystal structure of graphene highlighting the sub-lattice atoms α (dark blue) and β (light blue) where the primary unit cell is highlighted by the grey dashed rhombus. **b** Bernal stacking is the most common stacking configuration of graphite, where layer B is shifted in-plane by half a unit cell with respect to A.

The unit cell of graphene (indicated by the dashed line in Fig. 2.1a) consists of two non-equivalent sub-lattice atoms α and β. Every sub-lattice atom denoted α is surrounded by three β sublattice atoms and vice versa. The corresponding lattice vectors are;

$$\overrightarrow{\delta_1} = \frac{a}{2}(1, \sqrt{3}), \overrightarrow{\delta_2} = \frac{a}{2}(1, -\sqrt{3}), \overrightarrow{\delta_3} = a(-1, 0) \tag{2.1}$$

Where a (0.142 nm) is the nearest neighbour distance [16]. The hexagonal periodicity is defined by the lattice translation vectors $\overrightarrow{a_1}$ and $\overrightarrow{a_2}$;

$$\overrightarrow{a_1} = \frac{a}{2}(3, \sqrt{3}), \overrightarrow{a_2} = \frac{a}{2}(3, -\sqrt{3}) \tag{2.2}$$

The length of these vectors, $\sqrt{3}a$, is the lattice parameter 0.246 nm. The most common stacking configuration in graphite is where each carbon sub-lattice sits in the centre of the hexagon in the layer below and repeats every second layer. This is referred to

as AB/BA (Bernal) stacking as depicted in Fig.2.1b. Other possible high symmetry stackings include AA stacking where carbon atoms in adjacent layers sit on top of each other, however, this has a high energy cost and therefore does not regularly occur in the bulk crystal [17].

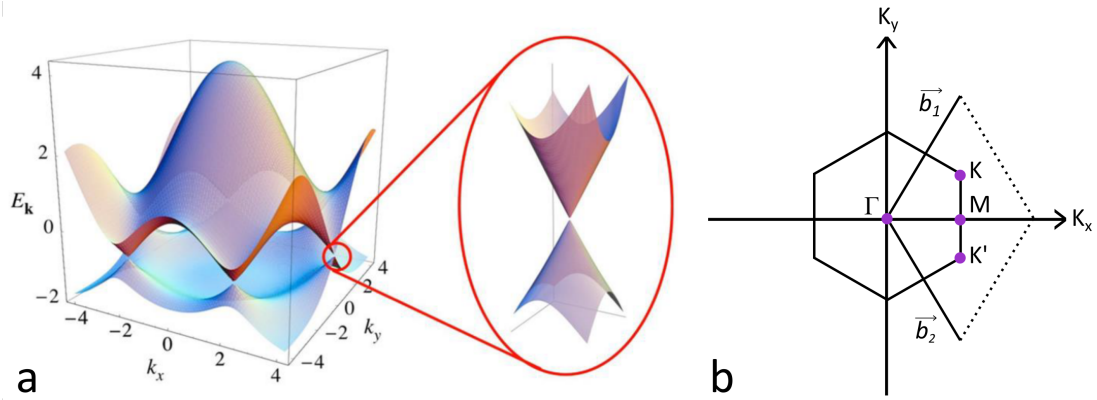

Fig. 2.2: **The electronic structure of graphene.** **a** The 3-dimensional electronic band structure of graphene highlighting the linear cone dispersion at the Dirac points within the Brillouin zone [reprinted (figure) with permission from [18] copyright (2021) by the American Physical Society]. **b** Schematic of the unit cell of graphene in reciprocal space which is commonly known as the Brillouin zone. The points highlighted in purple denote the high-symmetry points in the electronic band structure.

When we consider the electronic structure of graphene, we define it in terms of the Brillouin zone which is the Wigner-Seitz unit cell in reciprocal space. Figure 2.2b depicts the first Brillouin zone of graphene highlighting the high-symmetry points Γ, M, K and K′ as well as the lattices vectors in reciprocal (K) space. The exceptional ambipolar charge transport properties of graphene arise due the the unique band structure at the non-equivalent K/K′ points (referred to as the Dirac points) where the valence and conduction band meet. The linear energy dispersion (conical structure as depicted in the inset of Fig. 2.2a) of both the valence and conduction band causes the Fermi velocity to be independent of energy or momentum which leads to zero effective-mass for charge carriers. The dispersion relation is described as;

$$E_{K,K'} = \pm\hbar v_F|k|, \tag{2.3}$$

where $\hbar$ is the reduced planks constant, v_F is the Fermi velocity of charge carriers, k is the wavenumber ($\sqrt{k_x^2 + k_y^2}$) and $v_F \sim 10^6 ms^{-1}$ is the Fermi velocity [18, 19]. Unfortunately, the Dirac-fermion behaviour in graphene is perturbed by disorder due to topographic corrugations of the graphene and charge donating impurities in the

underlying SiO_2 substrate [20–22]. The disorder leads to inhomogeneous electron densities in the form of electron/hole puddles near the Dirac point suppressing the intrinsic electrical properties of graphene [21].

2.1.2 Hexagonal Boron Nitride

hBN is a colourless and transparent insulator with a large band-gap energy of ~ 6 eV [23]. Exfoliated bulk crystals of hBN have proven to be an excellent vdWs substrate for charge transport studies of other conductive 2D materials [24]. Unlike conventional substrates such as Si/SiO_2, hBN is a 2D material with an atomically smooth surface with a high quality dielectric environment. By having a thick enough hBN crystal (> 20 nm) we are able to screen the electron/hole puddles of the underlying Si/SiO_2 and dramatically reduce charge disorder in graphene which was a factor limiting electron mobility in charge transport studies. This was directly observed using a scanning tunnelling microscope where the electron/hole puddling directly correlated with the surface roughness of the commonly used substrate oxidised silicon [25]. Monolayer and few-layer hBN has also been found to be an excellent tunnelling barrier [26].

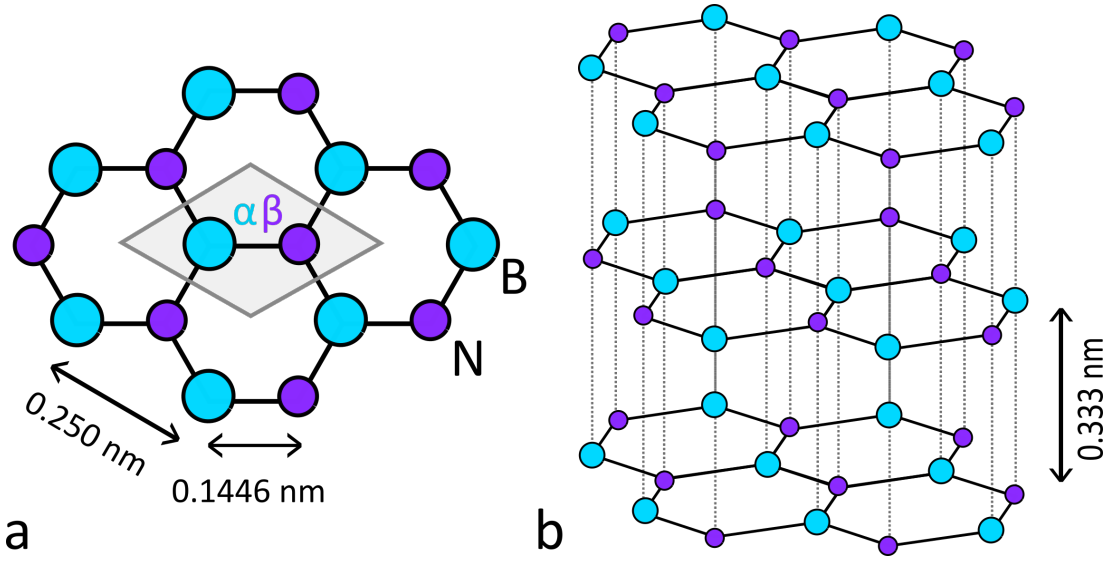

Fig. 2.3: **The crystal structure of hBN.** a Schematic illustration of the hexagonal crystal structure of hBN showing the sub-lattice atoms α and β in the primary unit cell marked with the grey outline. **b** Schematic of AA′ stacking which is the most common stacking configuration for hBN.

hBN has a similar crystal structure to graphene but with a hexagonal in-plane array of alternating boron and nitrogen atoms instead of carbon. In the bulk, the most common stacking configuration, due to the low energy cost of formation, is AA′ where

a boron atom in the top layer sits on top of a nitrogen atom in the layer below and vice versa (see Fig. 2.3) [27]. Other, more energy expensive, stacking configurations include AA (boron sits above boron atoms and nitrogen above nitrogen atoms), A′ B (shifted by half a unit cell with nitrogen sitting on top of nitrogen) and AB′ stacking (shifted by half a unit cell with boron sitting on top of boron) [28].

2.1.3 Transition Metal Dichalcogenides

Transition metal dichalcogenides (TMDs), with the chemical formula MX_2 (where M = metal and X = chalcogen) are a versatile group of layered materials. Depending on the choice of the metal and chalcogen as well as their metal coordination (see Fig. 2.4b), their optoelectronic properties can be strikingly different. For example, group VI transition metals with trigonal prismatic metal coordination, including tungsten and molybdenum, are semiconducting except when paired with the chalcogen tellurium where they become metallic [29]. In comparison, 1T-TaS_2 (a group V transition metal) exhibits exotic properties such as the Mott insulating state, superconductivity and charge density waves at cryogenic temperatures [30, 31]. The wide range of properties displayed by bulk TMDs and their high crystalline quality is what prompted a considerable research interest to probe monolayer and few-layer forms of these materials in the past decade.

Unlike the crystal structure of graphene and hBN, there are three atomic planes per layer consisting of a metal plane in-between two chalcogen planes giving hexagonal in-plane symmetry with a layer thickness of $\sim$ 0.6 nm. Each metal atom supplies four electrons filling the bonding states, giving the metal and chalcogen a charge of +4 and -2, respectively [32]. The metal atoms have six-fold coordination with two possible geometries including trigonal prismatic (chalcogens on top of each other) and octahedral (chalcogens are staggered) as depicted in Fig.2.4b. Different combinations of metal and chalcogens tend to favour either trigonal prismatic or octahedral geometry as their most energetically favourable [32].

In the bulk form, TMDs can also have various stacking polytypes which are characterised by both the type of metal coordination and stacking sequences. Common polytypes include 1T, 2H and 3R where the number corresponds to the number of layers in a unit cell and the letter indicates the symmetry type. The symmetry types include tetragonal (T), hexagonal (H) and rhombohedral (R) which have been

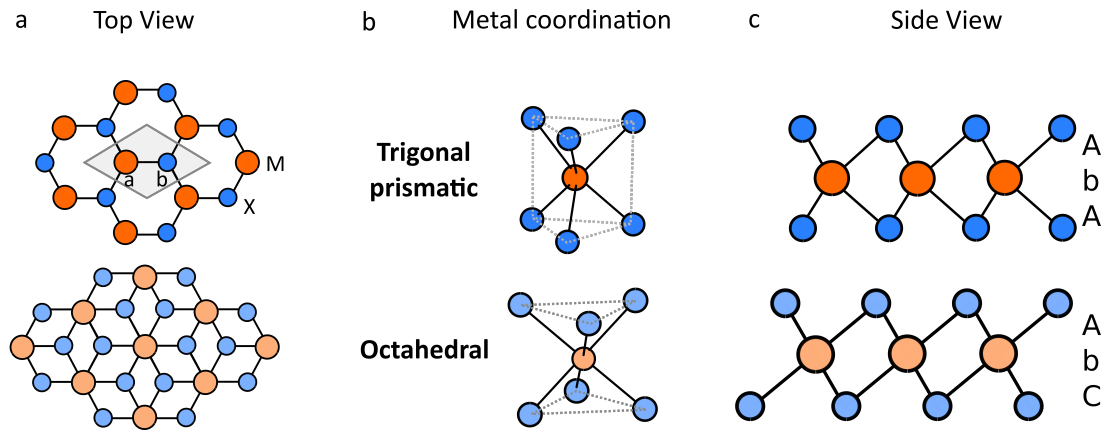

Fig. 2.4: **The two most common polymorphs of monolayer TMDs. a** Top view schematics and **b** the 3D view of TMD monolayers (where red atoms are metals and blue atoms are chalcogens) corresponding to two possible metal coordinations including trigonal prismatic and octahedral. **c** The side profiles of both metal coordinations where the capital letters denote chalcogens and lower case are metal atoms. the black arrows in **b-c** indicate whether adjacent layers are aligned **c** anti-parallel or **c** parallel to each other.

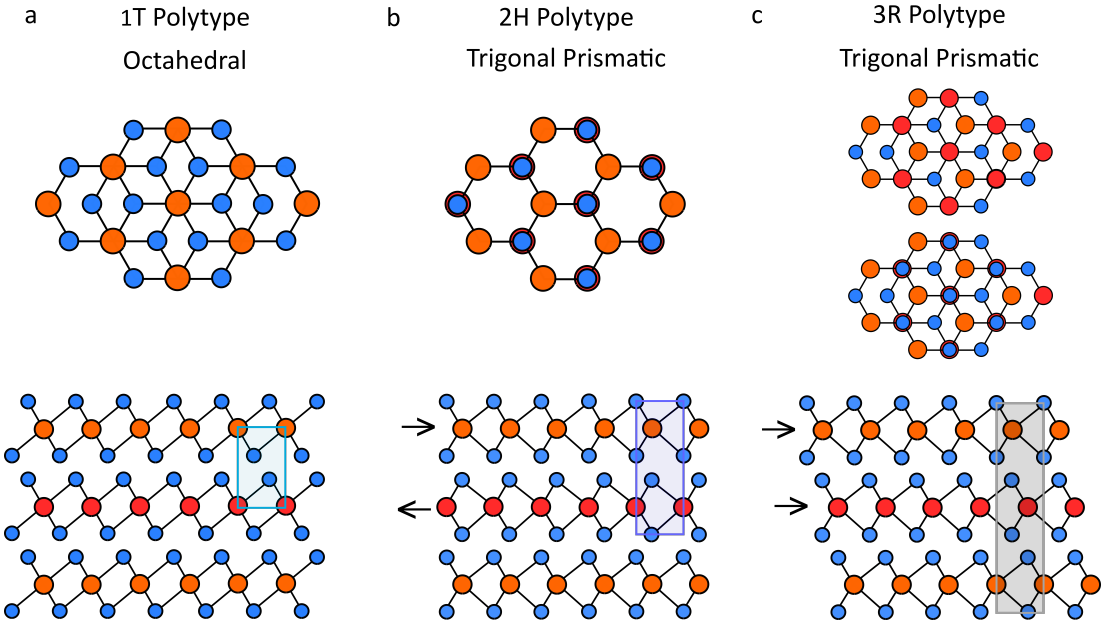

Fig. 2.5: **The top view (top line) and side views (bottom line) of common TMD polytypes including 1T, 2H and 3R.** Here, the red atoms are metals and the blue atoms are chalgocens. The blue, purple and grey boxes on the side view illustrations indicate the unit cell of the 1T, 2H and 3R phases, respectively.

illustrated in Fig.2.5. Some TMDs can be found in more than one polytype in standard conditions such as MoS_2; although it naturally occurs in the 2H phase, it can be synthetically grown with both the 2H and 3R phase [33].

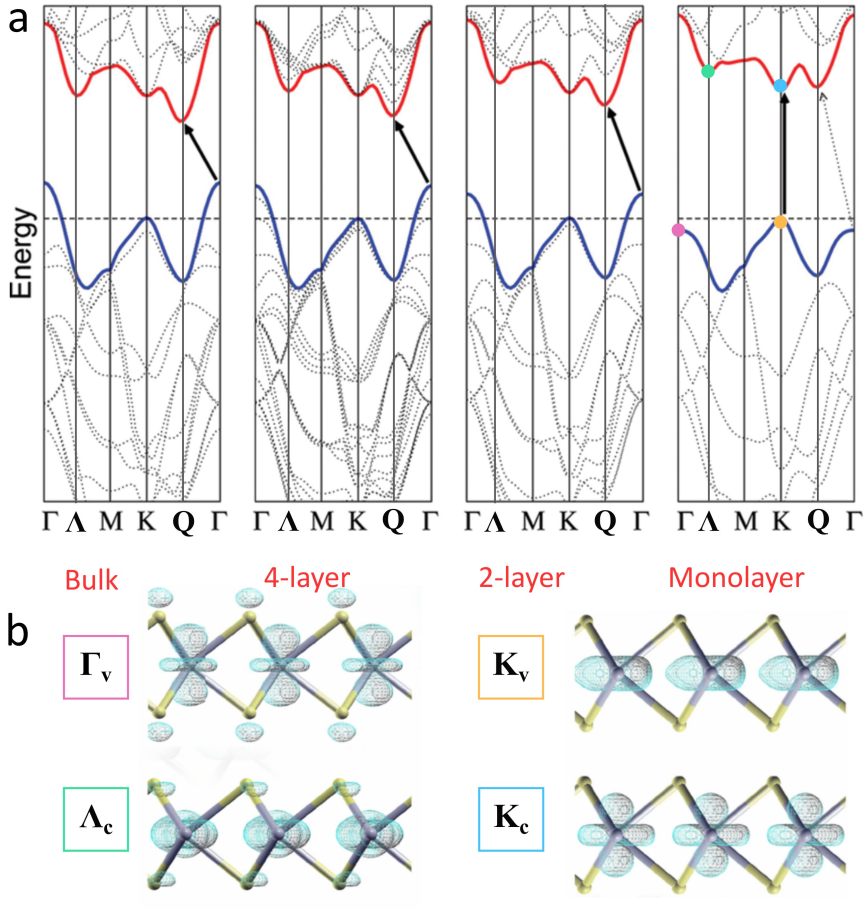

Fig. 2.6: **Electronic properties of MoS_2 from bulk to monolayer.** **a** Calculated band structures (using density functional theory) for bulk, 4-layer, bilayer and monolayer MoS_2 illustrating the transition from indirect to direct band gap [Reprinted with permission from [7]. Copyright (2010) American Chemical Society]. **b** Electron distribution in monolayer TMDs for the states at K_c, K_v, Γ_v and Λ_c high symmetry points in the band structure position in the Brillouin zone shown by the corresponding colours in **a**. [Reprinted with permission from [34]. Copyright (2021) American Chemical Society].

The electronic structure is dependent on the metal coordination as well as d-orbital occupancy. For octahedral coordination, two degenerate orbitals form (with 5 d-orbitals) that can hold up to 6 valence electrons [32]. Trigonal prismatic coordinated structures have their d-orbitals split into three groups [35]. For metallic TMDs, the highest d-orbitals are partially filled whereas for semiconductors they are completely filled.

For semiconducting (group VI) TMD monolayers with trigonal prismatic coordination, both conduction and valence band edges are located at the K-point of the Brillouin zone (see Fig. 2.6a). One of the most popular of the TMDs, MoS_2, has the wavefunction of the valence band states at the K-point (shown as K_v in Fig. 2.6b) comprised of d-orbitals of the central metal atoms. A consequence of this is that the position of K_v is largely unaffected as the number of layers changes. Conversely, the Γ-point features hybridised states of the outer chalcogen atoms (P_z-orbitals) and the metal atom (d-orbitals) (see Fig. 2.6b). Here, chalcogen atoms are most affected by vdWs forces between adjacent layers therefore the states at the Γ-point of the valence band and the Q point of the conduction band are more strongly modified when transitioning from monolayer to bulk. The shift of these band edges leads to the transition from a direct gap (at the K-point) in monolayer TMDs to an indirect band gap (at the $Q - \Gamma$-points) in the bulk (see Fig. 2.6). The band gap decreases in energy with increasing layer number.

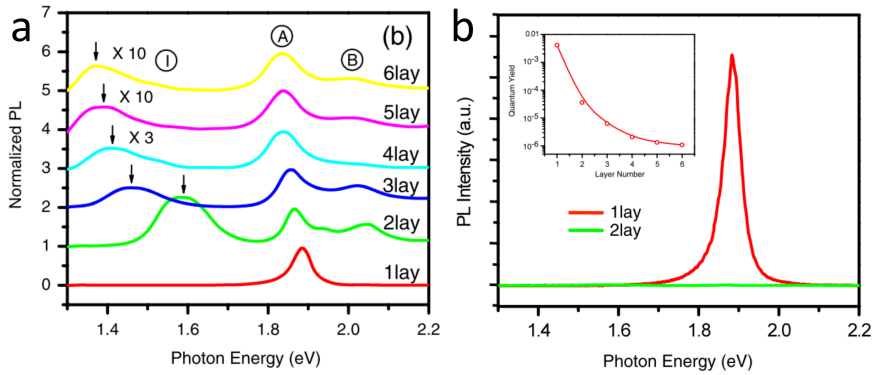

Fig. 2.7: **Optical properties of MoS_2 from bulk to monolayer.** **a** Photo-luminescence spectra for mono- and bilayer MoS_2. **b** The normalised (by intensity of peak A) photoluminescence spectra of MoS_2 with layer thickness 1-6. In the inset, quantum yield as a function of layer thickness. [Reprinted (figure) with permission from [8]. Copyright (2021) by the American Physical Society].

Light emission due to the absorption of photons (photoluminescence) in TMDs is a process which is largely dominated by the generation of excitons. Experimental studies demonstrated that the photoluminescence of MoS_2 sharply increases by 3 orders of magnitude when going from bulk to monolayer due to the transition to a direct band gap in a monolayer (see Fig. 2.7b). The lowest energy exciton peak for MoS_2 shifts from 1.29 eV in the bulk to 1.8 eV in the monolayer [7, 8]. The sharp increase in efficiency is related to the significant reduction of the momentum mismatch between the valence and conduction band edges owing to a lack of interlayer interactions in the monolayer

compared to the bulk. Upon photo-excitation, an excited electron in the the conduction band and hole in the valence band are created. If the binding energy is sufficient, they will form an exciton which in most materials at finite temperature is not the case. The reason for these excitons dominating photoluminescence in atomically thin TMDs is due to the large binding energy of exciton formation provided by quantum confinement which allows the observation of excitonic phenomena even at room temperature.

The remarkable properties of monolayer TMDs have rendered them ideal candidates for 2D electronic [9] and optoelectronic devices [36]. Initially, there was great interest in using monolayer and few-layer TMDs in 2D FETs due to their suitable bandgaps, lack of dangling bonds and high current ON/OFF ratios of up to 10^9 [9, 11, 37–39]. Here, FETs use semiconducting materials to moderate the flow of charge carriers (by acting as a switch through the use of a metallic gate) in integrated circuits. Importantly, high quality monolayers of MoS_2 and WSe_2 have relatively high carrier mobilities of $\sim$ 190 cm^2/Vs [13] and $\sim$ 250 cm^2/Vs [14] at room temperature, respectively.

It is possible to mix and match these materials to further modify their properties, for example, heterobilayers of group 6 transition metal TMDs including WS_2 and MoS_2 form staggered PN junctions with type II band alignment [40]. The type of band alignment that forms is governed by how the conduction and valence band of two band gaps align to each other combined with the effects of electrostatic potential. Type II alignment is when both the conduction and valence band of one material are lower than the other therefore confining electrons to one material and holes to the other [41]. This also strongly affects their optical properties [42, 43].

2.2 Moiré Superlattices

A simple manipulation of the twist angle between monolayers of 2D materials has led to one of the most important fundamental breakthroughs in 2D electronics since the isolation of graphene, the observation of superconducting and correlated insulating phases in twisted bilayer graphene [44, 45] and trilayer graphene/hBN [46]. When two periodic arrays are super-imposed on one another, a moiré pattern is formed with the period controlled by the angle of rotation between the two arrays. The periodic moiré pattern has a spatial structure much larger than the periodic atomic spacing in a 2D monolayer and is known as a moiré superlattice. Fig. 2.8 highlights the relationship

between the relative twist angle between monolayers and the moiré superlattice. For large (e.g. θ = 15°) twist angles the moiré pattern is small and for smaller angles (e.g. θ = 5°), the moiré pattern increases in size.

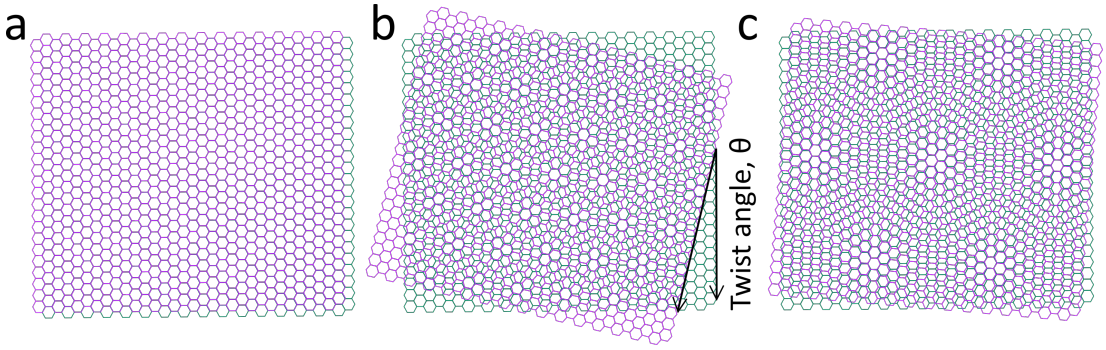

Fig. 2.8: **Schematic of two monolayers (with a hexagonal crystal lattice) twisted relative to each other to form a moiré pattern.** Two monolayers stacked on top of each other with relative rotation angle (θ) of **a** 0°, **b** 15° and **c** 4.8 °.

Moiré patterns in 2D materials were first experimentally observed on highly oriented pyrolytic graphite (HOPG) using a scanning tunnelling microscope; the periodic moiré pattern had a larger period than the lattice constant of graphene, hinting at the formation of a superlattice [47, 48]. The relationship between the size of the moiré pattern in such a crystal and the relative angle of rotation (θ) can be described mathematically as [48];

$$\lambda = a/[2\sin(\theta/2)] \tag{2.4}$$

Where λ is the moiré period (nm) and a is the lattice constant. Here, the period is the distance between the centres of each hexagonal moiré unit cell (see Fig.2.9a). When two monolayers with dissimilar lattice constant are twisted, the lattice mismatch ($\delta = a_x/a_y - 1$), where a_x and a_y denote the lattice constant of the top and bottom layer respectively, will limit the maximum wavelength [49];

$$\lambda = (1+\delta)a_x/\sqrt{2(1+\delta)(1-\cos\theta)+(\delta)^2} \tag{2.5}$$

Here, the lattice constant of the top layer (i.e. a_x) is used to calculate the wavelength limit due to lattice mismatch.

Figure 2.9 illustrates the evolution of moiré wavelength (i.e. the period of the moiré superlattice) as a function of the twist angle. The larger the lattice mismatch, the smaller the maximum wavelength. For example, a hBN/Graphene superlattice has a lattice mismatch of $\delta = (a_{hBN}/a_{Gr} - 1) \sim 1.8\%$ resulting in the largest moiré period of 14 nm. Bilayer graphene has sixfold symmetry which means the moiré wavelength

has mirror symmetry in the range $-30° \leq \theta \leq 30°$. It must be noted that group VI TMDs have two common polytypes in a bilayer configuration and do not have the same symmetry which has not been accounted for in this simple plot, however, will be discussed later.

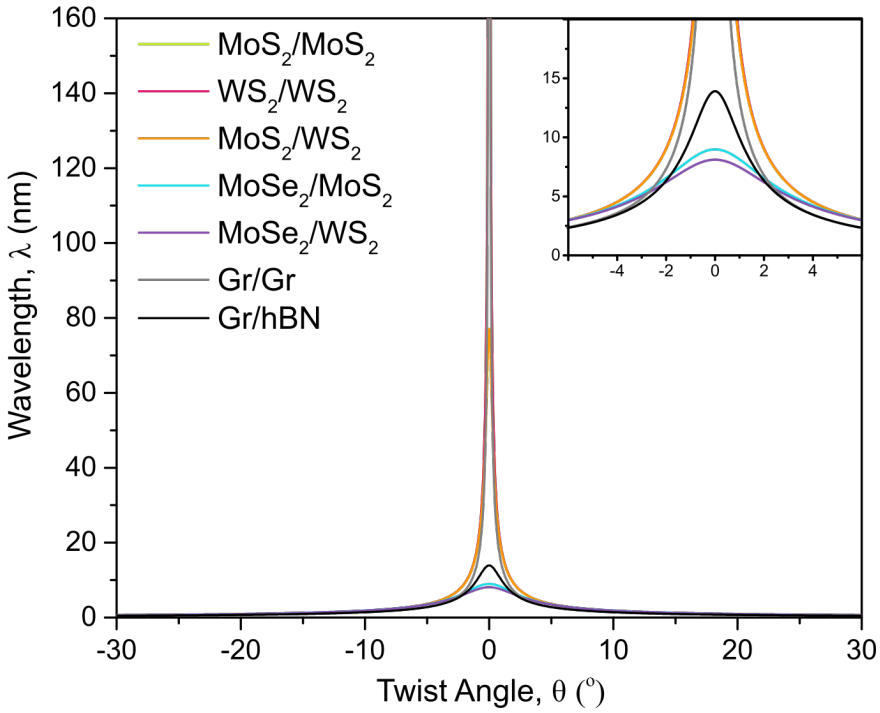

Fig. 2.9: **Moiré wavelength as a function of twist angle.** The moiré wavelengths at each twist angle were calculated using the lattice constants provided in Tab.2.1.

Tab. 2.1: **Lattice constant for different vdWs materials to calculate moiré wavelengths.**

Material	Lattice constant a, nm
MoS_2 [50]	0.316
WS_2 [51]	0.3153
$MoSe_2$ [50]	0.3297
Graphene [52]	0.246
hBN [53]	0.2504

2.2.1 Graphene and Hexagonal Boron Nitride

Precisely (0°) aligned graphene/hBN was one of the first moiré superlattice systems to be studied and is a particularly desirable system because it can be grown on a large scale using molecular beam epitaxy [54]. For mechanically exfoliated crystal stacks, the rotational angle appears to be temperature sensitive and they mechanically 'click' into place with precise alignment ($\theta = 0°$) at high temperature [55]. Exceptional advances in device fabrication have even led to the development of dynamically rotatable heterostructures, allowing for different twist angles to be examined in a single sample [56].

The graphene/hBN superlattice has been found to possess a new set of superlattice Dirac points with reduced Fermi velocity which generate massless Dirac Fermions observed in localised density of states (LDOS) measurements [49]. Here, the position of the secondary Dirac points is angle dependent. The wavelength of precisely aligned Gr/hBN ($\theta \sim 14$ nm) has been shown to present experimental features of the Hofstadter butterfly. This is a complex quantum fractal energy diagram materialised from the periodic electrostatic potential (due to the moiré superlattice) under an external magnetic field [57–59]. Mini-gaps in the fractal energy spectrum appear because the moiré period is the same length (or close to) the magnetic length allowing for the orbital motion of electrons to be quantised i.e. one magnetic flux per moiré unit cell.

Additionally, a surface reconstruction described as a commensurate-incommensurate transition occurs in graphene/hBN superlattices with nearly aligned lattices [60]. This can be better understood using the Frenkel-Kontorova model applied to the 2-dimensional hexagonal structure [61]. Here, the incommensurate state describes stacking with no long-range order. At near perfect alignment ($\theta = 0°$) it becomes energetically favourable to reduce incommensurability to a finite region whilst increasing regions of energetically favourable stacking configurations. Essentially, the model describes a periodic strain compensation across the surface of the bilayer which is concentrated at the boundaries between commensurate regions forming a domain wall that is separating regions of commensurate stacking. Woods et al. [60] used atomic force microscopy to experimentally confirm this.

2.2.2 Twisted Bilayer Graphene

In twisted bilayer graphene, periodic modulation of three stacking configurations occur, including AB/BA (Bernal stacking) and AA stacking where the top and bottom lattice are rotated with a twist angle $0° < \theta < 10°$. In reciprocal space, the Brillouin zone of the top and the bottom layer are twisted with respect to each other by the same rotation angle in real space. A mini (superlattice) Brillouin zone is created from the difference between the two wave vectors (K'^1/K'^2) in each layer (see Fig. 2.10b).

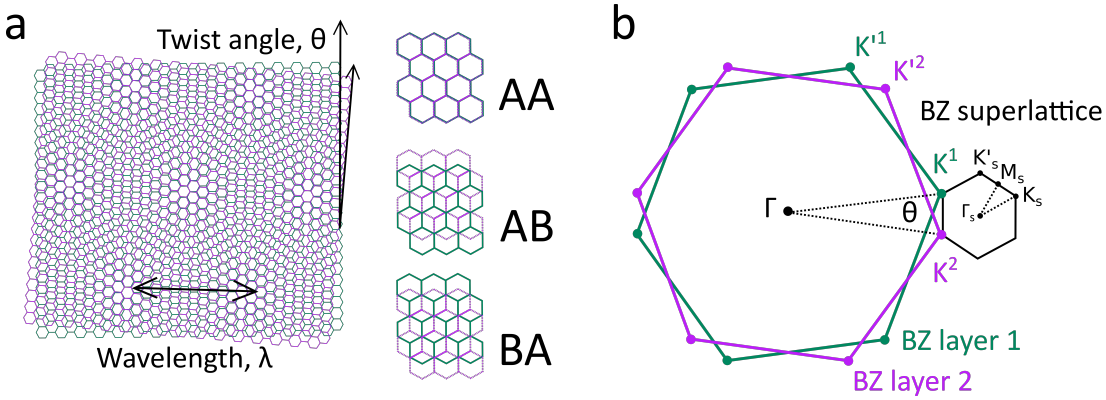

Fig. 2.10: **Moiré superlattice of a twisted bilayer graphene.** **a** Two hexagonal lattices of graphene twisted relative to each other in real space and the three primary stacking configurations including AA, AB and BA. **b** Two lattice Brillouin zones (BZ) corresponding to layer 1 and layer 2 overlapping to form a superlattice Brillouin zone in reciprocal space.

The band folding and hybridisation leads to significant modification of each individual monolayer dispersion and the electronic wavefunctions. For relative twist angles $10° < \theta < 1.5°$, the Dirac cones of each layer begin to interact causing the formation of 'saddle points' in the Brillouin zone. These saddle points lead to van Hove singularities (vHs), described as 'kinks' of logarithmic scale, in the density of states (DOS). Here, DOS is the density of states that can be occupied by electrons. The twist angle defines the energy separation of the vHs, corresponding to the two lowest energy band thresholds, where decreasing twist angle decreases the energy separation between the vHs bringing them closer to the Dirac point (see Fig. 2.11). This phenomenon has been experimentally observed in scanning tunnelling spectroscopy [62, 63]. The significance of this is that the lowest energy sub-bands in twisted bilayer graphene retain the same linear (Dirac) dispersion around (K'^1/K'^2) as in the monolayer case. This is attributed to interlayer coupling (interaction) of the two layers [63].

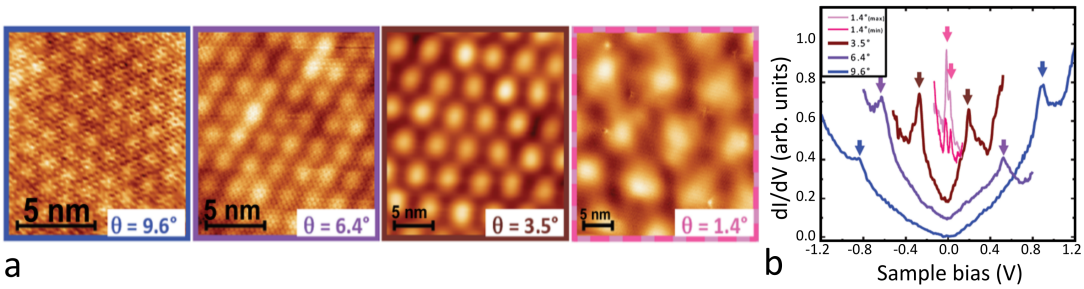

Fig. 2.11: **Van Hove singularities in twisted bilayer graphene** ($\theta > 1°$) **a** Scanning tunnelling microscopy topographic images showing increase of moiré wavelength with decreasing angle. **b** Local density of states (LDOS) spectra for each of the twist angles identified in **a**. For 1.4°, 'max' refers to the (AA stacking) bright spots and 'min' refers to the (AB/BA stacking) dark regions in **a**. [Reprinted (figure) with permission from [63]. Copyright (2021) by the American Physical Society].

At specific 'magic' angles ($\theta \approx 1.1°$, 0.5°, 0.35° 0.24° and 0.2°), the Fermi velocity tends towards zero and the energy bands become flat [64]. The two lowest-energy valence and conduction mini-bands become non-dispersive in the vicinity of the Dirac points and become further separated from the higher energy bands [64]. At the first magic angle of 1.1°, both superconducting [45] and insulating states [44, 65] were observed in transport measurements in striking contrast to semi-metallic behaviour of monolayer graphene. In this work, the researchers used the Mott model to explain the origin of these states, however, this has quickly been disputed in the field. Pizarro et al. [66] highlighted the need to include non-local correlations which the Mott model does not do. Padhi et al. suggested an approximation using Wigner crystalline states [67]. Others have suggested that electron-electron interactions in s-wave superconducting states were mediated by electron-phonon interactions [68], however, the pursuit for an appropriate description is still ongoing and will require further theoretical and experimental work to confirm or disprove the various propositions.

More recently, STS experiments have been used to directly probe the electronic structure of magic angle graphene as a function of charge carrier density. In total, four different groups independently studied the system, presenting results with key similarities, including the observation of rotational symmetry breaking and correlated insulating states at half-filling of the low energy band [69–72]. Most of the groups observed two peaks in the density of states at the AA-site such as the STS spectra illustrated in Fig.2.12a. Xie et al. further observed that one of these peaks becomes distorted as the flat bands are partially filled (See Fig.2.12c). Despite the findings, it is

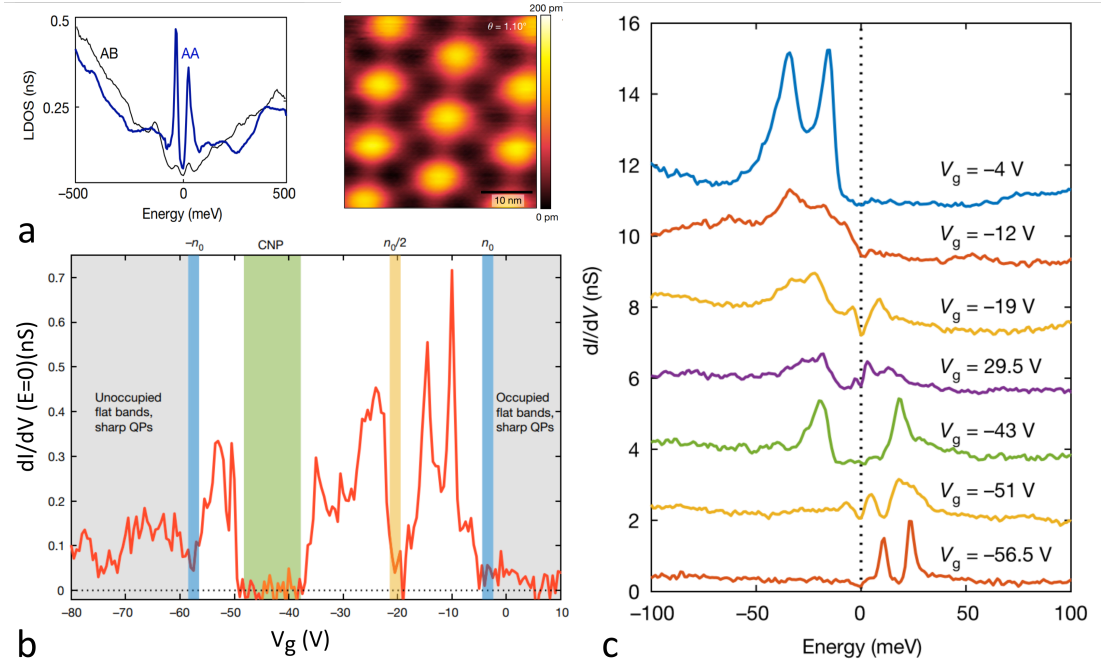

Fig. 2.12: **Scanning tunnelling spectroscopy of magic angle graphene. a** Atomic resolution scanning tunnelling microscopy topography of the moiré superlattice twisted to $\sim 1.1^\circ$ with corresponding STS LDOS on AA sites compared to AB sites. [Reprinted with permission from Nature [69]. Copyright (2021)]. The topography image was taken at 0.5V and 30pA. **b** Conductance at the Fermi level as a function of gate voltage highlighting the evidence of a correlated insulating state at half-filling ($n_o/2$, the region shaded yellow). The blue shaded regions signify two filled flat bands and the green region is the location of the charge neutrality point. **c** Individual STS spectra taken from different voltages in **b**, the dashed line indicates the Fermi level [**b-c** Reprinted by permission from Nature [70] Copyright (2021)].

still unclear whether the rotational symmetry breaking is truly an intrinsic property of the structure or whether it is a factor of strain within the system.

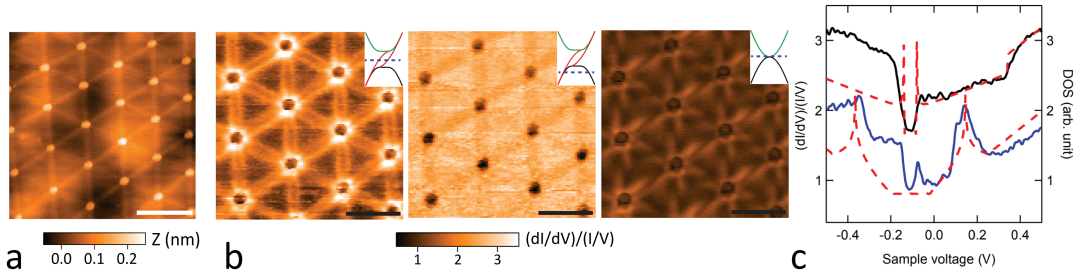

Fig. 2.13: **Scanning tunnelling spectroscopy of minimally twisted bilayer graphene. a** STM topography of twisted bilayer graphene ($\lambda \sim 58$ nm) at 0.5 V and 200 pA (scale bar = 80 nm). **b** Spatially resolved mapping of density of states at V_s = -0.11 V/V_{gate} = 60 V, V_s = -0.245 V/V_{gate} = 60V and V_s = -0.1 V/V_{gate} = -50 V, respectively (scale bar = 50 nm). The band diagrams in the insets indicate the conduction (green line) and valence bands (black line) of the Bernal stacked domains and the red lines are due to the topologically protected helical states on the domain wall **c** Single dI/dV/(I/V) spectra at the domain wall (blue) and a AB stacking region (black). The tip was stabilised with a current of 200 pA at 0.5 V. Here, the back gate voltage is 60 V. The red dashed lines are the corresponding theoretically calculated DOS. [Reprinted (figure) with permission from [73] copyright (2021) by the American Physical Society].

In 2019, Yoo et al. [12] described the effect of atomic reconstruction which occurs due to a high energy cost of AA stacking configuration (higher local adhesion energy) compared to AB/BA stacking [74, 75]. At a critical transition angle of $\theta_c \sim 1°$, large triangular domains of commensurate Bernal stacking form with alternating AB/BA stacking. The domains are separated by incommensurate boundaries, which are commonly referred to as 'solitons' [76, 77]. The change in local stacking configuration, compared to larger twist angles, further alters the electronic properties. For instance, the band dispersion of 'magic angle' graphene in an atomically reconstructed moiré pattern is notably altered, with reduction in the DOS, though the underlying 'magic angle' physics still remains true as this is near the critical transition angle for reconstruction.

The difference between reconstructed and non-reconstructed systems becomes more apparent well below the critical transition where the electronic structure drastically changes to form a connected network of topologically protected conducting channels along the boundaries between Bernal stacked domains [12, 78]. The local

density of states mapping in 2.13b clearly highlights the (double) lined network connecting AA sites at V_s = -0.11 V; V_{gate} = 60 V [73].

2.2.3 Twisted Bilayer TMDs

Optical Studies

Though this body of work does not contain any optical studies, it is important to highlight the reasons why there is such interest in the study of twisted TMDs. There are significant differences in the moiré potential landscape where 3R type configurations have significantly higher confining potential and interlayer exciton emission compared to the 2H-type configuration [79] and therefore optical studies have focussed on the 3R-type configuration. The spatial variation in moiré potential generates a nano-patterned array of quantum dots that could be used for applications such as quantum computing and as single photon-emission [80]. This is because exciton energy peaks observed in photoluminescence spectra become altered by the periodic potential landscape generated by the moiré superlattice which impedes the free movement of electrons resulting in strong interlayer interactions.

Optical measurement techniques such as second harmonic generation (SHG) and low frequency (10-70 cm^{-1}) Raman spectroscopy have also been used for identifying polytypes and global twist angles. Second harmonic signal intensity is very sensitive to the breaking of inversion symmetry (stronger signal for 3R-type) [81, 82]. In Raman spectroscopy, there is a shift in shear and breathing modes which can be directly correlated with twist angle [83] and polytype [84].

Theory of Atomic Reconstruction in Twisted TMDs

Similar to graphene, twisted TMDs are expected to undergo reconstruction at a given critical twist angle owing to the tendency for energy minimisation of incommensurate moiré superlattices. Here, the strain induced by twisting into commensurate adjustment is concentrated at the edges of the formed domains.

Naik et al used Kolmogorov-Crespi potential to effectively describe relaxation in twisted TMDs but the high computational cost causes implications for the larger moiré unit cell ($< 3°$) [86]. Carr et al implemented a theoretical model with low computational cost (a continuum model with generalised stacking fault energy for interlayer interactions) for relaxation of MoS_2 bilayers and described how the

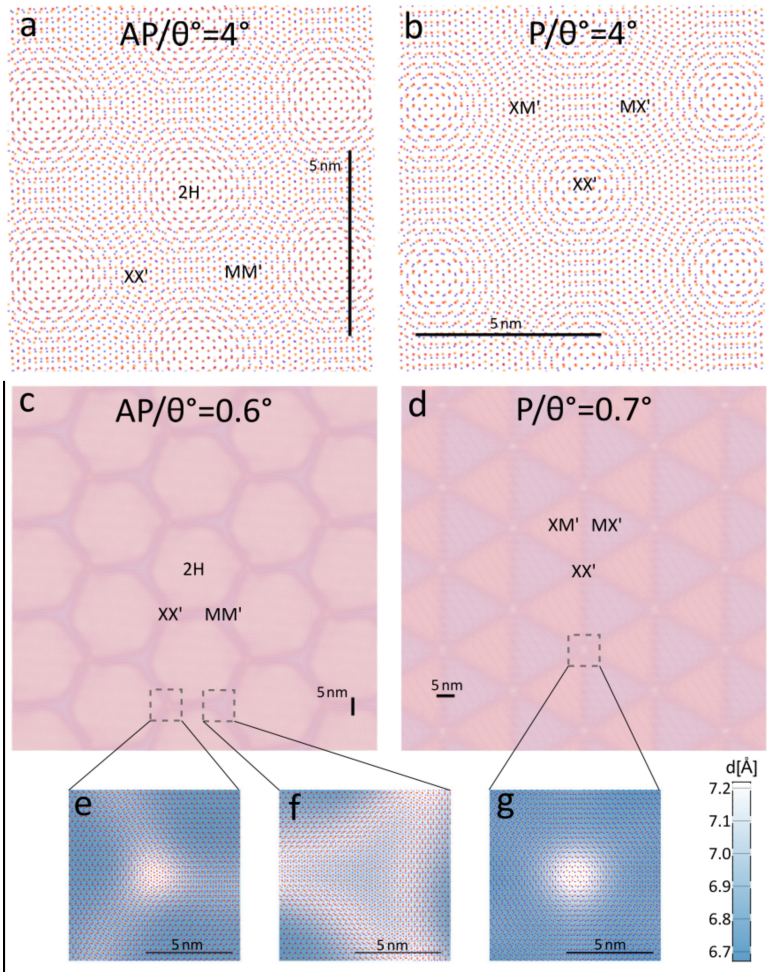

Fig. 2.14: **Theoretically calculated atomic structure of reconstructed lattices of WSe_2 homobilayer.** Rigid superlattices of **a** 2H-type (anti-parallel (AP)) and **b** 3R-type (parallel (P)) configurations twisted to $\theta = 4°$. Reconstructed superlattices of **c** 2H-type (anti-parallel) and **b** 3R-type (parallel) configurations twisted to $\theta = 0.7°$ and $0.6°$, resectively. **e-g** are the modelled atomic structure of the intersections of domain walls overlaid onto a spatial map of the varied interlayer distance [reprinted from [85]].

bilayers twisted to a small angle near two common polytypes (2H and 3R) to form commensurate domains of the stacking configuration with corresponding to the lowest energy stacking [87]. Enaldiev et al. applied a multiscale modelling approach to lattice reconstruction by considering interlayer adhesion energy (as modelled by density functional theory (DFT)) and elasticity theory. Both of these studies suggested that 3R-like reconstructed superlattice has two commensurate stacking configurations that are energetically equal (namely AB/BA or MX′/XM′ depending on prefered nomenclature) and should form triangular domains [85, 87] (see Fig.2.14). 2H-like stacking has inversion symmetry and therefore has only one low energy stacking configuration, 2H, which is expected to lead to hexagonal commensurate domains at $\theta \to 0°$ [85, 87].

These models suggest a far more complex energy potential landscape and the formation of metastable hexagonal and kagome-like structures for twisted angles in the range $0.5° < \theta < 2°$ [85, 87, 88]. Domain formation due to lattice reconstruction is dependent on lattice mismatch and will have significantly higher influence on twisted bilayers with < 2% mismatch.

Preliminary Studies of the Electronic Properties of Twisted Bilayer TMDs

Twisted bilayer TMDs are becoming a particularly exciting system for tuning electrical properties. Early research focused on heterobilayers of TMDs which have an inherent lattice mismatch which allows for the epitaxial growth of perfectly aligned large area moiré superlattices. Early STM studies on perfectly aligned MoS_2/WSe_2 (where $\lambda \sim$ 8.7 nm) observed that the direct band gap (typically observed in monolayer TMDs) is preserved in the bilayer system and the valence and conduction band edges reside at the same K-point but in different layers [89]. Fig. 2.15c illustrates the long range moiré periodicity of the MoS_2/WSe_2 electronic structure which is generated by local band gap modulation due to local variations in atomic registry. Pan et al. were also able to demonstrate quantum confinement in the same system [90]. This is apparent in the local STS data taken of the three different high symmetry stacking configurations (see Fig. 2.15d-e) in which we observe sharp peaks at the valence band edges in locations B and C as well as in B in the conduction band edge. More recent studies of heterobilayers have revealed Mott-like and Wigner insulating phases identified in WS_2/WSe_2 by using optoelectronic measurements which overcome the inherently high contact resistance due to metal-semiconducting Schottky barriers [91]. The study

also found that relative spin relaxation time increases when operating in the Mott-like phase.

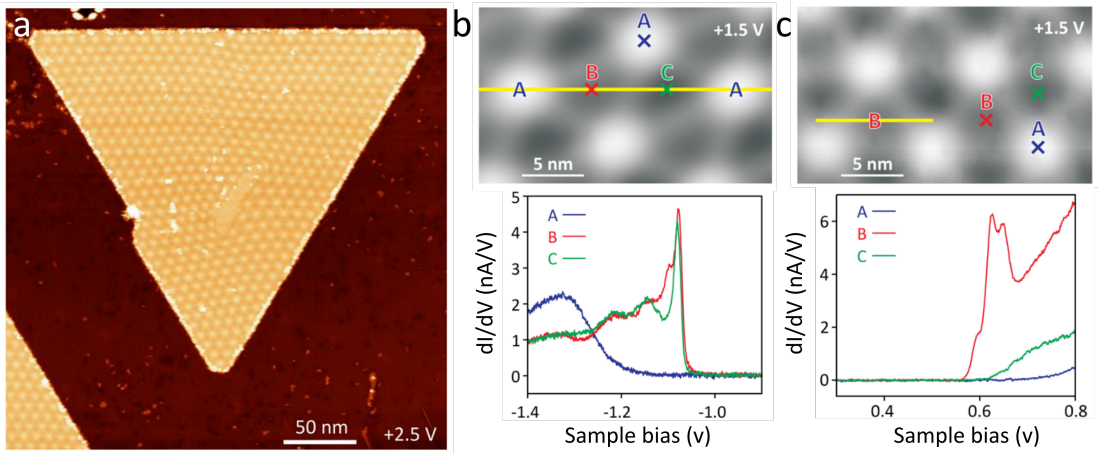

Fig. 2.15: **Quantum confinement in twisted heterobilayer TMDs. a** STM topography image of aligned MoS_2/WSe_2 grown by metal-organic chemical vapour deposition. STS spectra in the **b** valence and **c** conduction bands corresponding to the topographic image above each plot [reprinted with permission from [90] copyright (2021) by the American Chemical Society].

Lattice reconstruction is expected to have a significant effect on electronic properties of twisted homobilayers. Some experimental work has been done on homobilayers but in the regime near the critical angle for reconstruction. Here, ultra flat bands have been observed in WSe_2 in the 3R-type configuration and the 2H-type configuration [92, 93]. Additionally, there is no 'magic angle' in twisted TMDs which means that flat bands persist over a wide range of twist angles [92, 93].

Theoretical Predictions of the Electronic Properties of Reconstructed Twisted Bilayer TMDs

Ferroelectric behaviour in 2D materials has garnered a lot of excitement in recent years due to the interest in replacing current silicon based semiconductor technologies used for memory based devices [94]. Here, ferroelectricity describes a material with two or more polarisation states that can be switched upon application of external electric field, strain and/or temperature [95]. A number of key challenges remain in finding suitable replacement materials that are non-volatile (their binary logic "0" and "1" states remain when there is no power input), operate at room temperature, compatible with current semiconductor technologies and are suitable for the continuously reducing dimensions of electronic devices [96]. It has become no longer possible to reduce the

lateral dimensions of traditional ferroelectric materials such as $BaTiO_3$ below a critical thickness ($\sim$ 3 nm) [97], where the out-of-plane ferroelectricity disappears due to the effects of the electrostatic field that reduces polarisation stability [98]. So far, 2D materials such as such as SnTe [99, 100] and In_2Te_3 [100] have revealed in-plane room temperature ferroelectricity and In_2Te_3 [101], WTe_2 [102] as well as $CuInP_2S_6$ [103] have revealed out-of-plane ferroelectricity. Out-of-plane ferroelectricity is much more desirable for high-density memory storage applications [104].

More recently, out-of-plane ferroelectric behaviour has been observed in minimally twisted bilayer/multi-layer hBN with experimental observations in eletrical transport measurements [105] as well as scanning probe microscopy techniques such as Kelvin Probe Force Microscopy (KPFM) [106] and Electrostatic Force Microscopy (EFM) [107]. This creates a two-layer thick ferroelectric material in which adjacent domains have oppositely polarised dipoles. DFT calculations highlight that the lack of inversion symmetry in 3R-type bilayers can cause layer wave-function asymmetry at the Q-point and K-point band edges, which are located in MX$'$ and XM$'$ domains, leading to different tunnelling characteristics between the two domain types [85]. Inversion asymmetry in MX$'$ and XM$'$ domains is also expected to lead to charge transfer and therefore a potential difference ($\Delta^P \sim 60$ mV) between the top and bottom layers [108]. The possibility of ferroelectric behaviour in TMDs opens new possibilities since TMDs are not only semiconducting but also have strong light-emitting capabilities [36] which means that they can be directly integrated into semiconductor technologies (such as silicon based integrated circuits) and provide novel functionalities, such as light emitting memristors.

For 2H-type bilayers, it is expected that the inhomogeneous strain concentrated at the intersections of domain walls (MM$'$ and XX$'$) can create spatially separated pseudomagnetic fields (B_* = 20-30 Tesla) for electrons and holes [85]. This means that the concentrated strain at the domain walls and intersections induces similar electron densities (a piezoelectric/strain induced charge) that would be expected when a magnetic field is applied [85, 109]. This phenomena can be likened to quantum-dot wells with a depth of $\sim$ 150 meV [109].

2.3 Summary

In this chapter, I have introduced 2D materials and discussed the properties of the three materials groups that represent the main focus of this thesis including graphene, hBN and TMDs. The concept of moiré superlattices (the field of twistronics) has been introduced and the key findings of graphene/hBN, twisted bilayer graphene and twisted bilayer TMDs have been discussed in detail. Importantly, it was highlighted that the strong light-matter interaction of TMDs and the potential to tune the optoelectronic properties through interfacial twist angle renders them highly interesting platforms to study correlated physics.

At the start of my project, there was still a lack of experimental evidence of the structure of reconstructed superlattices of TMDs at the atomic scale. Although techniques such as STM are capable of atomic resolution, the image contrast is due to the electronic structure which doesn't directly correlate to the underlying atomic structure and therefore other imaging techniques such as atomic resolution Scanning Transmission Electron Microscopy (STEM) should be used.

Another key challenge that was highlighted was the direct correlation of the local structure of moiré superlattice to their physical properties. This type of information is essential to the interpretation of their novel electrical and optical properties especially with two possible regimes including rigid and reconstructed moiré patterns as well as two possible polytypes. Unfortunately, both SHG and Raman spectroscopy characterisation methods are not sensitive enough to local variations of twist angle due to contamination bubbles, cracks and creases that have accumulated during fabrication. This is because of the diffraction-limited diameter of the laser used for probing optical properties. Additionally, the majority of microscopy techniques are surface sensitive, therefore samples encapsulated with hBN have been challenging to image. This is currently the biggest bottleneck to further research. The aforementioned challenges can be overcome with key characterisation techniques such as atomic force microscopy and scanning electron microscopy (back-scattered electron channelling contrast imaging) which has been one of the primary aims in this project.

Chapter3

Fabrication Techniques

3.1 Introduction

This chapter will cover the sample fabrication techniques including the mechanical exfoliation, crystal identification, crystal transfer as well as methods to reduce sample contamination. When considering suitable fabrication methods of vdWs heterostructures, it is optimal to select a method where possible contamination such as polymer residue is minimised. A good example of this is when hBN is used to pick-up subsequent flakes to construct a vdWs heterostructure where hBN encapsulation is required [110]. This reduces the amount of possible polymer contamination due to the use of clean vdWs interfaces instead of a polymer for each consecutive transfer. In instances where encapsulation is not possible (i.e. samples required for surface studies) the PMMA dry transfer technique is used to build the heterostructure layer-by-layer. vdWs heterostructures were constructed using the PMMA dry transfer process [111] for the deterministic placement of the aforementioned layered materials. Twisted homo/hetero bilayers are the main focus of the studies in this thesis and therefore will also be discussed in some detail.

3.2 Mechanical Exfoliation and Crystal Identification

To date, mechanical exfoliation from bulk crystals provides the highest quality 2D materials required to study the fundamental physics in novel vdWs heterostructures. All the vdWs materials discussed in this thesis have been mechanically exfoliated

using an adhesive tape and cleaved onto various substrates depending on the material and/or step in the fabrication process. Generally speaking, high-tack (where tackiness refers to the strength of adhesion) tape such as (ELP BT-150E-KL) was used for TMDs and low-tack tape such as (ELP BT-130E-SL) was used for graphite/graphene and hBN mechanical exfoliation. Providing optimal coverage of the thin 2D crystal (when exfoliated onto a substrate), the device quality is reliant on high quality low-defect density bulk crystals. The maximum lateral dimensions of an exfoliated monolayer or few layer crystal is also reliant on the lateral size of the source crystal. The coverage is dependent on how well a crystal will adhere to the surface of a substrate and how easily the crystal is released from the adhesive tape. This is also dependent on factors including surface roughness/cleanliness of the substrate, humidity as well as surface chemistry of the crystal/substrate. The highest quality hBN was produced by the group of Taniguchi and Wantanabe [23] and is used throughout the body of this work. The TMDs used in this project are all purchased from hq graphene. Bulk graphite crystals are purchased from NGS Naturgraphit GmbH.

The easiest method for identifying the layer thickness of exfoliated crystals is by utilising visible light optical microscopy. In this work a Nikon Eclipse Lv150 series microscope with a DS-Ri2 camera was used. The optical contrast of 2D materials is determined by the interference of light in the cavity formed by the 2D material, dielectric (SiO_2) layer and the reflective silicon underneath. Therefore the contrast was optimised by selecting a silicon wafer with an SiO_2 thickness that produced optimal interference conditions in the visible light. For example, an oxide thickness of $\sim$ 290 nm is used for monolayers of graphene. In addition, contrast can be further enhanced using a narrow (green) band-pass filter in the optical microscope [112]. The contrast of hBN monolayers is significantly lower due to the sizable band-gap of the material, however, contrast can be improved using the oxide thickness of $\sim 80 \pm 10$ nm and a band-pass filter with wavelength of $\lambda \sim 590$ nm [113]. Optical contrast is equally important for identifying bulk crystals to be used as substrates with large area atomically-flat area with no step edges. In Fig. 3.1d, the bulk hBN crystal can be seen with a characteristic turqouise colour which corresponds to a thickness of $\sim$ 15-30 nm. Monolayers of TMDs have optimal contrast with SiO_2 thickness of $\sim$ 90 nm [114] and due to its band structure and strong light-matter interaction, optical contrast is sufficient with white light. When using silicon substrates coated with polymers (PPC or PMMA/PVA) it is important to replicate the relative contrast achieved with oxidised

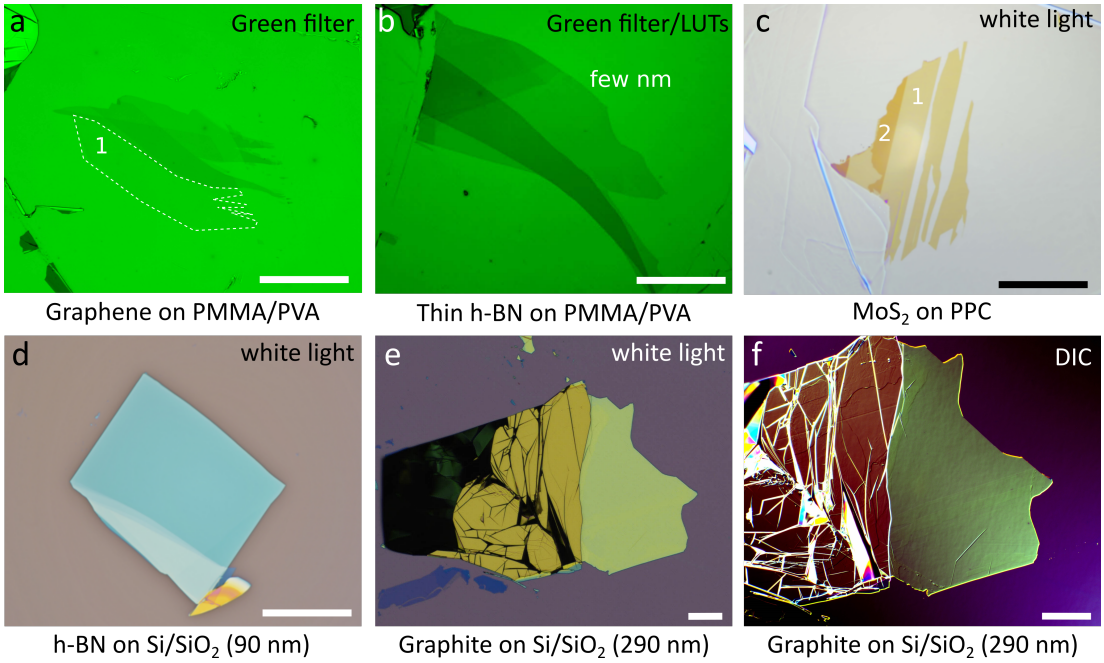

Fig. 3.1: **Exfoliation of monolayer and bulk van der Waals crystals on different substrates.** **a** Optical image of monolayer graphene on PMMA/PVA (outlined in white dashed line) using a green filter (λ = 590 nm). **b** Optical image of 2-3 nm hBN on PMMA/PVA using a green filter and contrast enhanced with LUTs. **c** Optical image of monolayer MoS_2 on a PPC coated Si/SiO_2 (90 nm) substrate using white light. **d** Optical image of bulk hBN on Si/SiO_2 (90 nm) substrate using white light. **e** Optical image of graphite on a Si/SiO_2 substrate using white light and **f** the same bulk crystal with contrasted enhanced using the DIC imaging mode. Scale bars in **a-d** are 50 μm and **e-f** are 100 μm.

silicon to achieve good visibility of 2D materials (see Fig. 3.1c).

The three main substrates used in mechanical exfoliation of vdWs crystals in this work included oxidised silicon wafers (where the oxide layer of 290 nm or 90 nm is used depending of the vdWs crystal), polypropylcarbonate (PPC 5 %) or Polymethylmethacrylate (PMMA 8 %)/ polyvinyl acetate (PVA 3 %) where the polymer solutions are spin coated onto a silicon wafer substrate. Typical uses of each substrate are as follows;

(1) Oxidised silicon wafer: Primarily used for exfoliation of bulk layered materials to be used as an atomically flat substrate. This can either be hBN or graphite and employed here as atomically flat substrates for twisted bilayer TMDs. Bulk crystals with relative thickness of 30-60 nm are selected using optical microscopy for optimal atomic 'flatness'. In Fig. 3.1d, the turquise colour of the hBN crystal is reflective of a 20-30 nm thickness. At this thickness it is possible to optically identify step edges on the surface (undesirable for an atomically flat substrate), however thicker crystals require optical enhancement with the use of additional differential interference contrast (DIC). The DIC imaging mode enhances the edge contrast of the crystal giving an almost 3-dimensional appearance as demonstrated in Fig. 3.1f. This allows for the identification of cracks, folds, step edges, surface roughness and contamination which are otherwise hard to notice in the standard reflected white light imaging (see Fig. 3.1e). Graphite has been used in this work as an atomically flat conductive substrate for c-AFM and as a back-gate for electrical transport measurements. Si/SiO_2 substrates can also be used to apply a back-gate (V_{BG}) of vdWs heterostructures if necessary. In the case where a conductive substrate is required, the silicon can be coated with a conductive layer such as gold or platinum to allow an electrical connection to be made macroscopically at the edge of the silicon substrate. Alternatively, metallic contacts can be made directly to the graphite crystal using electron beam lithography or a stencil mask (see Section 3.6). To ensure good mechanical exfoliation and flake adhesion, the oxidised wafer is typically plasma cleaned using an argon/oxygen gas mixture in a Moorfield Nano-etcher (pressure $\sim$ 5 x10^{-2}).

(2) PPC coated oxidised wafer: PPC substrate has been primarily used here to exfoliate air-sensitive materials in an atomosphere-controlled environment such as a glovebox where the fabrication of a crystal suspended on a PMMA membrane (to be discussed in the next section) is not possible. Here, the PPC solution is spin coated (at 3000 rpm) onto a Si/SiO_2 (90 nm) substrate and baked at 150° for 5 mins to remove the

solvent. In Fig. 3.1c the optical colour contrast of the MoS_2 monolayer is dictated by the total thickness of the PPC and the SiO_2 dielectric stack, therefore spin conditions of the PPC solution and its concentration have been optimised for optical contrast. PPC has the advantage of significantly enhancing exfoliated crystal density as well as producing large monolayers (>100 μm) across the substrate surface. Disadvantages include higher levels of surface PPC residue remaining on 2D materials after the contact. For reduced contamination, PMMA can be used as an alternative.

(3) PMMA/PVA coated wafer: This substrate is utilised for the deterministic transfer of monolayer/few-layer vdWs materials to construct, layer-by-layer, a vdWs heterostructure [111]. Here, the PMMA layer acts as the carrier layer and PVA is the sacrificial layer used to release the membrane from the silicon wafer. Fig. 3.1a-b demonstrate the typical optical contrast of monolayer graphene and few layer hBN, respectively. As before, the total thickness of PVA/PMMA stack is optimised to achieve good contrast of thin crystals using the green band-pass filter.

3.3 PMMA Dry Transfer Technique

To prepare the PVA/PMMA substrate, a PVA solution (3 % 50 K dissolved in H_20) is spin coated onto a 4 inch silicon wafer using a spin speed of $\sim$ 3000 rpm for 90 seconds. The substrate was annealed at 130 °C for 5 minutes. A PMMA solution (8 % 950K dissolved in anisole) is then spin coated (2700 - 3000 rpm depending on the batch of PMMA used to achieve good optical contrast) for 90 seconds. The substrate is annealed again at 130 °C for 5 minutes to evaporate any remaining solvent. Then, the following steps are taken to produce a free-standing PMMA membrane with a selected 2D crystal attached;

(a) Exfoliation: Prepare a piece of tape with a high density coverage of thick 2D crystals. Dice up the 4 inch PMMA/PVA covered wafer into square pieces (roughly $\sim$ 5 cm^2) and place those on a hot plate for a few minutes (at 130 °C). Remove the PMMA/PVA covered wafer from the hot plate, immediately cover with the prepared tape and peel it away after $\sim$ 1 minute.

(b) Cut out membrane: Using an optical microscope, a crystal of desired thickness/size is located and the membrane is "cut out", by drawing a circular ring around the crystal ($\sim$ 5 mm in diameter) separating it from the rest of the PMMA layer to expose the PVA sacrificial layer underneath (see Fig. 3.2b).

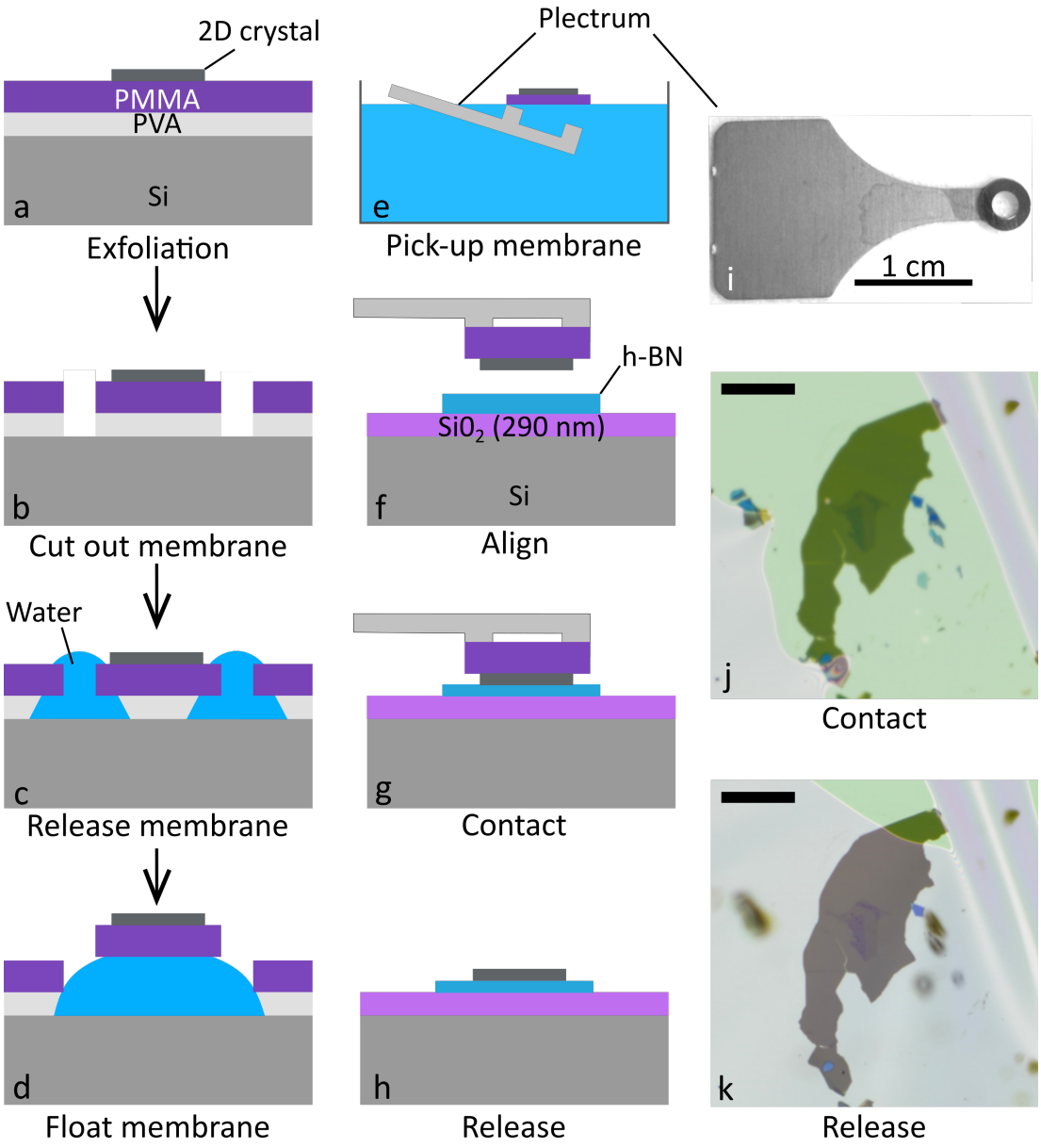

Fig. 3.2: **Step-by-step schematics for the PMMA dry transfer technique. a-e** Fabrication steps involved in the preparation of a 2D crystal suspended on a PMMA membrane. **f-g** Using the PMMA membrane to deterministically place and release crystal on top of a vdWs heterostructure. **i** Photograph of the stainless steel plectrum used to pick up the PMMA membranes (scale bar is 1 cm). Optical microscope images of the two main crystal transfer steps including **j** contact of the membrane supporting the 2D crystal and the substrate and **k** release of the membrane that correspond to **g** and **h**, respectively (scale bars are 20 μm).

(c) Release membrane: Deionised water is applied to the edges of the circularly cut membrane to dissolve the PVA layer underneath and detach the PMMA layer.

(d) Float membrane: The PMMA membrane is eventually released and left floating on the droplet of water used to dissolve the PVA as shown in Fig. 3.2d.

(e) Pick-up membrane: The floating PMMA membrane is transferred from the silicon substrate into a beaker of deionised water where a stainless steel plectrum (see Fig. 3.2i) can be used to pick up the membrane from underneath. In order to ensure adhesion of the PMMA membrane to the plectrum, the plectrum is firstly coated in PMMA solution (the same used for the PMMA membrane) and annealed on a hotplate (150 °C for 10 minutes). When the PMMA is suspended on the plectrum, it is annealed at 90 °C until the residual water has evaporated.

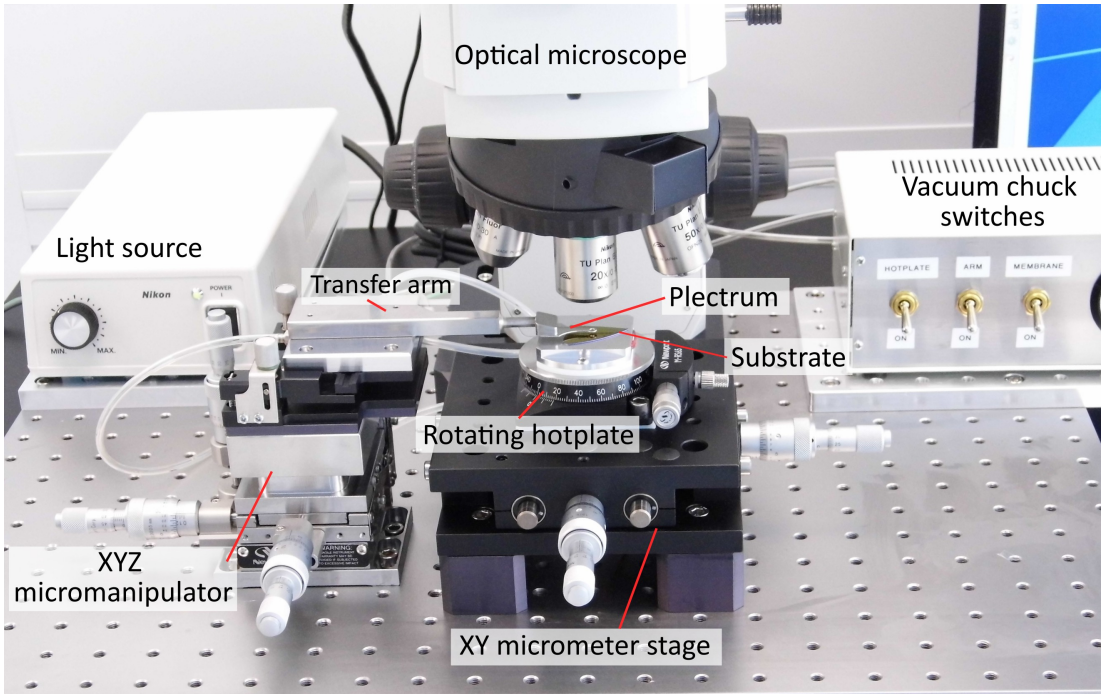

Fig. 3.3: **The transfer system utilised for PMMA dry-transfer of 2D crystals.** The primary components include a transfer arm, rotating hotplate, XY micrometer stage, XYZ micromanipulator, vacuum chuck and an optical microscope.

The prepared PMMA membrane can then be selectively placed onto a substrate (such as bulk hBN or graphite) using a custom-built micro-mechanical transfer system (see Fig. 3.3) that was developed at Manchester University. The transfer system is comprised of a rotating hotplate, XY micrometer stage and a XYZ micromanipulator holding the transfer arm using a vacuum chuck. The plectrum supporting the PMMA membrane can be attached to the transfer arm with an additional vacuum chuck and the substrate can be placed onto the rotating hotplate which, again, is held in place

with a vacuum chuck (see Fig. 3.3). Then, the PMMA membrane supporting the suspended crystal is aligned over the desired substrate using the XY micrometer and an optical microscope as shown in Fig. 3.2f. The membrane is lowered using the XYZ micromanipulator as seen in Fig. 3.3 until contact is made with the bottom substrate (see Fig. 3.2g and j). The bottom substrate (sitting on the rotating hotplate) is heated to $\sim$ 60 °C to improve the adhesion with the PMMA membrane. Once in contact, the membrane is slowly lifted off leaving the crystal behind as illustrated in Fig. 3.2h and k. Generally speaking, a vdWs crystal will prefer to adhere to another vdWs crystal compared to the PMMA membrane. It is also important to note that for release onto a bottom crystal, the suspended crystal must be smaller than the bottom. This can work in the reverse i.e. pick-up a number of crystals consecutively before the resulting stack is released onto a bulk bottom crystal.

The PMMA dry transfer can also be performed in a argon-atmosphere glovebox when air-sensitive materials are being utilised. The same method of producing a PMMA membrane is used but instead the membrane is left blank. The 2D crystals are instead exfoliated onto a PPC-coated oxidised silicon wafer inside the glovebox. To prepare the PPC substrate, a 4 inch (Si/SiO_2 90 nm) wafer is spin coated with a solution of 5 % PPC dissolved in anisole using a spin speed of $\sim$ 3000 rpm for 90 seconds. The coated wafer is annealed at 150 °C for 10 minutes. The wafer can then be diced up and transferred into a glove-box, following which, it must be annealed at 80 °C for a few minutes to remove the residual water vapour on the surface of the PPC (the coated wafer is kept on the hotplate for the tape exfoliation step). Bulk crystals are then exfoliated using the high-tack tape (ELP BT-150E-KL) onto the PPC substrate whilst still on the hotplate and slowly peeled off. Once a crystal is optically located, the transfer stage should be heated to $\sim$ 55 °C (roughly the glass transition temperature of PPC) to allow for the release of the crystal. The blank PMMA membrane can now be brought into contact with the crystal/PPC for subsequent pick-up. The crystal is now suspended on a PMMA membrane and ready to be implemented into a vdWs heterostructure.

3.4 Fabrication of Twisted Bilayer Heterotructures

Crystalline materials with a hexagonal crystal lattice (such as graphene, hBN and TMDs) often cleave along preferred crystallographic planes corresponding to either zigzag or armchair orientation. This can be experimentally observed in monolayers of graphene with a significant number of straight edges with angles that are multiples of 30° [115]. Angles of 60°/120° correspond to a zig-zag/zig-zag or armchair/armchair edge and angles of 30°/90° correspond to armchair/zig-zag edges. To control the twist angle between two dissimilar 2D materials, 2D crystals with straight crystallographic edges must be selected. Rotational alignment can be achieved by matching edge orientations in the two different crystals. TMD bilayers with trigonal prismatic metal coordination are able to produce two possible moiré superlattices including a 3R-type (unit cells are parallel (0°) with each other) and a 2H-type (unit cells are anti-parallel (180°) to each other) configurations referring to the two possible polytypes that can be created in a bilayer stack. It is nearly impossible to selectively construct one type over the other as there is an equal probability to create each type. Furthermore, accuracy of rotational alignment is limited by the optical microscope resolution as well as the accuracy of deterministic placement when using the transfer system, when trying to resolve the straight edges (i.e. $\pm$ 0.1°).

Fabricating twisted homobilayers can be achieved simply by cutting a single monolayer into two sections and re-stacking these into a bilayer. Unlike heterobilayer fabrication, this method does not rely on the alignment of crystallographic edges or optical microscope resolution. When the monolayer is cut in half, the effective rotational angle between the two monolayer segments is 0° and can be selectively rotated to the desired twist angle with high accuracy determined by the quality of stage as well as polymer membrane deformations. This was first achieved by Kim et al. [116] by bringing a relatively thick hBN crystal into contact with one half of a graphene monolayer using an alternative dry-transfer technique that uses a bulk Polydimethylsiloxane (PDMS) stamp supported by a glass slide instead of a steel plectrum (for more details see ref. [111]). The part of the monolayer in contact with the hBN is picked up and the other segment remains on the oxidised silicon wafer. The substrate is twisted and the second graphene segment is then picked up with

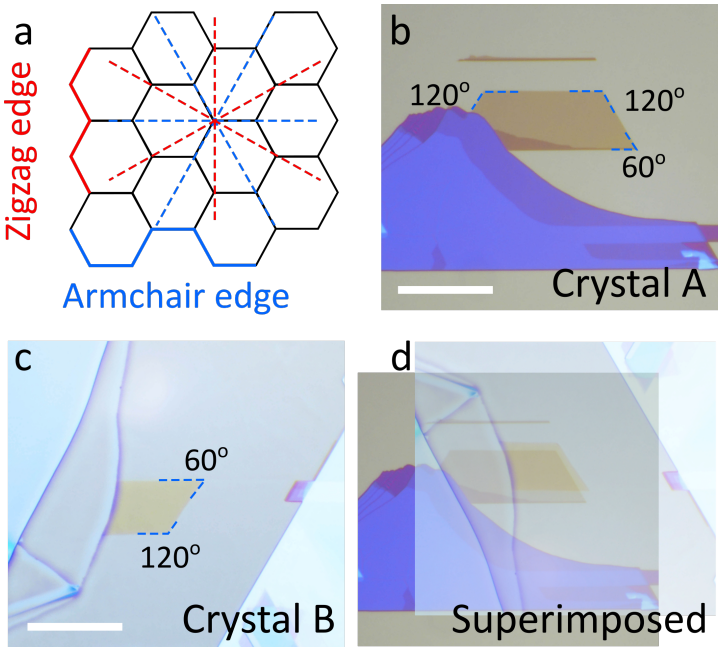

Fig. 3.4: **Fabricating twisted hetero-bilayers of TMDs.** The two possible crystallographic orientations of vdWs materials with a hexagonal crystal lattice include zigzag (red dashed lines) or armchair (blue dashed lines). If two crystals (**b-c**) possess one or more edges of the same orientation they can be **d** optically aligned where the edges lay parallel to each other (scale bars = 20 μm).

hBN/Graphene stack. It is possible that anisotropic strain in the moiré superlattice can be reduced by cutting a monolayer crystal prior to pick-up which can be achieved with an AFM tip or by laser cutting [117].

In instances where encapsulation with hBN is not possible, such as samples for STEM/SPM studies, a modified PMMA dry transfer technique can be employed. In Fig. 3.5 one half of a monolayer (mechanically exfoliated onto a PPC coated substrate) is selectively picked up by a blank PMMA membrane. Then, the transfer stage is rotated to angles close to $\theta \sim 0°$ for parallel alignment with a 3R-type stacking configuration or angles close to $\theta \sim 180°$ for anti-parallel alignment with a 2H-type stacking configuration (as shown in Fig. 3.5b). This allows for a blank PMMA membrane to be used to pick-up subsequent segments of a single monolayer by heating the PPC coated wafer to 55°C (making PPC less adhesive than the PMMA) to release the monolayer.

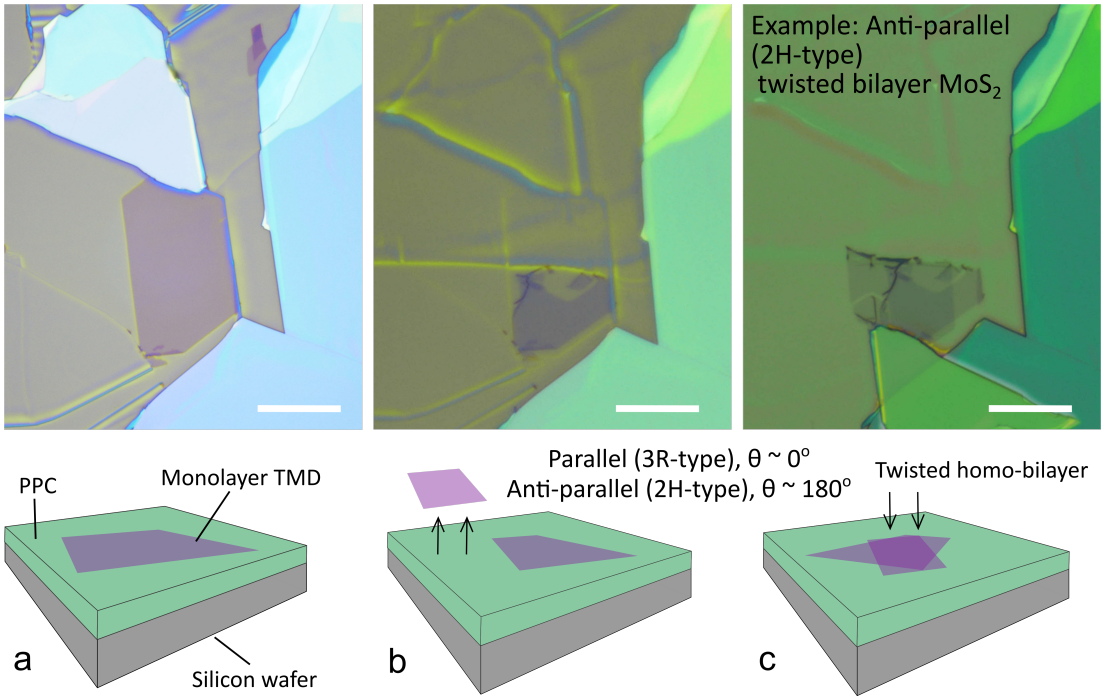

Fig. 3.5: **PMMA dry transfer twisting technique for homo-bilayers of TMDs. a** A large monolayer is selected using optical microscopy. **b** One half of the monolayer is selectively picked up with a PMMA membrane. **c** The remaining half can be rotated to angles close to 0° or 180° to selectively construct a 3R-type or 2H-type superlattice, respectively. All scale bars are 20 μm.

3.5 Contamination and Air-Sensitivity in vdWs Heterostructures

It has been shown that group VI TMD's have the lowest oxidation rate and are able to withstand $\sim$ 500-700 K before they start to breakdown[118, 119]. Though, even stable vdWs materials such as graphene show improved optoelectronic performances after encapsulation with a hBN capping layer, primarily due to the improved dielectric environment and atomically flat surface of hBN [24]. Additional benefits of encapsulation include prevention of contamination during device fabrication and storage. For optimal results, the fabrication process including both encapsulated and non-encapsulated devices should be performed in a glove box with a controlled environment of inert gas such as argon (can reduce interlayer contamination).

It is widely known that contamination such as polymer residue, airborne and mobile surface hydrocarbons can become trapped between layers in vdWs heterostructures. The trapped contamination leads to bubble formation under the surface layer. It

is common for relatively small bubbles in close proximity, particularly when the heterostructure is heated > 60°C, to coalesce into larger bubbles leaving behind larger regions of clean interfaces. This is a process known as 'self-cleaning' and is promoted by the vdWs forces between the top and bottom layer(s). The size and density of contamination bubbles limit the maximum size of fabricated devices.

Graphene and hBN are very good at self-cleaning, whereby contamination converges into larger pockets leaving large atomically sharp interfaces [120]. TMDs have a similar (though slightly weaker) self-cleaning ability, but other layered oxides such as muscovite mica and bismuth strontium calcium copper oxide do not, most likely due to the different interactions between the contaminant molecules and the crystal surface preventing diffusion, and therefore, self-cleaning [121]. In addition, the ability to self clean is heavily dependent on the interface roughness, e.g. etching processes such as reactive ion etching are common causes of increase surface roughness. A common method to remove contamination is by thermal annealing in high vacuum whereby thermal energy causes contamination to further aggregate although the maximum annealing temperature is dependent on thermal stability of the selected material.

Due to the lower adhesion energy of commensurate stacking, thermal annealing can be used to macroscopically align monolayer crystals in vdWs heterostructures such as graphene/hBN which can be extremely beneficial to the efficiency of sample fabrication of aligned devices [55, 122]. However, samples such as 'magic angle' bilayer graphene possess physical properties that are highly sensitive to twist angle and thermal annealing can be highly detrimental to achieving the correct rotational twist angle; therefore in this instance annealing should be avoided and it is imperative to minimise the possibility of contamination during the fabrication process in order to make devices with clean interfaces over a large area. One method is to use much slower flake contact/release times (up to a few hours) and raising the temperature during the flake transfer process in order to push out the mobile contamination from the collapsing interface during the vdWs transfer technique [110, 123].

Another possibility for removing contamination is the method of 'nano-squeegee' cleaning, where an AFM tip is used to physically brush the surface contamination as well as interlayer contamination. This can even be achieved on encapsulated samples where inter-layer contamination is buried deep within the heterostructure [124]. This technique is demonstrated in Fig. 3.6b-c using a monolayer WSe_2

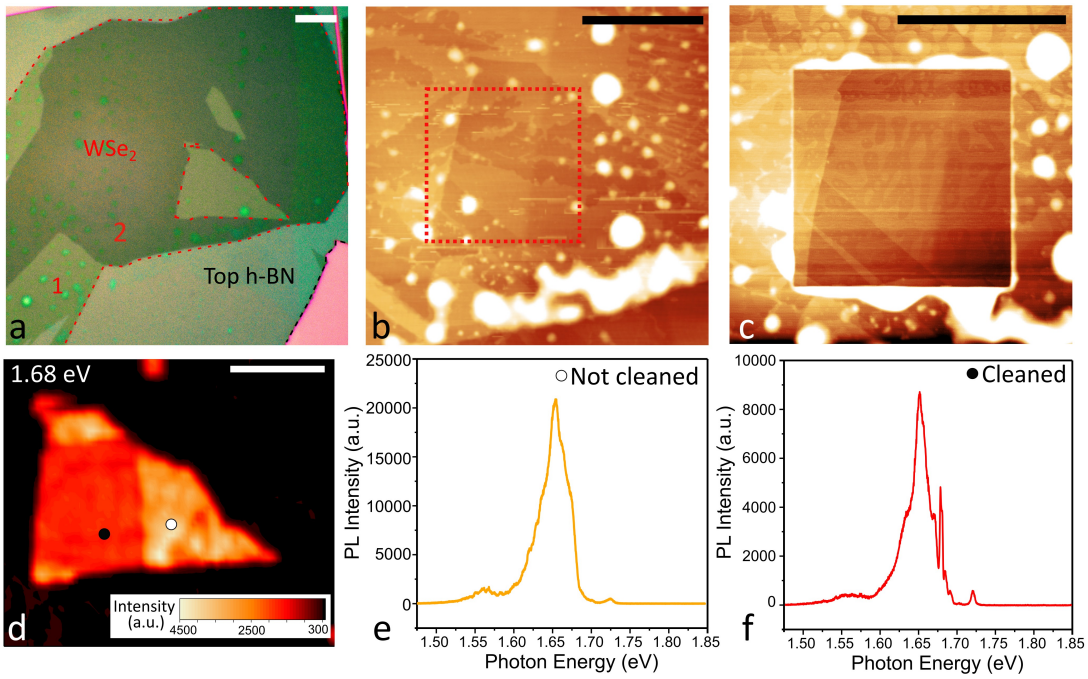

Fig. 3.6: **Removing inter-layer contamination in monolayer WSe_2 using the nano-squeegee technique.** **a** Optical image of the encapsulated heterostructure where the red dashed lines indicate the WSe_2 (numbers represent layer thickness of the WSe_2) and the black dashed line indicates the top hBN. Tapping mode topography image of hBN encapsulated WSe_2 **b** before and **c** after the nano-squeegee cleaning technique was performed. **d** Room temperature photoluminescence (PL) map of PL intensity at a photon energy of 1.68 eV. Low temperature PL single spectra of the **e** un-cleaned and **f** cleaned area taken at the location indicated by the white and black dot in the RT photoluminescence intensity map, respectively. Scale bars for **a-c** are 20 μm and **d** is 10 μm.

sample (highlighted by the dashed red lines in Fig. 3.6b) encapsulated with $\sim$ 40 nm thick hBN (highlighted by the dashed black line in Fig. 3.6a). Here, an AFM scan area of 10 x 10 μm was selected on a monolayer region of the encapsulated sample and was repeatedly raster scanned in contact mode with increasing force until the contamination was no longer visible. For this experiment, Bruker AFM probes (BRUKER TESPA-V2) with high nominal stiffness of 37 N/m and 320 kHz resonant frequency were used in order to apply forces up to 50-60 nN onto a vdW heterostructure. Typically a line density of 512 lines/scan or higher was used to ensure the overlap between adjacent scan lines ensuring contamination was pushed out. It is clear from Fig. 3.6c that the contamination bubbles were sufficiently removed (note that surface hydrocarbons are still visible). To confirm the removal of interlayer contamination, room temperature (Horiba Raman spectrometer) and low temperature (4 K in a cryostat) photo-luminescence (PL) measurements were performed on the cleaned area as well as an un-cleaned area. The room temperature PL intensity map (532 nm laser, 600 gr/mm grating and 0.1 $\%$ laser filter) in Fig. 3.6d highlights a reduced intensity at 1.68 eV in the cleaned region, suggesting that the PL full-width-half-maximum (FWHM) is becoming narrower. At low temperatures the un-cleaned area displayed a single broad peak centred around 1.65 eV whereas the cleaned sample demonstrated multiple sharp peaks with the first centred around 1.69 eV. Previous optical studies demonstrated that hBN encapsulation leads to narrowing of the neutral exciton emission in TMDs as the intrinsic quality of the crystal is retained [125]. This is also improved when the inter-layer contamination is removed. The optical measurements were performed by J. Zultak.

3.6 Fabrication of Electrical Contacts

A number of characterisation techniques such as electrical scanning probe microscopy and electrical transport measurements require electrical connection of the vdWs heterostructure to external measurement circuitry. Depending on the specific device requirements, the heterostructure can either be transferred onto a metallic coated silicon wafer or patterned metal contact pads can be evaporated on top of the structure. For electrical scanning probe microscopy techniques such as Kelvin probe force microscopy, the vdWs heterostructure can be electrically grounded to prevent surface charging effects. The ground refers to a common electrical current path that provides

a means to limit the build-up of charge when a voltage is applied. The techniques used in this thesis include the use of TEM grid shadow masks and electron-beam (e-beam) lithography as tools to pattern metal contacts. E-beam evaporation was then used for metal deposition.

Shadow Mask Contacts

For all scanning probe studies, it is preferable to avoid the use of lithographic patterning as it typically results in a significant amount of residual surface contamination from polymer resists and liquid processing [126]. To avoid this, copper TEM grids can be used as shadow masks for metal deposition.

A shadow mask is a mechanical mask that is placed over the top of the vdWs heterostructure but is not directly touching the surface (metals are not atomically flat and there will always be an air gap). Here, the patterned shadow masks act to shield regions underneath the mask leaving the exposed regions free for metal deposition. A short ($\sim$ 8 mm) copper wire was attached to the back of each TEM grid (with silver paste) to aid with the handling of grid (directly handling the grids with tweezers can cause significant damage) and to assist with the deterministic placement over the vdWs heterostructure. The shadow masks were aligned using an optical microscope and manually positioned with an accuracy of $\pm$ 5 μm. Then, the TEM grid shadow masks are secured to the Si/SiO_2 substrate with conductive silver paste. It is important that the silver paste is particularly viscuous to avoid it leaking under the TEM grid (as seen in 3.7c) which can lead to electrical shorting or sample damage.

For two-terminal electrical devices (such as the SEM device illustrated in Fig. 3.7) two large contact pads were required. Fig. 3.7a demonstrates a typical two-terminal vdWs heterostructure with a metal contact pad connected to a graphite backgate and a graphene top-gate where the spacing between metal contact pads is $\sim$ 90 x 90 μm. For the SEM device measurements, the metal contact pads are connected to external thin (0.25 mm diameter) gold wires secured with silver paint. In the photograph shown in Fig. 3.7c, the device is glued (with silver paint) to the back-side of a chip carrier to allow the vdWs device to be electrically isolated from the steel SEM sample holder underneath. Here, the top gate and the bottom gate are electrically isolated from the rest of the silicon wafer such that the gates can be independently controlled. The rest of the silicon wafer is electrically connected to the steel SEM sample holder by an additional bonding wire indicated by the orange dashed circle in Fig. 3.7c. Similarly,

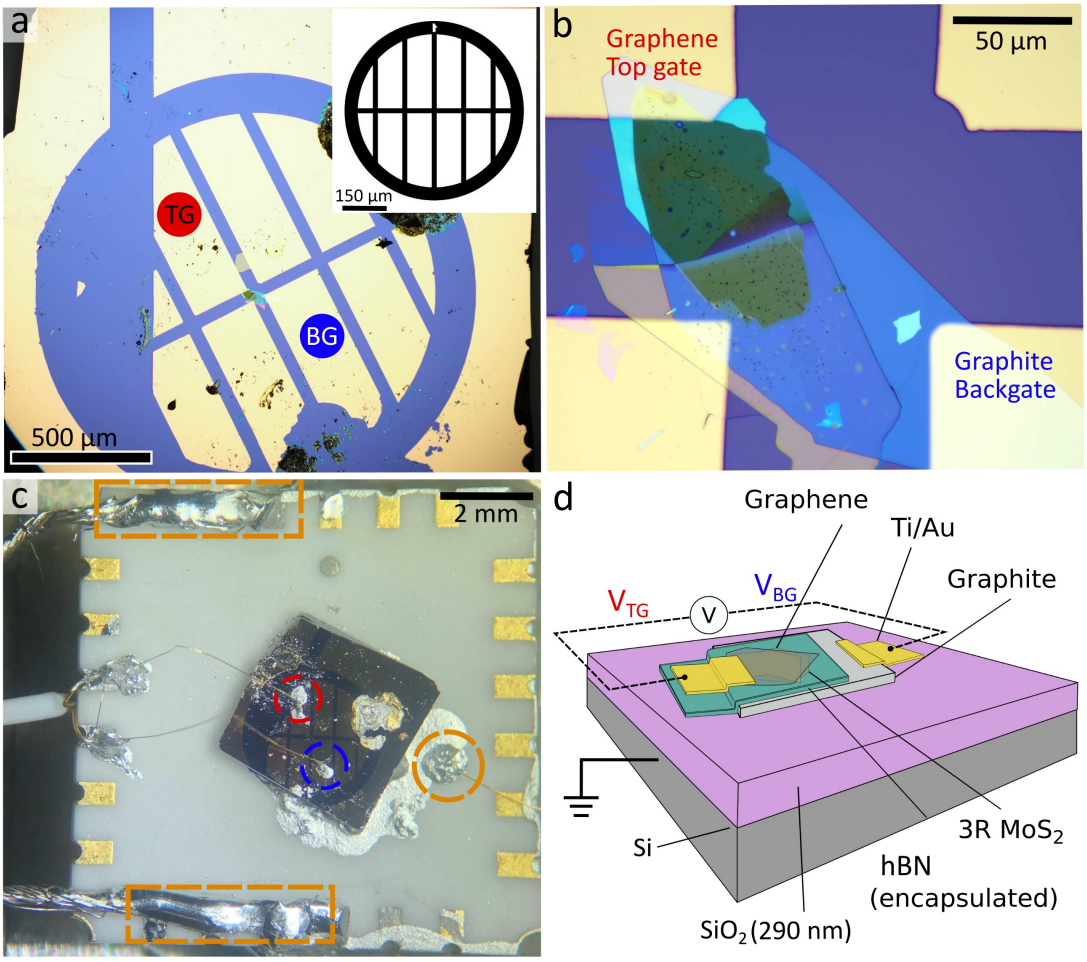

Fig. 3.7: **Using TEM grid shadow mask to deposit metal contacts for two-terminal SEM devices. a** Optical image multiple metal contacts deposited with a TEM grid shadow mask where top gate (TG) and bottom gate are indicated by the red and blue circles, respectively. The inset illustrates the geometry of the TEM grid used. **b** A zoomed in optical image of the vdWs heterostructure that has been electrically connected with the metal contacts with the top gate and bottom gate labelled. **c** Photograph of the wire bonded SEM 2-terminal device using silver paste to hold the wires in place. Here, the device is glued to the back-side of a chip carrier to allow the device to be electrically grounded to the steel SEM sample holder underneath while the top and bottom gates (indicated by the red and blue circles, respectively) are electrically isolated from the SEM sample holder. The contacts indicated in orange are used for grounding purposes only. **d** Schematic of the SEM device structure.

the up-side-down chip carrier has been electrically grounded using the external wires highlighted by the orange square boxes in Fig. 3.7c.

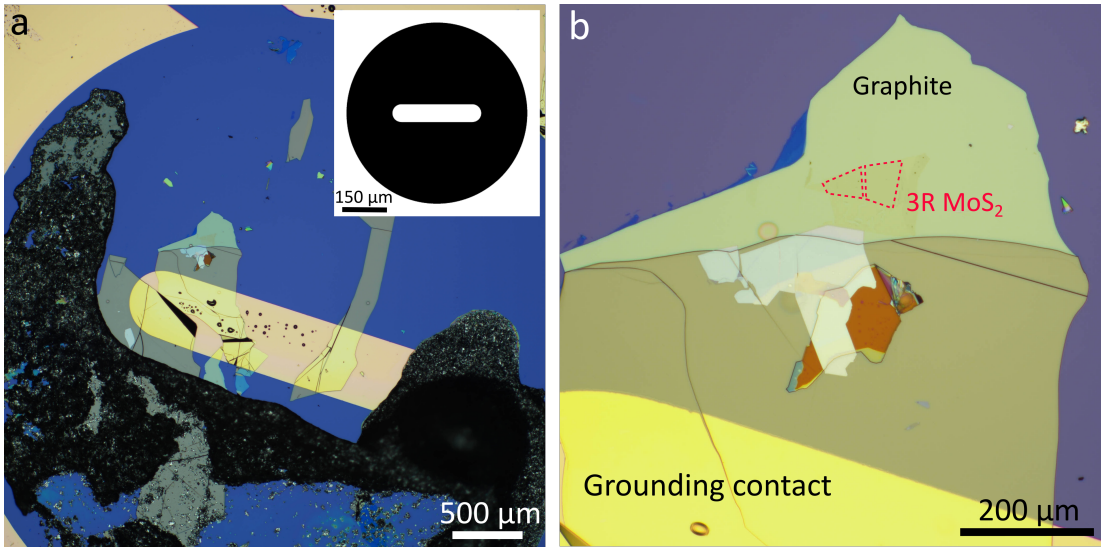

Fig. 3.8: **Shadow mask geometry for electrically grounding vdWs heterostructures. a** Optical image of a graphite/twisted MoS_2 heterostructure with a large (1.5 mm x 0.3 mm) metal contact deposited on top using a TEM grid shadow mask. The metal contact is electrically connected to the outer metal coating with silver paste. The inset illustrates the geometry of the mask. **b** A zoomed in optical image of the graphite/twisted MoS_2 heterostructure where the region of 3R-type twisted bilayer MoS_2 has been highlighted with a red dashed line.

VdWs heterostructures (e.g. a TMD transferred onto a bulk hBN crystal) on Si/SiO_2 (290nm or 90 nm) substrates are not electrically grounded and therefore need a metallic contact to connect it to the ground. For electrical SPM techniques, poor sample grounding leads to surface charge accumulation and a significantly accelerated build-up of surface contamination. The grounding connection is illustrated in Fig. 3.8a where a large metallic bar has been deposited onto the edge of a graphite/twisted bilayer TMD heterostructure.

Electron Beam Lithography Contacts

E-beam lithography can be been used to create tailored pattern designs for metal contacts on the surface of vdWs heterostructures. This technique is ideal for samples fabricated for electrical transport devices that have a relatively small lateral size (1-10 μm), require multiple electrical contacts (> 2) and have complex geometries. The technique uses an electron sensitive polymer resist layer that can be selectively exposed with a primary electron beam that modifies the solubility of the exposed region [127].

The lithography process is performed in a scanning electron microscopy in order to implement the electron irradiation. In this work, an EVO MA10 model was used. Here, the resolution limit of the exposed features is limited by the aberrations associated with the electron microscope (discussed in Section 4.2.2). For the SEM used in this project, the resolution was limited to 50 -100 nm, therefore the minimum spacing requirements of the fabricated tunnelling devices i.e. $\sim$ 500 nm was achievable.

PMMA was the polymer resist used in this thesis. This is a positive resist that, upon irradiation, will undergo polymer-chain scission which effectively increases the polymer solubility. Areas exposed to the primary electron beam are then washed away using a resist developer (discussed later). There are a number of key factors that effect the sharpness and resolution of the final exposed pattern. Electrons tend to scatter as they travel through the resist where the scattering volume broadens out the further the electron travels (see Section 4.2.1). Therefore, the thickness of the resist determines the final undercut profile of the polymer resist which in turn effects the final resolution of the exposed feature. To achieve a good undercut profile, two different molecular weight polymers can be used as a double resist layer (see Fig. 3.9a-e). Tuning the energy of the irradiating electrons will also help optimise the undercut profile, for example, higher energy electrons tend to have a more linear trajectory as they travel through the sample. It is important to note that a larger undercut is useful to aid the final 'lift-off' step after metal deposition. Additionally, over-annealing can reduce the overall solubility of the polymer resist layer.

The e-beam lithography procedure has been carried out in the following steps;

PMMA polymer resist: Two layers of PMMA were used to increase the undercut profile (see Fig. 3.9a). The first layer was 3 % 495K PMMA spin-coated at 3000 rpm and annealed at 150° for 5 mins. The second layer was 3 % 950K PMMA and was spin-coated using the same conditions as layer one. The combined layer thickness of the resist was approximately 220 nm.

Device coordinate location: The substrate was loaded onto a coordinate stage to record the local coordinate position of the sample with respect to the (0,0) coordinate i.e a macroscopic feature such as the edge of the substrate that can be identified in the SEM. **Expose markers:** E-beam lithography was used to expose a patterned coordinate system around the vdWs heterostructure within a 1500 μm^2 'writefield'(see Fig. 3.9b).

Develop markers: The polymer developer used was a mixture of IPA and deionised

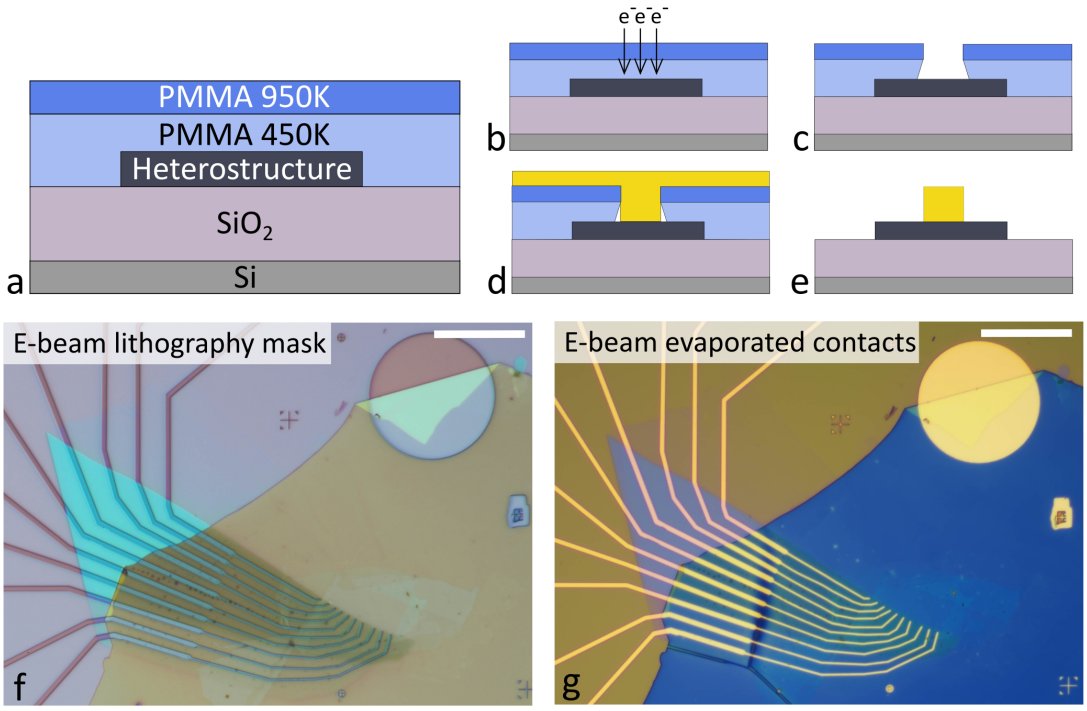

Fig. 3.9: **Using e-beam lithography to pattern metal contacts for electrical transport measurements.** **a** Schematic of the two polymer resist layers spin coated on top of a vdWs heterostructure. **b** Selected regions of the resist layer are exposed by e-beam irradiation. **c** The exposed regions are dissolved used the developer. **d** Metal is deposited using e-beam evaporation. **e** The resist layer is dissolved lifting off the gold film above. **f** Optical image of exposed resist used to define the shape of the electrical contacts in a tunnelling junction device and subsequent deposited metal contacts. Both scale bars are 25 μm.

water with a 3:1 ratio. The substrate was placed in a beaker of the developer for 30 seconds then into a beaker of IPA for 30 seconds before being dried with compressed nitrogen gas leaving exposed regions in the resist (see Fig. 3.9c).

Design contacts: Optical images of the vdWs heterostructure with the exposed coordinate markers were loaded into the Layout Editor software package to design the contact patterns. Here, the coordinate markers ensure that the design is to the correct scale and exposed in the correct location on the substrate.

Expose contact pattern: Procedure performed as before. Typically, the small and large parts of the electrical contacts are exposed separately so that the beam dose can be optimised for the varying degree of resolution required. For example, a higher beam current can be used for the large contacts where resolution and accuracy is less essential to reduce the time required to expose the pattern. For example, 500 pA was used for large contacts and 10-20 pA was used for the small contacts. In Fig. 3.9f-g, the folded edge of the bulk crystal has also been exposed. Here, the metal acts to pin the bulk crystal to the silicon substrate which can often come loose during the lift-off process.

Develop: Procedure performed as before (see Fig. 3.9f).

Deposit metal: a thin film of titanium (3 nm) as an adhesion enhancing layer and gold (40 nm) was deposited over the polymer resist mask using e-beam evaporation (see Fig. 3.9d).

Lift-off: The PMMA resist layer is dissolved, removing the metal layer above the PMMA. This is performed in a sealed beaker of acetone which is left to dissolve for 1 hr. A pipette is then used to generate a turbulent flow in the acetone helping the metal film lift-off. For the final step, the substrate is transferred into IPA before being dried with compressed nitrogen gas (see Fig. 3.9e,g).

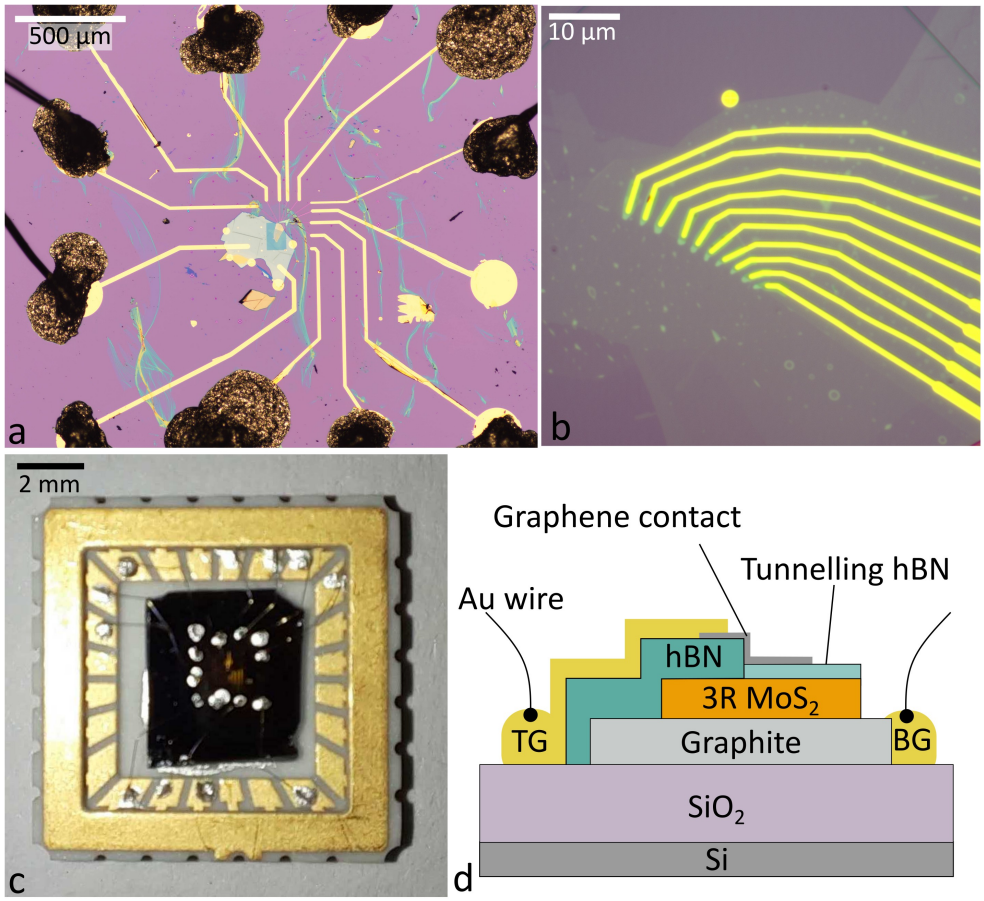

Fig. 3.10: **Wire bonding of patterned metal contacts and device geometry for electrical transport measurements.** **a** Optical image of a typical electrical transport tunnelling device where each individual metal contact has been wire bonded to an external chip carrier. **b** A zoomed in optical image of the tunnelling devices, where each individual metal contact connects a single tunnelling device (device area typically 500 nm^2 - 1μm^2). **c** Photograph of the tunnelling devices wire bonded to an external chip carrier which are commonly used for electrical transport devices. **d** A side-view schematic of the device geometry of a single tunnelling device.

In this project, E-beam lithography was used to design a patterned mask for metal contact deposition as well as an etch mask to prepare 3R-type minimally twisted bilayer MoS_2 tunnelling junction devices. The motivation for this was to fabricate prototype ferroelectric switches in order to evaluate their switching behaviour in electrical transport measurements (discussed further in Section 6.4). The devices were designed according to the samples local domain structure and, therefore, the electrical contacts as well as the top graphene etch mask required precise alignment to the regions of interest.

The 3R-type twisted bilayer MoS_2 tunnelling junction devices, fabricated using e-beam lithography, were designed such that each individual metal contact was used to

electrically connect a single tunnelling device as well as a metal contact to the graphite back gate (see Fig. 3.10a-b). In Fig. 3.10d, the top metal contact is used to connect a top graphene contact, which has been positioned over a hBN tunnelling barrier region, to the external bonding wires. An additional e-beam lithography mask is used as an etch mask for reactive ion etching (RIE) to shape the individual graphene contacts (see Fig. 3.10b). RIE is performed in a vacuum chamber (pressure 2 x10^{-2} mbar) with a flowing mixture of argon and oxygen with a ratio of 2:1. Then, a capacitively coupled plasma is ignited at a forward power of 10 W to selectively etch the graphene but not the underlying hBN. Each individual metal contact is then wire bonded to an external chip carrier as illustrated in Fig. 3.10c.

Electron Beam Metal Deposition

Common methods of metallisation include thermal evaporation, e-beam evaporation and sputtering. In this work, only electron-beam evaporation was used. E-beam evaporation is particularly efficient (higher deposition rate) for evaporating the highest purity metal contacts, necessary for low contact resistance at the metal/vdWs crystal interface. A high vacuum (<5×10^{-6} mbar) is used to ensure that electrons propagating from the electron gun are able to reach the metal to be evaporated and ensuring the high purity of the deposited metal. The electron beam is accelerated and directed at the metal target, where upon collision, the kinetic energy of the electrons is converted to thermal energy causing the metal target to melt or sublime. The generated metal vapour propagates throughout the vacuum chamber and condenses onto the sample. Metals such as chromium and titanium are commonly used in small amounts (3-5 nm coating) to improve adhesion of the metal to the silicon wafer substrate. A 30-40 nm film thickness of gold (Au) is then used for the metal contact pad for a continuous thin film that can be easily lifted off. Gold is commonly used as the metal contact owing to its good electrical conductivity, stability in ambient conditions and relatively low contact resistance (energy barrier) between Au and graphene [128]. For vdWs heterostructures that require high temperature annealing (>300 °C) for surface-sensitive characterisation techniques, platinum has been used due to it's higher melting point compared to gold. To achieve optimum metal deposition, a beam voltage of 9.5 kV and a beam current of 30-35 mA was used for titanium and gold deposition on a Moorfield E-beam evaporation system. This achieved an average deposition rate of 0.1 Å/s and 1.1 Å/s, respectively.

3.7 Summary

In this chapter, the fundamental fabrication techniques for building vdWs heterstructures have been discussed. Firstly, 2D materials are exfoliated from their bulk crystals using a technique called mechanical exfoliation. 2D crystals of interest are then identified using optical microscopy. The PMMA dry-transfer technique was then used to transfer the 2D crystals onto a vdWs heterostructure. For rotationally aligned heterobilayers, straight edges of crystallographic orientation (corresponding to zig-zag/zig-zag or armchair/armchair) were identified in order to determine possible alignment close to $\theta \sim 0°$ or $\theta \sim 180°$, though it is not possible to decipher between the two alignments. For twisted homobilayers, a modified 'tear-and-stack' crystal transfer method was employed. Due to the ability to precisely control the desired twist angle, this latter technique was employed for the majority of the devices discussed in this project. Then, techniques for reducing contamination were introduced. Finally, the techniques used for fabricating electrical contacts including shadow masks, E-beam lithography and E-beam metal deposition were discussed in detail.

Chapter4

Characterisation Techniques

In this section, the characterisation tools including atomic force microscopy (AFM)[129], scanning transmission electron microscopy (STEM) and scanning electron microscopy (SEM) that are used throughout this thesis are outlined in detail.

4.1 Scanning Probe Microscopy

AFM is a versatile tool that can provide information far beyond simple topography maps. For instance, advanced contact mode techniques including piezo-responsive force microscopy (PFM) and conductive-AFM (C-AFM) can provide insights into electronic properties of vdWs heterostructures. Advanced tapping mode techniques including electrostatic force microscopy (EFM) and Kelvin probe force microscopy (KPFM) offer information regarding a materials local electric fields, surface potential and work function [130, 131]. These imaging methods provide fast and effective moiré superlattice mapping as well as unveiling unique moiré induced properties.

The fundamental concept of scanning probe microscopy is the ability to bring a very sharp tip in contact (or close proximity) by means of a piezoelectric crystal that allows for movement in xyz-directions with sub-nm precision [129]. As the tip is scanned over the sample surface, the interaction between the tip and the sample cause the tip and its supporting cantilever to bend. These interactions are a combination of both long-range (such as electrostatic, vdWs and capillary) and short-range (chemical bonding and Pauli repulsion) forces. In ambient conditions, the capillary force dominates over the other forces acting on the tip/sample and originates from the liquid layer adsorbed on the tip/sample surface or by capillary condensation. Although it doesn't alter the image aqcuisition process, it increases the frictional force between

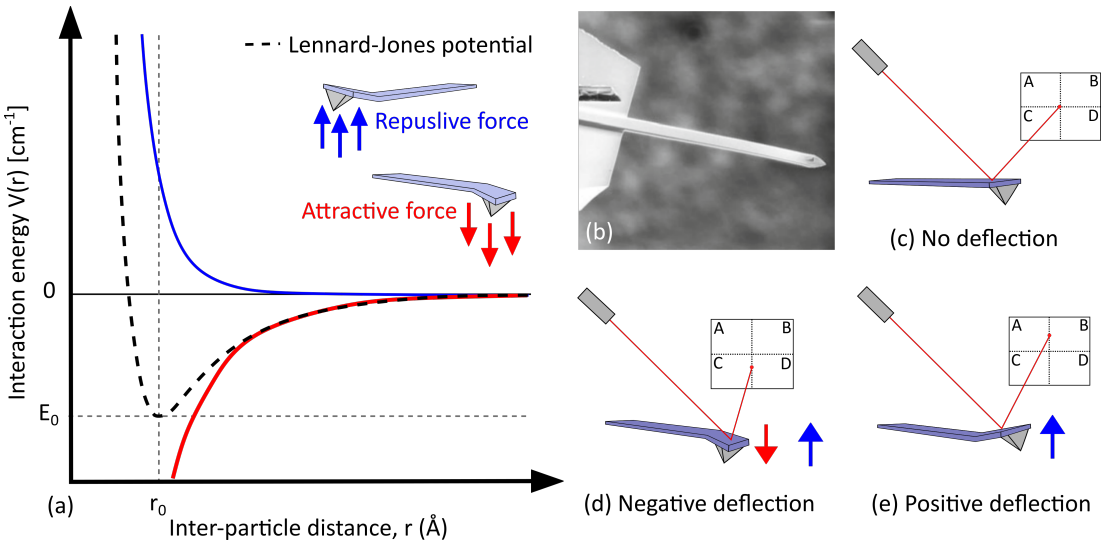

Fig. 4.1: **Tip-sample interaction described using the Lennard-Jones potential and the forces associated with tip deflection.** **a** The Lennard-Jones potential, the model potential for tip-sample interaction where attractive (red line) and repulsive (blue line) parts of the potential are highlighted. The vertical dashed line (at r = r_0) indicated the transition between repulsive (left side) and attractive (right side) interactions. **b** SEM image of an AFM tip and cantilever [reprinted from ref. [132]]. **c-e** Schematics of the cantilever deflection highlighting the degree of bend to the cantilever relative to the sample surface where a **d** negative deflection feels a both attractive and repulsive forces and **e** positive deflections feel a repulsive force.

the tip and the sample leading to increased wear of the sample/tip [133]. The origin of vdWs forces in the case of tip-sample interaction is predominantly the London dispersion force [15]. It can be described simply as the spontaneous formation of the dipole-dipole moment between two inert atoms resulting in an attractive force between these atoms. The total force acting on the tip is the sum of individual interactions not just in the vicinity of the tip apex but also in the surrounding volume, provided by the long-range nature of the London dispersion force. VdWs attraction is the dominating force for tip-sample distances > 1 nm and below this, short-range forces take over [132]. Short-range forces such as chemical bonding forces originate from the overlap of the outermost shell electron wavefunctions and is repulsive. A simple model that quantifies inter-atomic potential is the Lennard-Jones potential combining both the attractive and repulsive forces as described by [134];

$$V(r) = E_0[(\frac{r_0}{r})^{12} - 2(\frac{r_0}{r})^6] \tag{4.1}$$

Where E_0 is the depth of the potential well, r is the inter-particle distance and r_0 is the inter-particle distance at which the interaction energy $V(r)$ is minimised (see Fig. 4.1e). Here, the r^{-12} term is the (Pauli) repulsive force indicated by the blue curve in Fig. 4.1e and r^{-6} is the attractive (primarily vdWs) force indicated by the red curve in Fig. 4.1e. The tip-sample interactions are in the attractive regime for $r > r_0$ and in the repulsive regime for $r < r_0$.

Long-range electrostatic interactions originate from differences in work function of the tip and sample, applied potential (if both are conductive) or the presence of trapped charges in the sample or tip. The tip-sample system can be considered as a capacitor where the capacitance, $C(z)$, depends on a potential difference ($\Delta V(z)$) which is the sum of the externally applied potential (V_{bias}) and the difference of work functions ($\Delta\phi$) of the sample and the tip. The resulting electrostatic force can be described as [132];

$$F_{el}(z, \Delta V) = -\frac{\delta \epsilon_{el}(z)}{\delta z} = -\frac{1}{2}\frac{\delta C(z)}{\delta z}\Delta V^2 \tag{4.2}$$

where ϵ_{el} is the electrostatic energy. As a rough approximation, we can consider the electrostatic tip-sample force as a parallel plate capacitor with capacitance;

$$C_{plate}(z) = \epsilon_0 \frac{A}{z} \tag{4.3}$$

where ϵ_0 the dielectric permittivity of vacuum, A is the area of the capacitor plate and z is the tip-sample distance. The equations highlight the $1/z$ tip-sample dependence on capacitance. This leads to a force dependence of $1/z^2$.

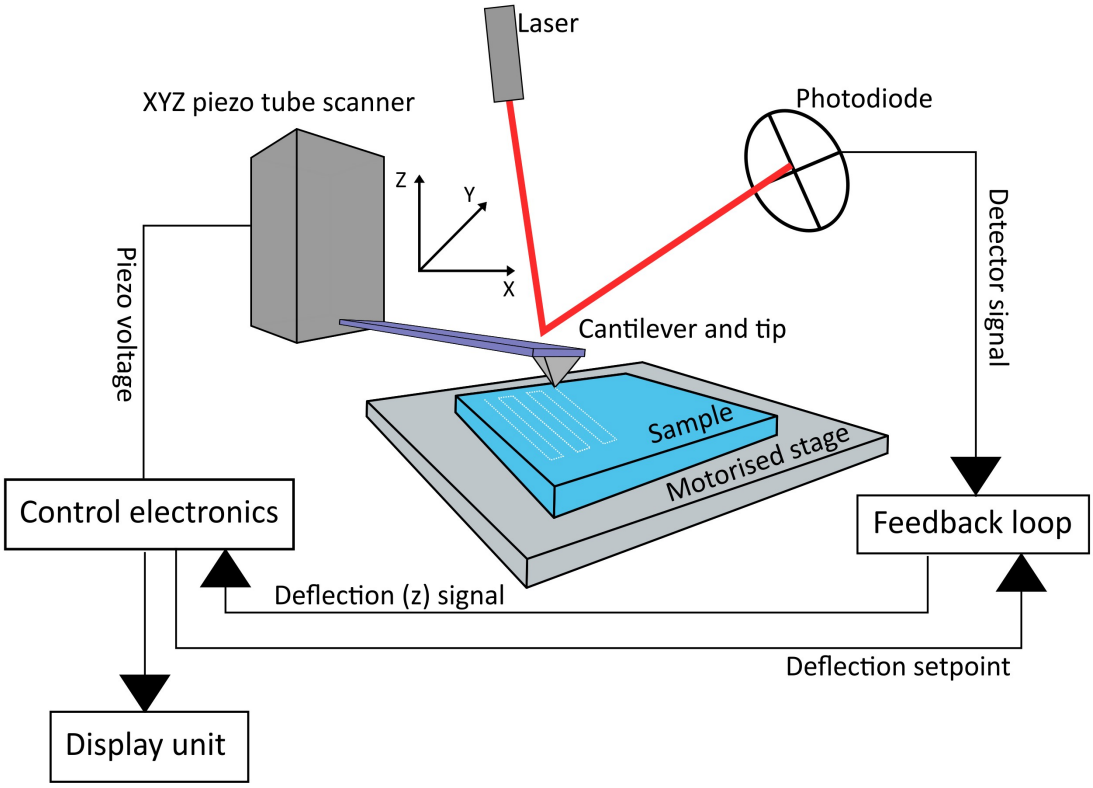

Fig. 4.2: **Schematic of an atomic force microscope.**

The common experimental SPM set-up is shown in Fig.4.2. The probe at the end of a cantilever is raster scanned across the surface of a sample (as indicated by the dashed line in Fig. 4.2). Changes in the surface morphology cause the cantilever to deflect in the z-direction. A laser beam is reflected off of the back of the cantilever and the deflection signal is detected by a photodiode (as seen in Figs. 4.2 and 4.1). Other detection sensors are used but will not be discussed here.

The cantilever can be considered as a spring fixed at one end, so that where the torque acting on the cantilever is translated into its deflection or bending. Fig. 4.1b-d, demonstrate the forces associated with cantilever degree of bending relative to the sample surface, for example, positive deflection corresponds to repulsive forces acting on the tip (see Fig. 4.1d). The primary signal output of the photodiode is a current that can be converted into a voltage using a pre-amplifier. The standard type of probe used for AFM imaging consists of an Si/SiN cantilever that has a lithographically etched tip at the very end of the cantilever with a nominal apex of 5-50 nm. A common probe geometry is illustrated in Fig. 4.1b. The force applied to a sample can be described by Hooke's law;

$$F(x) = -k(\Delta)z \tag{4.4}$$

Where k (N/m) is the spring constant of the cantilever (which is provided by probe

manufacturers) and $(\Delta)z$ is displacement in the z-direction of the tip. The larger the spring constant of a cantilever, the higher the force that is applied to the sample. Typically, high-k probes (2-40 N/m) are used for sample cleaning in contact-mode and low-k probes (<2 N/m) are used for high resolution tapping-mode and contact-mode imaging.

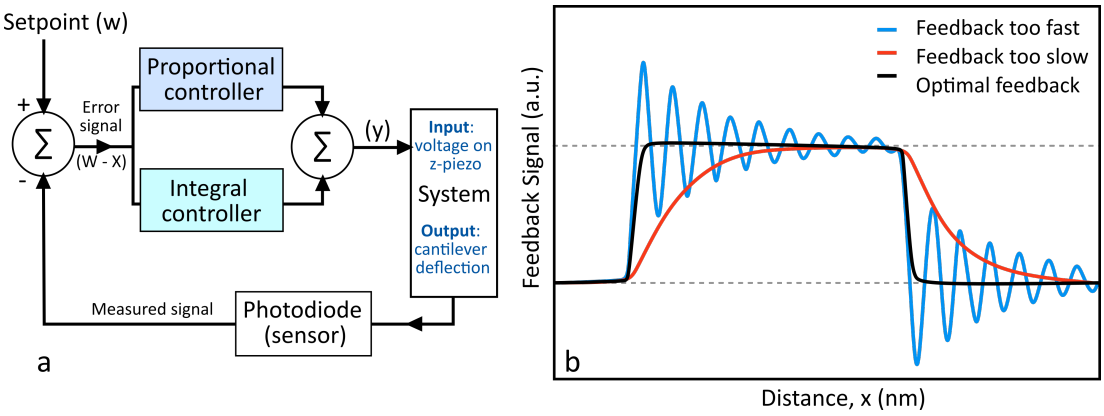

Fig. 4.3: **Controlling AFM signal feedback loop using a Proportional-Integral (PI) controller. a** Schematic of a PI feedback loop where the short-term deviations from the setpoint are controlled by the proportional controller and the long-term deviations are controlled by the integral controller. **b** Schematic of the response of the AFM feedback signal with respect to a sharp change in topography when the feedback is too fast (blue curve), too slow (red curve) and when the feedback is optimal (black curve).

A feedback loop is used to control the distance (in the z-direction) between the probe and the sample by using a piezo actuator. Here, piezoelectricity describes a crystals ability to deform under an applied electric field (or vice versa) which is a property of some crystals with a lack of inversion symmetry. This is essential to the precise control of the AFM probe motion. The most common feedback loop is a proportional-integral (PI) loop (see Fig. 4.3). Here, the setpoint (w) is a user-controlled value that is stabilised by the feedback loop such that the tip-sample distance is kept constant. The proportional gain settings controls the response to short-term deviations from the setpoint and integral gain settings then controls the response to long-term deviations from the setpoint.

If the feedback is too slow (red curve in Fig. 4.3b), there is a delay in stabilising the setpoint which leads to loss of detail. A common indicator of slow feedback is the tip 'flying' off the edge of a sharp topographic feature. If the feedback is too fast (blue curve in Fig. 4.3b), there is an overshoot where the tip (z)-postion oscillates around a

given setpoint. This can be seen in the measured signal as oscillating noise.

4.1.1 Contact Mode

For contact mode AFM, the tip is in constant contact with the surface of the sample. Here, sample topography is measured by the vertical or lateral deflection of the probe and works in the repulsive tip-sample interaction regime. Typically tip deflection is kept constant by adjusting the deflection setpoint to ensure a constant force is applied to the sample surface. In order to calculate the deflection sensitivity (V/nm) of a tip, one can press the tip into a hard surface (such as Si/SiO_2). For accurate calculation of deflection sensitivity, the tip must be in full contact (static ramping) with the surface to ensure the signal is only due to deflection of the cantilever. In this project, low stiffness tips have been used for topography imaging however, high stiffness tips are used for surface contamination cleaning as well as inter-layer cleaning of heterostructures as described by Rosenberger et al [124].

4.1.2 Tapping Mode

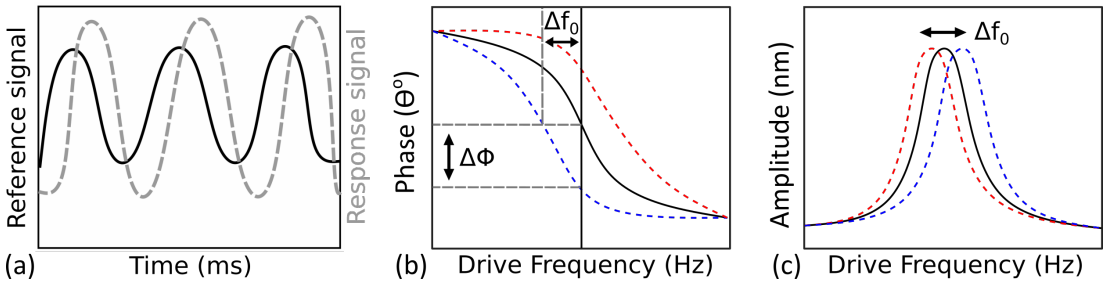

Fig. 4.4: **Schematics of hardware required in tapping mode AFM.**

Tapping mode AFM is a dynamic mode where an AC voltage $\sim V_{AC}sin(\omega t)$ (where ω is frequency and t is time) is applied to the the tip, generating a sinusoidal oscillation [135]. To maximise the signal output, the frequency of the applied AC voltage is typically selected to be within ($\pm$) 5 ($\%$) of the cantilever's resonant frequency [132]. Here, the resonant frequency describes the natural frequency of free oscillation determined by the physical parameters of the probe.

When the oscillating tip is brought closer to the sample surface, the short-range tip-sample interactions lead to a net shift in the resonance frequency. Here, the signal detected by the photodiode is the average amplitude of a complete oscillation cycle of

the cantilever as compared to a reference input signal (see Fig. 4.4a). The output signal used to build up the topography map of the sample is the change in z-piezo position required to keep the amplitude of the cantilever at a user-defined amplitude setpoint. In Fig. 4.4b-c, the repulsive forces (blue dashed curve) increase the resonant frequency and stiffens the cantilever whereas attractive forces (red dashed curve) reduce the resonant frequency [135]. Additionally, smaller amplitude setpoints (tip oscillating closer to the sample) have a higher feedback response but cause unwanted tip-sample interactions. The forces required to maintain a given amplitude setpoint are much lower compared to the force required in contact mode, therefore, tapping mode AFM is more suitable for imaging delicate samples such as monolayers of vdWs crystals.

Furthermore, the phase (φ) and amplitude (A) signals captured in parallel to topography can provide complementary information about a material. The deflection is described as;

$$d = Asin(2\pi\omega t + \varphi) \tag{4.5}$$

Where d is the deflection, ω is the frequency and t is time. Amplitude and phase have been used to map edges (such as grain boundaries) and compositional changes across surfaces [136]. Unfortunately, it is particularly challenging to quantify the phase and amplitude signals in terms of physical properties of the sample in conventional tapping mode imaging and more advanced methods should be used to better interpret the contrast. This is in part due to cross-talk between signals. For example, topographic features with a similar shape/size to the tip will interact with the tip differently than a flat surface, such that "valleys" can have a stronger net attractive force (higher tip-sample interaction) and the top of high peaks can have a weaker net repulsive force relative to the rest of the sample.

4.1.3 Electrical SPM Modes

Conductive Atomic Force Microscopy

Conductive-AFM is a technique used in contact mode that can be employed to characterise the electronic properties of moiré superstructures. Both topographic and current images are acquired simultaneously allowing direct correlation of topographic features with the underlying electrical features (see Fig. 4.5b-c). Conductive-AFM can be implemented on conductive, semiconducting and insulating surfaces because

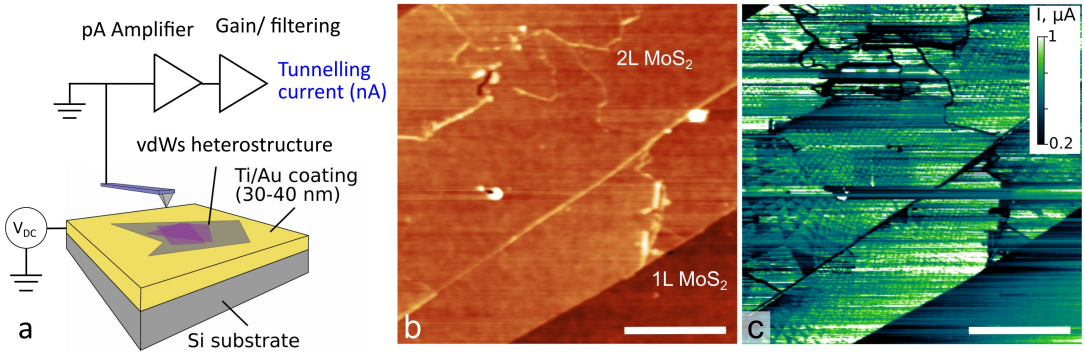

Fig. 4.5: **Principle operation of Conductive-AFM imaging mode.** **a** Schematic of the experimental setup for Conductive-AFM. **b** Topographic image of twisted bilayer MoS_2 in the 3R-type stacking configuration on a graphite crystal graphite transferred onto a Ti/Au coated substrate and **c** the corresponding tunnelling current signal acquired in conductive-AFM mode. Scale bars are both 1 μm.

the feedback loop is only reliant on the deflection signal and the tunnelling current is measured independently.

A conductive tip (typically a Pt/Ir coated probe) is electrically grounded and the sample is electrically connected to a sample stage with direct current (DC) voltage supply (or vice versa). Here, electrical continuity is achieved by transferring the sample onto a conductive surface such as graphite exfoliated onto a Ti/Au coated silicon substrate. Silver paint is then used to connect the conductive substrate to the sample stage. As the tip scans across the sample surface with a constant applied force with an applied DC voltage, the current is measured using a linear amplifier with a current range of 80 fA to 1 μA, as illustrated in Fig. 4.5a.

Piezo-response Force Microscopy

Piezo-response force microscopy (PFM) is another electrical imaging technique operated in contact mode. Imaging in PFM mode allows for the direct measurement of the electromechanical response to an applied electrical field. In Fig. 4.6a, the sample (a non-centrosymmetric crystal) is actuated using an out-of-plane electric field (AC bias applied to the probe) resulting in expansion and/or contraction of the sample under the probe due to a process known as the inverse piezoelectric effect (i.e. volumetric change with applied electric field). This signal is detected via the deflection of the probe [137]. The z-displacement measured by the AFM probe is [137];

$$d = d_{33} V_{AC} sin(\omega t + \phi), \tag{4.6}$$

where the AC voltage applied to the tip is $V_{AC} = Vsin(\omega t)$, d_{33} is the piezoelectric constant and, here, (ω) is the drive frequency operated at the contact resonance of the probe. The contact resonance (i.e. when the AFM probe is in contact with the sample at a particular deflection setpoint) is when the AC bias voltage causing deformation of a sample is driven at the same frequency of the system. For PFM, the contact resonance is used because the signal-to-noise ratio is significantly enhanced due to a strong dependence on the elastic properties of both the cantilever and the sample [138].

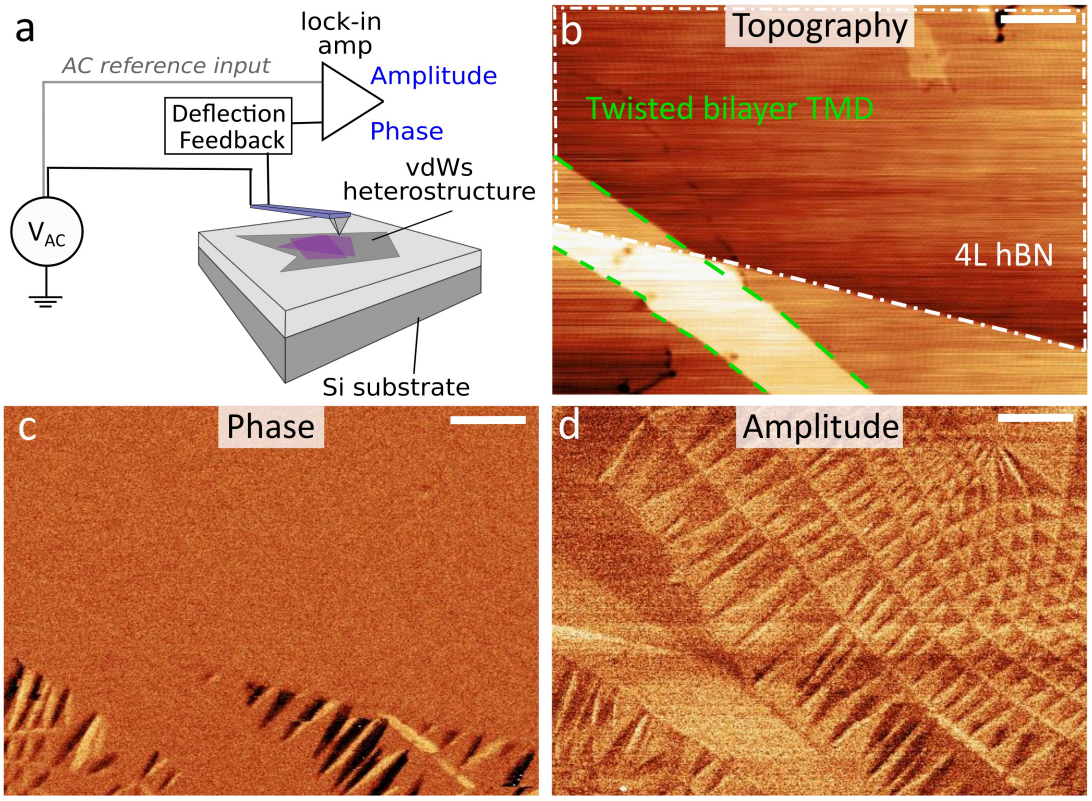

Fig. 4.6: **Principle operation of Piezo-responsive force microscopy imaging mode. a** Schematic of the experimental setup used for PFM imaging. **b** The topographic contact-mode image acquired of a graphite/3R-type twisted bilayer MoS_2 (indicated by green dashed line) that was partly encapsulated with 4-layer hBN (top half of image indicated by the white dashed line) and the corresponding **c** phase and **d** amplitude. All scale bars are 400 nm.

PFM is sensitive to both in-plane (vertical deflection) and out-of-plane (lateral deflection) surface displacements. The surface displacement due to material expansion/contraction that is typically detected by the feedback loop (see Fig. 4.6) is on the order of picometres. Detecting such small signals requires a lock-in amplifier to maximise the signal-to-noise ratio. Here, the applied AC voltage (typically in the range

of 1-10 V) is also used as the reference signal for the lock-in amplifier. Additionally, the sample must have a low surface roughness (similar order of magnitude as the strain induced z-displacement) for reasonable stability of the measured signal. The deflection signal is then acquired as an amplitude and phase signal.

For the phase signal (i.e. the difference between the cantilever vibration and the AC voltage)the probe oscillates either in-phase (0°) or out-of-phase (180°) with the applied AC voltage as the probe interacts with the sample [137]. The amplitude signal is dependent on the magnitude of the piezoelectric coefficient (d_{33}) thus providing information about the piezoelectric properties of the sample where as the phase signal is dependent on the polarisation direction of the spontaneous electric dipole i.e. the ferroelectric properties of the sample [95]. An additional DC voltage bias can be applied to the tip or sample which can be useful for spectroscopic measurements of material polarisation as a function of DC-bias [137].

A recent publication highlighted the suitability of this imaging mode to directly visualise moiré superlattices without the need for specific (and sometimes complicated) devices because the sample is not required to be electrically connected to external hardware [139]. In this study, the acquired PFM signal was related to flexoelectricity where an electromechanical response is induced through the strain gradients present across the moiré superlattice. Fig. 4.6b-f highlights the corresponding amplitude and phase signals as well as the amplitude and phase signals from the lock-in amplifier acquired from a 3R-type twisted bilayer of MoS_2 that has been half encapsulated with thin (4 layer) hBN. Here, the lock-in signals correspond to the first harmonic derivative of the amplitude and the phase. As expected from previous PFM studies [139], there is an electromechanical response at the boundary between triangular domains due to the presence of a strain gradient concentrated at the boundary which can be seen in the non-encapsulated region of the sample (see Fig. 4.6c,d and e). Importantly, we are also able to detect the underlying amplitude signal of the TMD moiré superlattice when encapsulated with a thin dielectric hBN layer which is extremely beneficial if we want to characterise the structure of encapsulated electrical transport devices (see Fig. 4.6d).

Electrostatic and Kelvin Probe Force Microscopy

Advanced tapping modes such as electrostatic force microscopy (EFM) and Kelvin probe force microscopy (KPFM) are techniques operated in tapping mode. These

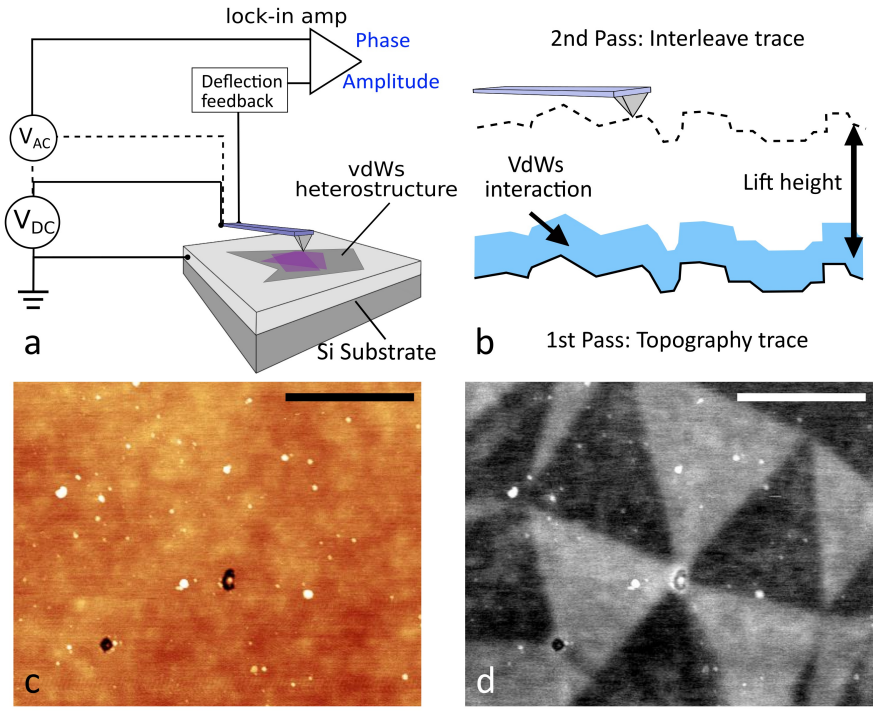

Fig. 4.7: **Electrostatic force microscopy imaging technique.** **a** Schematics of the set-up for electrostatic force microscopy. **b** Illustration of the operating principles of the two-pass life-mode technique used in EFM. **c** Topographic tapping mode signal of a graphite/3R-type twisted bilayer MoS_2 acquired on the first pass of the lift mode technique. **d** The tapping mode phase signal acquired on the second pass with a lift height of 10 nm and applied DC bias = -0.4 V. All scale bars are 500 nm.

techniques measure the electrostatic interaction between the tip and the sample providing that there is a difference in work function and/or trapped charges in the tip/sample [130, 131]. EFM and KPFM have been previously used to image buried interfaces in encapsulated van der Waals heterostructures [140, 141]. Both techniques have provided evidence of strain induced piezoelectricity in monolayers of hBN [142] and MoS_2 [143].

The attraction/repulsion of separated charges in a given sample are sensitive to long-range electrostatic forces and are dependent on the probe-sample distance. With electrical contact (V_{AC} and V_{DC} applied to the probe) a net negative/positive charge accumulatesat the tip apex inducing a potential difference between the sample and the probe. In order to remove the effects of long-range electrostatic and vdWs forces, tapping mode AFM can be operated in a two-pass lift mode. On the first pass, the tip traces the topography in the standard tapping mode. The tip returns to the starting point with the AFM feedback switched off and, lifted by a finite height (in the range of nms to tens of nm), performs a second pass retracing the previously acquired topography trajectory but this time with an applied bias voltage (see Fig. 4.7b). The resultant topographic and phase mapping acquired with a lift height of 10 nm and DC bias of -0.4 V is shown in Fig. 4.7c and d, respectively. The acquired signal for EFM and KPFM slightly differ due to the manner in which data is collected. EFM is a more simple and indirect approach where an electrostatic force gradient can be calculated by measuring the phase shift as a function of applied DC-bias and commonly has a quadratic response. As the potential difference between the tip and sample increases, the contact resonance frequency decreases and leads to a reduced phase signal. The difference in electrostatic potentials between two dissimilar regions in a sample can then be calculated from the difference between two maxima of two quadratic curves corresponding to the dissimilar regions [144].

For phase-modulated KPFM, the phase of the demodulated signal (Cos θ) obtained by a second lock-in (specifically a phase-locked loop) is proportional to the electrostatic force gradient and is used to minimise the electrostatic interaction by finding a DC bias that nullifies the electrostatic force. This provides an absolute value of surface potential but is a more complex means of analysis that requires an additional lock-in amplifier to extract the electrostatic signal from additive mechanical signals as illustrated in Fig. 4.8. On the second pass, the AFM feedback is switched off and this time an AC and DC voltages are applied to the tip. The AC voltage creates an

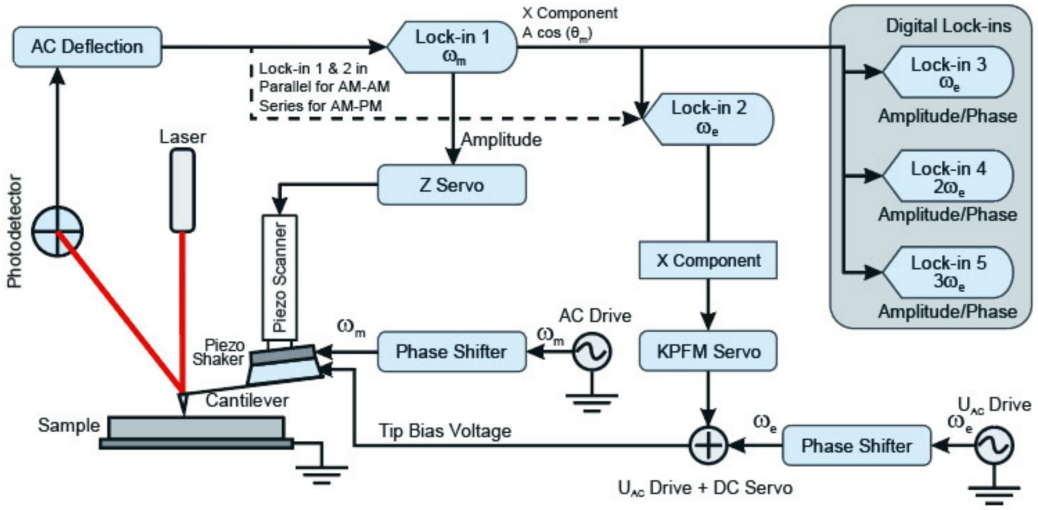

Fig. 4.8: **Experimental set up for Kelvin probe force microscopy in an NT-MDT SI NTEGRA prima AFM [reprinted from [145]].**

oscillating electric force between the tip and sample and the resulting AC oscillation amplitude also depends on the surface potential difference and the DC bias applied. Therefore, the AC oscillation amplitude can be used as a feedback to find the DC voltage that nullifies the DC electrostatic force using a second lock-in amplifier and hence to obtain the local surface potential difference [145]. For a known material of the tip, the workfunction map of the sample can be recovered. The oscillation amplitude of the second pass is typically reduced to compensate for the increased tip-sample distance as this, together with the lift height, will improve the feedback and lessen the chances of a tip crashing event.

4.1.4 AFM Image Processing

The software package Gwyddion [146] was used to process all AFM data discussed in this thesis. Scanning probe data is typically exported as raw data files to allow the user to apply their own selection of image processing techniques. There are four common sources of image artifacts including the piezo scanners, image feedback parameters, the probe and the sample surface. The feedback parameters can be optimised during data acquisition, however the affects of probe, sample and piezo scanner artifacts can be minimised with post acquisition processing. It is important, however, not to over-process the data such that important information is lost/altered. The two most commonly used image processing tools in this thesis include 2D levelling to compensate for piezo-scanner error and a scan line correction.

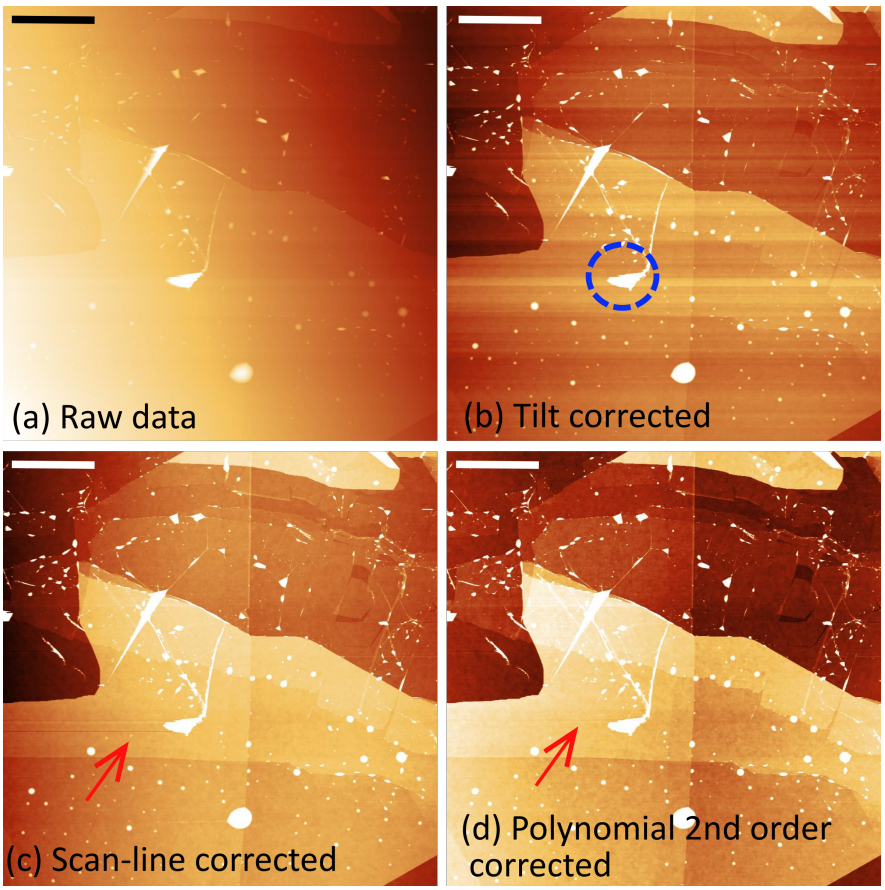

Fig. 4.9: **Using Gwyddion software for AFM image processing.** **a** Raw unfiltered topographic tapping mode AFM image of a typical graphite/TMD/hBN heterostructure and subsequent image processing steps including **b** plane fitting (blue circle indicates sharp/high topographic feature), **c** 'median of differences' scan line correction and finally **d** horizontal 2nd order polynomial fitting (with additional scar removal indicated by red arrow in **c** and **d**). All scale bars are 10 μm.

Common levelling tools include plane fitting, three-point fitting or polynomial background removal. Here, plane fitting is typically used to remove background tilt (which is illustrated in Fig 4.9a and removed in Fig. 4.9b). Three-point fitting can also be used to level the plane i.e. by manually selecting three common points that are expected to be on the same plane. For more complex background extraction (such as bowing), a polynomial fitting can be used. Bowing, in particular, is related to the non-linear nature of piezo scanner motion (probe holder has curved trajectory) as it scans in the x-y direction. In Fig. 4.9d, a horizontal polynomial of 2nd order has been used to remove the bowing effects induced by the piezo scanner.

Scan line artefacts have a number of origins, however, it is important to note that the nature of raster scanning means that individual (traced and retraced) lines are never perfectly parallel leading to displacement in the slow-scan (top to bottom) direction [135]. Damaged and/or contaminated probes as well as contaminated surfaces can lead to smearing across the image. Sudden mechanical/acoustic noise and/or unexpectedly high surface features (such as the region circled in Fig. 4.9b), where the feedback parameters can't adjust quickly enough, produce streaking across the image. In Fig. 4.9d, these line artefacts have been removed (from previous images in Fig. 4.9b-c) by aligning rows using median of (height) differences. In this method, the scan lines are shifted such that the median of the height difference of vertical neighbouring lines becomes zero producing the final processed image.

4.2 Electron Microscopy

This section will focus on the discussion of scanning electron microscopes (SEMs) and scanning transmission electron microscopes (STEMs). Electron microscopes were first introduced back in the early 1930's by the scientists Ernst Ruska and Max Knoll [147] and have been developed over time to possess analytical capabilities that are essential to modern materials characterisation.

Both SEM and STEM operate with a focused electron beam that is raster scanned over a sample (pixel-by-pixel) to probe the atomic and chemical structures of materials [148–150]. The fundamental difference between these techniques is which electron-matter interactions are being studied. SEMs are typically used to image bulk specimens with a resolution of $\sim$ 1-20 nm depending on the microscope set-up. In an SEM, the resolution is limited by both the electron beam diameter and the interaction volume of electrons in a bulk sample. STEM microscopes are capable of sub-angstrom resolution where the resolution is limited by the diameter of the focused electron beam. For electrons to 'transmit' through a sample, the sample itself must be as thin as possible and must be carefully considered during sample preparation.

In electron microscopes, a sample is probed using an accelerated electron beam where the output electron emissions are detected and converted into a digital signal. In order to generate a beam with low energy spread and small spot size, the incident beam is focused using a series of lenses and apertures which make up the condenser system and the objective system. The accelerated beam of electrons undergoes scattering events upon passing through matter and therefore a high vacuum environment is essential for electron microscopy to ensure that incident electrons are not scattered by air particles en route to the specimen. In order to interpret the resulting signal it is essential to understand the underlying physics of electron-matter interactions and how this generates image contrast. Subsequently, one must also recognise how different materials are affected by the electron beam and how to avoid beam-induced damage.

4.2.1 Principles of Electron-matter Interaction

In order to interpret data in electron microscopy, it is essential to understand how electrons from the electron beam interact with the atoms and electrons in a sample. We begin with the concept of de Broglie's particle-wave duality; During scattering events, electrons are acting as charged particles influenced by strong Coulomb forces. Electrons are also acting like a wave with a specific wavelength depending on their coherency (phase nature). Particle momentum (p) is related to wavelength (λ) simply by $\lambda = h/p$ where h is planks constant. Through accelerating electrons (the incident beam) through a large potential, momentum of kinetic energy (eV = $m_o V^2/2$) is transferred to the specimen. This can be related to the wavelength by $\lambda = h/(2\, m_o eV)^2$ to define the relationship between the accelerating voltage and electron wavelength of the electron gun [151].

The scattered electrons can be classified as either forward or backscattered depending on the scattering angle, with large angles $\sim 180°$, for example, backscattered electrons are scattered back towards the incident beam. Forward scattered electrons are the source of most signal types in STEM while backscattered and secondary electrons are utilised in SEM. Scattered electrons can either be coherent or incoherent relating to the phase of the wave-like nature of electrons. Additionally, electrons can be scattered elastically or inelastically.

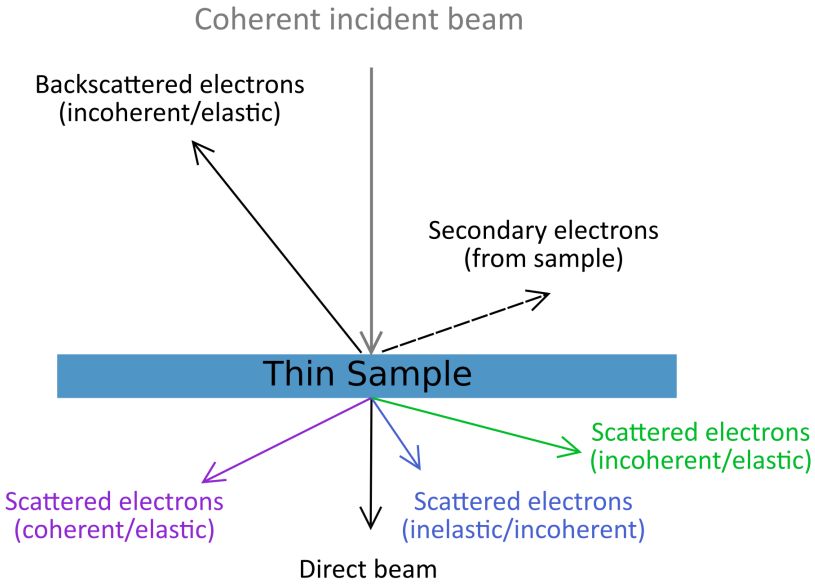

Fig. 4.10: **Beam induced scattering events in atomically thin samples.**

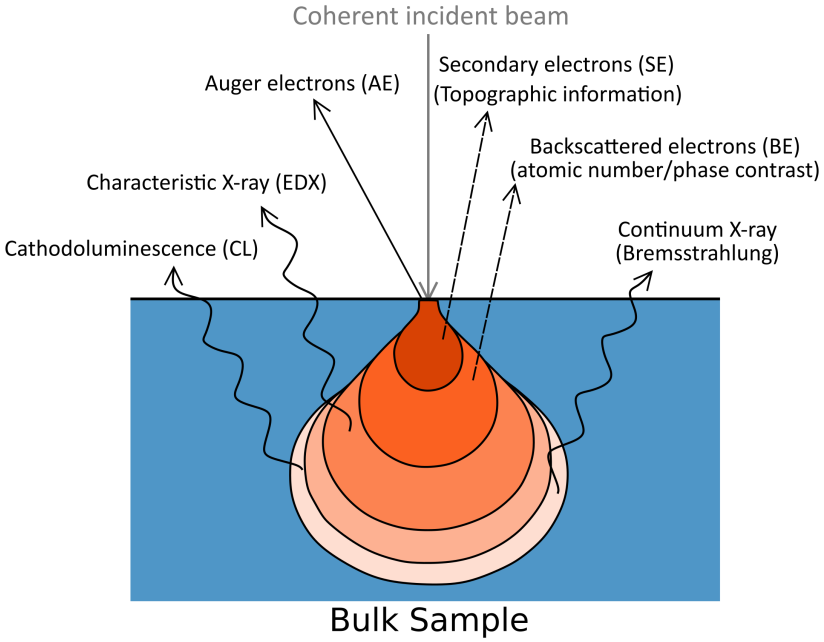

Fig. 4.11: **Beam induced scattering events in bulk samples.** The electron interaction volume (highlighted as the pear shape under the beam) is dependent on the acceleration voltage.

The electron-matter interaction is heavily dependent on sample thickness. Figures 4.10 and 4.11 highlight the scattering events associated with atomically thin and bulk samples. Though the type of interactions are the same in each case, there are a few key differences. Forward scattered electrons can penetrate through an atomically thin sample and escape given they have sufficient energy (see Fig. 4.10). In bulk samples, the electrons continue to interact as they penetrate into the bulk of the sample while the interaction volume broadens due to scattering (as illustrated in Fig. 4.11). As a result, in bulk samples imaged in an SEM, the forward scattered electrons aren't detected but the secondary and back-scattered electrons are.

Elastic scattering is when the incident electron is only interacting with the electron cloud surrounding the nucleus of each atom where there is no energy transfer. Elastic scattering is usually coherent and thus resembles characteristic wave-like nature occurring at low (1-10 mrad) scattering angles. If coherent elastically scattered electrons satisfy Bragg's condition ($n\lambda = 2d\sin\theta_B$), whereby the lattice plane is at a specific angle (θ_B) to the incident beam such that the incident beam is reflected due to constructive interference, a diffracted wave of high intensity (and specific direction) results [151]. This is the basis of electron diffraction patterns.

For incoherent elastic scattering, there is no phase relationship between scattered electrons. Instead of Bragg's law, we now enter a new regime where electrons are

treated as charged particles. The scattering cross-section σ of a single atom at an angle θ, also known as relativistic Rutherford scattering can be used to describe the probability of an incoherent elastic scattering event [151];

$$\frac{d\sigma(\theta)}{d\Omega} = \frac{e^4 Z^2}{16(4\pi\epsilon_0 E_0)^2 \sin^4(\theta/2)} \tag{4.7}$$

where $d\Omega$ is the solid angle of scattering, e is the elementary charge, Z is the atomic number, E_0 is the energy of the incident electron beam and ϵ_0 is the vacuum permittivity. The larger the cross section, the higher the probability of scattering. The electron intensity at a given scattering angle is also proportional to Z^2.

Inelastic scattering events occur when an electron interacts with the nucleus causing loss of their kinetic energy. Inelastic scattered electrons are scattered to higher angles and are typically incoherent. The volume of the sample containing such scattering events, illustrated in Fig. 4.11, is called the interaction volume [152]. The characteristic 'pear' shape relates to how the penetrating electron loses energy as it travels through the sample. The penetration depth and size of the interaction volume are dependent on both the electron acceleration voltage, a materials atomic number (Z) and density. Other important interactions that are occurring include secondary electron scattering, electron absorption, generation of electron and hole pairs (which can recombine) in the specimen, Auger electrons, visible light (cathodoluminescence) as well as characteristic and continuum X-rays [151].

Inelastically scattered electrons are essential for high resolution contrast (in annular dark field STEM), analytical analysis and for electron energy-loss spectroscopy (EELS). The emission of secondary electrons is a much less likely process compared to other inelastic scattering event, though enough to be detected for SEM imaging. Secondary electrons aren't associated with specific atoms (no elemental information provided) and can only escape if they are near the sample surface [151].

A single electron can be scattered multiple times and the more scattering events occur, the larger the scattering angle. In STEM, elastic and inelastic scattered electrons hold the key chemical/structural information about our specimen and single scattering events are desirable. This can be controlled by preparing samples as thin as possible and choosing an appropriate beam current. This also helps with interpretation, as most electron scattering models used for data analysis assume single scattering events.

4.2.2 Scanning Electron Microscopy

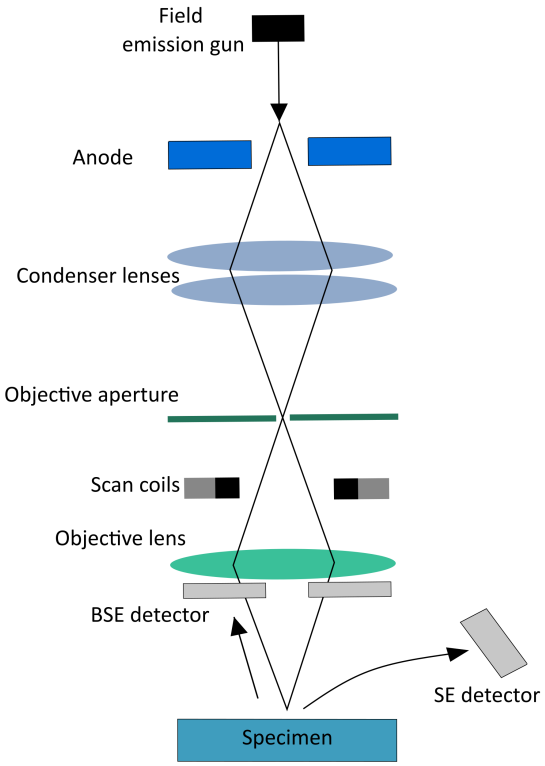

Fig. 4.12: **Schematic illustration of a scanning electron microscope.**

Fig. 4.12 illustrates the common components that make up a scanning electron microscope (SEM). The electron source in the field emission gun is commonly a tungsten filament. The electron source is passed firstly through an anode (positively charged) that attracts and accelerates the incident electrons. The condenser lenses converge the beam to a fine point towards an objective aperture to control the beam diameter. After passing through the aperture, electrons are re-converged by the objective lens to focus the beam on the sample. The scanning coils are then used to raster scan the beam across the sample [152].

The key parameters for operating an SEM include the electron acceleration voltage (kV), the working distance between the sample and the objective lens and the beam diameter. As discussed in the previous section, the acceleration voltage determines how far an incident electron can penetrate into a sample. The typical working distance range for SEM imaging is 4 - 10 mm (depending on sample thickness) and determines the depth of field. The diameter of the beam determines the spatial resolution and is mostly limited by lens imperfections such as chromatic and spherical aberrations [152].

Contrast in SEM Imaging

The two primary sources of signal including secondary-electron (SE) and back-scattered electron (BSE) signals in SEM imaging can be collected simultaneously from separate detectors. They both provide complimentary information; for example, SE imaging is regarded as topographic imaging, where as BSE imaging contrast is related to the atomic number and phase of the constituent components of a given sample.

Secondary electron (SE) contrast is caused by inelastic scattering events with electrons in the sample. Some of the energy lost on the incident electrons is gained in the atomic electrons, where a small part becomes potential energy and the rest becomes kinetic energy. The gain in kinetic energy allows atomic electrons to overcome their potential well and travel through a sample gradually losing their energy, with an average distance travelled of several nanometres [152]. Some of the secondary electrons that are generated close to the surface (up to 2 nm) are able to escape from the specimen and can be collected by a SE detector. Because the number of SE emitted at any specific location strongly depends on the samples topography, the generated contrast provides mostly topographical information.

SE contrast is inversely proportional to the energy of the primary electrons such that higher energy electrons generate less inelastic scattering. Typically, a minimum beam voltage of ~ 5 eV is required to give electrons enough energy to be ejected from the sample. Contrast is also dependent on the tilt angle between the sample and the incident beam. This is because there is a larger specimen volume emitting SE under the incident beam when there is a tilted surface. This volume, with a normal incident beam, can be described as;

$$V(0) = (\pi/4)d^2\lambda \tag{4.8}$$

Where the escape volume is a cylinder of radius $d/2$ and the escape depth is λ. For a tilted sample, the escape volume increases with tilt angle (ϕ) as;

$$V(\phi) = \pi(d/2)^2(\lambda/cos(\phi) = V(0)/cos(\phi) \tag{4.9}$$

As depicted in Fig. 4.12, the SE detector (such as the SE2/Everhart Thornley (ET) detector) is situated to one side of the vacuum chamber. This causes SE contrast images to appear 3-dimensional. Any peaks or valleys across the surface of a sample will have a brighter outline with apparent "shadow" in an SEM image as illustrated in Fig. 4.14. The signal of the SE detector can be maximised if the sample is tilted toward the detector.

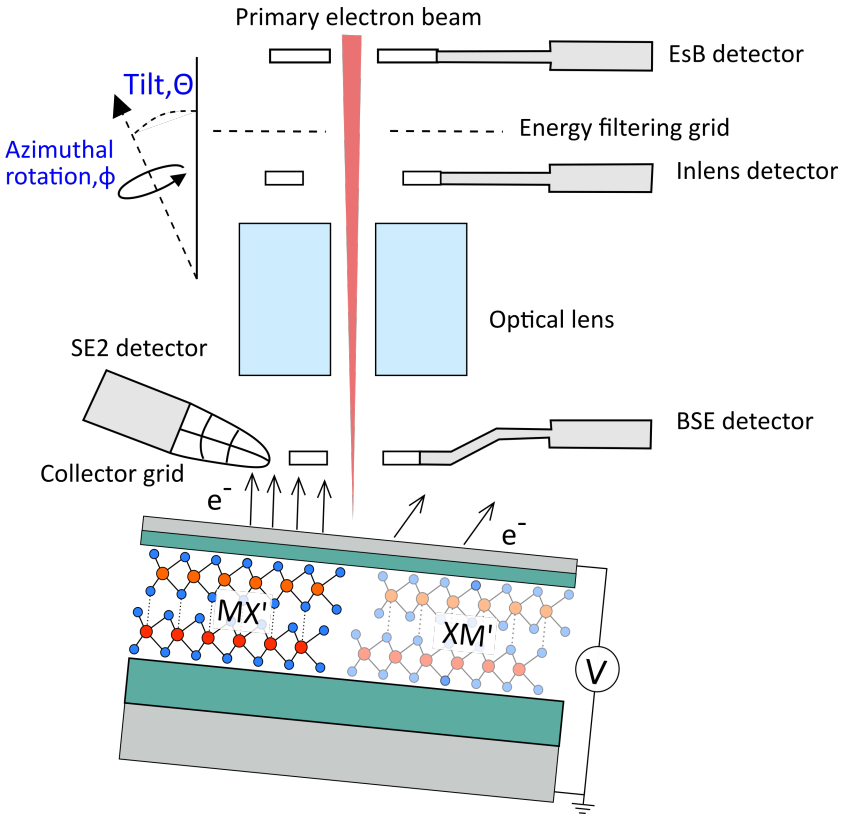

Fig. 4.13: **Crystal orientation dependence on SEM image contrast of a 3R-type bilayer of MoS_2 encapulated in thin (< 2nm) hBN and graphene.** By tuning the sample tilt and azimuthal rotation angle, contrast between stacking configurations is maximised.

In BSE imaging, the detector is placed much higher up and collects electrons within a small angle as compared to an in-lens SE detector (see Fig. 4.13). The signal is proportional to Z^2, therefore, the number of back-scattered electrons that escape the surface increases with the atomic number of the material and can also provide chemical composition contrast. The fundamental difference between secondary-electron and backscattered electron contrast is the type of electron being detected. Energy filtering can also be employed to enhance contrast, for example, the energy selective backscattered (EsB) detector only detects electrons with an energy greater that 0.5 kV. The higher the electron acceleration energy, the higher the penetration depth (in the range of 10 to 100 nm). This means that the contrast associated with BSE is related to both the surface and the internal structure of a given sample.

At specific sample tilt (θ) and azimuthal rotation (ϕ) angles, crystallographic materials demonstrate contrast due to variations of crystallographic orientation which can be detected in a BSE detector (see Fig. 4.13). This is due to a phenomena known as 'electron channelling' [153]. When the incident electron beam is normal to one of the primary atomic planes of a crystal, the incident electrons propagate along the atomic columns and therefore the amount of both backscattered and secondary electrons changes. For samples where multiple polytypes or crystal phases are present on the surface, the angle of incident electrons can be selected so that contrast between them is achieved. Fig. 4.13 highlights how the sample orientation is optimised to acquire such contrast. This method of imaging demonstrated excellent constrast of XM′ and MX′ stacking domains in reconstructed 3R-type bilayers of TMDs in a non-invasive manner [154] and will be discussed in detail in chapter 5.

All SEM measurements in this project have been performed using a Zeiss (Germany) Merlin SEM operated at 1.5 keV with a probe current of 1.1 nA. Backscattered electrons were collected at a take-off angle of 73° and collected by an in-lens Energy selective Backscattered (EsB) detector with an applied energy selected grid bias of 500 V, at 5 mm working distance (WD). The optimal tilt angle that provided maximum contrast was experimentally found to be 20.2° and the azimuthal rotation was optimised for each individual sample.

In the SEM images presented in Fig. 4.14, the sample is a 3R-type minimally twisted MoS_2 bilayer that has been encapsulated with 2 nm thick hBN. The encapsulated bilayer sits on top of a bottom hBN (5-20 nm) and a graphite back-gate. Finally, a graphene top-gate covers the entire bilayer structure. Despite there being

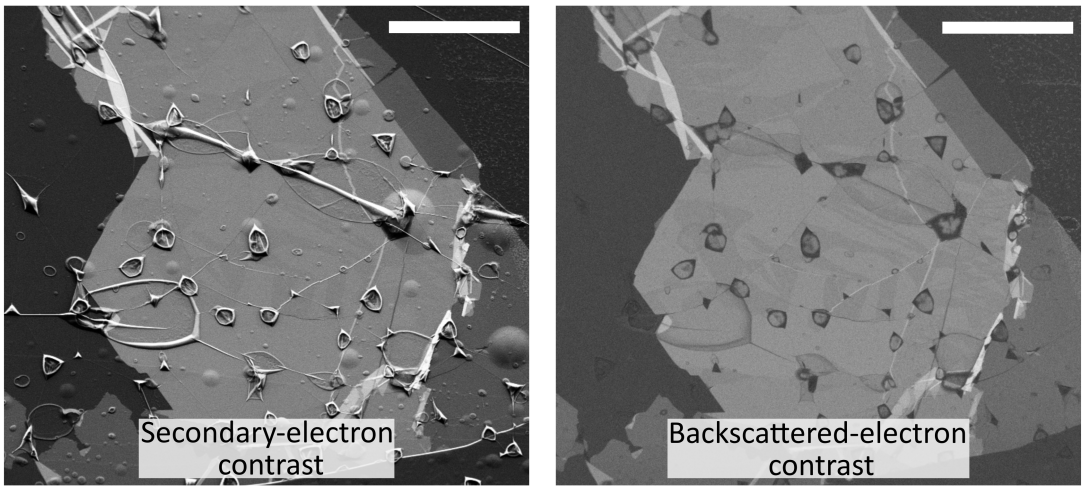

Fig. 4.14: **SEM image contrast for secondary-electron and back-scattered electron signals.** The acceleration voltage was 1.2 kV and the optimised sample tilt (θ) and azimuthal rotation angles (ϕ) are 20.2 ° and 356.6 °, respectively. The scale bars are both 5 μm.

a hBN/graphene capping layer, there is bright and dark contrast between domains of XM′ and MX′ stacking configurations in both the backscattered and secondary electron signals. In contrast to the SEM imaging method proposed in [154], we found that the contrast of the back-scattered electron signal was higher than that of the secondary electrons and therefore this was used in this body of work. At the optimised acceleration energy range of 1.2 - 1.5 kV (lower than standard SEM imaging parameters), the contrast between bright and dark domains appears to drop off when the thickness of the top hBN layer exceeds 5 nm and therefore an average top hBN thickness of 2 nm has been used for all samples.

4.2.3 SEM Image Processing

Image filtering of SEM images was performed using Weiner/Hunt deconvolution [155, 156] which was applied using the open source python package Hyperspy [157]. Image filtering was necessary in instances where electrical noise and contamination reduced the image quality. Electrical noise commonly appears periodically in microscopy images with a periodic frequency of 50 Hz (as seen in Fig. 4.15a). The type of noise observed in Fig. 4.15a is due to random fluctuations of an electrical (DC) current. This noise may be a consequence of grounding loops between the gated vdWs heterostructure and the SEM microscope. Another potential source of noise can be external noise such as nearby construction work (mostly mechanical noise).

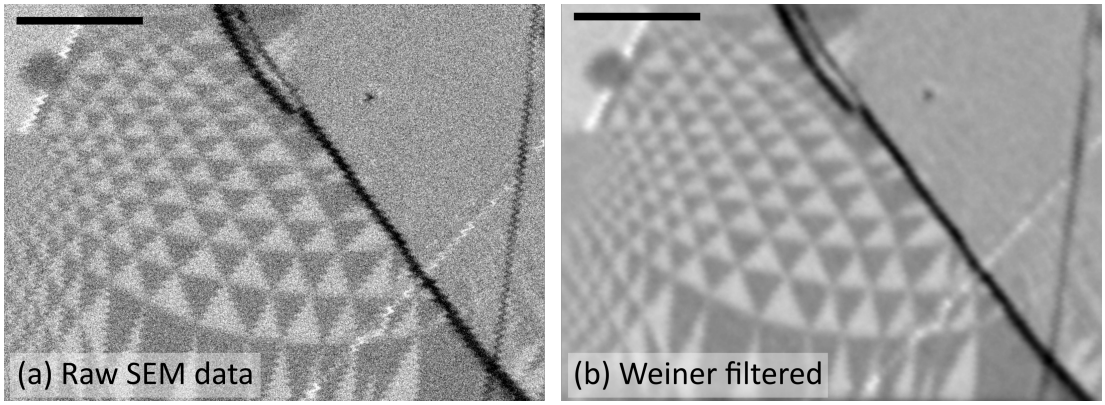

Fig. 4.15: **Using Weiner filtering to process SEM images. a** Raw unfiltered SEM image of a top and bottom gated 3R-type twisted bilayer MoS_2 heterostructure image using the electron channelling contrast technique. **b** The Weiner filtered image with reduced (electrical) noise artefacts. Scale bars are both 500 nm.

The Weiner filter is commonly used to remove the adverse affects of frequency based noise. It is a point spread function that is applied via a finite impulse response in order to estimate an unknown signal using a known data signal as the input and filtering the known signal to generate an estimated (mean square error) output. Here, the known signal is the convoluted (desired and erroneous) signal. The mathematical data model is described as;

$$y = Hx + n, \tag{4.10}$$

Where n is noise, H is the point spread function and x is the original data image. The Weiner filter applied to the original data is [155, 156],

$$\widehat{x} = \mathbf{F}^{\dagger}(|\Gamma_H|^2 + \lambda||\Gamma_D|^2)\Gamma_H^{\dagger}\mathbf{F}_y \tag{4.11}$$

Where $\mathbf{F}$ is the Fourier transform, $\mathbf{F}^{\dagger}$ is the inverse Fourier transform and Γ_H is the Fourier transform of the point spread function. Here, using Fourier space means that we assume the noise (H) is circular. Γ_D is the filter that analyses the restored image frequencies (here, a Laplacian smoothing filter) and λ is the parameter that controls the balance between high frequency signal the desired and erroneous signal. In Fig. 4.15b, the unwanted periodic signal has been removed and the signal is much smoother.

4.2.4 Scanning Transmission Electron Microscopy

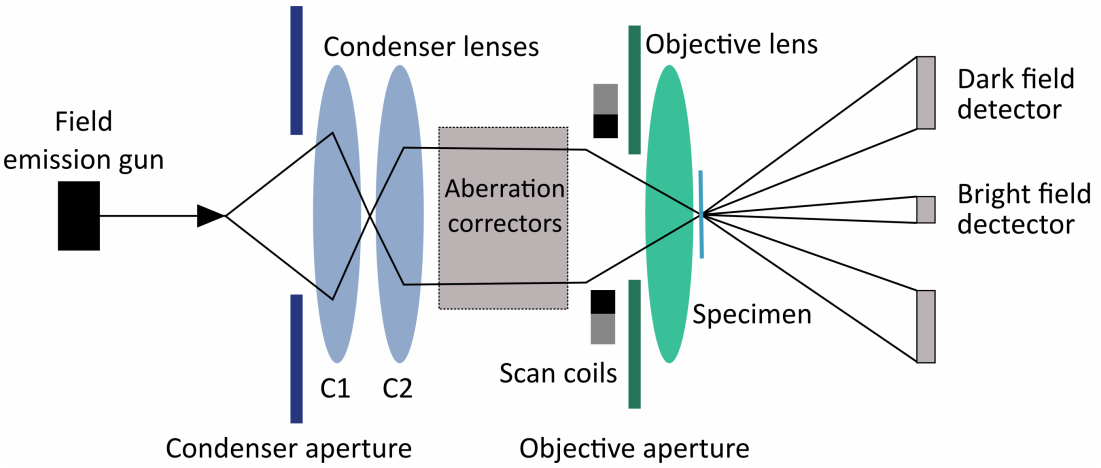

Fig. 4.16: **Common components of a STEM imaging microscope.**

In a STEM microscope the condenser and objective lenses (illustrated in 4.16) shape and focus the electron beam using a strong magnetic field. Magnets with poles of alternating polarity form a round rotationally symmetric lens [158]. A force is produced perpendicular to the velocity of incident electrons which allows for manipulation of the electron beam. Scherzer was first to explain that aberrations (lens imperfections) are intrinsically positive and therefore limit the practical resolution of an electron microscope [159]. Assuming that the microscope is well-aligned to the optical axis, the aberrations that contribute to the image distortion the most are chromatic (C_c) and spherical aberrations (C_3). Chromatic aberration relates to the spread of incident electron energies which are not all focussed at the same point. In this case, a monochromator can be used to filter electrons with different energies. Spherical aberration causes electrons travelling at larger angles (α) to be deflected more and generates a positional error of the electron trajectory [160]. Aberrations can be defined in terms of a geometrical aberration function ($\chi[\theta]$) describing a coherent phase shift of the wavefront as a function of the angle to the optical axis [158]. Such angles are relatively small so higher order terms can be ignored. Here, spherical aberration is a third-order aberration ($C_3\theta^3$) with a fourth-order phase shift ($\frac{2\pi}{\lambda}\frac{1}{4}C_3\theta^4$). Generally speaking, spherical aberration can be corrected by employing an 'aspherical' lens which can be achieved with a series of 'multi-pole' magnetic lenses [161].

The magnetic scanning coils used to shift the probe can be adjusted to raster scan

the electron beam across the specimen. The condenser lens (situated before the sample) and objective lenses (sample sits within the upper and lower pole piece of this lens) are used to project the incident beam onto the specimen to form the probe as well as to reduce the final spot size of the probe. Unlike TEM, STEM images are not magnified by a projection system as the stationary detectors read each pixel at a time with a projection system allowing us to change the collection angle that determines the contrast. STEM images are scaled by the scan dimensions formed pixel-by-pixel at each xy coordinate in the imaged region.

STEM Imaging Modes

STEM imaging modes are related to the electron scattering angle of the transmitted electrons which can be selectively separated into low, medium and high angle scattering as depicted in Fig. 4.17. Electrons with low scattering angle (>10 mrad with respect to the optical axis) are defined as direct beam electrons and generate bright field images. Electrons with intermediate scattering angle generate low angle annular dark field images (LAADF) with a scattering angle range of 10-50 mrad or high angle annular dark field (HAADF) with scattering angles of 50-200 mrad [151]. STEM systems are able to accumulate each data type simultaneously which provides complimentary information on a local crystal structure.

Bright Field STEM

Generally speaking, bright field imaging is a result of coherent elastically scattered electrons. Conventional TEM and STEM bright field imaging are, in principle, the same and can be related to each other by the principle of reciprocity if we simply assume that the sample is inverted (i.e. swap around the source and detector) [162]. Contrast is achieved due to phase change as well as electron diffraction and the atomic mass of a specimen. Phase contrast can be described as the interference between the direct beam and the first Bragg diffracted beams from the specimen. Similarly to conventional TEM, bright field imaging suffers from aberration of the electron optics. The contrast contribution due to electron diffraction is in fact rather small in this case due to the small/negligible electron collection angle. Contrast due to the mass of atoms and sample thickness is simply an increase/decrease of electron scattering. If we assume the specimen is a weak phase object (i.e. electron transparent and mainly light atoms), imaging can be described mathematically as a phase contrast transfer

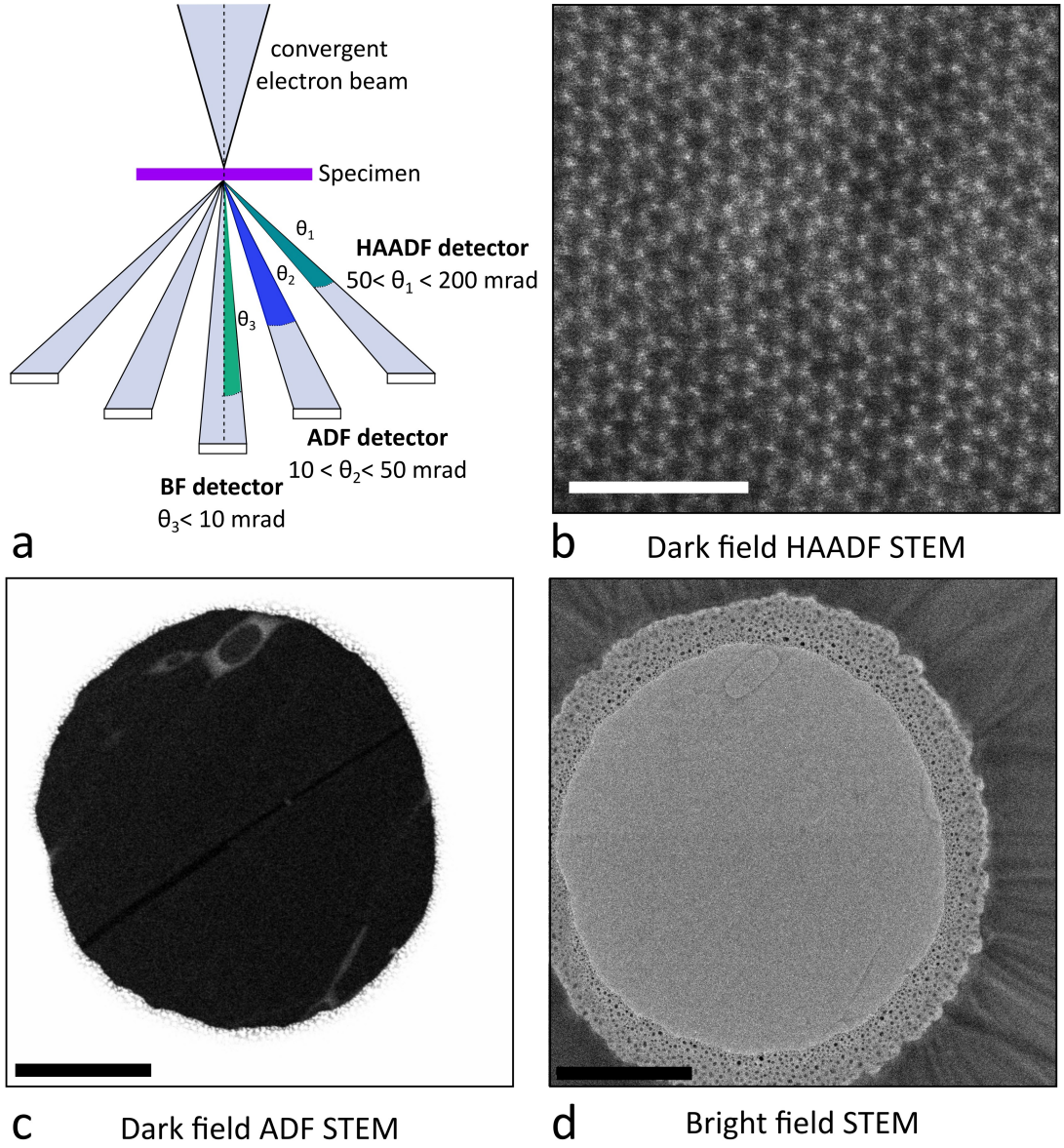

Fig. 4.17: **STEM imaging modes. a** STEM imaging techniques catergorised by the collection angle of the electron detector and includes bright field, ADF dark field and HAADF dark field. **b** Atomic resolution image of a monolayer region of MoS_2 achieved using HAADF STEM. Scale bar is 2 nm. **c** Dark field and **d** bright field contrast images taken of the same region on a suspended TMD bilayer sample. Scale bars for **c** and **d** are 0.5 μm.

function [163];

$$I_{coh}(R) = |P(R) \otimes \psi(R)|^2 \tag{4.12}$$

Where P(R) is the complex point spread function of the electron microscope passing through point R and $\psi(R)$ is the exit surface electron wavefunction. Here, aberrations cause blurring of the exit wavefunction as it travels through the electron optics and is defined by a convolution of the point spread function. Therefore, what is measured is the intensity of the convolution [163]. The ideal case is that we have a transfer function that is flat and has the same sign over a range of spatial frequencies as well as a consideration for Scherzers minimum aberration function ($\chi[\theta]$). Irrespective of the Scherzer conditions, the point spread function is complex and scattering from different spatially separated regions of the specimen can cause instabilities in image intensity and in some cases image contrast reversal [163]. Though it is important to have an understanding of bright field imaging, it was not well suited for this particular project and therefore only dark field imaging techniques were used.

LAADF STEM: Diffraction Contrast

LAADF is an intermediate STEM technique that can use Bragg diffracted or inelastically scattered electrons using the ADF detector allowing for either diffraction contrast or mass-thickness contrast. The convergence angle in STEM is too large for coherency so instead we use the principal of reciprocity and equate the objective aperture collection angle in conventional transmission electron microscopy (CTEM) to the convergence angle in STEM. Thus, if a small collection angle is used (in STEM) this can be equated to a small convergence angle in CTEM [151]. Although CTEM and STEM diffraction contrast imaging can be equated, it is important to understand the key differences to help aid correct data interpretation. For example, the data acquisition is notably different. Due to the high beam convergence angle required in STEM imaging, the diffraction pattern has large and overlapping diffraction spots instead of sharp/small spots observed in CTEM diffraction patterns.

In order to interpret CTEM diffraction contrast image, a two beam approximation is used. The approximation implies that there are only two waves in a crystal including the transmitted wave (incident beam direction) and the Bragg-reflected wave which is reflected from a specific lattice plane. Diffraction contrast can then be described as the change in intensity when there is a change in diffraction condition [151]. In CTEM, the spots in the diffraction pattern are the lattice points (denoted g) in reciprocal space.

An example of CTEM diffraction imaging includes the use of selected area electron diffraction (SAED) and selecting only the diffraction peak at g = $(10\bar{1}0)$ to image domain formation due to lattice reconstruction in twisted bilayers of graphene[12, 76]. The contrast in this case is due to the change in lattice stacking configuration from AB to BA (Bernal) stacking.

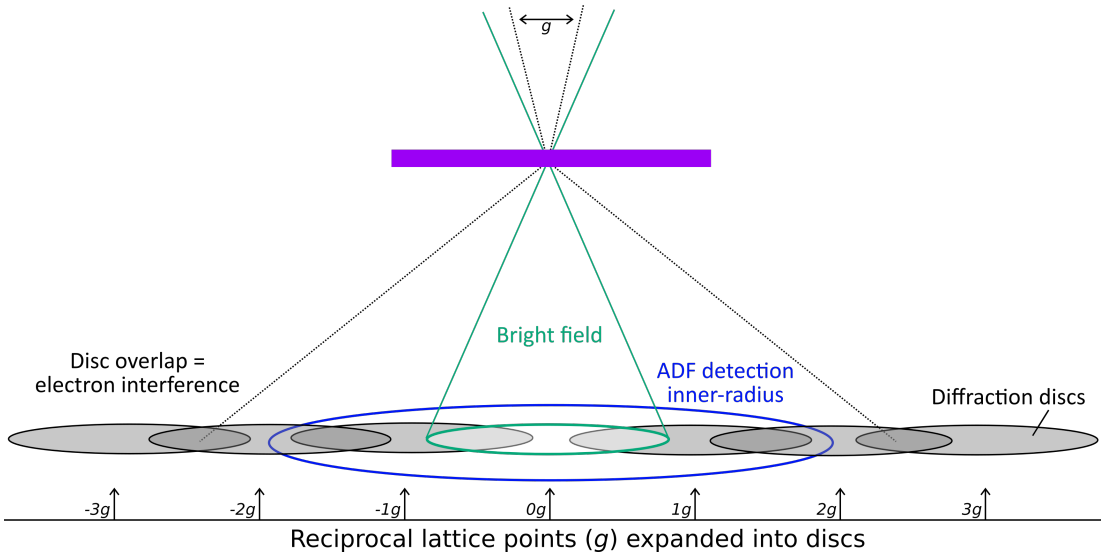

Fig. 4.18: **STEM nanodiffaction.** STEM diffraction patterns, referred to as convergent beam electron diffraction (CBED) patterns, have diffraction peaks expanded into overlapping discs where each disc corresponds to a reciprocal lattice point g of the crystalline specimen (scale bar = 100 nm).

In order to interpret diffraction contrast in STEM we must know the beam convergence angle and detection collection angles. The LAADF imaging regime refers to the inner detection angle of the ADF detector close to the bright field disc as depicted in Fig. 4.18. In this regime, diffraction contrast is largely due to lattice defects and strain whereas the MAADF/HAADF regimes are more sensitive to compositional changes [164]. This is due to elastic scattering of the probe (collected by the ADF detector) decreasing with increasing detector inner-angle [165]. LAADF has been used to image twisted bilayers of graphene where contrast was enhanced due to sensitivity to the amount of in-plane atomic overlap in the translation direction i.e. higher sensitivity to AA stacking compared to AB/BA stacking in graphene [166].

HAADF STEM: Z Contrast

HAADF images are formed from incoherent elastic/inelastic scattered electrons where contrast is very sensitive to the atomic number and therefore can be interpreted directly. For detection angles above $\sim$ 50 mrad, Bragg diffraction becomes negligible and

Rutherford scattering dominates. Incoherent imaging has a resolution limit that is twice as good as coherent imaging and is the convolution in intensity instead of in complex amplitude such as the case for coherent bright field imaging. This is mathematically written as [163];

$$I_{incoh}(R) = |P(R)|^2 \otimes |\psi(R)|^2 \tag{4.13}$$

As previously discussed, if we are able to exclude all diffraction signal then electron intensity at a given scattering angle is proportional to Z^2. A better estimation, however, would be to include the effect of screening due to the electron cloud surrounding atoms (because we aren't just imaging a single isolated atom). This requires modification to the Rutherford cross section. If we now include the screening parameter (θ_0) into equation 4.7, we must replace the term $\sin(\theta/2)$ with $[\sin^2(\theta) + (\theta_0/2)^2]$ [151]. The electron cloud effectively reduces the scattering cross section meaning that the scattering angle is in fact proportional to $Z^{1.5-2}$ [150, 161]. If we filter the detector collection angle to exclude inelastically scattered electrons we will have a much stronger Z contrast [167]. Due to microscope and atomic vibrations, thermally diffusive scattered electrons are also generated which causes the image contrast to also be dependent on the mean square displacement of the atom [168].

4.2.5 Atomic Resolution STEM Image Processing

Image filtering of atomic resolution STEM images was performed using a patch based principal component analysis (PCA) denoising algorithm [169] which was applied using the open source python package Hyperspy [157] and performed by Dr. Nick Clark.

Fig. 4.19 compares the original acquired data of rigidly twisted TMD bilayers in both 3R and 2H configurations. Here the quality of the image filtering is dependent on the original image pixel count (pixel count in Fig. 4.19 c and d is lower than that in a,b). The principle of the PCA filtering technique includes taking small patches of the image, centred on local bright peaks, and recompiling them to form a 3D image stack. This is a form of dimensionality reduction where the common features (i.e useful signal and stacking configurations) that appear multiple times in a large number of the patches are reinforced and less frequent features (single or few patches) i.e. noise

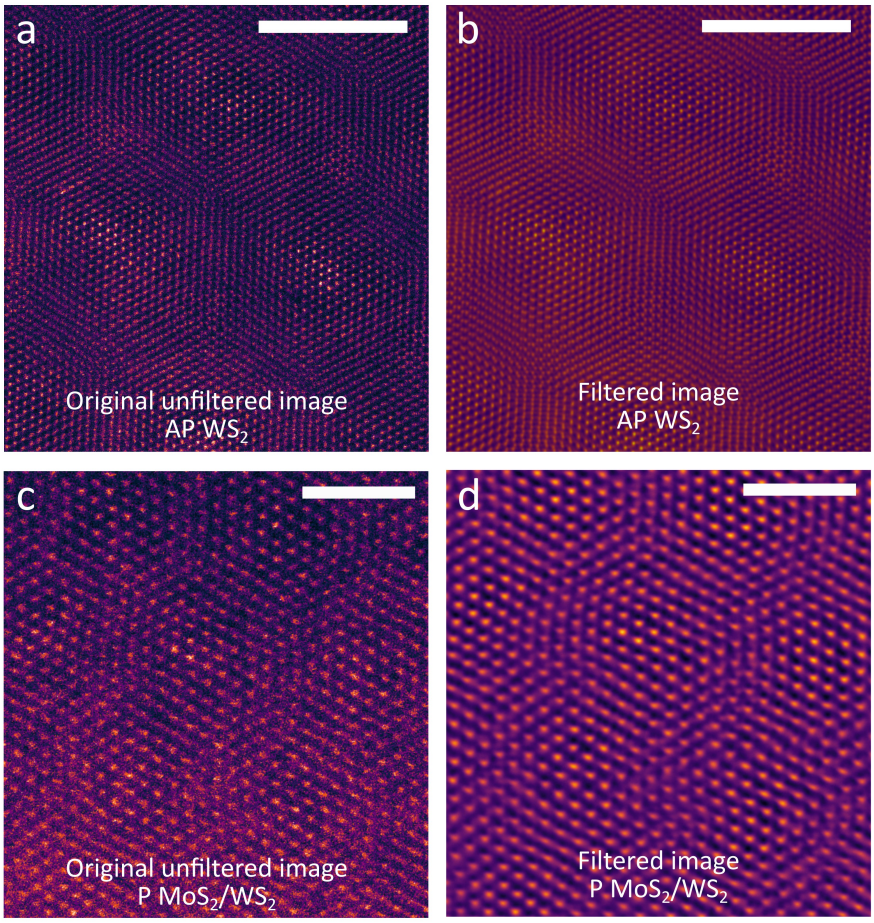

Fig. 4.19: **Atomic resolution ADF STEM image comparison between original and filtered data (PCA and high pass filtered) of non-reconstructed bilayer TMDs. a** Raw unfiltered image and **b** PCA filtered image of 2H-type (anti-parallel) rigidly twisted bilayer WS_2 (scale bar is 5 nm). **c** Raw unfiltered image and **b** PCA filtered image of 3R-type (parallel) rigidly twisted bilayer MoS_2/WS_2 (scale bar is 2 nm).

is suppressed. PCA denoising was implemented on the 3D image stack and patches from the denoised stack then were averaged at their original locations in the image to generate a denoised image. A high-pass filter was then applied to the image in order to remove long range signals associated with local surface contamination. The PCA filtering process can be briefly summarised in 5 key steps;

1. Local ADF peak intensity values are found (typically centred on metal atoms). Values are extracted and multiplied by a centralised gaussian fitting. Typically patches are 40(60) x 40(60) pixels per patch (dependent on pixels per source image).

2. Patches are decomposed into different components with decreasing magnitude (factor/eigenvector multiplied by loading/eigenvalue) such that the strength of each component is acquired. Typically, the generated components were simplified features that can be linearly combined into patches representing the common stacking configurations.

3. Components of significance (higher strength) are then selected to re-build the image with a cut-off of 15-18 components per image.

4. The patches are reconstructed in their original location in the source image with the selected denoised components effectively removing high frequency noise.

5. The patches per pixel are counted to normalise the image. This is necessary as the peak locating in step one doesn't sufficiently find every atom, however, the process is significantly improved with the image processing technique.

The denoised/reconstructed images were filtered with a high-pass filter to improve visibility of the atomic structure. This filter uses a radial mask in Fourier space to remove low frequency spatial variation.

4.2.6 Electron Beam Induced Effects

This section will discuss how changes induced by elastic and inelastic scattered electrons from the incident beam can be a limiting factor in STEM imaging of vdWs heterostructures. It must be noted that there are a number of cases where this can be used to our advantage; some useful examples include selective cutting and manipulation of a sample and the study of atomic defects. Generally speaking, beam

induced damage is dependent on the electron energy and the radiation dose rate which is the amount of electrons passing through a specimen of a given area during imaging.

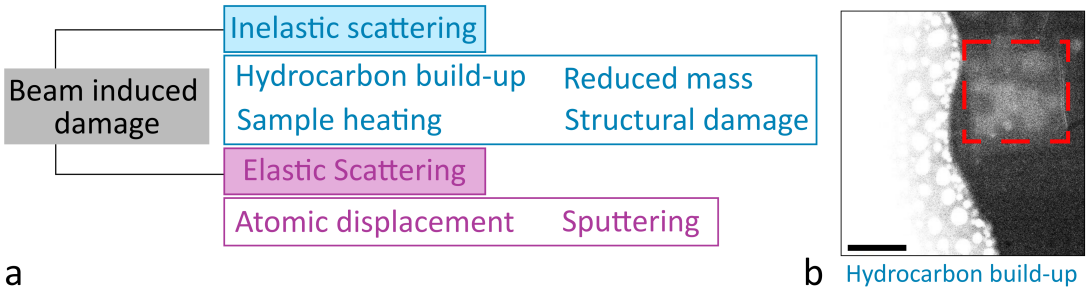

Fig. 4.20: **Beam induced damage. a** Common sources of electron beam induced effects from both elastic and inelastic electron scattering. **b** ADF STEM image of hydrocarbon build up (indicated by the red dashed box) that has accumulated in the region of interest in a suspended bilayer TMD sample (scale bar = 100 nm).

Figure 4.20 summarises the adverse effects that occur during electron-matter interaction. In addition, electrostatic charges can also build up across the surface of a specimen, primarily affecting insulating materials, which can be detrimental to imaging [170]. Elastic scattered electrons can be responsible for atomic displacement and sputtering (which is a similar process in 2D materials) which is commonly known as knock-on damage. If the transferred kinetic energy from the incident beam is higher than the displacement energy threshold (E_d) then the atom can be displaced from its lattice site[170, 171]. The type of displacement is dependent of the energy required to overcome the threshold energy, i.e. a dependence on the atomic weight of the atom, its bonding environment and the crystal lattice type. Knock-on displacement requires $\sim$ 10-50 eV whereas sputtering only requires a few eV [171]. Limiting the radiation dose will counteract these mechanisms, however, lower dose rates will limit the image resolution [172].

Inelastic scattering can cause a number of adverse effects, including sample heating, hydrocarbon build up, mass reduction and damage to the specimen structure. These are affects caused by ionisation damage (radiolysis) in which excitation of the sample (caused by the incident beam) does not return to its original state after de-excitation [76, 170]. Sample heating due to inelastic scattering results in phonon excitation; as only the area under the probe is being irradiated (sub nm), the temperature increase shouldn't increase dramatically as any excess heat can be dissipated through the rest of the sample [170]. Hydrocarbons (present on all specimens, but on some more than others) are often mobile and can diffuse across the

surface of a specimen. During the imaging they begin to accumulate in the scanning region and become polymerised by the electron beam, over time building a thick layer of contamination in the region of interest [170]. This can be accelerated if other forms of contamination are present such as polymer residue and organic solvents from the fabrication process. Such effect can clearly be seen in Fig. 4.20b where the thick hydrocarbon build-up appears bright in the square region that has been scanned for a period of time. The contamination effectively blurs out the fine atomic structure and thus is a limiting factor during imaging. Common methods to counteract these affects include sample annealing, plasma cleaning and beam showering [173]. Beam showering is a cleaning method that is employed in-situ by 'showering' the specimen with the condenser aperture removed and defocussing the illumination to polymerise the hydrocarbons over a larger area and stop them accumulating (diffusing towards the incident beam) in the region of interest [170].

4.3 Summary

In this chapter, the theoretical concepts and principles of operation of electron microscopy and scanning probe microscopy techniques have been introduced. Details of their applicability to moiré superlattice characterisation were then identified. In particular, the origins of image contrast and how they relate to a material's physical properties have been outlined for each of the microscopy techniques used in this project. Electrical SPM techniques have not only proven to be essential to the study of electrical properties but also are a useful tool for fast domain mapping of electronic devices. Finally, the data processing tools relevant for each microscopy technique have been discussed.

Chapter5

Atomic Structure of Reconstructed Lattices of Twisted Bilayer TMDs

With such great research interest into the novel optical and electronic properties of twisted TMDs, it is essential to gain a fundamental understanding of the atomic structure and how it evolves with the twist angle. TMDs have an asymmetric crystal structure which leads to numerous polytypes with the most common including 3R and 2H (see Fig. 2.5). Each polytype will form a different superlattice (see Fig. 2.14) and their structural properties evolve differently with the twist angle. Theoretical studies suggest lattice reconstruction will occur in twisted bilayers of TMDs with low/zero lattice mismatch below a critical angle [88, 174–176]. Twisted bilayers of MoS_2 (3R like) in the rigid regime (>3°) have already been imaged [81, 177] but microscopy studies in the reconstructed regime have been lacking prior to this work, especially with atomic resolution.

In this chapter LAADF and HAADF STEM imaging has been used to study both the long range periodicity and atomic detail of the lattice reconstruction of twisted homo and heterobilayers of TMDs. Details of the sample fabrication procedure have also been discussed. To validate the results, multi-scale modelling of the interlayer adhesion energy has also been used. This work was carried out in collaboration with Dr Yi-Chao Zou who performed the electron microscopy imaging, Dr Nick Clark who processed the atomic resolution data with a patch-based principle component algorithm (PCA), Dr David Hopkinson who generated QSTEM simulations of the atomic resolution data and Dr Vladimir Enaldiev who carried out the bulk of the theoretical calculations, as well as other authors presented in [178]. My personal contribution to this work was to design and implement a fabrication technique allowing for twisted bilayer TMDs to be suspended on silicon nitride grids.

5.1 Sample Fabrication

In order to study the atomic structure of lattice reconstruction in TMDs, twisted bilayers were transferred onto home-made custom TEM grids [179]. The construction of the bilayer was carried out using the methods discussed in Chapter 3. Both bilayer construction and TEM grid transfer were carried out in an argon atmosphere glove-box to ensure minimal oxidation, particularly at the interface between the monolayers.

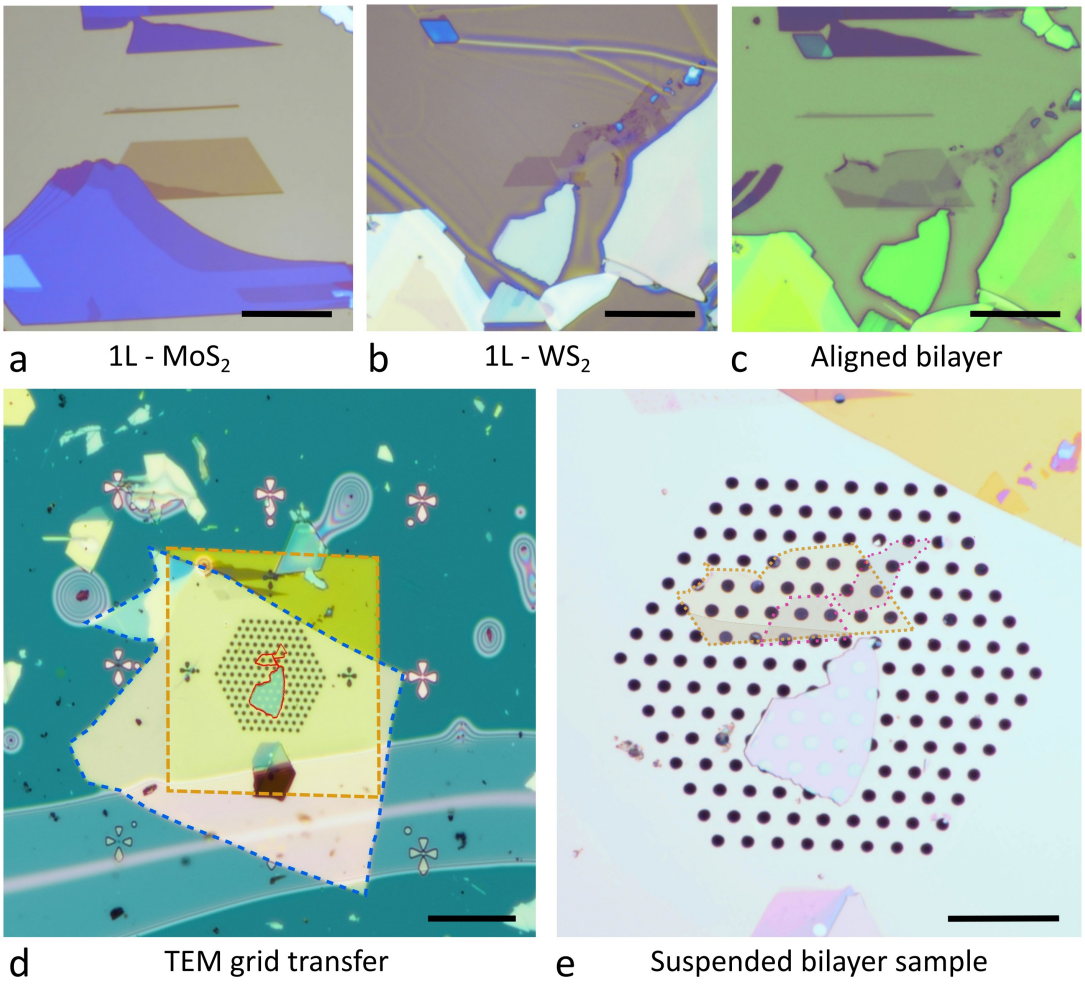

Fig. 5.1: **Example fabrication of suspended bilayers of TMDs.** **a** MoS_2 monolayer with edges oriented at 60°.**b** WS_2 monolayer with edges oriented at 60°. **c** The subsequent aligned bilayer during PMMA flake transfer. **d** TEM grid transfer where the MoS_2 adhesion layer and the thin ($\sim$ 100 μm) SiN membrane are highlighted by the blue and orange dashed line respectively. The bilayer region is highlighted in red. **e** The suspended bilayer sample after cleaning with the TMD flakes highlighted for visibility. Scale bars for **a-c,e** = 20 μm and scale bar for **d** = 50 μm.

The custom grids were developed by our group at Manchester to greatly enhance adhesion of vdWs heterostructures to TEM grids which has been a significantly

limiting factor in sample fabrication. Adhesion was improved by firstly transferring a mechanically exfoliated bulk MoS_2 crystal onto a silicon nitride (SiN) etched membrane (supported by a thick SiN substrate). The MoS_2 crystal was then back-etched to generate 2 μm (diameter) holes for the bilayer to be suspended over (further fabrication details in Ref. [179]). The bilayers were transferred on the grids using a wet transfer technique whereby the PMMA membrane was cut out after transfer and the PMMA was removed using the following cleaning procedure;

(1) Anneal the TEM grid at 150 °C to ensure that the bilayer is in contact with the bulk MoS_2 adhesion layer.

(2) Immerse the TEM grid in a beaker of acetone heated to 60 °C. If the PMMA layer is thick, include a magnet stirrer into the beaker to assist removal by generating shear forces. Leave the submerged grid for a minimum of 10 minutes.

(3) Immerse the grid in a separate beaker of IPA and return to the beaker of acetone. The grid must always be kept in a solvent environment until all of the polymer is removed before drying because it becomes increasingly harder to remove once dry. Check the progression of PMMA removal in an optical microscope (still in acetone). To check that the PMMA is gone, tap the side of the grid; if you can see string-like residues moving then further repetitions of acetone and IPA are needed.

(4) Dip the TEM grid finally into a beaker of hexane (or hot IPA ($\sim$ 80°) as an alternative) before drying with a compressed nitrogen gun. Hexane is used here because it has a very low surface tension compared to the other solvents used. The surface tension can cause the suspended membranes to rupture upon drying.

Prior to loading the sample into the microscope, we must remove as many surface hydrocarbons as possible. This is most effectively achieved in a vacuum annealing system providing that we have sufficiently removed the bulk of the transfer polymer during the cleaning process. Here, a Moorfield vacuum annealer (pressure $\sim$ x10^{-2} mbar) was used at 150-170 °C with an argon atmosphere.

5.2 Dark Field LAADF-STEM

The LAADF imaging technique was used to first identify regions of interest for atomic resolution HAADF and also to examine the long range order within suspended samples of twisted homobilayers of MoS_2 and WS_2 and heterobilayer WS_2/MoS_2. LAADF is a particularly useful technique for imaging lattice strain and defects in

crystalline materials [164]. For LAADF imaging, structural features that are strained appear darker and the unstrained commensurate regions as well as contamination bubbles/creases appear brighter. LAADF images were acquired on a FEI Talos X-FEG STEM operated at 80 kV. In this study, the high contrast was achieved with a convergence angle of 6 mrad and an annular dark field (ADF) collection angle range of 14-85 mrad.

At this stage it is important to introduce the nomenclature used for each of the stacking configurations described in this chapter as there are many variations used in the field [87, 174, 180]. Due to the asymmetric nature of the crystal structure, bilayers of TMDs can form two possible moiré superlattices. Twist angles close to 0° in TMD bilayers have a resemblance to the 3R polytype stacking configuration and we describe the unit cells of these layers to be parallel (P) to each other. The 3R-like stacking lacks mirror (reflection) and centre of symmetry (inversion) and thus can have two possible stackings including MX′ and XM′ where the nomenclature refers to the alignment of the metal atom (M) in the top/bottom layer to the chalcogen atoms (X) in the bottom/top layer, respectively (schematics shown in Fig. 5.5). Another intermediate stacking configuration is possible (denoted XX′ (P)) where M in the top/bottom layers as well as the X in the top/bottom layers are in alignment with each other.

Twist angles close to 180° (where the unit cells of the two layers are anti-parallel (AP) with respect to each other) in TMD bilayers resemble 2H polytype stacking (schematics shown in Fig. 5.8). Other intermediate configurations include MM′ (metal aligned with metal only) and XX′ (AP) (chalcogen aligned with chalcogen only). Both MM′ and 2H configurations have inversion symmetry.

If we first consider the lattice relaxation in a 3R-like moiré pattern, we expect to observe an extended network of tessellated triangular domains separated by thin boundaries that meet at pinning points expected to be XX′ stacking [87, 88, 174, 176]. In Figure 5.2, we do observe a triangular domain network where the high symmetry stacking configurations (expected to be MX′, XM′ and XX′) appear brighter and the boundary regions appear darker. Unlike diffraction contrast TEM [12], there is no distinction between the high-symmetry stacking configurations. Additionally, the variable contrast within the high-symmetry stacking regions is due to sample rippling and surface hydrocarbons. The contrast at the boundaries correlates to the loss of coherent stacking due to lattice reconstruction leading to changes in the diffraction pattern. In Fig. 5.2a, there are large contamination bubbles filled with amorphous

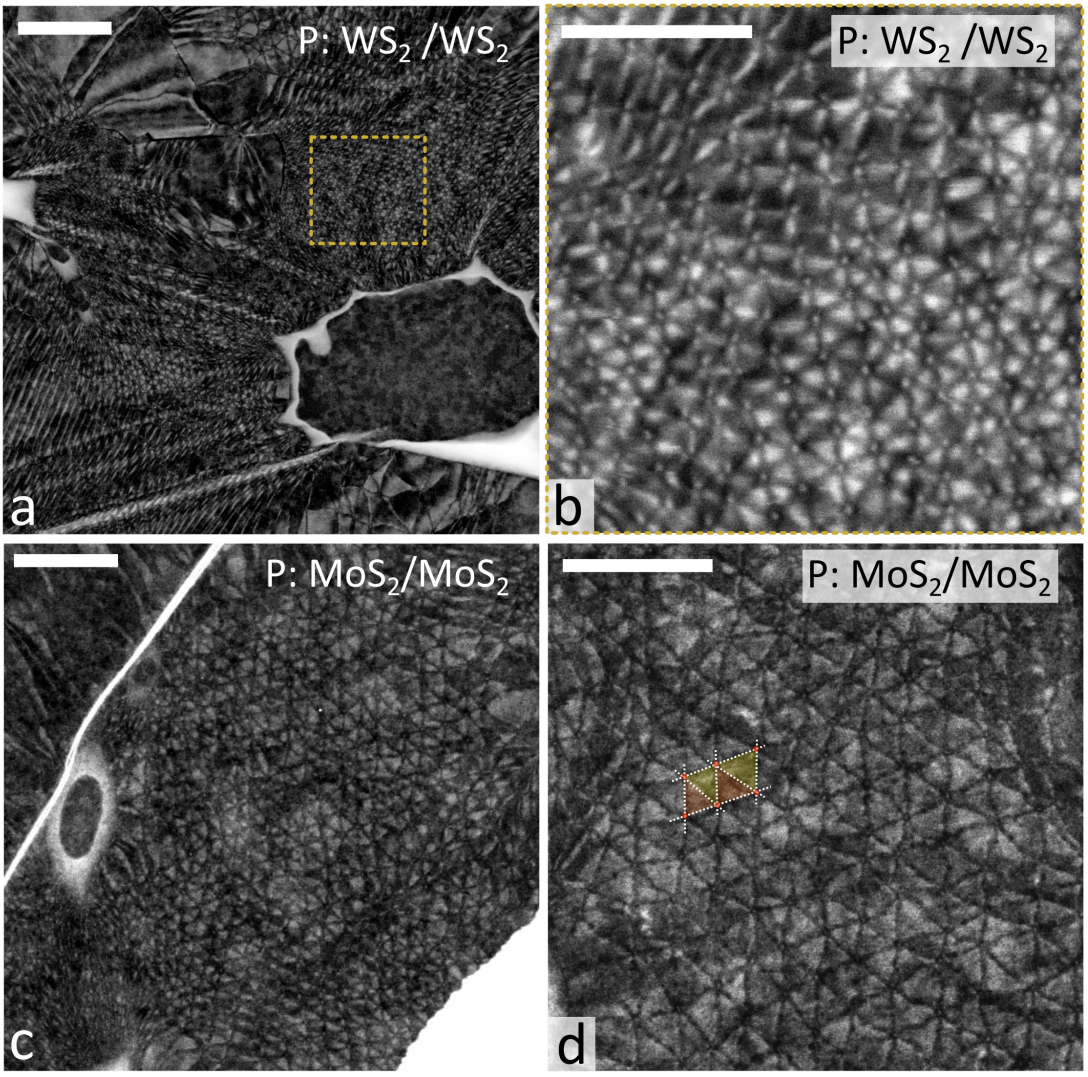

Fig. 5.2: **LAADF STEM of reconstructed homobilayers of WS_2 and MoS_2 twisted to angles close to 0°. a** Long-range periodicity in twisted WS_2. **b** Details of a periodic moiré superlattice as indicated by yellow dashed box (scale bar = 20 nm). **c** Long-range periodicity in twisted MoS_2. **d** Details of a periodic (MoS_2) moiré superlattice with reconstructed domain structure indicated by the orange and yellow triangles (Scale bars **a,c-d** = 100 nm).

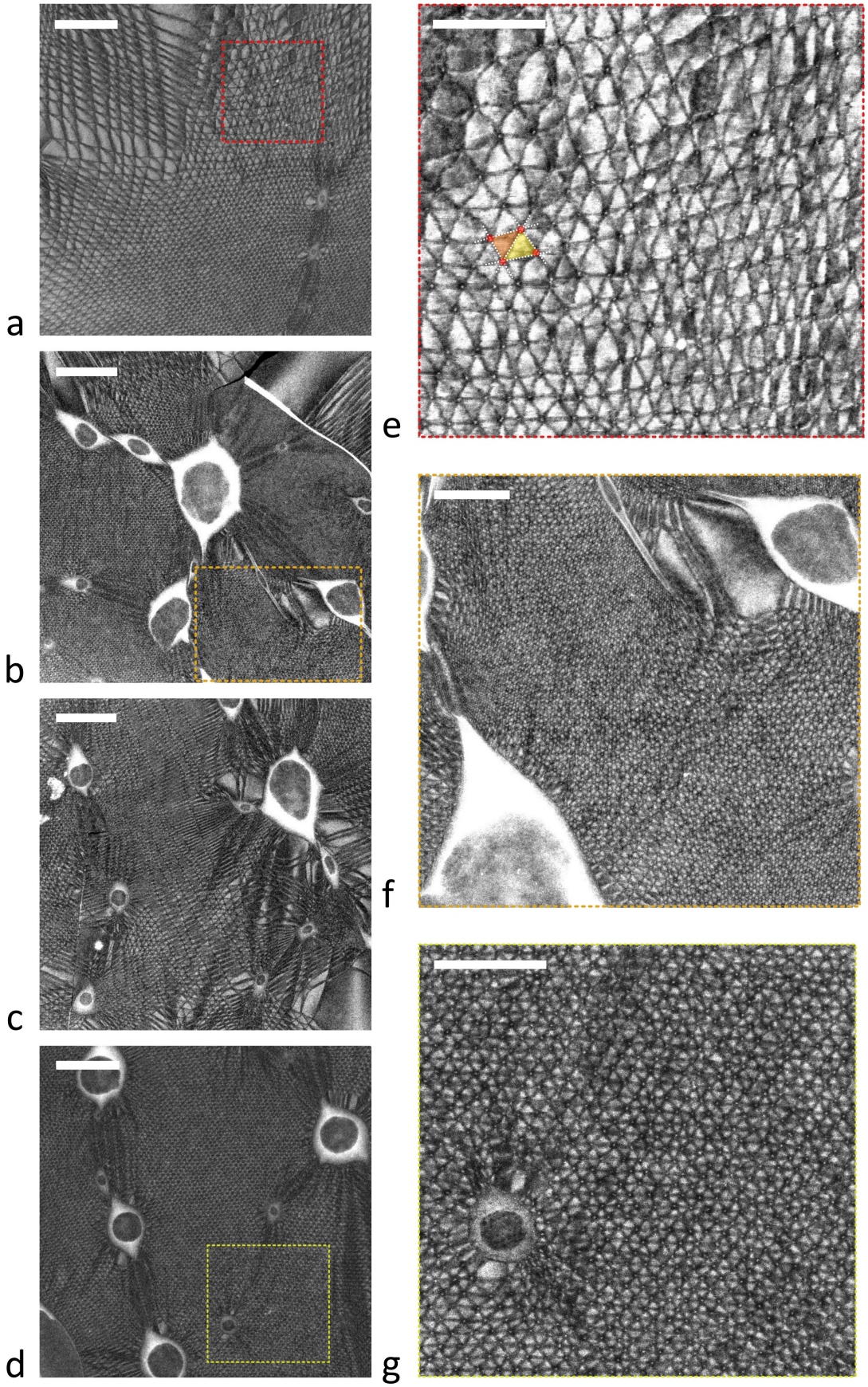

Fig. 5.3: **LAADF STEM of reconstructed heterobilayer of WS_2/MoS_2 twisted to angles close to 0°. a-d** Examples of long-range periodicity where the coloured dashed boxes correlate with detailed moiré reconstruction observed in **e-g**, respectively. Scale bars in **a-d** are 200 nm and **e-g** are 100 nm.

hydrocarbons which do not display any reconstruction pattern which further allows us to confirm that the observed pattern is a consequence of the interaction between the two monolayers.

In Figure 5.2, it is apparent that the long-range uniformity of the moiré pattern has been affected by the sample fabrication process due to the presence of contamination bubbles, cracks and creases. Rippling across the suspended bilayers further adds to the contrast non-uniformity. Both samples presented in Fig. 5.2 were suspended on TEM grids with an average hole diameter of ~ 4 μm, however, later samples were fabricated with an average hole diameter of ~ 1.8 μm which significantly reduced the rippling effect. In Fig. 5.7, we observe reconstruction in WS_2/MoS_2 heterbilayers. In Fig. 5.3e-f we observe increased long-range uniformity compared with that of the homobilayer (Fig. 5.2) with uniform domain sizes of 35 nm/8 nm/ 15 nm, respectively. This is likely associated with improved sample quality and the presence of a lattice mismatch of ~ 0.4 %. The mismatch leads to a maximum domain size of ~ 77 nm assuming no additional external strain. It must be noted that twist angle inhomogeneity (i.e. variation in twist angle) across the entire sample is significantly more apparent when the moiré periodicity is large.

Now we consider the relaxation of 2H-like (AP) moiré pattern; theoretical studies indicate 2H polytypes will generate hexagonal 2H domains at minimal twist angles [87]. This matches well with our observations, particularly at low twist angles ($\theta \sim 0.25°$) and is highlighted in Fig. 5.4d. At twist angles of $\sim 182°$ (see Fig. 5.4c) there are regions where domains appear roughly triangular in shape and equal in size (~ 5 nm). As the twist angle decreases to $\sim 1°$, the moire pattern transitions to a kagome-like (star of David) structure in which one of the domains is energetically dominant (2H stacking). Compared to the 3R-type moiré superlattice, the 2H-type domain structure appears to be significantly less uniform, favouring extended 2H/2H boundaries and expansive regions of commensurate 2H-stacking. In Fig. 5.4c, the onset of a crack has allowed for strain relaxation in one direction, where the perpendicular direction is pinned by the rest of the domain structure.

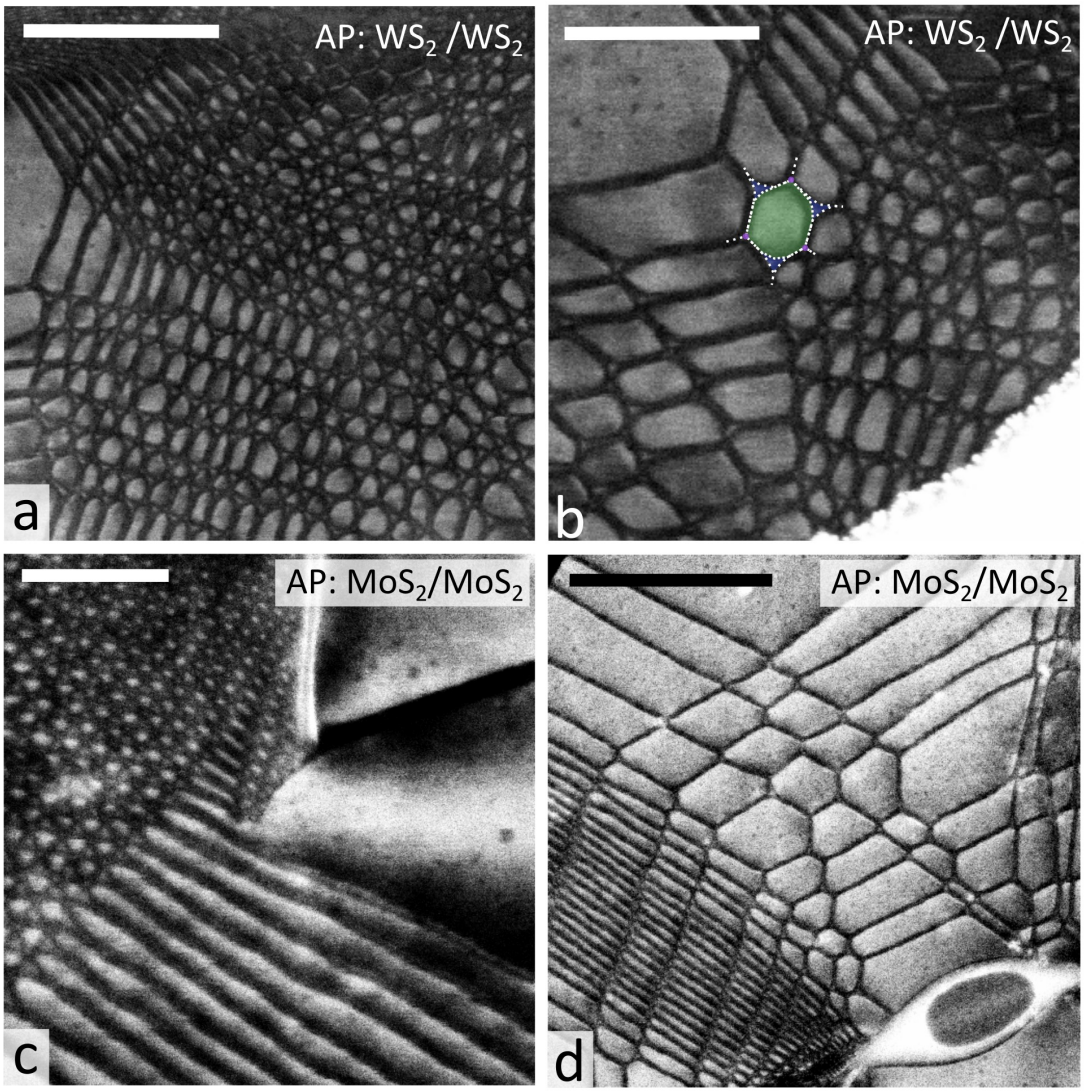

Fig. 5.4: **LAADF STEM of reconstructed homobilayers of WS_2 and MoS_2 twisted to angles close to 180°.** Details of an WS_2/WS_2 moiré superlattice with twist angle of **a** $\theta \sim 1^\circ$ and **b** $0.5^\circ < \theta < 1^\circ$ where domain is growing at the expense of the neighbouring domains. Scale bars for **a-b** are 100 nm. **c** An MoS_2/MoS_2 moiré superlattice with twist angle of $\sim 2^\circ$ (scale bar = 20 nm). **d** Large hexagonal domains formed in MoS_2/MoS_2 at the lowest twist angles ($\theta \sim 0.25^\circ$)[scale bar = 200 nm].

5.3 Atomic Resolution HAADF-STEM

In this section, the high resolution ADF STEM imaging was acquired using a FEI Titan G2 80-200 STEM ChemiSTEM microscope. The Titan was operated at 200 kV with a probe current of 40 pA, a 21 mrad convergence angle, a 48-191 mrad ADF collection angle and all aberrations up to the 3rd order were corrected to better than a phase shift at 20 mrad. Along with the atomic resolution imaging, multislice ADF image simulations were performed with the software QSTEM by matching the experimental parameters that were used in the FEI Titan microscope. Simulations were acquired using an effective source size of 0.1 Å.

When twisted to below a critical angle of 2°, homobilayer TMDs atomically reconstruct. In Fig. 5.5, Atomic resolution HAADF STEM reveals this structural reconfiguration into a 3R-type (parallel) triangular domain network. The observed periodically repeating stacking configurations including XX′, MX′, XM′ and B (boundary/domain walls) match very well with the QSTEM (See Fig. 5.5c). It is important to note that HAADF STEM produces Z-contrast ($Z^{1.67}$), therefore, there is a higher signal from the metallic (Mo/W) atoms compared to the sulphur atoms. Tungsten has an atomic number of 74, molybdenum is 42 and sulphur is 16, therefore, we expect the contrast of twisted bilayer WS_2 to be dominated by tungsten as the sulphur signal will be too weak to observe. Additionally, it is apparent that the data in Fig. 5.5 still contains hydrocarbon build-up (observed as long range intensity variation).

Fig. 5.5 highlights the key structural features of alternating domains of XM′ and MX′ stacking configurations (outlined with white dashed lines). Owing to the z-contrast ($\sim Z^{1.67}$) we observe varying intensities for each atomic column oriented along the electron beam path. XM′ and MX′ stacking configurations both have atomic columns consisting of S_2, Mo and Mo-S_2/S_2-Mo that increase in intensity, respectively. The ADF contrast observed for XM′ in this work agrees well with previous experimental observations of XM′ ADF imaging [181]. For MX′ stacking, however, the Mo column appears to have the same contrast as Mo-S_2. In previous experimental studies, the intensity difference between atomic columns of S_2(top)-Mo(bottom) and Mo(top)-S_2(bottom) was found to be 15 $\%$ for 2H bilayer MoS_2 [182]. This highlights the importance of not only the atomic number of atoms in the vertical column but also their ordering within the column. Due to the nature of sample

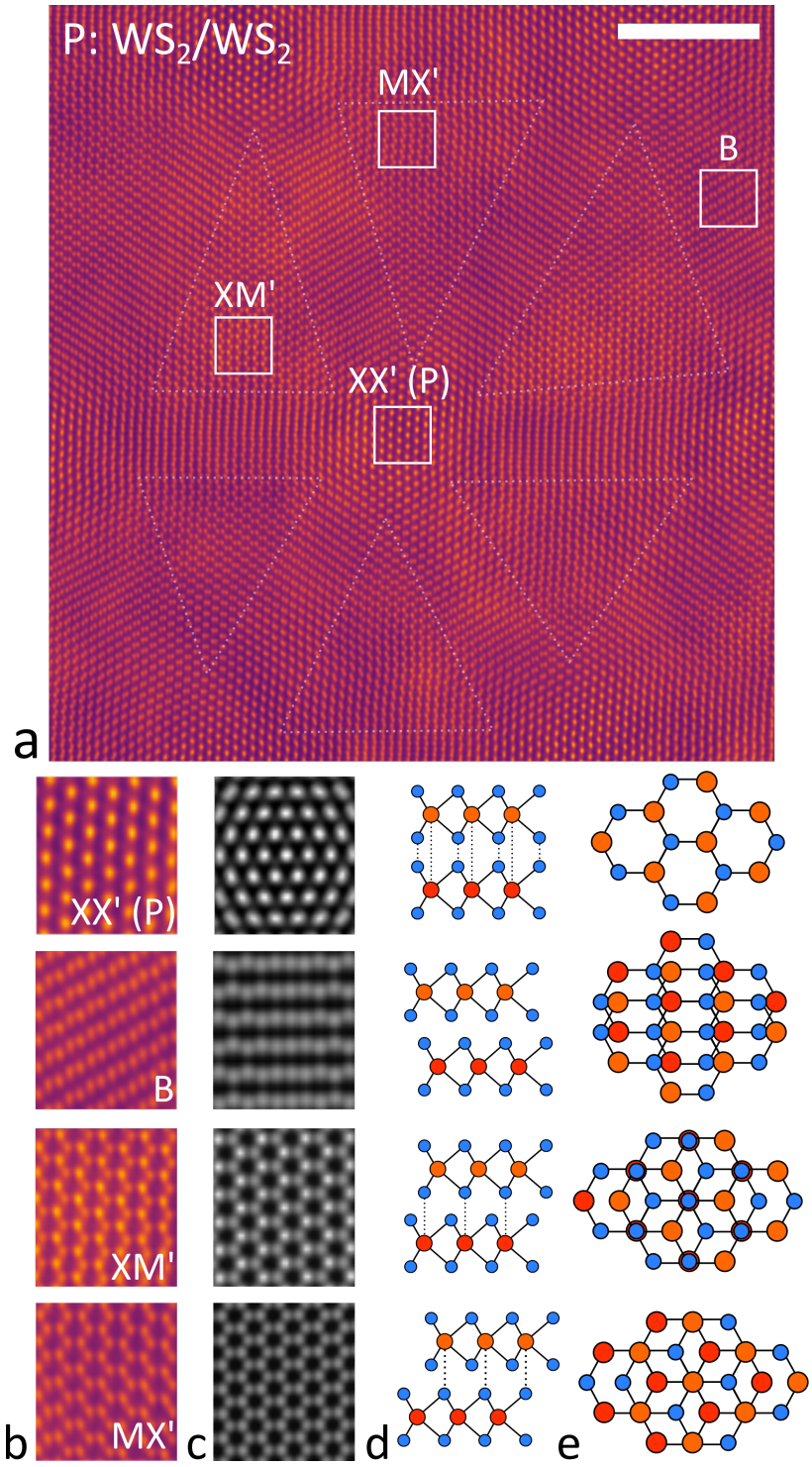

Fig. 5.5: **Atomic reconstruction in homobilayer WS_2 twisted to $\sim$ 1.29° in the parallel configuration ($\theta \sim 0°$).** **a** Atomic resolution HAADF STEM image (PCA and Weiner filtered) with the key stacking configurations labelled and triangular domains highlighted with white dashed lines (scale bar = 5 nm). **b** Magnifications of key stacking configurations corresponding to the white labelled boxes in **a**. **c** Corresponding simulated stacking configurations performed using QSTEM. Schematic illustrations of the **d** side-view and **e** top-view for each configuration where sulphur atoms are blue and top(bottom) MoS_2 atoms are orange(red).

fabrication (i.e. sample is suspended over SiN grid with holes), there is additional strain impacting the uniformity of the domain structure.

The alternating triangular domains are separated by domain boundaries which all meet at intersections of XX′ stacking configurations. In this stacking configuration, the two possible atomic columns include S_2-S_2 and Mo-Mo. Here, the signal from the Mo-Mo clearly dominates. When comparing the QSTEM of a rigid and a reconstructed bilayer with a twist angle of $\sim 1.29^\circ$ (see Fig. 5.6), one would expect the XX′ stacking region to grow with decreasing twist angle if there was no reconstruction (as depicted in Fig. 4.19 in bilayers with larger (above 2°) twist angle), however, we instead observe the growth of MX′ and MX′ regions at the expense of XX′, indicating reconstruction has occurred. Importantly, we have observed that the domain boundaries are ~ 3 nm in width and provide gradual transition between MX′ and XM′ stacking configurations. The domain boundaries can be described as partial screw dislocations with a Burgers vector $a/\sqrt{3}$ that is parallel to the armchair direction of the lattice.

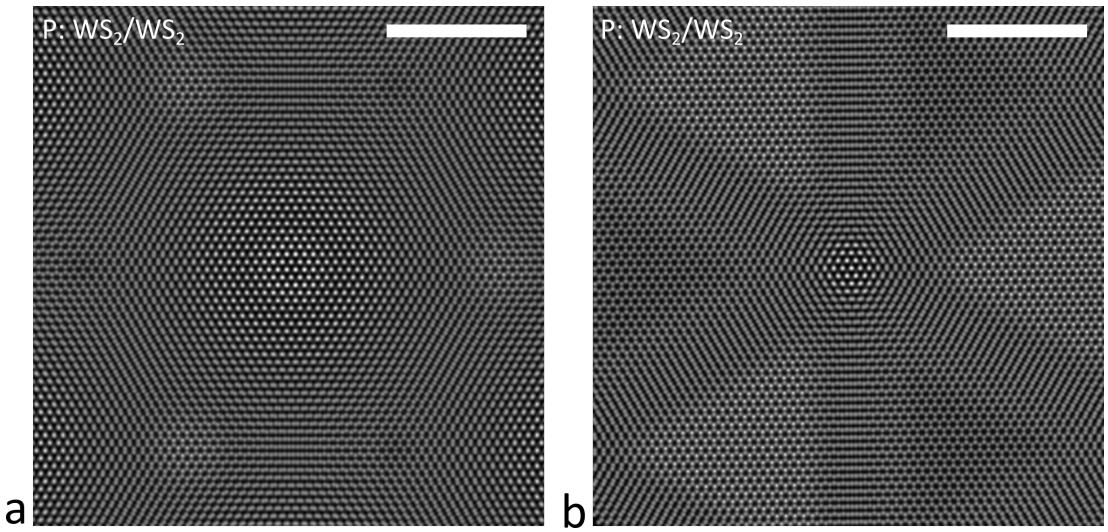

Fig. 5.6: **QSTEM simulation of parallel twisted WS_2. a** Rigid and **b** reconstructed bilayer WS_2 twisted to $\sim 1.29°$. Scale bars = 5 nm.

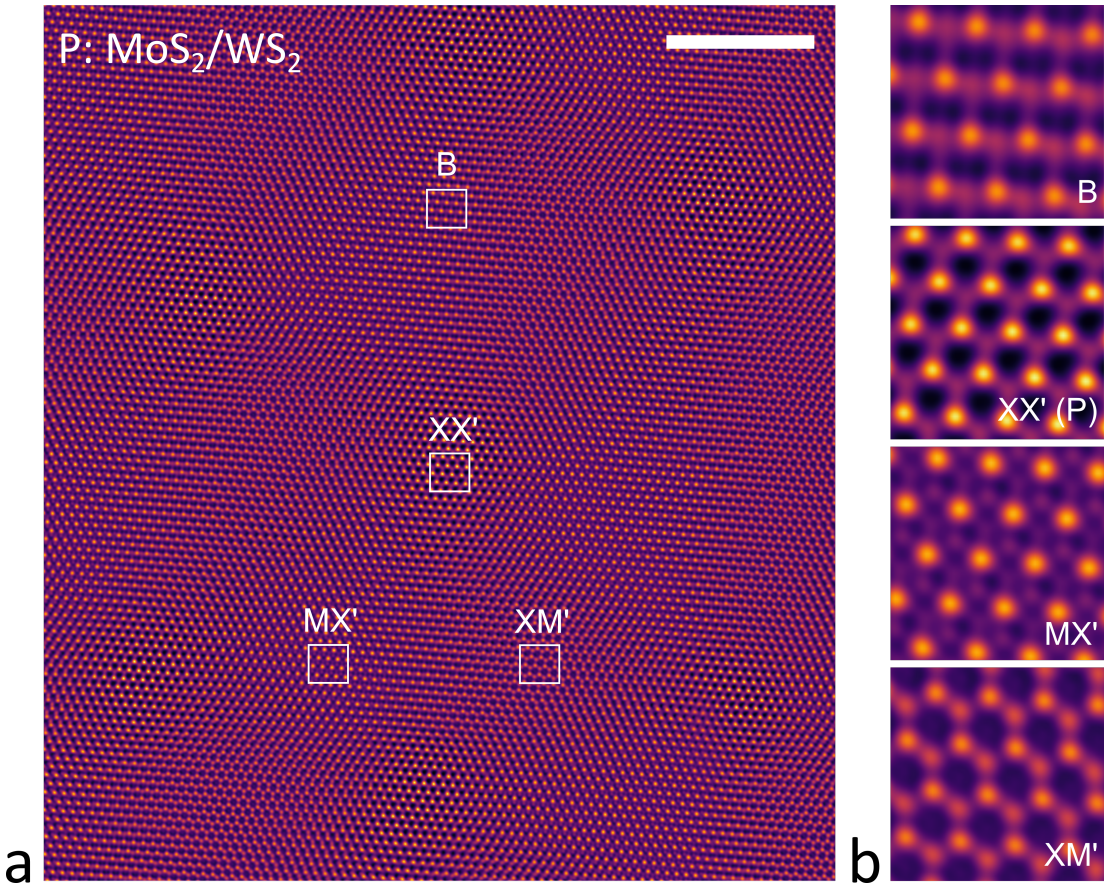

Fig. 5.7: **Atomic reconstruction in heterobilayer WS_2/MoS_2 twisted to $\sim 1.62°$ in the parallel configuration ($\theta \sim 0°$). a** Atomic resolution HAADF STEM image (PCA and low-pass filtered) with the key stacking configurations labelled (scale bar = 5 nm). **b** Magnifications of key stacking configurations corresponding to the white labelled boxes in **a**.

For twisted heterobilayers such as WS_2/MoS_2 with a low lattice mismatch ($\delta =$

($a_{WS_2}/a_{MoS_2} \sim 0.31\%$), lattice reconstruction has also been observed (see Fig. 5.7). Due to the differences in atomic weight of tungsten and molybdenum atoms, the contrast of each stacking configuration differs to those seen in the homobilayer. Additionally, the reduced amount of contamination in this sample means the contrast in atomic structure is much more uniform with increased sharpness where sulphur atoms are more clearly resolved.

For twisted bilayers twisted to an 2H-type (AP) configuration, the observed atomic reconstruction significantly differs from the 3R-type configuration. Fig. 5.8 highlights the primary stacking configurations, including XX′ (AP), 2H, MM′ and B (boundary/domain walls). At the intermediate angle of $\theta \sim 1.59°$, the MM′ and 2H domains are roughly equal in size, but for twist angles below 1° the MM′ domains maintain a lateral size of $\sim$ 5 nm while the 2H domains increase in size. In Fig. 5.9c-d, 2H domains grow and the triangular MM′ domains remain the same size, leading to a kagome-like structure. Here, the domain boundaries are a complex combination of 2H/2H and 2H/MM′ boundaries. This agrees with the QSTEM simulation illustrated in Fig. 5.9b. From the long range data acquired from LAADF experiments, we know 2H eventually transitions into a hexagonal shaped domain. In this respect, we can define two critical transitions in the reconstructed regime for 2H-type configurations; (1) 2H and MM′ reconstruct to form triangular domains with an onset of reconstruction at around $\sim 2°$,(2) 2H domains begin to outgrow the MM′ domains as MM′ reaches a maximum domain size of 5 nm, indicating a secondary reconstruction regime at $\sim 0.9°$. It should be noted that in Fig. 5.8a, the horizontal shift in atom positions is a consequence of scan noise.

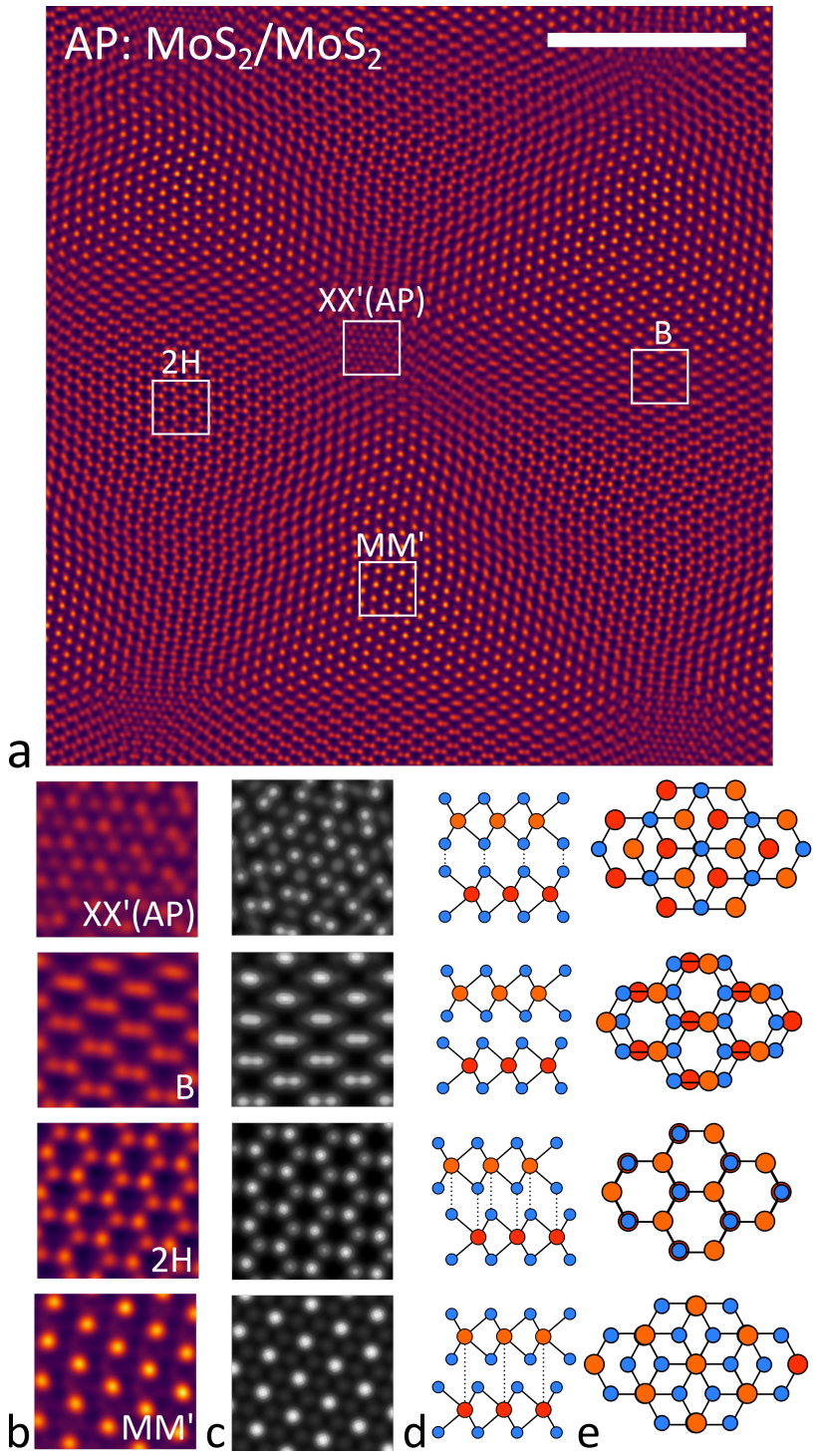

Fig. 5.8: **Atomic reconstruction in homobilayer MoS_2 twisted to $\sim$ 1.59° in the anti-parallel configuration ($\theta \sim$ 180°).** **a** Atomic resolution HAADF STEM image with PCA and low-pass filters with the key stacking configurations labelled (scale bar = 5 nm). **b** Magnifications of key stacking configurations corresponding to the white labelled boxes in **a**. **c** Corresponding simulated stacking configurations performed using QSTEM. Schematic illustrations of the **d** side-view and **e** top-view for each configuration where sulphur atoms are blue and top(bottom) MoS_2 atoms are orange(red).

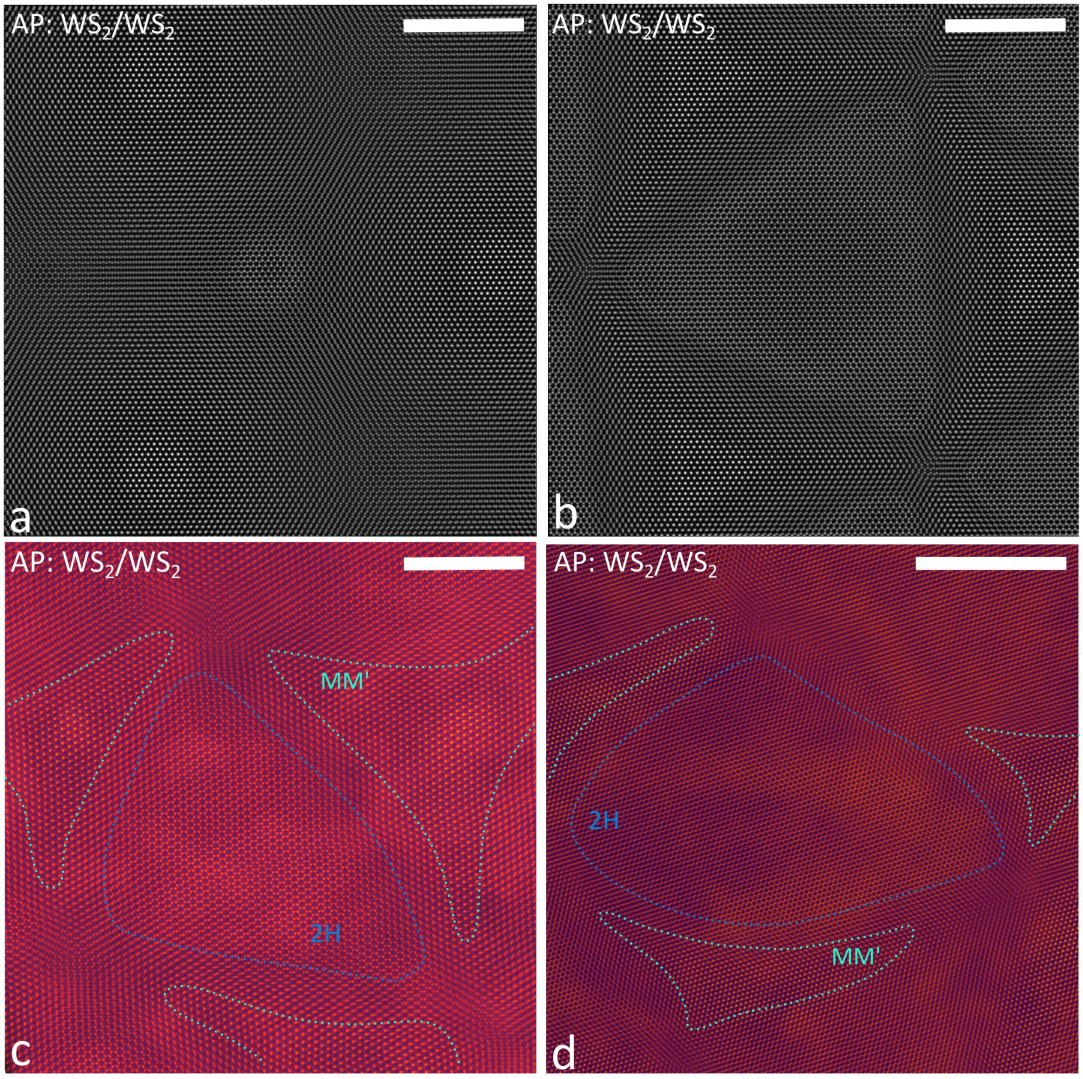

Fig. 5.9: **Evolution of atomic reconstruction in homobilayer WS_2 twisted close to the anti-parallel configuration ($\theta \sim 180^\circ$).** QSTEM of **a** rigid and **b** reconstructed bilayer WS_2 twisted to $\sim 0.87^\circ$ in the anti-parallel configuration. HAADF STEM (PCA/Weiner filtered) of anti-parallel bilayer WS_2 twisted to **c** $\sim 0.87^\circ$ and **d** $\sim 0.75^\circ$ where the light green/blue dashed lines correspond to MM′ and 2H stacking respectively. **a-c** scale bars are 5 nm and **d** is 10 nm.

5.4 Multi-scale Modelling of Atomic Structure

To better understand the driving force for lattice reconstruction, the theory group, led by Prof. Fal'ko, developed a multiscale modelling approach to simulate lattice reconstruction in twisted TMD bilayers. This approach exploits adhesion energy density, $W(\boldsymbol{r}_0, d)$, that determines the interaction between two layers with a lateral offset (r_0) and an interlayer distance (d). The expression obtained for $W(r_0, d)$ can be defined as [85],

$$W_{AP/P}(\boldsymbol{r}_0, d) = f(d) + \sum_{n=1}^{3} \left[A_1 e^{-qd} \cos\left(\boldsymbol{G}_n \boldsymbol{r}_0\right) + A_2 e^{-Gd} \sum_{n=1}^{3} \sin\left(\boldsymbol{G}_n \boldsymbol{r}_0 + \varphi_{AP/P}\right) \right]. \tag{5.1}$$

where the first term, $f(d) = -\sum_{i=1}^{3} C_{4i}/d^{4i}$, is the configuration-averaged adhesion energy and accounts for the long range vdWs interaction. The second term, $\sum_{n=1}^{3} A_1 e^{-qd} \cos\left(\boldsymbol{G}_n \boldsymbol{r}_0\right)$, defines effective Coulomb and exchange interactions of the electrons located at the chalcogen-chalcogen interface between the two adjacent layers which have a stronger orbital overlap compared to the metal atoms. Such interaction has a inversion symmetric form that is exponentially dependent on d. Here, q is determined by the spatial extent of the chalcogen orbitals. The third term, $\sum_{n=1}^{3} A_2 e^{-Gd} \sin\left(\boldsymbol{G}_n \boldsymbol{r}_0 + \varphi_{AP/P}\right)$, is used to describe the inversion asymmetry of TMD monolayers (related to Coulomb interaction of metal atoms). In the 3R-type configuration, the alignment of the metal atoms in XX′ stacking (where $r_0 = 0$) maximises interlayer repulsion and is accounted for by defining φ_P as $\pi/2$. For the 2H-type configuration, the misalignment of the metal atoms in the XX′(AP) stacking (where $r_0 = 0$) leads to a large metal-metal separation and, therefore, a much smaller interlayer repulsion (here, $\varphi_{AP} = 0$). For equation 5.1, $\boldsymbol{G}_{1,2,3}$ are the reciprocal lattice vectors in the first star of the TMD monolayer, $G = |\boldsymbol{G}_{1,2,3}|$. The values of the fitting parameters in Eq. 5.1 acquired using DFT calculations of fixed lattice configurations are listed in Tab. 5.1. Further details of the calculations can be found in Ref. [85].

Lattice reconstruction in twisted bilayers of TMDs occurs when the interlayer adhesion energy gain due to the formation of favourable commensurate stacking overcomes the elastic energy cost of local readjustment of stacking that produces confined regions of strain. This is because the intralayer bonding wants to maintain a rigid lattice and therefore opposes lattice reconstruction. Therefore, to calculate

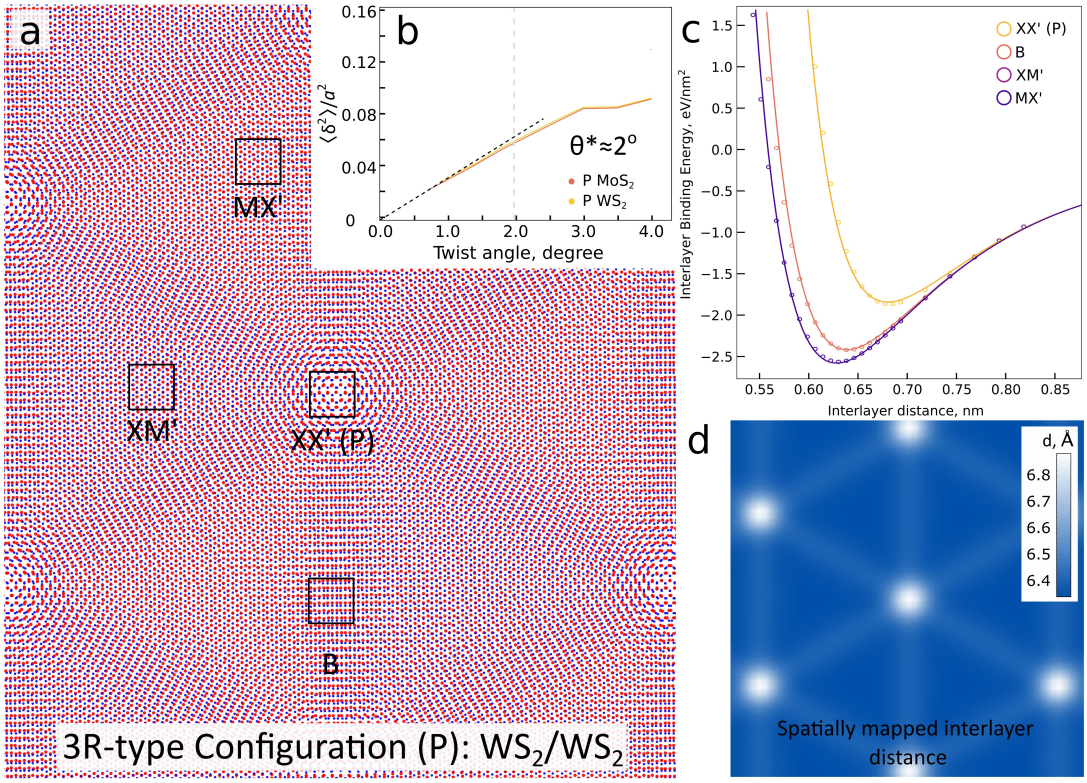

Fig. 5.10: **Multi-scale modelling of interlayer adhesion energy of WS_2 homobilayer $\sim$ 1.29° in the parallel configuration (Pθ $\sim$ 0°).** **a** Calculated atomic structure of reconstructed superlattice. **b** Calculated deformation parameter ($\langle\delta\rangle^2/a^2$) as a function of twist-angle, highlights the critical angle θ^* $\sim$ 2° for reconstruction that occurs when values of $\langle\delta\rangle^2/a^2$ deviate from the linear gradient highlighted by the black dashed line. **c** Calculated interlayer binding energy as a function of interlayer distance for the 4 primary stacking configurations. **d** A spatial colour map of interlayer distance across the repeating moiré superlattice.

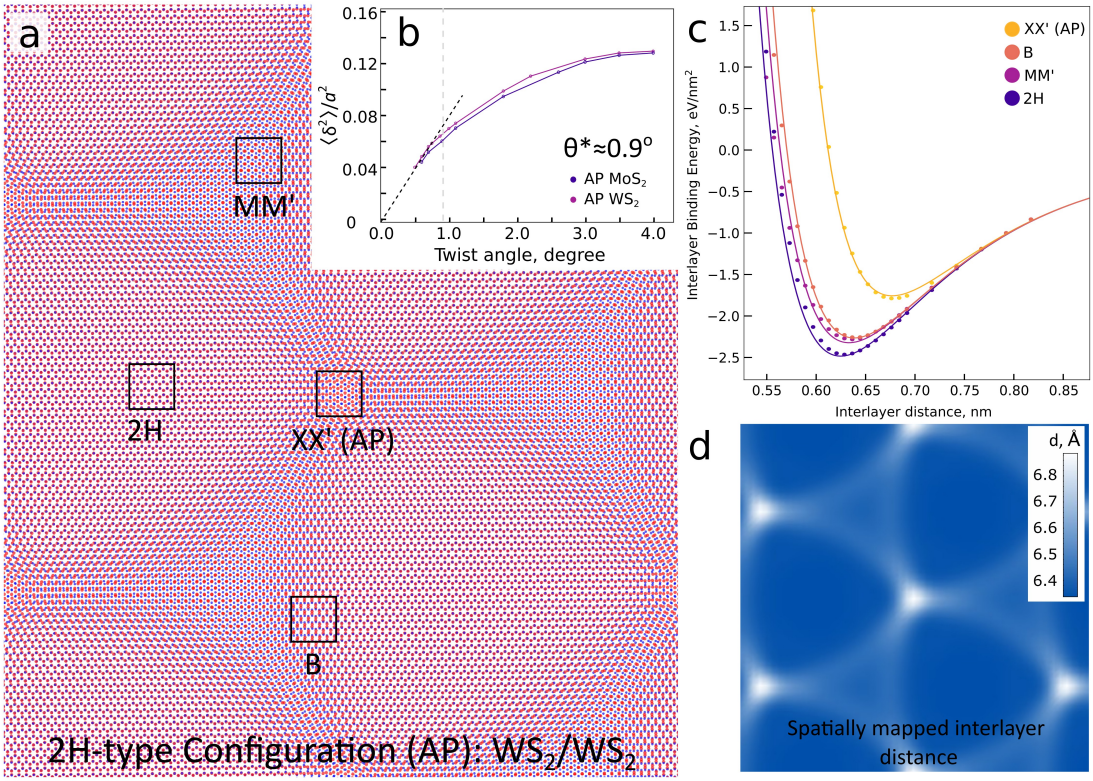

Fig. 5.11: **Multi-scale modelling of interlayer adhesion energy of 2H-type WS_2 homobilayer $\sim 0.87^\circ$ (AP$\theta \sim 180^\circ$). a** Calculated atomic structure of reconstructed superlattice. **b** Calculated deformation parameter ($\langle\delta\rangle^2/a^2$) as a function of twist-angle, highlights the critical angle $\theta^* \sim 0.9^\circ$ for reconstruction that occurs when values of $\langle\delta\rangle^2/a^2$ deviate from the linear gradient highlighted by the black dashed line. **c** Calculated interlayer binding energy as a function of interlayer distance for the 4 primary stacking configurations. **d** A spatial colour map of interlayer distance across the repeating moiré superlattice.

Tab. 5.1: **Fitting parameters for adhesion energy density for bilayers.**

bilayer	C_4, eV·nm^2	C_8, eV·nm^6	C_{12}, eV·nm^{10}	A_1, eV/nm^2	A_2, eV/nm^2	q, nm^{-1}
WS_2/WS_2	0.137976	0.159961	-0.020753	84571600	70214	30.877
MoS_2/MoS_2	0.134661	0.161589	-0.0209218	71928800	56411	30.534
MoS_2/WS_2	0.135693	0.162478	-0.0211387	79160000	63427/65461	30.695
	ω_{3R}^{LBM}, cm^{-1}	ω_{2H}^{LBM}, cm^{-1}	ω_{2H}^{LBM} (exp.), cm^{-1}	d_0, nm	ε, eV/nm^4	ω_{θ}^{LBM} cm^{-1}
WS_2/WS_2	29.4	29.6	31 ÷ 33	0.65	213	28.3
MoS_2/MoS_2	36.9	37.2	39 ÷ 41	0.65	214	35.3
MoS_2/WS_2	33.3	33.6		0.65	214	32

lattice reconstruction, we minimise the sum of the elastic and adhesion energies over local deformations in the constituent layers and find the relation between optimal interlayer distance and local stacking configuration. Here, each stacking configuration is determined by both the interlayer distance d and interlayer displacement $\boldsymbol{r}_0$ and the energy cost of out-of-plane bending of the layers is described by expanding $W_{AP/P}$ into a Taylor series about the minimum point (d_0). Further information can be found in Ref. [85].

In Fig. 5.10c, the binding energies of the four primary stacking configurations in the 3R-type configuration are plotted as a function of interlayer distance. The highest energy was found to be XX′ stacking (when $\boldsymbol{r}_0 = 0$) and XM′ and MX′ were found to be equal in energy as well as the lowest energy stacking configuration. This is reflected in the reconstructed lattice as the XM′ and MX′ domains grow equal in size with decreasing twist angle. Similarly, the spatial mapping of interlayer distance in Fig. 5.10d highlights the increased out-of-plane displacement at XX′ and at the domain boundaries.

For 2H-type configurations, commensurate 2H stacking has the lowest energy, MM′ has an intermediate energy and XX′ stacking is the most energetically costly (see Fig. 5.11c). This is reflected well in the atomic structure depicted in Fig. 5.10a where the 2H domains are growing larger than the MM′ domains and no XX′ domains form. Again, stacking configurations of higher interlayer binding energy (XX′, MM′ and B) generate regions of larger interlayer distance across the moiré superlattice (see Fig. 5.11d).

The deformation parameter ($\langle\delta\rangle/a^2$), describing the amount of deformation due to

strain averaged over a single supercell, was used to define the critical angle for the onset of reconstruction. In Figs. 5.10b and 5.11b, the critical angle is defined by the point at which the plotted deformation parameter deviates from the linear behaviour marked by the black dashed line. This was found to be $\theta^* \sim 2^\circ$ for 3R-type configuration. Once in the reconstructed regime, the region of concentrated strain decreases at a linear rate as the MX′ and XM′ domains grow. For the 2H-type configuration full reconstruction occurs in the secondary regime where 2H domains dominate. The deformation parameter defines this to be $\theta^* \sim 0.9^\circ$ which matches well with our experimental observations.

5.5 Summary

In this chapter, the LAADF (STEM) imaging technique was employed to study the long range periodicity in reconstructed lattices of the two polytypes (3R and 2H) for homo and heterobilayer TMDs. For atomic resolution imaging, HAADF was utilised. These imaging techniques revealed a triangular domain network of alternating XM′ and MX′ stacking domains for the 3R-type configuration and hexagonal domain network for the 2H-type configuration. The study of domain evolution as a function of twist angle also revealed two distinct critical transitions from a rigid to reconstructed 2H-type bilayer. Namely, the equal growth of triangular MM′ and 2H domains until a maximum length is reached and secondly the dominating growth of 2H domains (kagome-like geometry) at the expense of the energy expensive MM′ domains.

To verify our results, DFT modelling was used with a multi-scale approach to help explain the driving force behind lattice reconstruction in terms of the interlayer adhesion energy of each constituent stacking configuration. The modelling also helped to define the critical angle at which the rigid-to-reconstructed transition occurs which matched well to our experimental observations.

Chapter6

Electrical Properties of Reconstructed Lattices of Twisted Bilayer TMDs

The structural changes due to lattice reconstruction, as discussed in the previous chapter, have provided essential information that is required to interpret their corresponding electronic properties. In this chapter, techniques such as Conductive-AFM, KPFM, SEM as well as electronic transport measurements were implemented to characterise the electronic properties of twisted bilayer TMDs.

Conductive-AFM was used to directly correlate the atomic structure of reconstructed bilayers of TMDs to their local conductivity. This revealed local layer-polarised wavefunctions in 3R-type homobilayers and piezoelectric textures in 2H-type homobilayers. The Asylum Research Cypher-s AFM was used to perform conductive AFM experiments in collaboration with Professor Peter Beton (University of Nottingham) and Dr Alex Summerfield (University of Manchester). A NT-MDT spectral instruments NTEGRA AURA AFM system [145] was used to perform Kelvin probe force microscopy (KPFM) measurements in vacuum to characterise the differences in potential of XM′ and MX′ domains in collaboration with Dr Héctor Corte-León, Dr Eli Castanon and Dr Olga Kazakova at the National Physical Laboratory. To further study the ferroelectric nature of 3R-type twisted MoS_2, an SEM (Zeiss Merlin) equipped with an electric feed-through was used to study domain switching dynamics through in-situ sample biasing. This was performed by Dr. Terou Hashimoto and Prof. Roman Gorbachev. The KPFM and SEM studies are part of a wider collaborative project entitled 'Interfacial ferroelectricity in marginally twisted 2D semiconductors' and has recently been accepted to Nature Nanotechnology [183].

Finally, to test the viability of twisted 3R-type bilayers in ferroelectric tunnelling junction memory devices, low temperature (1.5 K) electrical transport studies were

performed by Yunze Gao. My personal contribution in this project was the fabrication of each device, performing C-AFM experiments (with Dr Alex Summerfield) and performing electrical SPM domain mapping of the electrical transport devices.

6.1 Conductive-AFM Study of TMD Homobilayers

Samples were prepared for C-AFM such that the semiconducting TMDs were transferred on graphite crystal pre-exfoliated onto a Ti/Au (3 nm/40nm) or Ti/Pt (3nm/40 nm) coated silicon oxide substrate. The metal-coated silicon substrate was glued to a conductive sample holder with silver paint assuring electrical connection between the holder and the vdWs stack. Before imaging in C-AFM mode, each sample was AFM brushed (as described in [124]) to remove contamination.

The sample region of interest (i.e. a region with no folds or bubbles) was located in AFM tapping mode and then switched over to the C-AFM mode to prevent damage to the tip. A Pt/Ir metal-coated tip (budget sensors ElectriMulti75-G) was used.

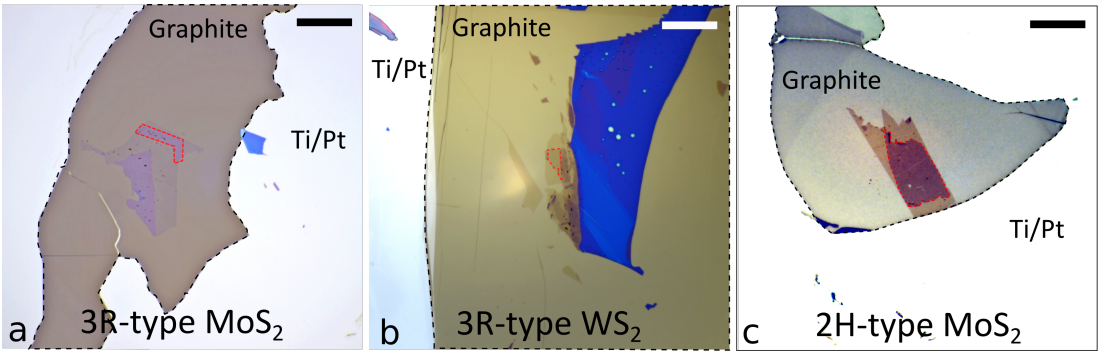

Fig. 6.1: **Optical images of samples fabricated for C-AFM.** 3R-type twisted bilayer **a** MoS_2 and **b** WS_2 on a graphite/ Ti/Pt substrate. **c** 2H-type twisted bilayer MoS_2 on a graphite/ Ti/Pt substrate. The black dashed lines indicate the edge of the graphite vdWs substrate and the red dashed lines indicate the twisted bilayer region of interest. All scale bars are 20 μm.

6.1.1 3R-type Twisted Homobilayers

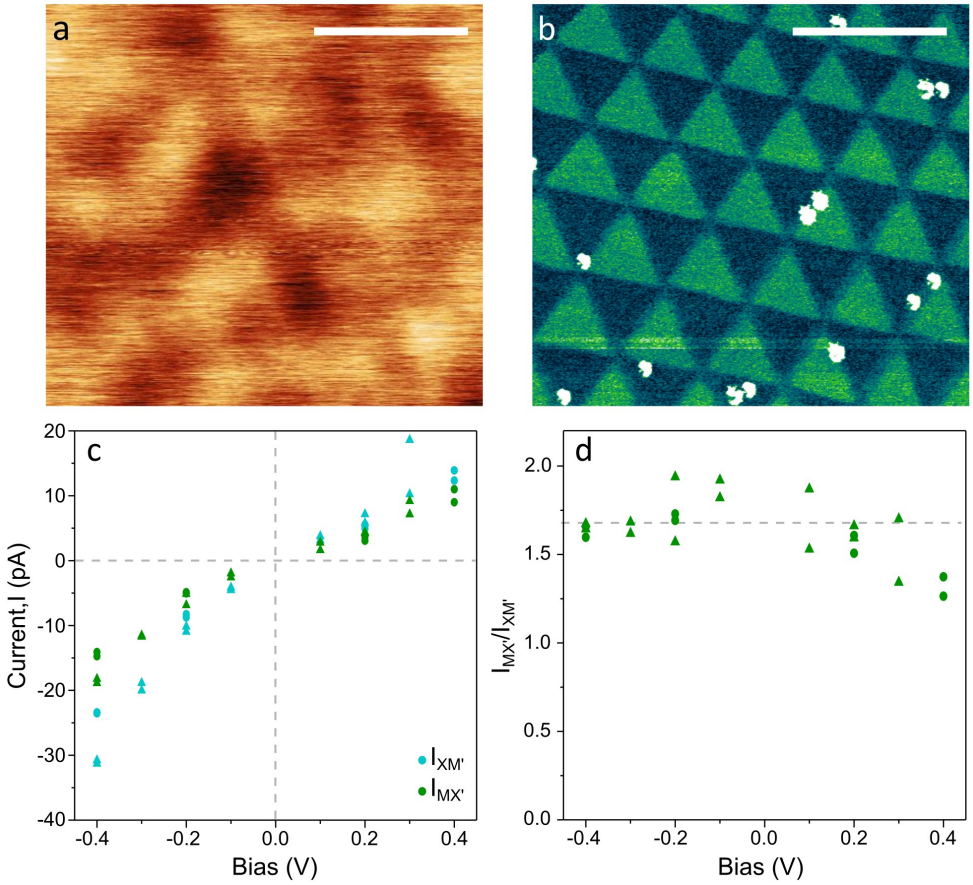

Fig. 6.2: **C-AFM of reconstructed 3R-type MoS_2 with a twist angle $\theta \sim 0.3°$. a** Topography image and **b** corresponding tunnelling current image measured with an applied bias of -0.4V. The scale bars in both images are 100 nm. **c** Average tunnelling current in XM′ and MX′ domains as a function of applied bias. **d** Average ratio between MX′ and XM′ domains as a function of applied bias.

Conductive-AFM was performed on 3R-type MoS_2 twisted to an angle of $\sim 0.3°$ to characterise the effect of lattice reconstruction on the electronic structure. In Fig. 6.2b, a triangular network of alternating XM′ and MX′ domains was revealed in the tunnelling current signal and such structure was not observed in the topographic image indicating that the contrast observed between adjacent domains is an electronic feature. Indeed, in the corresponding topography signal (Fig. 6.2a), only the topographic contrast due to the roughness of the underlying silicon substrate can be seen. Here, one type of stacking domain clearly dominates with a tunnelling current that is almost double that of the adjacent stacking domain. Such tunnelling current dependence on stacking configuration (namely that of XM′ and MX′) was studied in the bias range of -0.4 to 0.4 V. A low bias voltage range and low spring constant probes were used

(ElectriMulti75-G where k = 3 N/m) with an average applied force of 24 nN to reduce wearing of the tip and therefore maintain high spatial resolution. Conductive probes typically wear out faster due to high current densities passing through the probe as well as lateral friction causing the conductive coating to wear away. In this range, the Fermi level in the conductive graphite substrate is close to the conduction band edge in the 3R-type MoS_2 bilayer (similar to observations in monolayer MoS_2/graphene [184, 185]). The tunnelling currents for both XM′ and MX′ were extracted (and averaged over the image) from the tunnelling current maps of two different locations on the same sample and plotted as a function of tip bias (see fig 6.2c). Over the voltage range the tunnelling current associated with XM′ is persistently dominating with an average ratio of $I_{XM'}/I_{MX'} \sim 1.6$ to 1.7 which agrees well with the theoretically predicted ratio between the tunnelling currents of XM′ and MX′ [85].

The C-AFM study was repeated for 3R-type bilayer WS_2 twisted to $\theta \sim 0.15°$ and the same triangular domain network was observed in the tunnelling current map with no such structure in the corresponding topography image (as seen in Fig. 6.4a and b). Here, the surface roughness observed in the topography signal can also be seen in the underlying tunnelling current signal. Again, the XM′ domain appeared to have a consistently higher tunnelling current (as seen in Fig. 6.5). The tunnelling current ratio of $I_{XM'}/I_{MX'} \sim 1.3$ between the commensurate domains was slightly lower than the theoretically predicted tunnelling current ratio of 1:1.6 [85]. The discrepancies in values are likely due to pronounced non-uniformity due to the reduced thickness of the underlying graphite (vdWs) substrate (roughness of silicon substrate clearly visible) which has led to a non-uniform signal within each domain.

In order to better understand the origins of the local layer polarisation in adjacent MX′ and XM′ observed in C-AFM, the group led by Prof. Fal'ko utilised DFT to calculate the decomposed electron wavefunction weighting of the electronic states at both the valence and conduction band edges of the MoS_2 and WS_2 band structures (further detailed in Ref. [85]). In other words, the computed probability to find an electron of a specific energy at each atomic layer in the vertical stack (i.e. $X^tM^tX^tX^bM^bX^b$). Significant asymmetry in the top and bottom layers was computed particularly at the Q-point of the conduction band edge. Such layer-polarised wavefunctions are permitted due to the lack of inversion symmetry in the 3R polytype. As the tunnelling from the probe drops exponentially with the distance, the electronic states at the outermost sulfur atom is contribute to the tunnelling the most. In Fig.

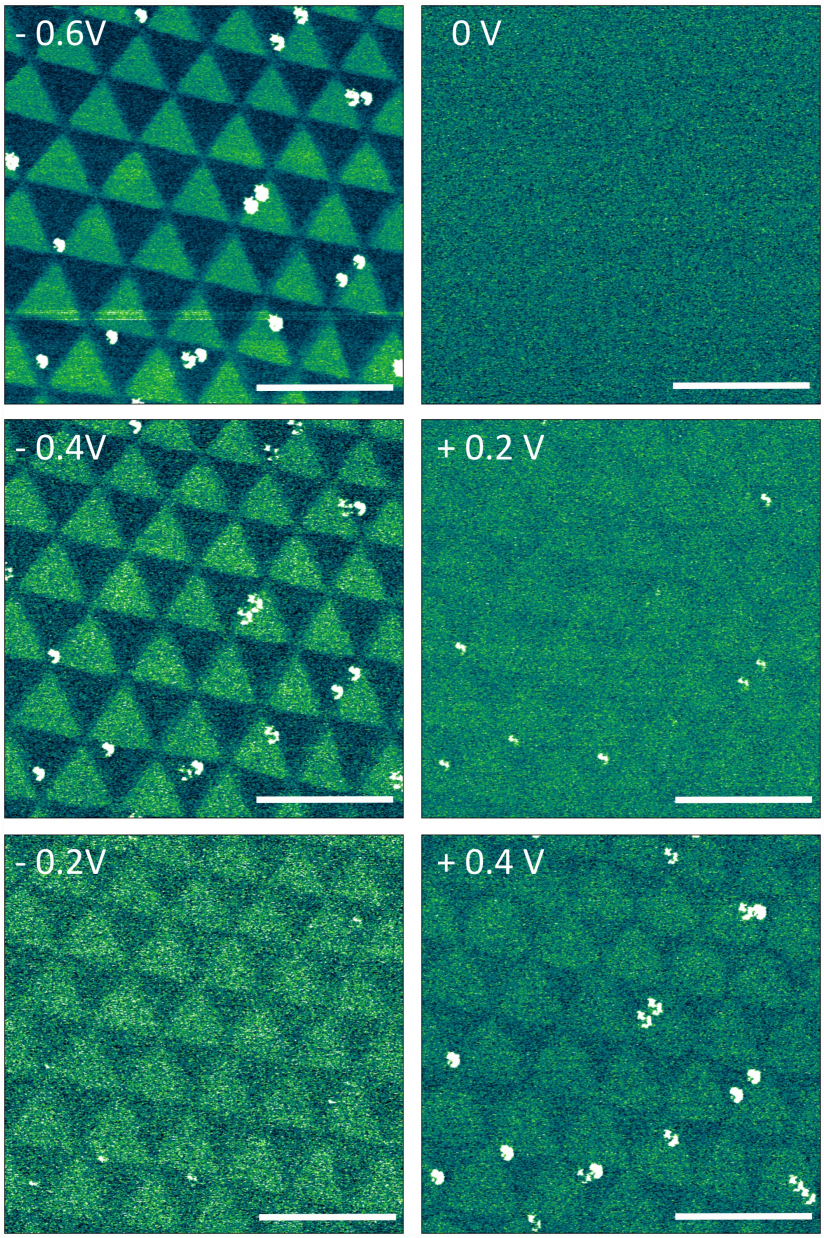

Fig. 6.3: **C-AFM tunnelling current maps of 3R-type twisted MoS_2 for varying surface voltages.** All images were acquired with tip force setpoint of 24 nN. Scale bars are all 100 nm.

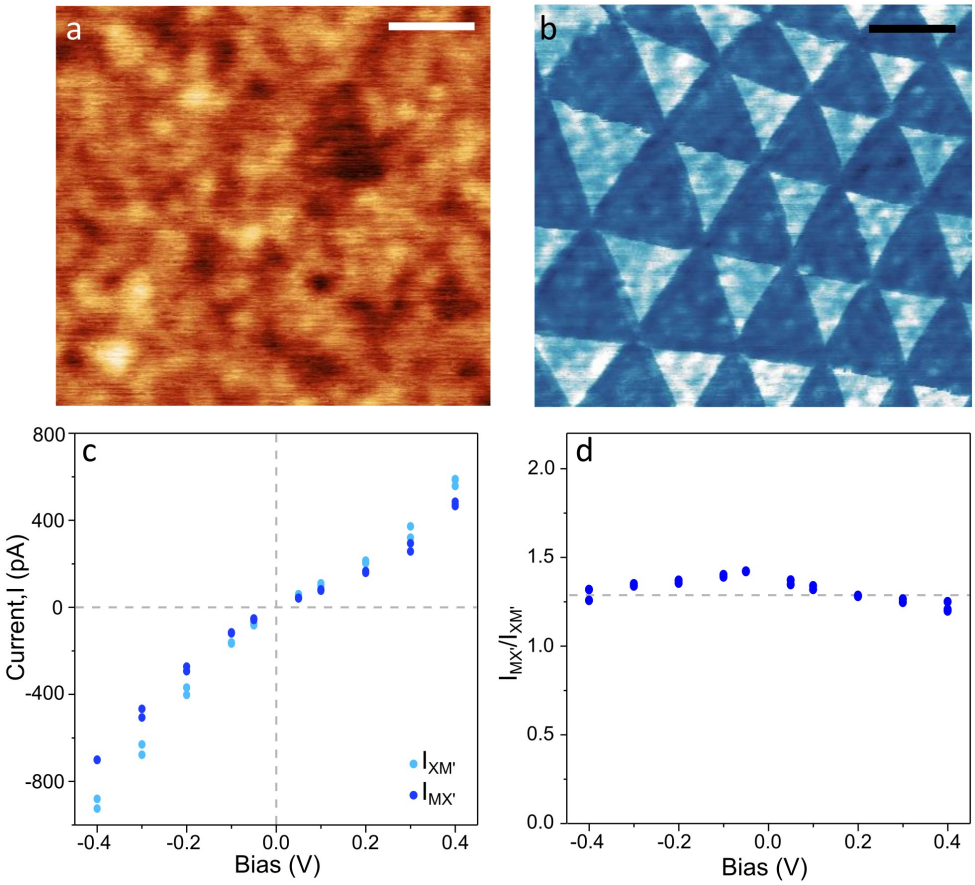

Fig. 6.4: **C-AFM of 3R-type WS_2.** **a** Topography image and **b** corresponding tunnelling current map measured with an applied tip bias of -0.4 V. The scale bars in both images are 100 nm. **c** Average tunnelling current in XM′ and MX′ domains as a function of applied bias. **d** Average ratio between MX′ and XM′ domains as a function of applied bias.

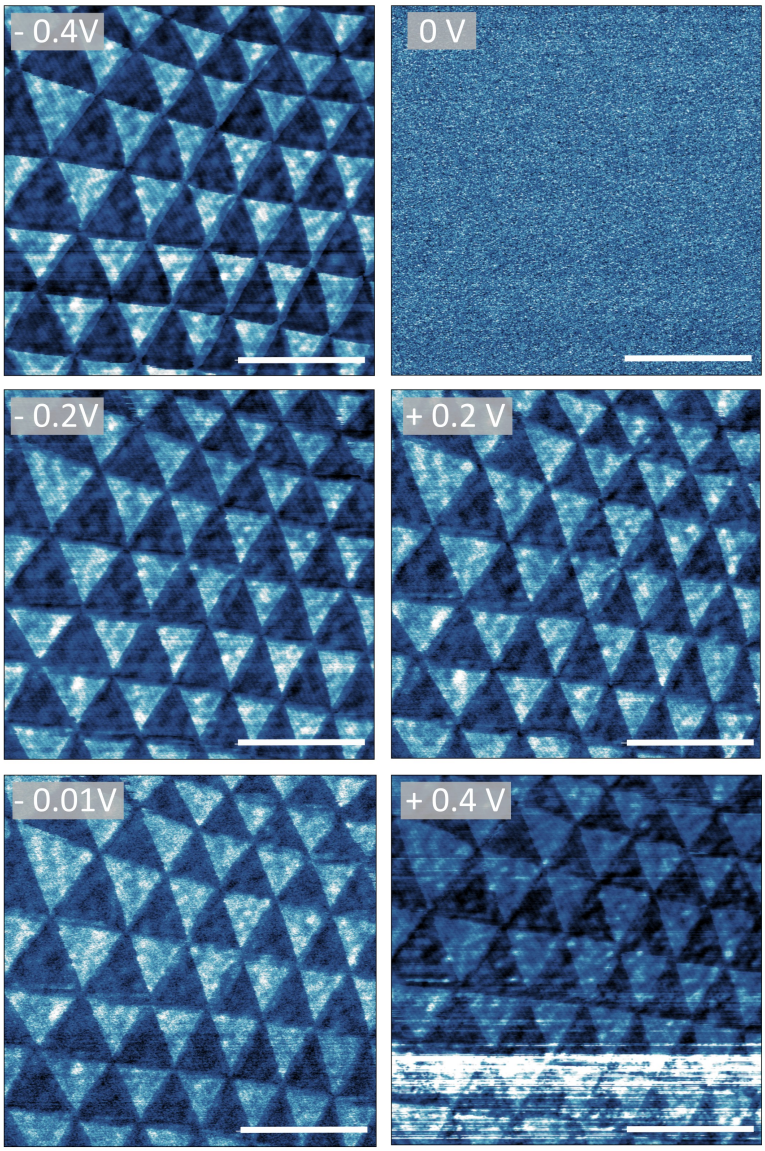

Fig. 6.5: **C-AFM tunnelling current maps of 3R-type twisted WS_2 for varying surface voltages.** All images were acquired with tip force setpoint of 35 nN. scale bars are all 100 nm.

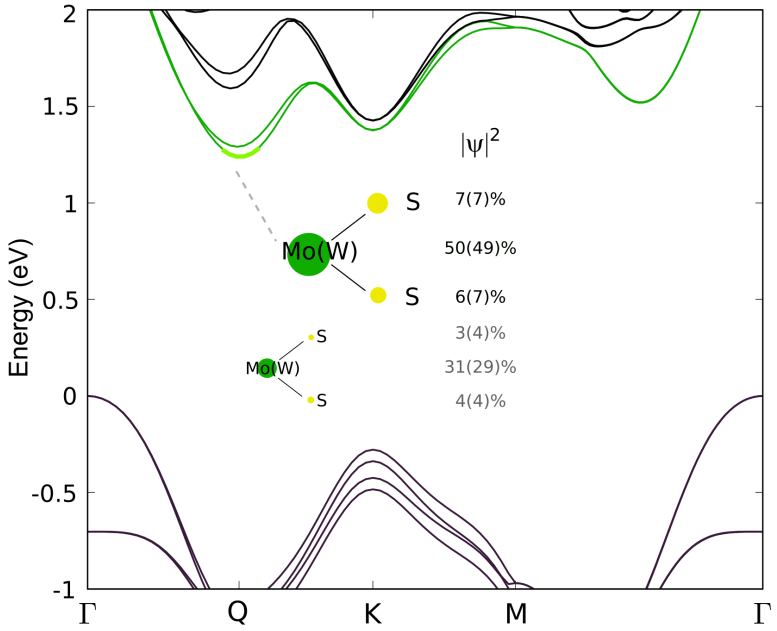

Fig. 6.6: **Origin of layer polarisation in 3R-type twisted TMD homobilayers.** Calculated DFT band structure of 3R-type bilayer MoS_2. Electron-wavefunction weighting for each individual atom (values taken from Ref. [85]) in the vertical stack (represented by the size of each coloured atom). XM′ and MX′ are related by mirror symmetry and therefore their wave-function weightings are reversed in the two separate stacking configurations.

6.6, the electron wavefunction weighting has been represented by the physical size of each constituent atom clearly highlighting that the top layer contributes more than the bottom. As we scan our conductive probe from XM′ to MX′ stacking regions, the electronic weighting of the top and bottom layer flips upside down leading to the corresponding reduction in tunnelling current.

6.1.2 2H-type Twisted Homobilayers

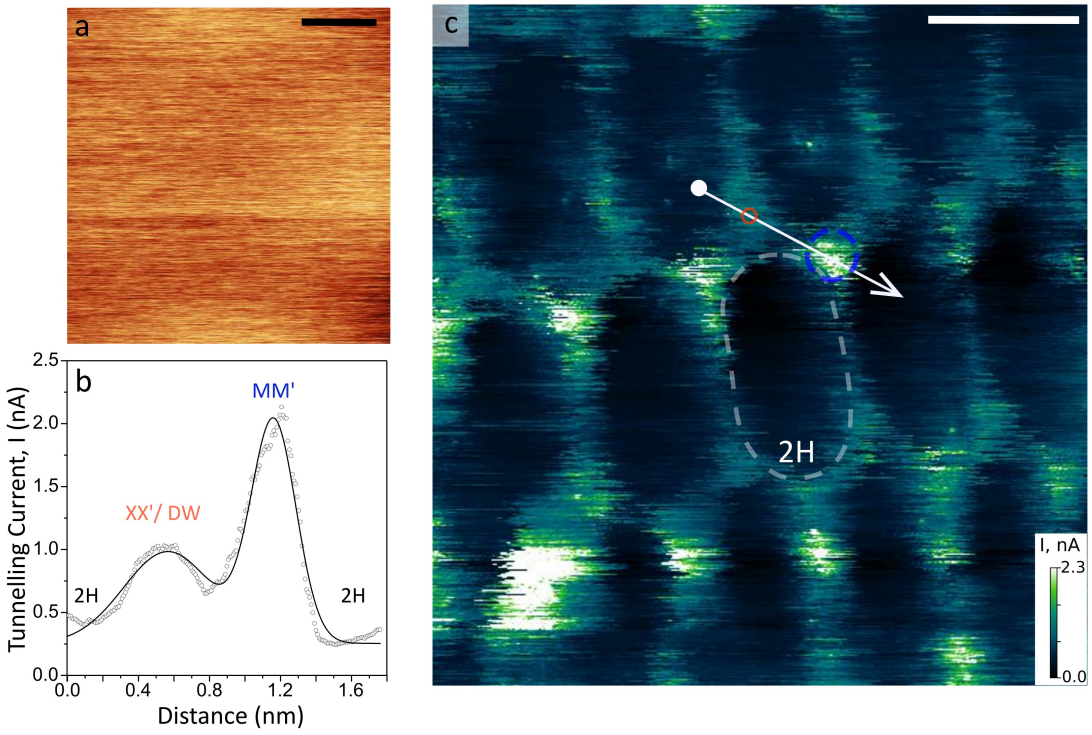

Fig. 6.7: **C-AFM of 2H-type twisted MoS_2.** **a** C-AFM topography image acquired simultaneously with **c** the tunnelling current map where V_b = + 300 mV. **b** Extracted line profile (taken along the white line drawn in **c**) illustrating the higher tunnelling current in the regions of MM′ stacking configuration compared to neighbouring XX′/domain walls and 2H domains. The images were acquired with tip force setpoint of 35 nN. Scale bars are all 10 nm.

C-AFM was also performed on twisted homobilayers in the 2H-type configuration. Due to the anisotropic domain dimensions in the 2H-type superlattice in Fig. 6.7c, the twist angle of $\theta \sim 1.2°$ was determined by the length of the domain in the enlongated direction. The tunnelling current map presented in Fig. 6.7c (where V_b = + 300 mV) exhibits elongated domains of 2H stacking configuration separated by domain boundaries of higher tunnelling current. Here, each commensurate 2H stacking domain exhibits a uniformly equal tunnelling current. The tunnelling current at the domain boundaries is more conductive than the 2H-type stacking domains. The regions of alternating domain boundary intersections corresponding to MM′ stacking display a tunnelling current that is almost one order of magnitude higher compared to their 2H-type domain counterparts (see Fig. 6.7b). It must be noted that the characteristic scratchy lines (blurring of fine features) is a common artifact in c-AFM

imaging as the tunnelling signal is 'smeared' when scanning over the nano-metre scale features (domain boundaries/intersections) due to the particularly large probe apex which unavoidably changes and becomes more blunt whilst scanning in contact mode.

Tunnelling current dependence on bias was performed on a region of the sample with a relative twist angle of $\sim 1.08^{\circ}$ in the bias range of + 500 mV > V_b > - 300 mV to determine tunnelling current evolution in each of the varying stacking configurations (see Fig. 6.8). Across the measured bias range, MM′ stacking had a consistently higher tunnelling current. The tunnelling current at the domain boundaries becomes more prominent at higher bias voltages (> $\pm$ 300 mV) indicating further that MM′ stacking is a locally confined region of increased tunnelling current.

Density functional theory calculations were performed (see Fig. 6.9) to acquire the band structure of both 2H and MM′ stacking configurations. 2H and MM′ clearly have a moderate off-set in bandgap energies which is expected to lead to a difference in tunnelling currents. However, both the conduction and valence band edges of 2H stacking have an earlier onset suggesting that 2H stack should have a higher tunnelling current in the experimentally measured bias dependence. This suggests the tunnelling 'hotspot' at the MM′ site originates from factors beyond the difference in bandgap energies. On the other hand, both 2H and MM′ stackings possess inversion symmetry, therefore the wavefunction cannot be layer-polarised.

Monolayers of TMDs are known piezoelectrics due to their lack of centro-symmetry [186]. Here, an electric polarisation can be induced by mechanical strain. The piezoelectric tensor relates the strain induced in a single layer to an induced charge polarisation and is described by the single component e_{11} [186]. The induced charge polarisation in a single layer can be described as [85];

$$\boldsymbol{P}^{t/b}(\boldsymbol{r}, z) = e_{11}^{t/b}\left(2u_{xy}^{t/b}, \left[u_{xx}^{t/b} - u_{yy}^{t/b}\right]\right)\delta\left(z - z_{t/b}\right) \tag{6.1}$$

Where $e_{11}^{t/b}$ = 2.9 $.10^{-10} Cm^{-1}$ [186] and u is the displacement vector in the xy plane. Typically, even layer numbers of TMDs do not produce a significant piezoelectric response due to inversion symmetry resulting in piezocharge compensation from odd and even layers (which is broken for odd numbers of layers). This is not the case for the reconstructed 2H-type homobilayers. The concentrated strain that is induced at the domain boundaries and intersections causes the strain tensor e_{11} for the top and bottom layer to have the opposite sign (i.e. $e_{11}^{b} > 0$, and $e_{11}^{t} < 0$). This is caused by the induced deformation (at domain boundaires/intersection) in each layer occurring in opposite directions owing to inversion symmetry. Therefore, the piezo-induced charge

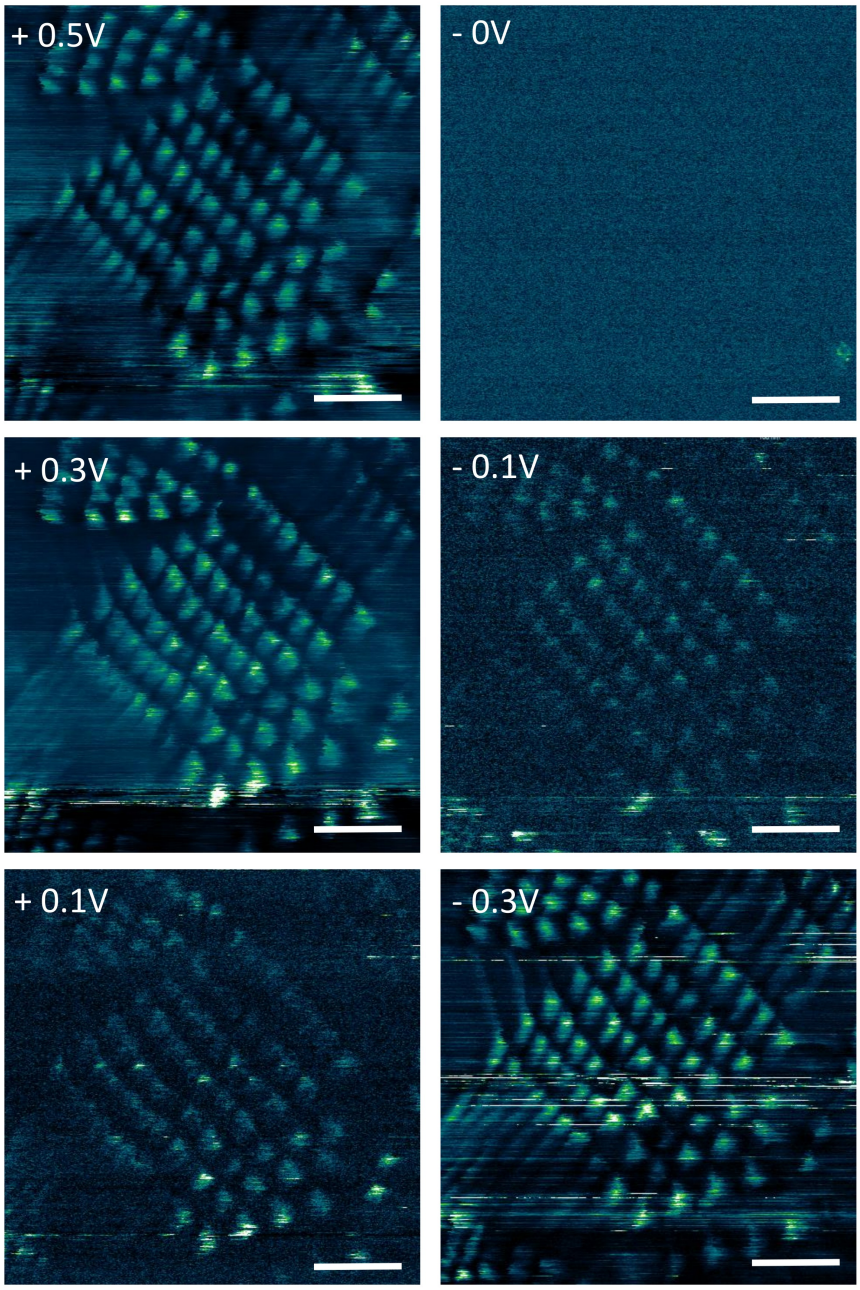

Fig. 6.8: **C-AFM tunnelling current maps of 2H-type twisted MoS_2 for varying surface voltages.** All images were acquired with tip force setpoint of 35 nN. Scale bars are all 50 nm.

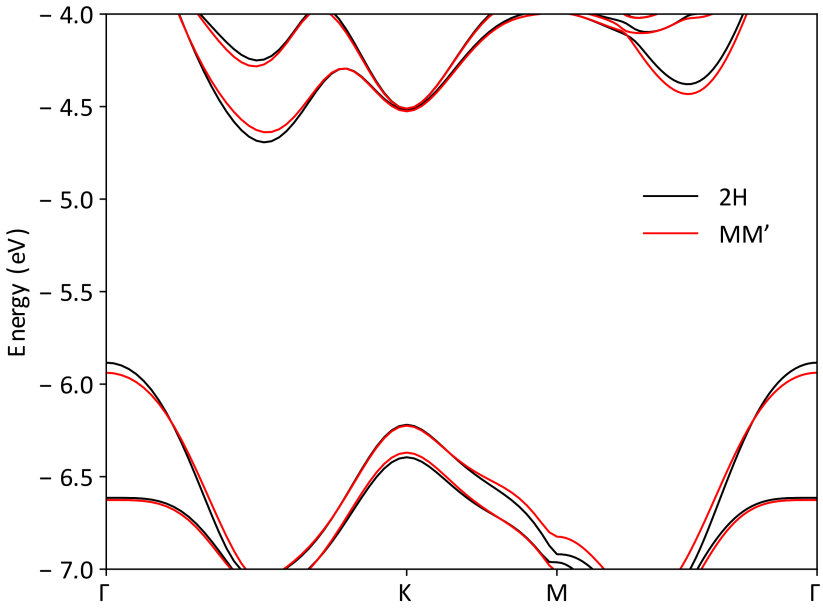

Fig. 6.9: **DFT calculated band structure for both 2H and MM′ stacking configurations of bilayer MoS_2.**

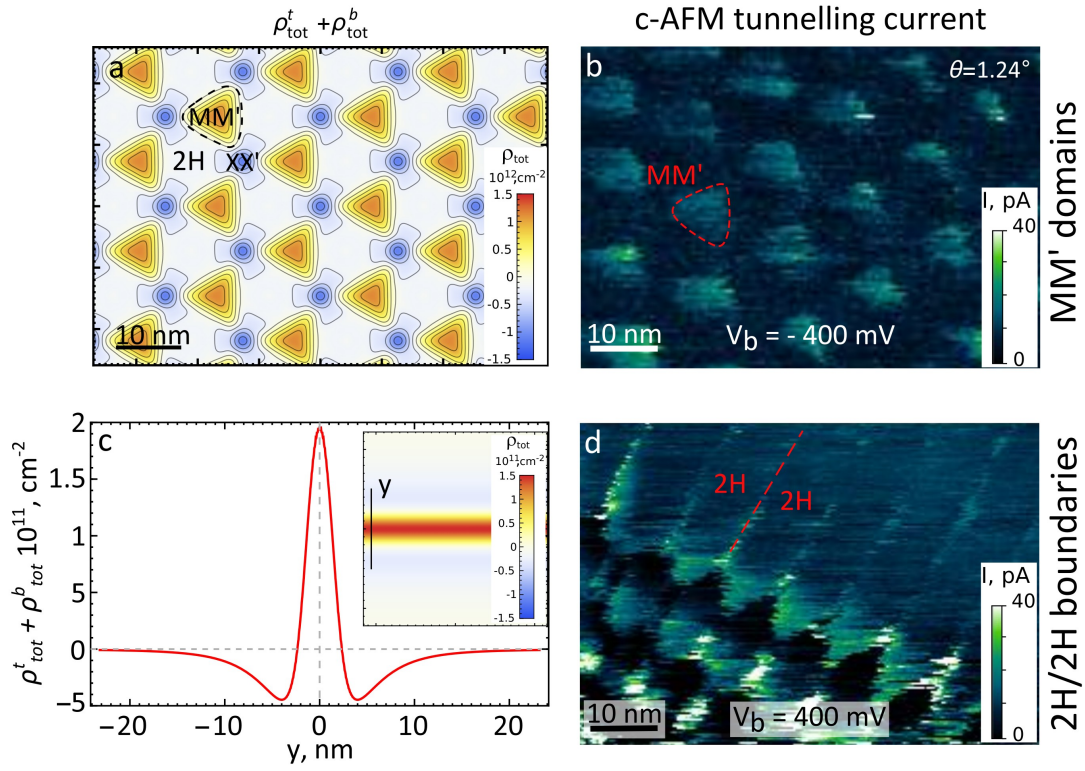

Fig. 6.10: **High piezoelectric charge densities in MM′ sites and 2H/2H boundaries of bilayer MoS_2.** **a** Spatial map of the total charge density (top and bottom layers) calculated for 2H-type bilayer of MoS2 twisted to 1.24° and **b** Experimental c-AFM data. **c** The total charge density (top and bottom layers) along a 2H/2H domain boundary and spatially mapped in the inset. **d** The corresponding c-AFM data highlighting higher tunnelling currents at the domain boundaries.

polarisation in the top and bottom layer have the same sign so are added together to give a piezocharge double that of a monolayer. Although C-AFM is not a direct measurement of this type of phenomena, the piezo-electric induced charge manifests as an observed increased tunnelling current at domain walls and intersections. In contrast, the reconstruction-induced deformation in 3R-type homobilayers occurs in the same direction and local induced charge densities are of opposite sign in the top and bottom monolayers due to the relation $u_{ij}^{t}(\boldsymbol{r}) = -u_{ij}^{b}(\boldsymbol{r})$, leading to a cancellation of the induced charge in the bilayer. In 2H-type homobilayers, the total charge density in the top/bottom layer is the sum of the piezo-induced and the screened charge densities [85];

$$\rho_{tot}^{t/b} = \rho_{piezo}^{t/b} + \rho_{ind}^{t/b}. \tag{6.2}$$

The induced piezo-charge density can be mathematically described as [85];

$$\rho_{piezo}^{t/b} = -\boldsymbol{\nabla}_{\boldsymbol{r}} \cdot \boldsymbol{P}^{t/b} \tag{6.3}$$

And the screened charge density can be described as [85];

$$\rho_{ind}^{t/b} = \alpha_{2D}^{t/b} \delta\left(z - z_{t/b}\right) \boldsymbol{\nabla}_{\boldsymbol{r}}^{2} \varphi(\boldsymbol{r}, z_{t/b}) \tag{6.4}$$

Where $\alpha_{2D}^{t/b} = d_0\left(\varepsilon_{||} - 1\right)/4\pi$ is the in-plane 2D polarizability of a monolayer that is associated to the static in-plane dielectric permittivity of the bulk TMDs. Here, an electrical potential $\varphi(\mathbf{r}, z)$ generated by the piezo-induced charge is slightly screened by the dielectric permittivity of TMDs.

The calculated total charge density of top and bottom layers presented in Fig. 6.10 indicates that regions of MM′ and XX′ in the domain structure have positive and negative total piezo-charge density. Therefore, in a slightly n-doped homobilayer such as MoS_2, the MM′ stacking will attract electrons and XX′ attract holes leading to spatially confined quantum dot-like states of both positive (MM′) and negative (XX′) charge. Similarly, the extended 2H/2H domain boundaries also exhibit a positive total charge density which matches well with experimental observations. Unfortunately, we were only able to pick up signal from the positive MM′ and 2H/2H regions. Since the experiments were conducted at room temperature, no signs of quantisation have been observed.

6.2 Kelvin Probe Force Microscopy Studies of 3R-type Twisted Bilayer MoS_2

Specialised heterostructures have been designed for Kelvin probe force microscopy studies in order to map the surface potential landscape in minimally twisted 3R-type bilayer MoS_2. For this, a 3R-type twisted bilayer was transferred onto a hBN substrate and electrically connected to a metallised (Ti(3 nm)/Au(40 nm)) contact and an overlapping layer of graphene (see Fig. 6.11a,b). Such electrical connection was used to ground the sample during the measurement. Alternatively, the bilayer was transferred onto a bulk graphite crystal and the bulk graphite was electrically connected to the ground with the same metallised contact as with the previous sample (see Fig. 6.11c,d). It is important to note that the metal deposition was performed using a TEM grid stencil mask (see Section 3.6) to avoid polymer resist contamination commonly observed with e-beam lithography assisted metal deposition.

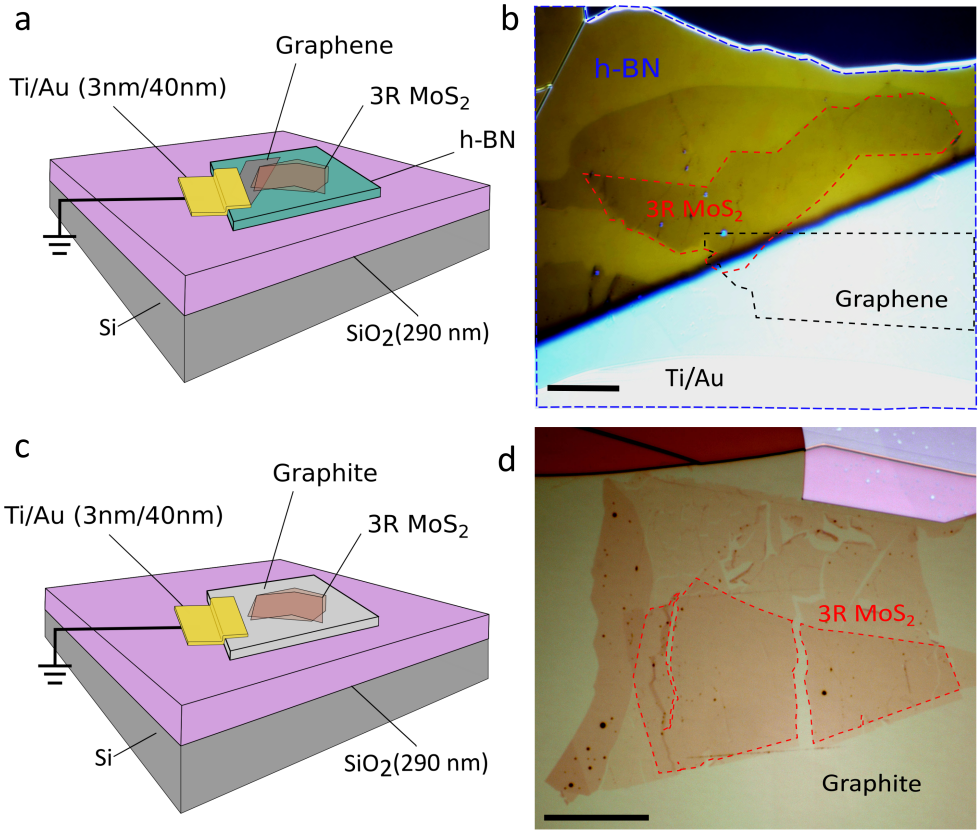

Fig. 6.11: **Sample fabrication for KPFM studies of 3R-type MoS_2 on hBN and graphite.** **a** Schematic of sample structure for 3R-type MoS_2 on hBN and **b** corresponding optical image (scale bar is 25 μm). Schematic of sample structure for 3R-type MoS_2 on graphite and **d** corresponding optical image (scale bar is 20 μm).

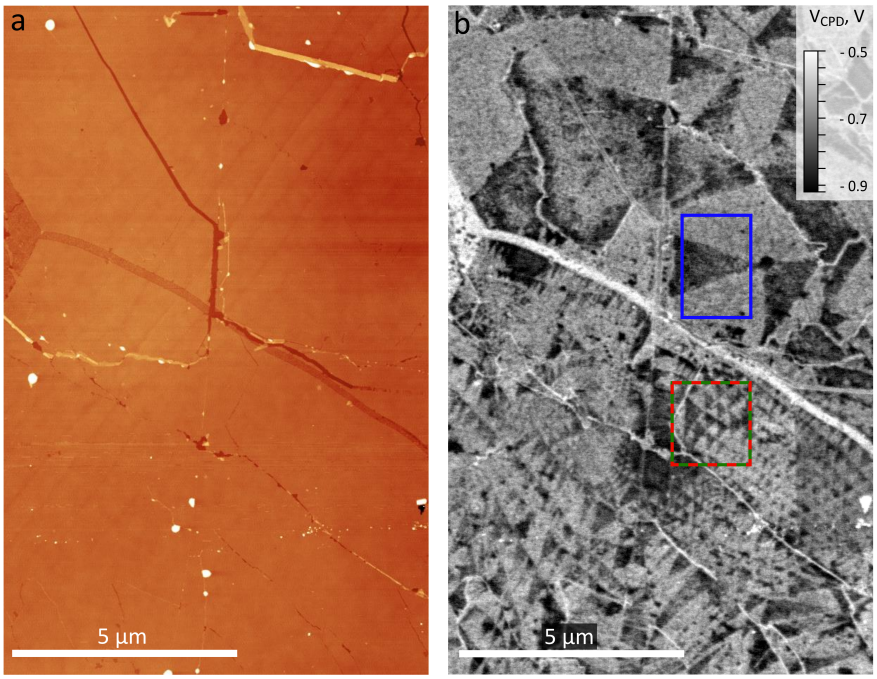

Fig. 6.12: **Surface potential mapping of 3R-type twisted bilayer MoS_2 on a hBN substrate. a** Topography image acquired on the first pass and **b** the surface potential acquired on the second pass in phase modulated-KPFM of MoS_2. The images were acquired with V_{AC} = 5.75 V and a time averaged probe-sample distance of 37 nm. The coloured (blue/green/red) boxes correspond to the area of the sample where data were analysed (see Fig. 6.13).

Surface potential maps of 3R-type twisted bilayer MoS_2 (on the hBN substrate) were acquired in vacuum using the two-pass lift mode in KPFM. Fig. 6.12 clearly highlights a distinct contrast between MX′ and XM′ domains indicating that there is a built-in transverse electric field that is polarised in the out-of-plane direction for each of the MX′ and XM′ regions. This field manifests a potential change (ΔV) relative to the equipotential back gate plate and has positive(negative) value for domains that are polarised up(down). We use this as a clear indication that 3R-type twisted bilayer MoS_2 is a 2D semiconducting ferroelectric material. This is measured as a gain of surface potential (ΔV_{CPD} = 2ΔV) as we scan across one type of stacking domain to the other.

The contrast within a singular domain (either MX′ or XM′) is non-uniform particularly for large domains. It is suspected that there is some influence from the topography (first pass scan), surface roughness of the underlying silicon substrate as well as charged impurities within the SiO_2 and hBN dielectrics that contribute to the contrast variation. Indeed, charged impurities in the SiO_2 substrate are known to induce potential variations in graphene (see Section 2.1.1).

In order to obtain consistent values of the surface potential (contact potential difference ΔV_{CPD}), several regions of the sample and various probes were used. Previous calibration studies were performed by Eli Castanon et al. [187] on the same AFM system and type of probes where the spatial and potential resolution was resolved. In this study, the cantilever was not calibrated by measuring the work function of a known metal such as gold but instead optimised (by assuming the spatial/potential resolution will be the same) using the procedures discussed in [187]. The optimisation procedure of the previous study was used to determine the probe-sample distance and the applied AC voltage (V_{AC}) by measuring the signal over a single area To optimise probe-sample distance, V_{CPD} was measured at different lift heights (see Fig 6.13b). The probe-sample distance of the first pass was taken as the average oscillation amplitude (half of one oscillation) and the second pass was calculated as the distance of the first pass plus the additional lift height. The dependence of probe-sample distance on the second pass was measured at a constant AC voltage (V_{AC} = 5.75 V) and frequency ($f_{AC} \sim$ 2 kHz) where the optimised distance was 32 nm. Additionally, the free oscillation amplitude (peak-to-peak) was 50 nm. Here, the frequency was selected based on the previous calibration study by Eli Castanon et al. [187]); from the available frequencies, 2 kHz was found to have a larger signal-to-

noise ratio and was dissimilar enough from the mechanical frequency not to be mixed with the mechanical excitation signal. In Fig. 6.13b the measured ΔV_{CPD} begins to saturate at a sample distance of 42nm and remains at a steady value at 37 nm and therefore was used. To note, the value of V_{CPD} tends toward zero when the tip-sample distance is above 42 nm because the capacitive coupling interaction between the probe and sample starts to reduce. As we lift the probe further away from the sample, a larger area under the probe contributes to the signal. At an infinite distance, the voltage will be zero due to the net averaging of both positive and negative contributions in the area under the probe. Below a certain distance (in this case 42 nm) V_{CPD} stabilises to a fixed voltage and the interaction is dominated by individual ferroelectric domains.

Next, the V_{CPD} dependence on ΔV_{AC} was measured to optimise the applied AC voltage. The measured ΔV_{CPD} tends to increase at higher V_{AC} due to electrostatic doping of the MoS_2 bilayer which leads to increased coupling with the probe. Additionally, the signal-to-noise ratio is too low when V_{AC} is too low (see Fig. 6.14). Therefore, values of ΔV_{CPD} were taken from images measured with an AC voltage 2 V < V_{AC} < 3 V.

To extract $2\Delta V$, a double Gaussian fitting was applied to histograms that were averaged over the regions marked in red/green (see Fig. 6.12). This produced an average value of 2Δ V = 100 $\pm$ 20 mV with an applied AC voltage of V_{AC} = 2.75 V and is in close agreement of the theoretically calculated value of $2\Delta V$ = 126 mV (see Fig. 6.17).

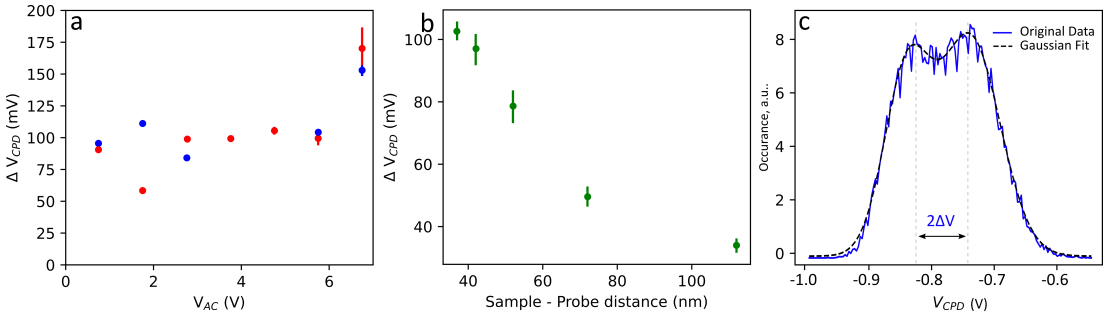

Fig. 6.13: **Analysis of the two-pass KPFM data of 3R-type MoS_2 on a hBN substrate. a** Surface contact potential difference (ΔV_{CPD}) as a function of applied oscillating voltage (V_{AC}). **b** Surface contact potential difference (ΔV_{CPD}) dependence on sample-probe distance. **c** Average histogram with Gaussian fitting of the contact potential difference between bright and dark contrast domains.

The same measurement was performed on 3R-type twisted bilayer MoS_2 on a graphite substrate. Again, the optimal probe-sample distance was experimentally

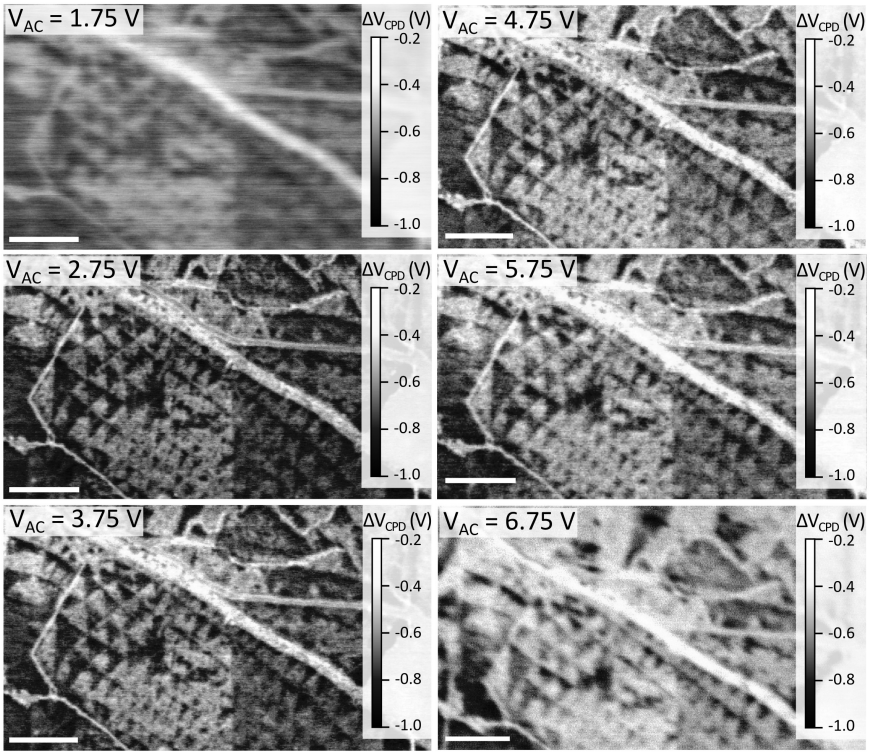

Fig. 6.14: **Spatially mapped surface potential (ΔV_{CPD}) dependence on AC voltage (V_{AC}).** Surface potential acquired on the second pass at a probe-sample distance of 37 nm. All scale bars are 1 μm.

obtained to be $\sim$ 37 nm. The AC voltage dependence revealed that the value of V_{CPD} = 100 mV was achieved with low AC voltage V_{AC} = 2 V which is within the same range of the experimentally measured values of the sample on a hBN substrate. The double Gaussian fitted histogram in Fig. 6.16c provides an average surface potential difference of $2\Delta V$ = 104 ($\pm$ 20) mV. The contrast within singular domains (see Fig. 6.15) is noticably more uniform compared to the sample on the hBN substrate though some small contrast variation seen in Fig. 6.15 is due to surface contamination. This is suspected to be due to the absence of a disordered dielectric as well as enhanced impurity (impurities in the Mo_2 bilayer) screening due to the metallic substrate.

The ferroelectric behaviour induced by interlayer charge transfer (which leads to a surface potential difference) was modelled by *ab initio* density functional theory calculations using the software package Quantum ESPRESSO [188]. The surface potential drop can be mathematically described as [108];

$$\Delta^P(r_0, d) = \Delta_a e^{-q(d-d_0)} \sum_{j=1,2,3} sin(G_j.r_0) \tag{6.5}$$

Here, r_0 is the in-plane offset between the layers, $d-d_0$ = -0.021 nm^{-1} is the interlayer distance (where d_0 = 0.636 nm), G_j is the shortest reciprocal vectors of the bilayer

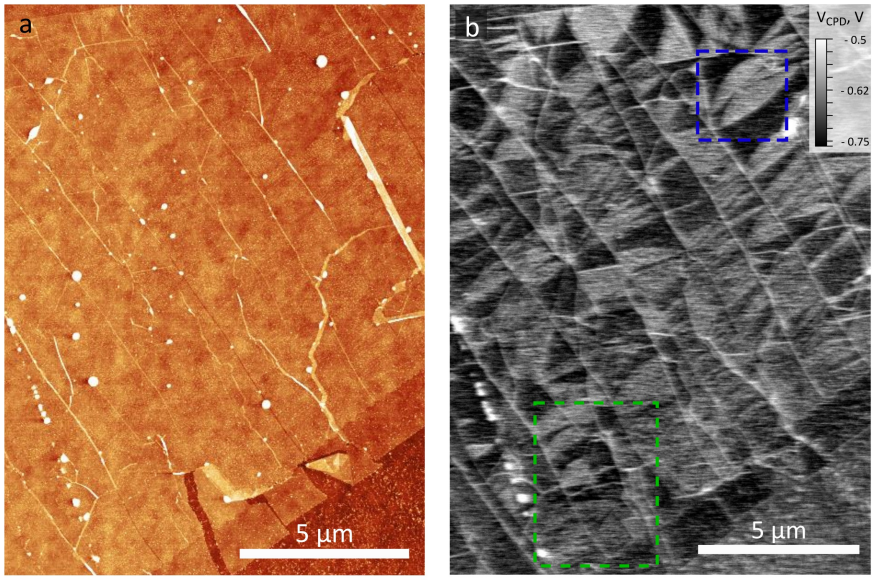

Fig. 6.15: **Analysis of the two-pass KPFM data of 3R-type MoS_2 on a graphite substrate.** **a** Topography image acquired on the first pass and **b** the surface potential acquired on the second pass in phase modulated-KPFM of MoS_2 on graphite. The images were acquired with V_{AC} = 2 V and a time averaged probe-sample distance of 37 nm. The coloured (blue/green) boxes correspond to the area of the sample where data were analysed (see Fig. 6.16).

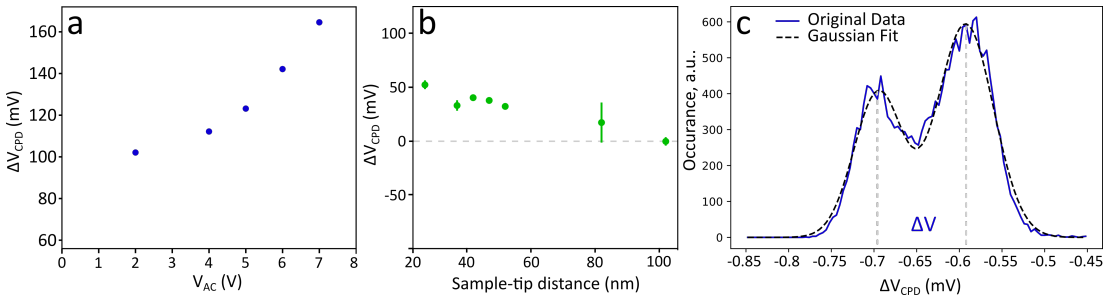

Fig. 6.16: **Analysis of the two-pass KPFM data of 3R-type MoS_2 on a graphite substrate substrate.** **a** Surface contact potential difference (ΔV_{CPD}) as a function of applied oscillating voltage (V_{AC}). **b** Surface contact potential difference (ΔV_{CPD}) dependence on sample-probe distance. **c** Average histogram with Gaussian fitting of the contact potential difference between bright and dark contrast domains.

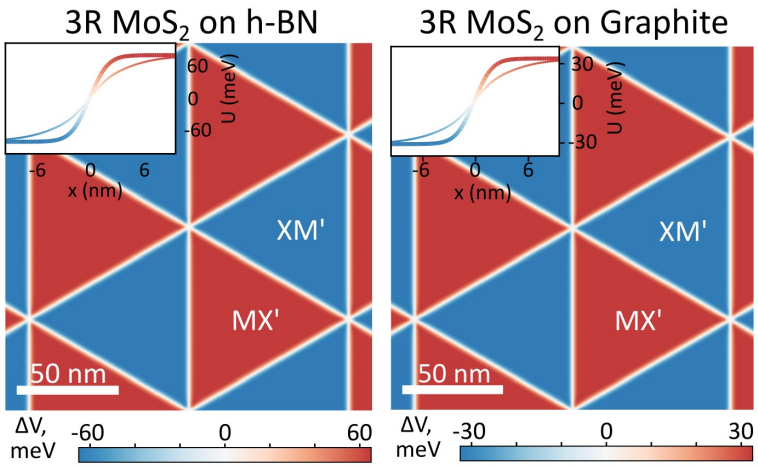

Fig. 6.17: **A spatial map of potential difference (ΔV) between XM′ and MX′ domains calculated by *Ab initio* density functional theory (DFT).** The potential drop across the domain walls are in the inset of of each spatial map, where the thin curve takes into account piezoelectric charge and the bold curve ignores it.

TMD. The potential jump per lattice period Δ_a = 16 mV and q = 0.2215 nm^{-1} was calculated from DFT Hartree potentials (for more details see ref. [108, 189]).

When the parameters are fitted into the model described in the equation above, the calculated surface potential drop is ($\Delta U = \Delta^P$) 66 mV. The calculated distribution is shown in Fig. 6.17 where there is a potential drop across the domain wall. The gradual drop in surface potential occurs over a distance of $\pm$ 6 nm away from the centre of the domain wall if we take into account the piezoelectric charge ($\pm$ 3 nm if we ignore it) as shown in the insets of Fig. 6.17a,b.

6.3 Scanning Electron Microscopy Studies of 3R-type Twisted Bilayer MoS_2

In order to better understand the mechanism of ferroelectric switching in 3R-type twisted bilayer MoS_2, samples were prepared for *in situ* two terminal electronic measurements in a scanning electron microscope. SEM was performed in collaboration with Dr Teruo Hashimoto at the Photon Science Institute (University of Manchester). When the oppositely polarised XM′ and MX′ stacking regions are under an applied vertical electrical field the domains are expected to expand and shrink leading to a device that is XM′ or MX′ dominated depending on the sign of the applied field [105, 106]. Here, the domain wall sliding is expected to reversibly switch between XM′ and MX′ through lateral translation by one-bond-length. It is noted that previous calculations (described in Chapter 5) highlight that MX′ and XM′ stacking configurations have equal (adhesion) energies and therefore are expected to occupy equal regions across the sample without the influence of vertical applied field (which is clearly demonstrated in all previous microscopy data).

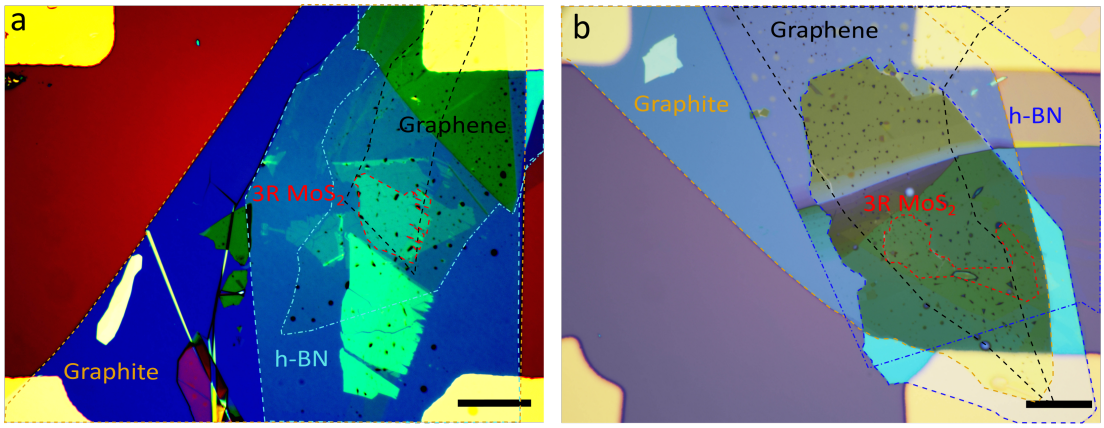

Fig. 6.18: **Optical images of the 3R-type twisted bilayer MoS_2 two-terminal SEM device.** **a** sample one and **b** sample two. Scale bars 20 μm.

For this experiment, samples were fabricated with a bottom graphite backgate and a top graphene gate to allow for control of the transverse electric field across the TMD bilayer. The 3R-type twisted bilayer was prepared using the modified tear-and-stack technique as illustrated in 3.5. A graphite/hBN heterostructure was prepared using the PMMA-based dry transfer technique and the twisted MoS_2 bilayer was placed on top avoiding overlap with the graphite back-gate. Following this, thin hBN and graphene layers were deposited on top of the structure, again avoiding direct electrical contacts

between the graphene top gate, MoS_2 twisted bilayer and graphite back-gate. The top graphene and bottom graphite electrode were contacted using Ti (3 nm)/ Au (40 nm) electrodes deposited through a shadow mask.

Domain contrast using the SEM electron channelling contrast technique was found to significantly decrease with increasing top hBN encapsulation thickness and therefore the top hBN was selected in the range of 2-3 nm to allow for gating without tunnelling [26] into the twisted bilayer. We found that a top hBN thickness above 5 nm was not compatible with the imaging technique regardless of the acceleration voltage used.

First we consider large MX′ and XM′ stacking domains (domain length $\ell \sim$ few μm) where the characteristic triangular domain shape is lost due to the random strain distribution caused by the transfer process. An out-of-plane electric displacement $D = \epsilon_0 V \epsilon_r / h$ was applied at increasingly higher voltages. Here, h is the total distance between the top and bottom graphene gates, ϵ_r = 3.5 is the permittivity of hBN and V is the applied voltage. In Fig. 6.19 the domain boundaries separating MX′ (bright) and XM′ (dark) domains are 2-3 μm in length and are sometimes pinned only by folds and contamination bubbles introduced during the fabrication process.

Upon application of a positive vertical displacement field ($\epsilon_0^{-1} D$ = +2.2 V/nm in Fig. 6.19) the XM′ domains expand laterally by $\sim$ 100 nm causing two dark contrast domains to appear to merge together in some regions where neighbouring XM′ domains are in close proximity. Importantly, the expanded XM′ retain their configuration upon removal of the field which is highly desirable for non-volatile memory applications. Upon application of a negative electrical field the XM′ domains shrink at the expense of MX′ domains. At $\epsilon_0^{-1} D$ = - 1.75 V/nm the XM′ shrink down to almost negligible width (close to the resolution limit of the SEM) generating a line defect consisting of two domain walls. We can better describe this as two partial screw dislocations merging to generate one perfect screw dislocation separating two domains of the same configuration. Importantly, the perfect screw dislocations are topologically protected [190] and therefore are not erased by the application of high electrical field. The modified domain structure persists upon returning to zero field. When the same ($\epsilon_0^{-1} D$ = + 2.2 V/nm) positive electrical field is reapplied to the device the XM′ domains re-expand to almost the same lateral dimensions compared to the previous switching (hysteresis) cycle.

For domains of intermediate lateral dimensions ($\ell \sim$ 400-600 nm) where the

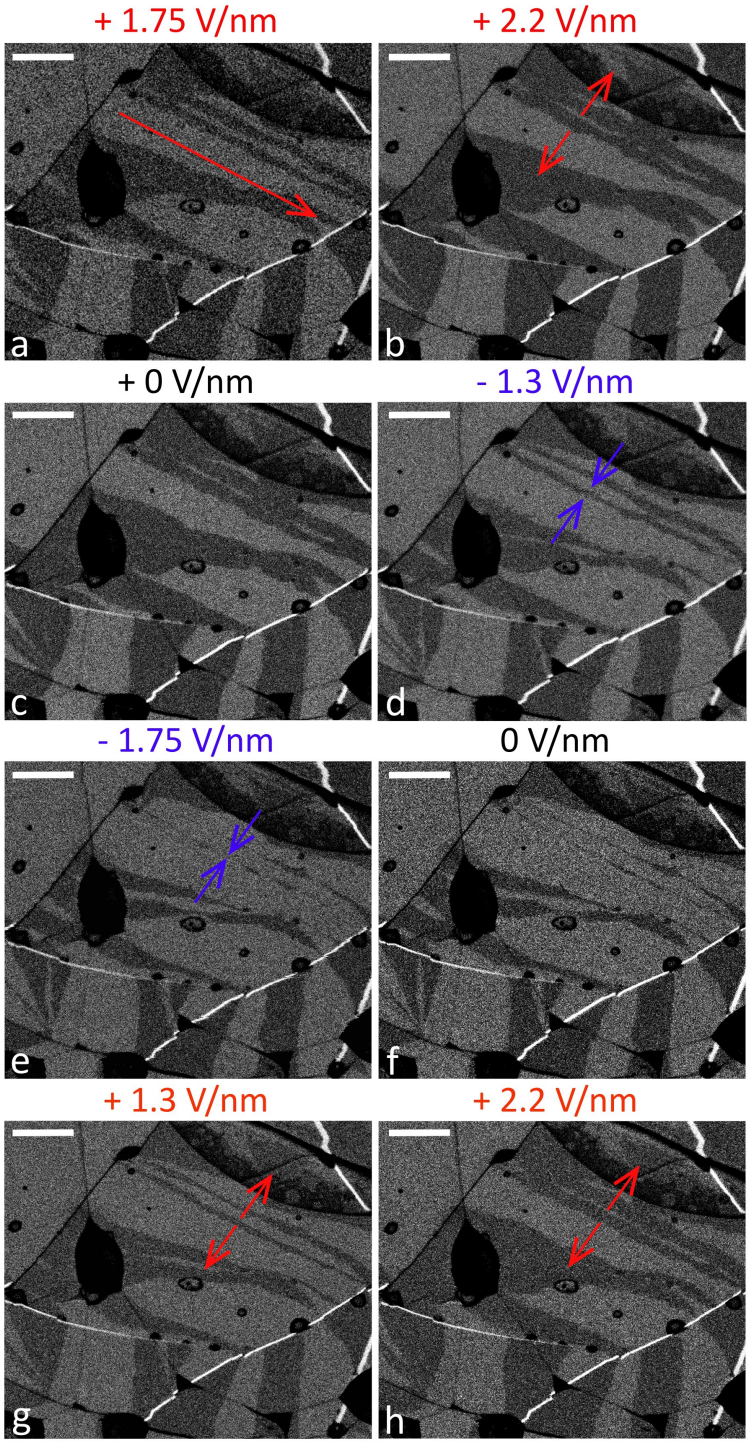

Fig. 6.19: **In-situ SEM imaging revealing global reversible switching in large twisted MoS_2 domains with applied electric field. a** Red and blue arrows indicate direction of domain wall motion with positive and negative applied field, respectively (scale bars 500 nm) .

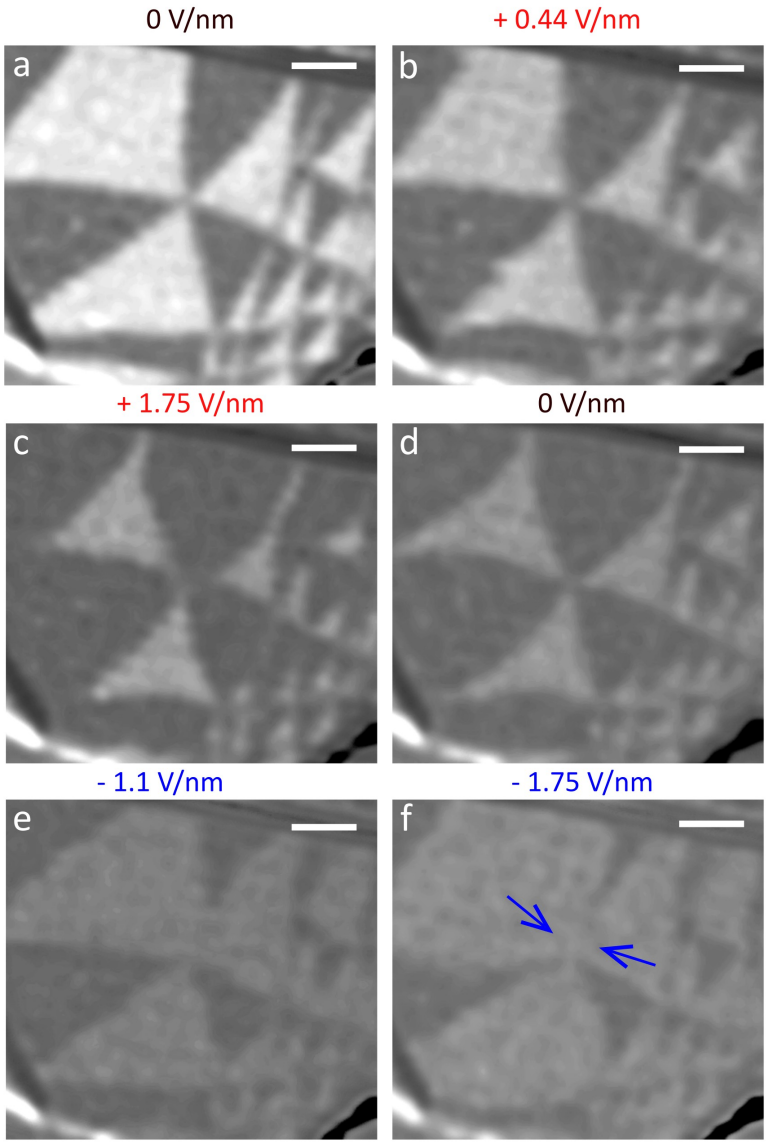

Fig. 6.20: **In-situ SEM imaging revealing global reversible switching in intermediate twisted MoS_2 domains with applied out-of-plane displacement field.** The SEM images labelled **a-h** are in the the order that they were acquired. Red and blue arrows indicated direction of domain wall motion with positive and negative applied field, respectively (scale bars 200 nm) .

characteristic triangular domain shape still persists, the domain wall motion is significantly different. It must be noted that the resolution and quality of domain contrast in 6.20 significantly degrades with each consecutive image due to the build up of hydrocarbon contamination.

When there is zero applied electrical field the adjacent XM′ and MX′ domains are roughly equal in size (slight variation caused by additional strain induced by folds in the bilayer) with relatively straight domain boundaries separating each region. On application of a positive electrical field, again the XM′ domains expand at the expense of MX′ domains but this time XX′ intersections act as pinning points that restrict the distance that the domain wall is able to slide. This generates pronounced concave (convex) curvature of the domain boundaries which becomes increasingly curved with higher displacement field. After the application of a positive electrical field, the domains remained 'switched', however, some noticeable deviations are apparent in Fig. 6.20 (from $\epsilon_0^{-1}D$ = + 1.75 V/nm to 0 V/nm). Again, application of a negative electrical field causes convex (concave) curvature in the opposite direction. In the final image in Fig. 6.20, where $\epsilon_0^{-1}D$ = - 1.75 V/nm, the MX′ domains have shrunk to less than half of their original size where the nearest-neighbour domain walls appear to merge in the regions close to the central XX′ intersection, similar to the observations seen in Fig. 6.19.

Finally, we consider relatively small XM′ and MX′ domains ($\ell \sim$ 200 nm) where there is a large density of XX′ intersections (see Fig. 6.21). It must be noted that due to the increased magnification of the image, the contamination build-up does reduce the visibility of the domain wall boundaries, nonetheless, the domain wall bending is still apparent. Compared to the intermediate domain lengths ($\ell \sim$ 400-600 nm) in Fig. 6.20, domain wall bending is much less pronounced with an out-of-plane displacement of $\epsilon_0^{-1}D$ = + 1.75 V/nm. Additionally, in Fig. 6.21 there is no sign of single domain walls merging together near the XX′ intersections for both positive and negative displacement fields. This suggests that the ferroelectric switching mechanism has a clear dependence on domain length as well as the strength of the displacement field.

To better understand the evolution of domain wall sliding under applied out-of-plane displacement field, an analytical model was employed taking into account the orientation dependence of two partial dislocations that merge to form a single full screw dislocation. The energy dependence on the orientation can be described as $\overline{w}$ +

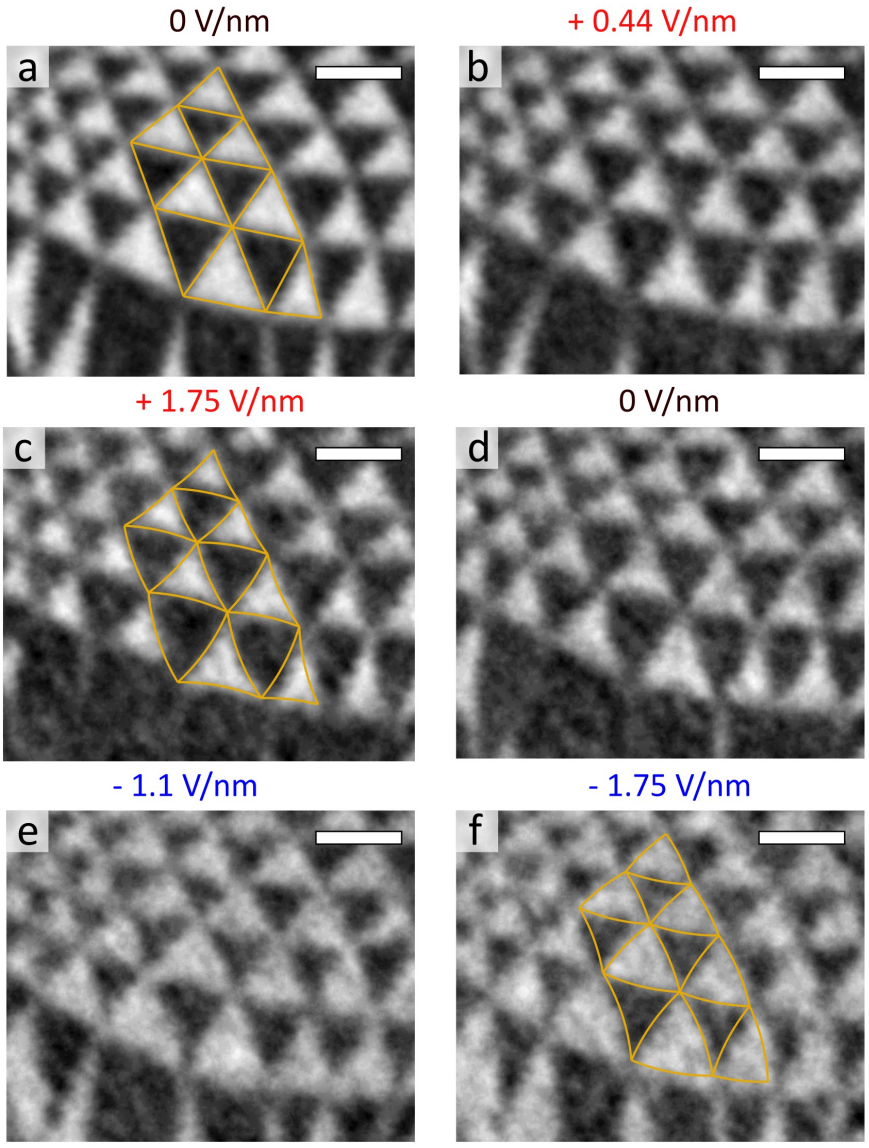

Fig. 6.21: **In-situ SEM imaging revealing global reversible switching in small twisted MoS_2 domains with applied electric field.** Raw SEM data is overlaid with an analytical model calculated from Eqs. 6.7 and 6.8 of domain wall curvature (yellow curves). All scale bars are 200 nm.

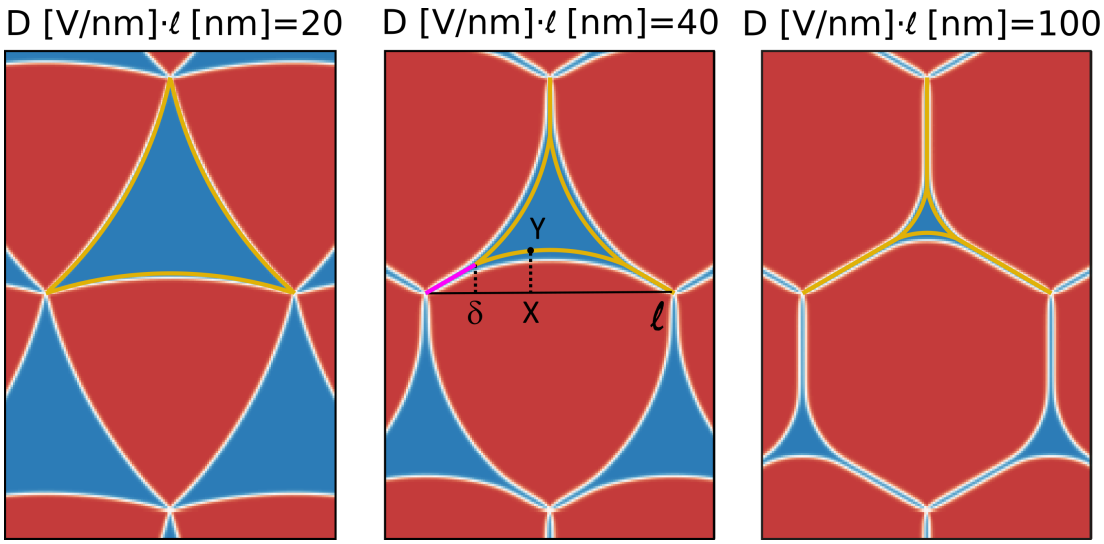

Fig. 6.22: **Theoretically calculated dependence of applied out-of-plane displacement (D) and domain length (ℓ) on the formation of perfect screw dislocation in 3R-type twisted bilayer MoS_2.** The evolution of domain wall bending described by the analytical model calculated from Eqs. 6.7 and 6.8 (yellow curves) superimposed over the map of electrostatic potential due to out-of-plane ferroelectricity in 3R-type twisted bilayer MoS_2 (same as Fig. 6.17). A perfect screw dislocation of length δ grows above a threshold displacement (D_*).

$\widetilde{w}sin^2\phi \approx \overline{w}+\widetilde{w}y'^2$, where $\overline{w}$ = 0.94 eV/nm [189] accounts for the energy density of the partial dislocation and $\widetilde{w}$ = 0.62 eV/nm accounts for the orientation dependence. Here $\phi = arctany' \approx y' \equiv \frac{dy}{dx'}$ is the deviation angle between the dislocation axis (where the zigzag orientation is energetically preferable for a perfect screw dislocation) and the armchair direction ($\pm$ 30°).

Domain wall sliding with applied vertical field can be described as a transverse displacement y($0 < x < \ell$) of a domain wall (with period ℓ) from a straight line y(x)=0 that is pinned at both ends at the domain intersections. If we then take into account the possible formation of a perfect screw dislocation from partial dislocations in a single domain, the transverse displacement becomes y(x)($\delta < x < \ell - \delta$). The two partial dislocations with Burgers vectors $\frac{a}{\sqrt{3}}(1,0)$ and $\frac{a}{\sqrt{3}}(\frac{1}{2},\frac{\sqrt{3}}{2})$ merge into a perfect dislocation with a Burgers vector of $a(\frac{\sqrt{3}}{2},\frac{1}{2})$ when a perfect screw dislocation is formed. Domain wall variation as a function of out-of-place displacement field is then [183],

$$\epsilon_\ell[y(x)] = 3\int_\delta^{\ell-\delta}[(\frac{1}{2}\overline{w}+\widetilde{w})y'^2 - 2\frac{DP}{\epsilon_0\varkappa}y]dx + 6[\frac{u}{\sqrt{3}} - \overline{w} - \frac{\Omega}{\sqrt{3}}\delta]\delta \qquad (6.6)$$

where the first part of the integral accounts for the elongation of domain walls and the second part is the energy gain $\pm 2\frac{DP}{\epsilon_0\varkappa}y$ from the redistribution of domain area of the

oppositely charged ferroelectric domains due to an applied vertical field. Here, P is the polarisation density, ϵ_0 is the dielectric permittivity in vacuum and $\varkappa$ is the dielectric screening parameter. The remaining terms account for the possible formation of a perfect screw dislocation.

Redistribution of domain area requires a threshold displacement field ($D > D_*(\ell)$) for the possible formation of a perfect screw dislocation. Below the threshold displacement field, the domain wall displacement can be described by [183],

$$y(x) = \frac{DP/\varkappa\epsilon_0}{\overline{w} + 2\widetilde{w}}(\ell - \varkappa)x \tag{6.7}$$

This analytical model fits well to our experimental data where the out-of-plane displacement field generates parabolic curvature of domain walls as shown in Fig. 6.21. At the threshold displacement (D_*), the perfect screw dislocations, with an energy density u = 2.19 eV/nm [189], are expected to start to touch each other from the XX′ intersections (nodes with intervals x = 0 and x = ℓ). Here, $y'(0)$= -y' and (ℓ)= $1/\sqrt{3}$ and the displacement scales as $D_* \propto \ell^{-1}$.

Above the threshold, the perfect screw dislocations become increasingly longer in length ($\frac{\delta}{\sqrt{3}}$) as show by the line in Fig. 6.22 at the expense of the two adjoining partial dislocations (nodes with intervals of 0<x<δ and $\ell - \delta < x < \ell$). By experimentally estimating the dielectric screening parameter $\varkappa$ = 1.5 we can then determine the domain-length (ℓ) dependent displacement threshold,

$$\epsilon_0^{-1} D_*(\ell) \approx \frac{400V}{\ell} \tag{6.8}$$

This means that for domain wall lengths of $\ell \sim$ 400 nm, the critical displacement threshold is easily reached at an experimentally achievable voltage range. Here, the experimental voltage range is limited by the dielectric breakdown field of hBN [26, 191].

6.4 Electron Tunnelling in 3R-type Twisted Bilayer MoS_2

For ferroelectric semiconductors such as 3R-type twisted TMDs, the domain switching (described in the previous Section) should lead to a hysteretic response in the onset of conductivity to an applied transverse electric field in electrical transport measurements. This is particularly useful for memory device applications that require a switchable 'read out' signal with an applied stimulus (see Section 2.2.3).

Our previous KPFM (see Section 6.2) and SEM (see Section 6.3) studies revealed that MX′(XM′) domains are polarised up(down) and can grow at the expense of XM′(MX′) with increasingly negative(positive) transverse electric field. In order to quantify the ferroelectric switching behaviour of 3R-type twisted bilayer TMDs, with MoS_2 used as the example, prototype ferroelectric tunnelling devices were fabricated with the aid of scanning probe microscopy. In this project, a tunnelling current has been measured as a function of the source-drain bias (V_{sd}) applied between a source (bottom graphite) and drain (top graphene) electrode in a tunnelling junction device (see Fig. 3.10d). Between the source and drain layers, a tunnelling barrier consisting of few-layer hBN (1-7 layers) along with the twisted bilayer MoS_2 have been sandwiched. Pre-mapping of the triangular domain structure was performed before and after encapsulation with a hBN tunnelling barrier using electrical SPM techniques. This was an essential step in the design and fabrication of each device and provided a means for the direct correlation between domain structure and electronic transport properties.

Hysteresis is the difference between the threshold voltages (onset of electron tunnelling) of the forward and backward bias voltage sweep directions. The measured tunnelling current should vary depending on the ferroelectric domain distribution. The transport measurements were performed on a reference 2H-type bilayer and 3R-type twisted bilayer MoS_2 tunnelling devices at low temperatures (1.5 K) by Yunze Gao. All measurements discussed in this section were performed at low temperatures to limit the effect of temperature-dependent hysteresis (discussed later in detail) commonly observed in MoS_2 electrical transport measurements [192, 193]. This section summarises the work in progress which shows promising results but is not yet concluded.

6.4.1 Reference 2H Bilayer MoS_2 Tunnelling Device

To test the device design and characterise its quality (e.g. extracting the carrier concentration of the graphene electrodes as well as using the position of the Dirac point to account for any extrinsic doping) we first tested a non-ferroelectric 2H bilayer reference device. For this, the top graphene electrode had multiple contacts as shown in Fig. 6.23b, the Dirac point has an offset of $\sim$ 0.6 V, presumably due to surface absorbates.

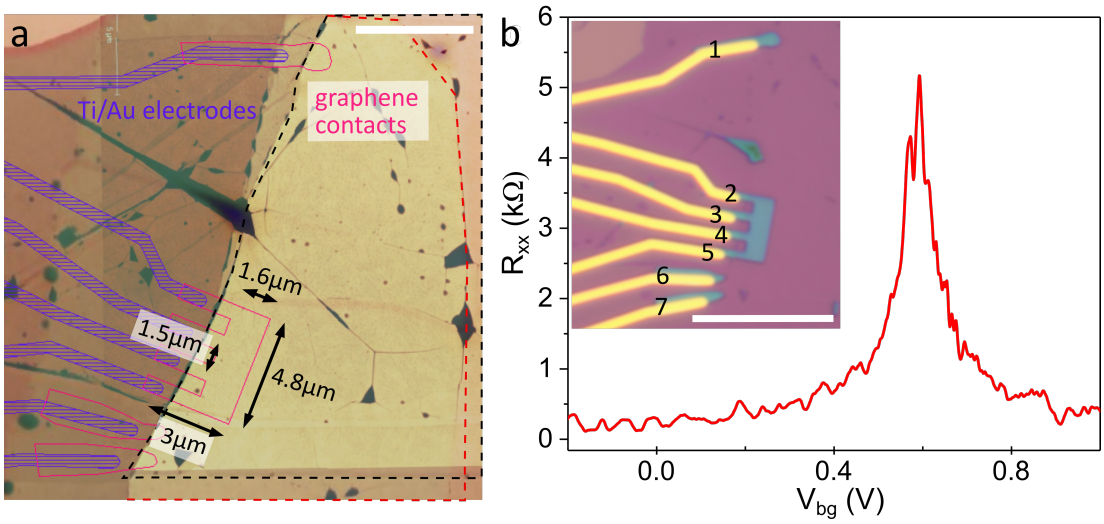

Fig. 6.23: **Reference 2H bilayer MoS_2 tunnelling device. a** Tapping mode topography image of the graphite/2H bilayer MoS_2/tunnelling hBN/graphene heterostructure where the black dashed lines indicate the outline of the tunnelling hBN and the red dashed line indicates the 2H bilayer MoS_2 region. Overlaid on the image are the location of the graphene contacts and Ti/Au electrodes designed in Layout Editor. **b** Longitudinal resistance R_{xx} as a function of back-gate voltage (V_{bg}), where R_{xx} was measured between contacts 3 and 4. Optical image of the 2H-type reference device shown in the inset. All scale bars are 5 μm.

We can also use the carrier concentration to accurately calculate the capacitance of our bilayer MoS_2/hBN stack and benchmark it for our 3R-type ferroelectric tunnelling devices shown later. One way to achieve this is to analyse the magnetic field-induced Shubnikov-de Haas (SdH) oscillations at a low temperature (1.5 K) in a four-terminal geometry. In this project, a cryogen-free magnet system (cryogenic limited) was used.

In the presence of an applied perpendicular magnetic field (B), electrons in the

graphene electrodes experience a Lorentz force causing them to travel along circular trajectories between electron scattering events with a frequency of $\omega_c = eB/m*$, where e is the charge of an electron and $m*$ is the effective mass of an electron. If there is a sufficiently high magnetic field, the electrons travel in complete orbits without being scattered, leading to a quantization of the orbit diameter. This means that electrons now only occupy states of quantised energy eigenvalues, called Landau levels (LL's), separated by an energy $\hbar\omega_c$.

The total energy (E_n^j) of electrons, with a parabolic dispersion relation, in a 2D system such as graphene becomes [15, 194];

$$E_n^j = E_z^j + \hbar\omega(n + \frac{1}{2}) + s\mu_B gB, n = 1, 2, 3... \tag{6.9}$$

where j is the number of filled subbands (j = 1,2..), n is the LL index, E_z^j is the energy of quantised electronic states (in z-direction), s (= $\pm\frac{1}{2}$) is the spin number, μ_B is the Bohr magneton (a physical constant of the magnitude of the magnetic dipole moment of an electron orbiting an atom) and g is the Landé factor which is material-dependent.

When there is zero applied magnetic field and sufficiently low temperatures, the density of states of graphene has a linear dispersion and the states are filled up to the Fermi energy, E_f. With the application of a magnetic field, LL's form with an energy separation of $\hbar\omega_c$. LL's that are below E_f are filled with N_l electrons. With increasing magnetic field, the number of filled states does not change as the carrier concentration remains constant. However, the energy separation and the degeneracy of the LL's changes. Once a LL is full and E_f resides between two LL's, we observe a peak in longitudinal resistance, R_{xx}, such an effect is described as Shubnikov-de Haas (SdH) oscillations. The peaks in R_{xx} that are equidistant with B, and their period, allows us to extract the carrier concentration, n. In Fig. 6.24a, the magnetic field (B) has been plotted as a function of gate voltage, V_g. The first minima away from the Dirac point is indicated by the yellow dashed lines. The carrier density at the first minima of the SdH oscillation in Fig. 6.24a corresponds to a filling factor $\nu = \frac{n_e}{\rho_{LL}} = \frac{n_e}{eB/h}$ = 0.5, where the filling factor is the ratio of carrier density, n_e, and density of states per LL, ρ_{LL}. For graphene, we must also consider spin/valley degeneracy where each state can be occupied by two spin and two valley electrons (filling factor becomes ν = 2). As we increase the magnetic field we get a set of R_{xx} minima, the corresponding carrier density becomes [15];

$$n = g_s g_v \nu \frac{e}{h} B_i = 2\frac{e}{h} B_i \tag{6.10}$$

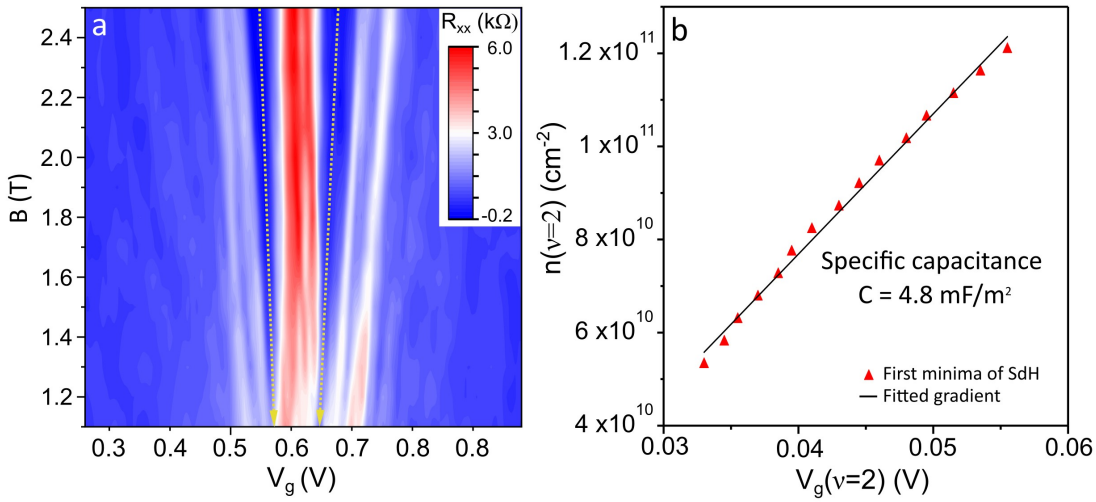

Fig. 6.24: **Shubnikov-de Haas oscillations in a 2H-type bilayer MoS_2 tunnelling device.** **a** Colour map of the longitudinal resistance (R_{xx}) with respect to gate voltage (V_g) for magnetic fields up to 2.5 T. The first minima of R_{xx} are indicated by the dashed yellow lines. **b** The extracted first minima of the Shubnikov-de Haas oscillations where the gradient ($\frac{n_i}{-V_g}.e$) allows us to calculate specific capacitance (C).

Once we obtain the first minimas of the SdH and their corresponding carrier concentration, we can plot this as a function of gate voltage (see Fig. 6.24b). Here, the gradient ($\delta n_i/\delta V_g$) is equal to the capacitance per unit area (C);

$$C = \frac{n_i e}{-V_g} = \frac{\epsilon\epsilon_0}{de} \tag{6.11}$$

where ϵ is the dielectric constant of SiO_2 (3.6) and d is the thickness of the dielectric layer ($\sim$ 290 nm). From the calculated plot in Fig. 6.24b we obtain a specific capacitance of 4.8 mF/m^2.

6.4.2 3R-type Twisted Bilayer MoS_2 Tunnelling Devices

Sample 1 shown in Fig. 6.25 was fabricated with a tunnelling barrier (hBN) thickness of four layers. Before hBN encapsulation, the domain structure was initially mapped using lateral force microscopy in contact mode where a conductive probe was used to achieve the domain contrast (as shown in Fig. 6.25b).

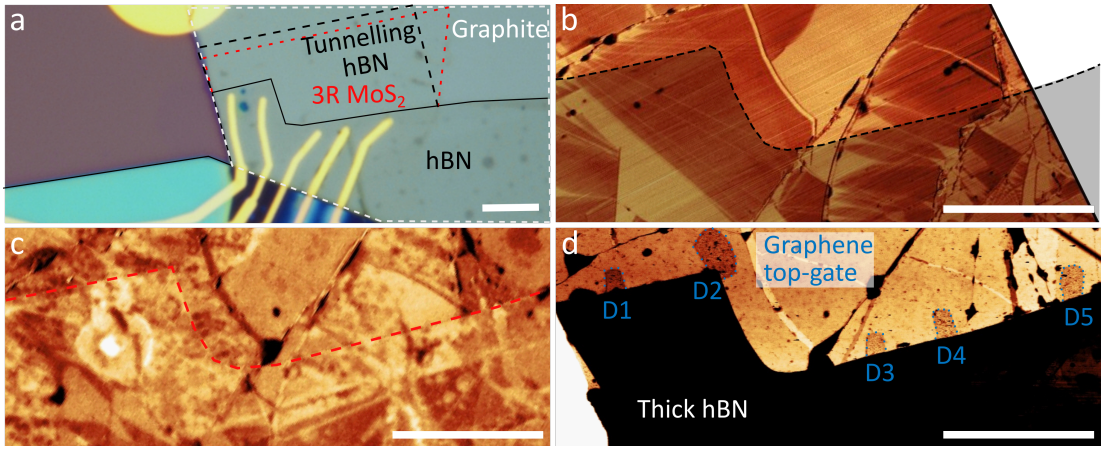

Fig. 6.25: **Sample 1: using SPM to design 3R-type twisted bilayer MoS_2 tunnel junction devices.** **a** Optical image of tunnelling junction sample one. **b** Contact mode lateral deflection mapping to identify the 3R-type MoS_2 domain structure in sample one. The thick hBN has been overlaid (black dashed line) for clarity. **c** EFM second-pass (lift height 30 nm and tip bias 1 V) phase image of domain structure underneath the 4-layer tunnelling hBN (red dashed line is thick hBN edge). Note that charged impurities in hBN gives patchy contrast within domains. **d** Tapping mode topography image of the finished sample where the graphene has been patterned into individual contacts. All scale bars are 5 μm.

For this first device, large uniform domains (few μm) were selected for each tunnelling device. Once the hBN tunnelling barrier was transferred on top, the graphite/ 3R-type twisted MoS_2 heterostructure was re-imaged using EFM as shown in Fig. 6.25c. When comparing Fig. 6.25b and c, there were notable similarities in domain structure, however, the domain contrast of the darker domains in Fig. 6.25b appear to have a more pronounced texture. This is likely due to the the presence of trapped charges in the dielectric hBN tunnelling barrier (similar to the contrast observed in Fig. 6.12b).

After imaging the domain structure, the top graphene electrode was transferred on

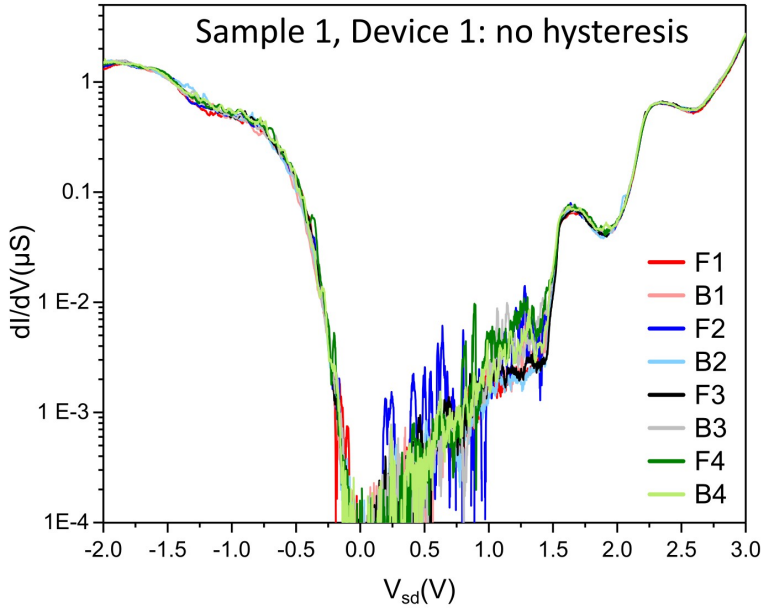

Fig. 6.26: **No hysteresis in differential conductance dI/dV observed in sample 1.** Plotted forward and backward bias voltage sweep (V_{sd}) for sample 1 measured at 1.5 K.

top of the heterostructure. The top graphene was etched using an e-beam lithography pattern and RIE to define the individual contacts. The area of each tunnel junction is defined by the area under the top graphene contact.

The differential conductance measured in device 1 is shown in Fig. 6.26. The dependence displays small dI/dV values at small biases and sharply raises above the threshold voltage on the negative side $\sim$ -0.2 V and the positive side $\sim$ 1.5 V. Unfortunately, no clear hysteresis was observed in the differential conductance signal despite the large voltage range (-2 < V_{sd} < 3 V). The lack of observed hysteresis on the positive size may be a factor of the high voltage threshold, however, does not explain the lack of hysteresis for negative voltages. The most likely explanation is the lack of domain boundaries in the individual tunnelling regions limiting the possibility for domain redistribution as the switching electric field is only created in the tunnelling junctions.

For sample 2 (see Fig. 6.27), domain mapping after encapsulation with thin (three layers) hBN was drastically improved using PFM, however, in the final step of fabrication, a crack in the bilayer MoS_2 meant that a number of devices became electrically shorted (top and bottom electrodes in contact with each other) leaving only one measurable device. In Fig. 6.28, clear hysteresis was observed between the forward (F2 and F3) and backward (B1, B2 and B3) voltage sweeps. The observed hysteresis was maximised by slowly increasing the sweep range until the measured

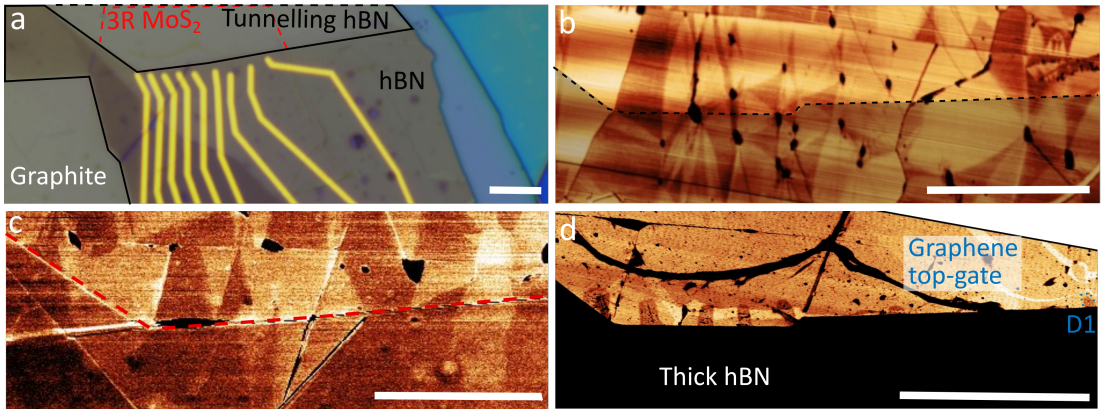

Fig. 6.27: **Sample 2: using SPM to design 3R-type twisted bilayer MoS_2 tunnel junction devices.** **a** Optical image of tunnelling junction sample. The metal contacts are connected to each individual graphene contact. **b** Contact mode lateral deflection image identifying the domain structure in sample 2. The thick hBN has been overlaid (black dashed line) for clarity. **c** PFM amplitude imaging of domain structure underneath a 3-layer tunnelling hBN (red dashed line is thick hBN edge). **d** Tapping mode topography image of the finished sample 2 where the graphene has been patterned into individual contacts. All scale bars are 5 μm.

current showed signs of instability (i.e. upper voltage limit before the sample becomes unstable). The optimum voltage range for this device was found to be -1.5 < V_{sd} < 2.25 (see Fig. 6.28). The equivalent out-of-plane displacement field is -0.47 < $\epsilon_0^{-1} D_*$ (V/nm) < 0.7 and was calculated using the dielectric constant of hBN ϵ_{hBN} = 3.5 [195] and dielectric constant of bilayer MoS_2 ϵ_{MoS_2} = 6.6 [195].

At the start of the voltage sweep (-1.5 V) MX′ stacking dominates the redistributed domain structure. From our KPFM measurements (see section 6.2), we know that MX′ has a higher electrostatic potential and therefore the redistributed domain structure favours the polarised 'up' state. As the voltage is dropped down to 0 V, there is negligible change to the domain structure. Upon increasing the voltage in the positive direction, the domain redistribution favours XM′ stacking which grows in size. The domain distribution under the tunnelling contact becomes polarised 'down'. When the voltage is swept in the backwards direction, the XM′ stacking persists and the tunnelling current does not follow the same trajectory (because more tunnelling paths are available). The same trend (larger voltage threshold/ band gap on the forward sweep compared to the backward sweep) is observed with consecutive voltage sweeps suggesting it is unlikely due to other common origins of hysteresis observed in electrical transport measurements. Hysteresis is typically seen as an offset between the

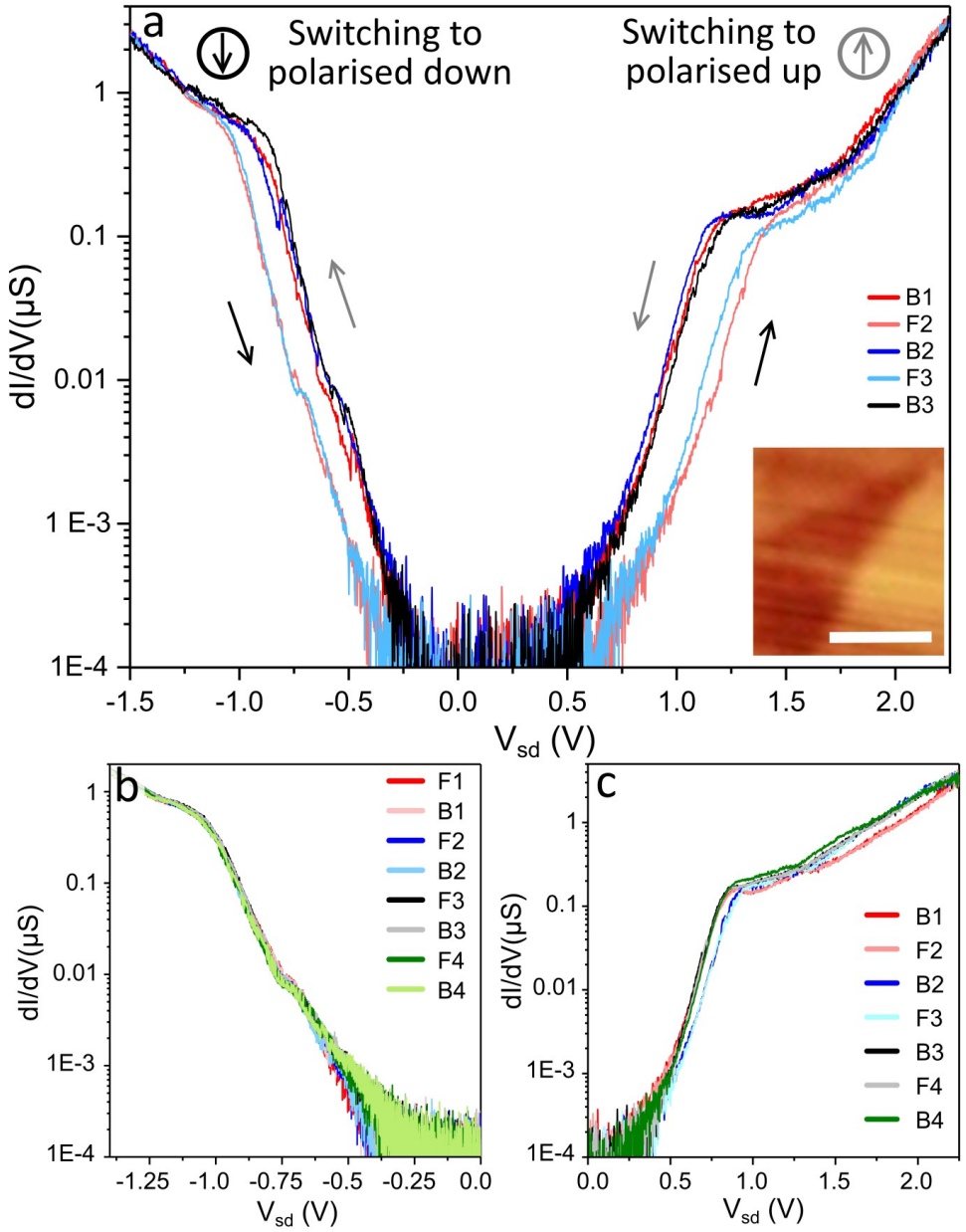

Fig. 6.28: **Hysteresis in differential conductance dI/dV between forward and reverse bias voltage sweeps for sample 2. a** dI/dV as a function of applied transverse electric field (V_{sd}). The forward and reverse voltage sweeps are indicated by the black arrows. As the voltage is swept from positive to negative, MX′ domains grow leading to a polarised up state. Upon reversal of sweep direction, the XM′ grow at the expense of MX′ leading to a polarised down state. The inset shows the tapping mode topography (extracted from Fig. 6.27b) map domain structure. Scale bar is 500 nm. No ferroelectric-induced hysteresis is observed when the forward and backward sweeps are only in the **b** negative or **c** positive direction.

forward and backward scans. Common origins of non-ferroelectric hysteresis include charge traps in the hBN dielectric [193], measurement instabilities due to high voltage sweeping [196] as well as hysteresis intrinsic to MoS_2 (i.e. charge traps due to sulfur vacancies) [197].

Ferroelectric-induced hysteresis was not observed when the voltage was swept in only one direction (i.e. negative or positive values only) (see Fig. 6.28b-c). In this case, there is no domain redistribution occurring, with the sample remaining either permanently polarised 'up' (see Fig. 6.28b) or polarised 'down' (see Fig. 6.28c). It is noted that some hysteresis can be observed in Fig. 6.28c, however, it is not seen between the forward and backward voltage sweeps indicating that is not related to ferroelectric-induced hysteresis.

For better understanding, the ferroelectric-induced hysteresis can be explained in terms of the voltage-dependent band alignment of the polarised 'up' and 'down' states in the MoS_2 bilayer. With zero applied voltage, the chemical potentials (μ) of the graphene and graphite electrodes are both aligned (the Fermi level) and are close to the K valleys in the conduction band of the top and bottom MoS_2 layers (see Fig. 6.29a). Due to the strong layer polarisation of the electronic states in the K valley of 3R MoS_2 these layers can be represented separately on the band diagram (see Fig. 6.29). From the previous KPFM studies (discussed in Section 6.2), we know the built-in energy potential difference between the polarised 'up' and polarised 'down' state is $\Delta V \sim$ 120 meV, resulting in a corresponding shift between the K conduction band edges of the top and bottom MoS_2 layers.

The application of a bias voltage leads to a potential drop distributed between the electrodes and a downward shift of the K valley in the top MoS_2 layer. Here, using the equation $D = \epsilon_o V \epsilon_r / h$, we know that ~ 60 % of the total potential drops between the electrodes occurs in the hBN tunnelling barrier and ~ 40 % of the potential drop occurs between the top MoS_2 layer and graphite. Due to the exponential decay of the tunnelling rate with distance, direct tunnelling from the graphene source to the graphite drain is negligible if states in the MoS_2 become available for tunnelling. This, however, does not occur until the top MoS_2 K point enters the bias window, at which point a finite current starts flowing through the device. This onset, however, is different depending on the polarisation of the MoS_2 ferroelectric state. We first consider the case when graphite is grounded and a positive potential (negative bias) is applied to graphene. When the system is weakly biased, the K valley edge of the top layer in the polarised

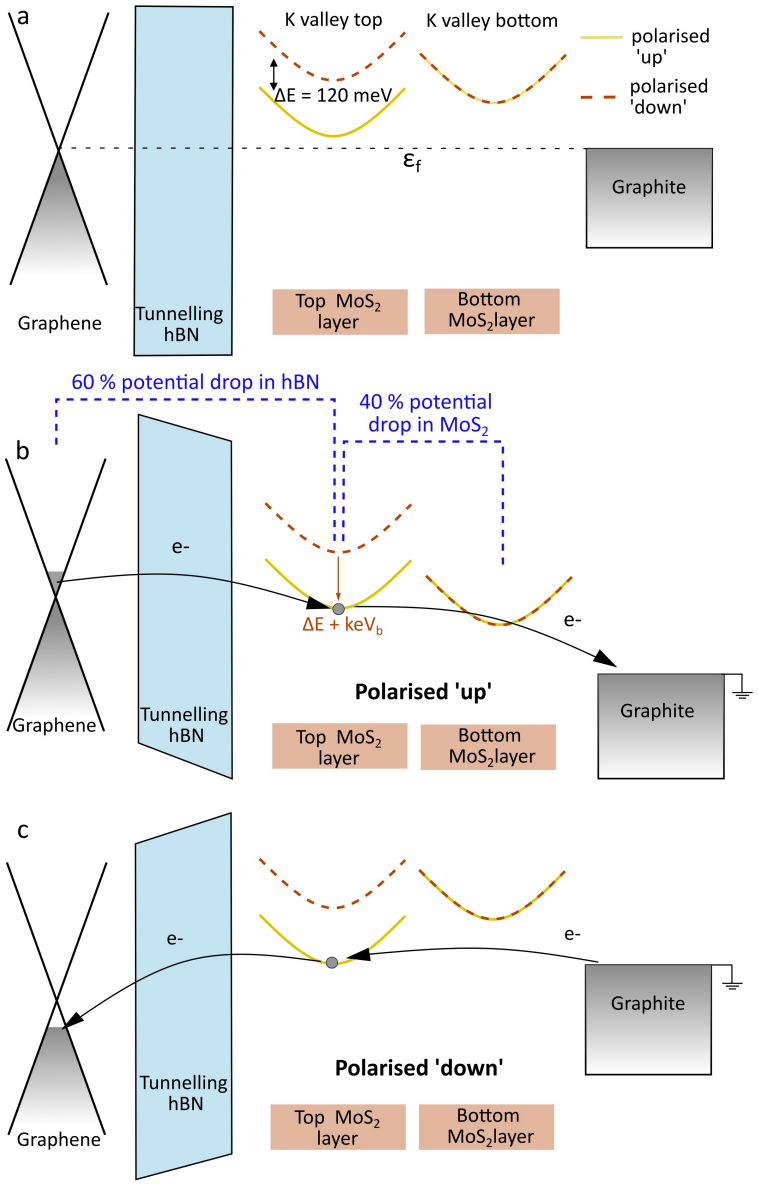

Fig. 6.29: **Schematic of the band-alignment in 3R-type twisted bilayer MoS_2 tunnelling devices. a** Electronic band alignment when no transverse electric field is applied. The graphene and graphite electrodes are aligned at the Fermi level (ϵ_f). **b** Upon application of a negative electric field, the K valley in the bottom MoS_2 layer shifts downwards leading to a polarised 'up' state. **c** Upon application of a positive electric field, the K valley in the top layer shifts downwards leading to a polarised 'down' state.

'up' state is in close alignment with the chemical potential of the graphene electrode and therefore electrons will tunnel through MoS_2 in the regions of the sample which are polarised 'up'. Note that for the 'down' state, a larger positive potential is required to enable such tunnelling (see Fig. 6.29b).

When a negative potential is applied, the K valley edge of the top layer in the polarised 'up' state is in close alignment to the chemical potential of the graphite electrode. Again, tunnelling will occur through the polarised 'up' state (see Fig. 6.29c). When a strongly negative potential is applied, a further downward shift of the K valley brings the polarised 'down' state in close alignment with the Fermi energy increasing the number of electron tunnelling paths. At this point, the polarised state becomes 'switched'. The polarised 'down' state persists until the backwards sweep reaches a strongly positive potential.

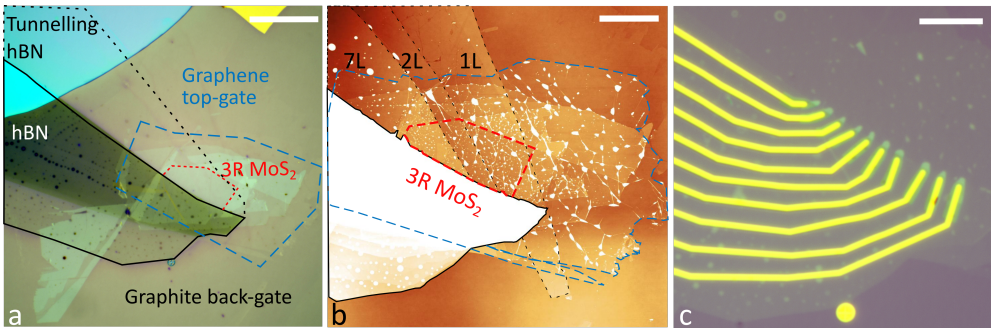

Fig. 6.30: **Sample three: 3R-type twisted bilayer MoS_2 tunnelling junction with multi-layer hBN tunnelling barrier.** **a** Optical image of the tunnelling junction heterostructure (scale bar = 20 μm) and corresponding **b** tapping mode AFM topography image (scale bar = 10 μm) where coloured dashed lines correspond to the outline of each vdWs crystal in the heterostructure. **c** Optical image of the finished sample 3 with etched individual tunnelling devices at the end of every metal contact. Scale bar is 25 μm.

Sample 1 (see Fig. 6.25) and sample 2 (see Fig. 6.27) were fabricated prior to the *in-situ* SEM which revealed a optimal domain length dependence for achieving a sufficient domain redistribution at an experimentally accessible voltage range. Sample three was designed with the intention of comparing the tunnelling characteristics of varying domain sizes. For sample 3, a hBN tunnelling barrier with three different layer thickness's (hBN thickness's are 7, 2 and 1 layers due to naturally occurring step edges) was used to allow for analysis of the tunnelling barrier thickness dependence on the measured tunnelling current (see Fig. 6.30b). For domain mapping before and after hBN encapsulation, tapping mode topography imaging was acquired with a conductive

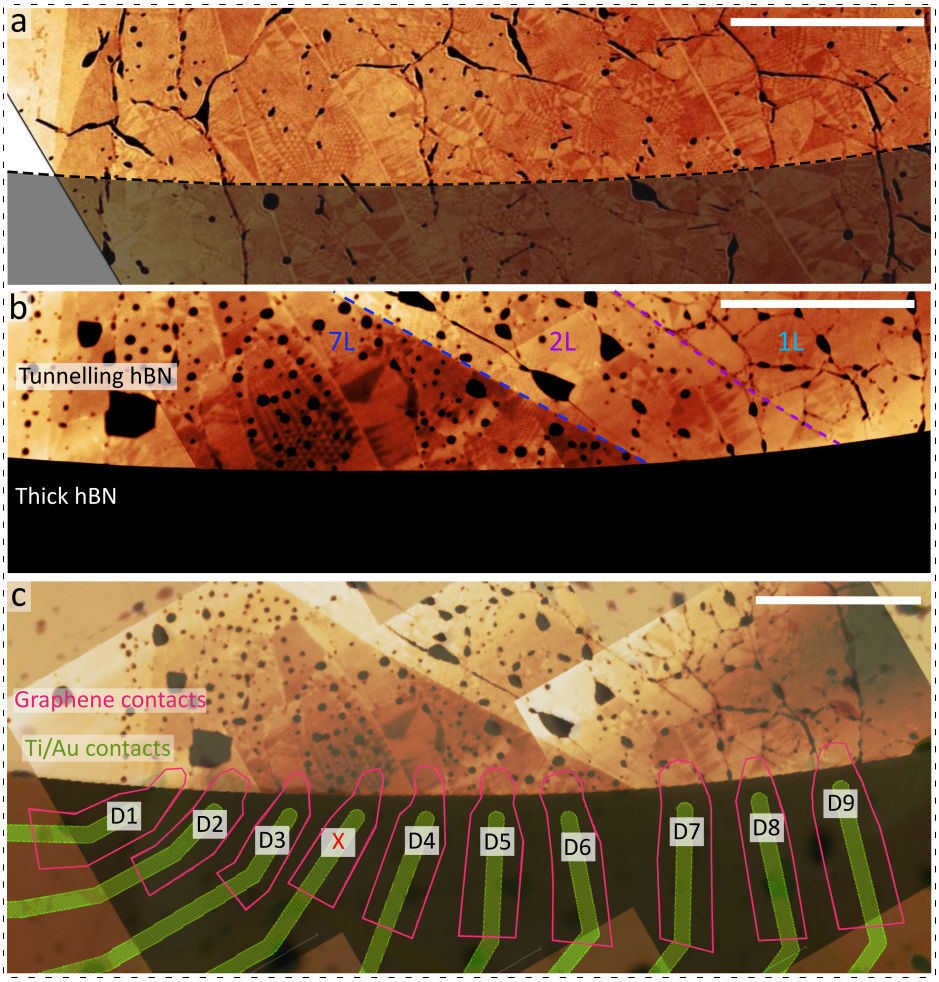

Fig. 6.31: **Sample 3: using SPM to design 3R-type twisted bilayer MoS_2 tunnel junction devices (see Fig 6.30).** Tapping mode topography image (using a conductive probe) of a twisted 3R-type bilayer MoS_2 **a** identifying regions of interest and **b** checking domain structure after transfer of the thick and thin tunnelling hBN. **c** AFM image of domain structure (same as **b**) overlaid with Layout Editor design of the top graphene contacts. All scale bars are 5 μm.

probe. With this imaging mode, the domains are more clearly resolved compared to post-encapsulation mapping acquired using EFM (see Fig. 6.25) and PFM (see Fig. 6.27). A key difference between sample 3 and the previous two samples is that during the final fabrication step, the etching duration was increased such that the underlying hBN and MoS_2 were etched as well as the top graphene contact. Here, the aim was to migitate possible interaction between devices and the surrounding unbiased bilayer. Here, it was assumed that only the regions in close proximity to the graphene contact could be subjected to domain redistribution.

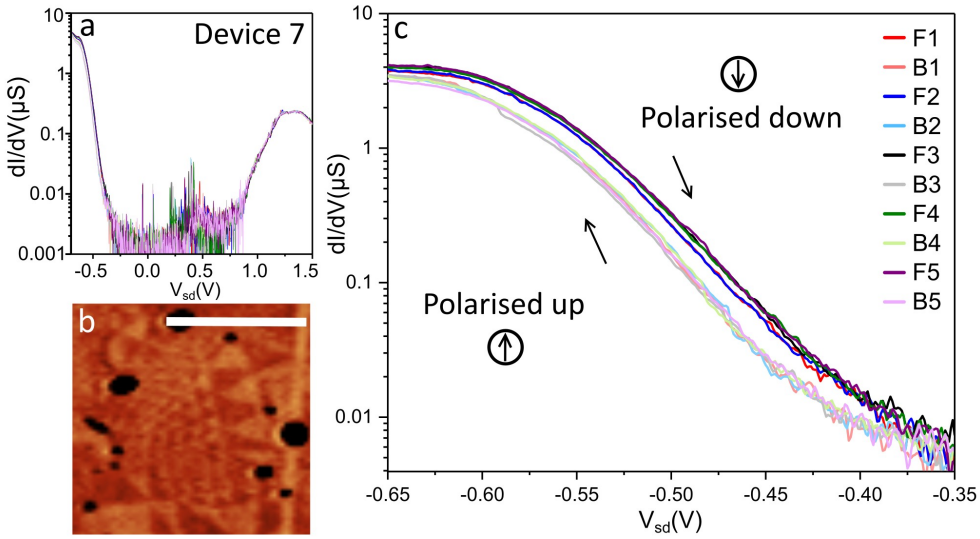

Fig. 6.32: **Hysteresis in differential conductance dI/dV for sample 3 device 7 with two layer hBN tunnelling barrier. a** dI/dV as a function of V_{sd} performed at 1.5 K. **b** Tapping mode topography image extracted from Fig. 6.31a of the domain structure under the top graphene electrode. Scale bar is 1 μm. **c** A zoomed in region of **a** where hysteresis was only observed when negative V_{sd} was applied. The black arrows indication the voltage sweep direction.

Devices labelled D1-D6 with a hBN tunnelling barrier thickness of 7 layers (see Fig. 6.31) were found to be too resistive during bias voltage sweeps i.e. the tunnelling current was only observed at relatively high biases beyond the point where the switching was expected. Device 9, with a monolayer hBN barrier, did show signs of hysteresis but was not indicative of ferroelectric behaviour and therefore only devices 7 and 8 are discussed.

Devices 7 and 8, with a 2-layer hBN tunnelling barrier, did show signs of ferroelectric-induced hysteresis (see Figs. 6.32 and 6.33) though not to the same extent as sample 2 (see Fig. 6.30). In Fig. 6.32a, the maximum voltage range achieved for device seven was - 0.8 < V_{sd} < 2. Beyond this, the tunnelling current through the

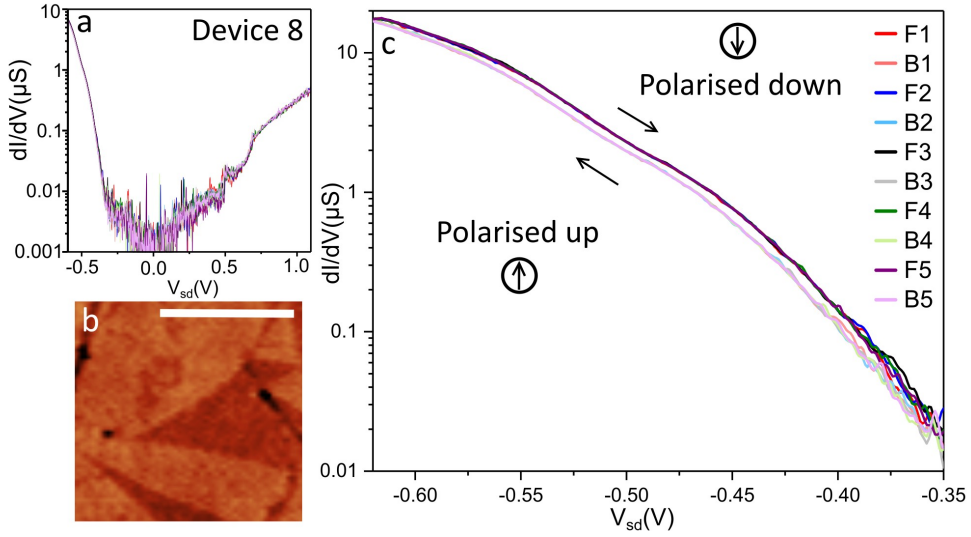

Fig. 6.33: **Hysteresis in differential conductance dI/dV for sample 3 device 8 with two layer hBN tunnelling barrier. a** dI/dV as a function of V_{sd} performed at 1.5 K. **b** Tapping mode topography image extracted from Fig. 6.31a of the domain structure under the top graphene electrode. Scale bar is 1 μm. **c** A zoomed in region of **a** where hysteresis was only observed when negative V_{sd} was applied. The black arrows indication the voltage sweep direction.

device was too high, causing permanent damage observed as a decay in the current over time. The corresponding out-of-plane displacement field due to applied bias is - 0.31 < $\epsilon_0^{-1} D_8$ (V/nm) < 0.79. The onset of tunnelling occurs at lower voltage thresholds on the negative side compared to the positive side (as described by the theoretical model in Fig. 6.29). The domain periodicity within the tunnelling junction was in the range of $\sim$ 50 to 400 nm (see Fig. 6.32). The length dependent displacement threshold ($\epsilon_0^{-1} D_*(\ell)$) discussed in Section 6.3 suggests the domain redistribution was not maximised in this voltage range, particularly for negative bias. Additionally, the significant instability and the higher tunnelling current threshold ($\sim$1 V) on the positive side may account for the lack of observed hysteresis in the positive direction.

In Fig. 6.33a, the maximum voltage range achieved before the onset of voltage instability (- 0.62 < V_{sd} < 1.48 corresponding to the tunnelling cuurent $\sim \pm$ 1x10^{-3} nA) was notably lower than the previous device (see Fig. 6.32a). The preliminary SPM characterisation (see Fig. 6.33b) highlights that, similar to sample 2 (see Fig. 6.28 inset), there were only two domain walls within the tunnel junction. For both sweep directions, the onset of conductivity is observed at the same V_{sd} value which suggests that the limited bias range did not result in sufficient domain redistribution and both domains are still present. However, the hysteresis is still present once the

current is detectable, suggesting that the relative area of MX′ and XM′ is different for forward and backward sweeps.

Although ferroelectric-induced hysteresis has been demonstrated in our tunnelling devices, it was significantly sample dependent. This, in part, was due to the complexity of the sample fabrication procedure limiting the number of samples that could be made in such a time scale. A high voltage range is essential to maximise ferroelectric switching and a measurable current is required to be able to detect the switching. This cannot always be experimentally achieved due to a dependence on a number of sample-specific parameters. The origins of the discrepancies in ferroelectric behaviour have been summarised;

Macroscopic pinning: The SEM study discussed in section 6.3 highlighted a clear dependence on macroscopic pinning due to crack/ folds/ bubbles that were introduced in the fabrication process. It is clear in Fig. 6.19 that some of the domains within the twisted bilayer structure remained unchanged even at high applied electric field. Unfortunately, it is not easy to predict the effect of macroscopic pinning with SPM imaging alone. For sample three, the additional device etching step may have introduced more pinning at the edges of the device leading to a obstruction of the domain redistribution.

Twist angle disorder: It is important to note that the measured hysteretic response is the average signal across the whole tunnelling junction, therefore, domains of different sizes will redistribute by different amounts at a given bias voltage. This can be limiting if the domain length is below $\ell \sim 400$ nm ($\epsilon_0^{-1} D_*(\ell) \approx \frac{400V}{\ell}$).

Band gap tuning: The application of an external electric field on a bilayer TMD (such as MoS_2) can lead to significant band gap tuning. Strong electric fields (2-3 V/nm) alter the position of the conduction band minima and valence band maxima such that the band gap eventually closes between them [198]. Our simple band diagram does not take this into account.

6.4.3 Ferroelectric Devices With Hall Bar Geometry

For completeness, we studied ferroelectric behaviour in 3R-type twisted MoS_2 ferroelectric devices (twisted mono- and trilayers) fabricated with a Hall bar geometry.

This study demonstrated clear repeatability and further validates the observed hysteresis in our tunnelling devices. The study was performed in collaboration with Dr Shiugang Xu and Dr Zefei Wu who fabricated the devices and Dr Shubhadeep Bhattacharjee who performed electrical transport measurements and was part of a wider collaborative project entitled "interfacial ferroelectricity in marginally twisted 2D semiconductors" [183]. Here, the twisted MoS_2 layers were encapsulated with hBN on both sides with a top gate (metal deposited only on the main channel) and a global back-gate (silicon wafer). Due to high source-drain resistance (MΩ) at room temperature, only two-terminal measurements were performed. The global back-gate (V_b) was used to increase the charge carrier concentration ($\sim$ 0.1 V/nm needed to induce mobile carriers) in the channel and the contact regions while the top gate (V_t) controlled only the channel region and was used to measure the hysteretic behaviour.

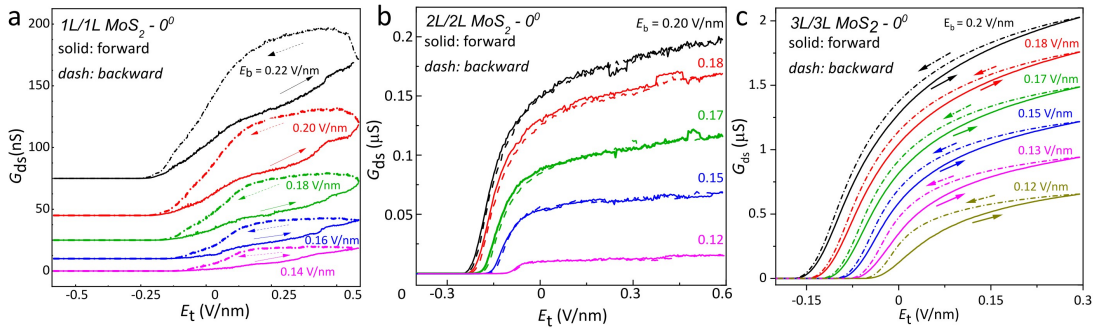

Fig. 6.34: **Hysteretic behaviour in electrical conductivity (G_{ds}) of 3R-type twisted mono- and tri- layer MoS_2 and 2H-type bilayer-bilayer MoS_2.** G_{ds} as a function of top-gate displacement field (V_t) for different backgate displacement fields (V_b) in **a** 3R-type twisted bilayer MoS_2, **b** 2H-type twisted double-bilayer MoS_2 and **c** 3R-type twisted trilayer MoS_2. All measurements were performed at room temperature.

By sweeping V_t, both the carrier concentration and out-of-plane electric field were controlled. Clear hysteresis was observed in the samples with 3R-type configuration (see Fig. 6.34a and c) where the sample-averaged carrier densities are shifted for the forwards and backwards sweep. This is consistent with the previously observed built-in potential (see Section 6.2) in the oppositely polarised XM′ and MX′ stacking domains. The forward and backward bias sweeps follow the same trend as our tunnelling devices where the built-in potential of the polarised 'up' states act against the forward sweep but adds to it in the backwards sweeps due to the redistribution of domains in favour of the polarised 'down' states that persist until a strongly negative out-of-plane field is applied in the backwards sweep. As expected, this was not observed in the reference

2H-type device (see Fig. 6.34b).

6.5 Summary

In this section, C-AFM revealed layer polarised wavefunctions in 3R-type reconstructed bilayers of TMDs and piezoelectric textures in 2H-type configuration. Although it wasn't directly demonstrated in this work, the piezoelectric textures observed in C-AFM are expected to lead to spatially confined quantum dot-like states of positive (MM′) and negative (XX′) charge which should be observable in low-temperature (1.5 K) measurements.

Next, KPFM studies revealed an out-of-plane potential difference between oppositely polarised XM′ and MX′ stacking configurations. This was a key indicator of out-of-plane ferroelectricity and prompted further investigation into the possibility of ferroelectric switching devices for memory applications. An SEM equipped with an electric feed-through was then employed to elucidate the mechanism of ferroelectric switching. With this technique, we were able to observe domain redistribution as a function of applied out-of-plane displacement field. DFT calculations were used to provide a domain length dependence on out-of-plane displacement field required to experimentally achieve optimal switching behaviour.

Finally, electrical SPM techniques were used to aid the fabrication of prototype ferroelectric devices with a tunnelling junction geometry. Electrical transport measurements were performed at low temperature to demonstrate the ferroelectric switching behaviour in 3R-type twisted bilayer MoS_2. This data was presented alongside ferroelectric devices prepared with a Hall bar geometry that were studied as part of a larger collaboration.

Chapter7

Final Conclusions and Future Outlooks

The work presented in this thesis has revealed lattice reconstruction in twisted bilayer TMDs at the atomic scale which was then correlated with their electrical properties. This work provides an excellent fundamental understanding of this materials system, which previously has been lacking in the field.

The room temperature out-of-plane polarisation revealed by KPFM measurements prompted further studies to investigate the potential for ferroelectric-based memory device applications utilising 3R-polytype configurations. The preliminary data acquired from the ferroelectric tunnelling devices was promising but will require a more in-depth study to demonstrate the true potential of twisted bilayer TMD ferroelectric switches for memory storage applications.

Firstly, the tunnelling junction geometry needs further improvement and the ferroelectric switching ability was sample dependent. The Hall bar/FET geometry (as shown in Fig. 6.34) demonstrated significantly better repeatability even for room temperature electrical transport measurements. Unfortunately, the domain structure of these samples was not pre-mapped using scanning probe microscopy meaning that we are not able to correlate the specific domain layout and its switching with the magnitude of hysteresis in conductivity. Repeating these measurements in the SEM for *in-situ* electrical transport measurements would provide better clarification of the domain switching ability. This would be further aided by real-time videos that could elucidate the switching time for domain redistribution.

It is clear from the data acquired from this project that the fabrication techniques employed require further optimisation. Firstly, we must improve device uniformity (reducing twist angle disorder) and reduce fabrication-induced contamination. A

significant hindrance to the observed ferroelectric switching was the macroscopic pinning of domain walls due to bubbles and folds. Fabricating these devices in an ultra high vacuum (UHV) chamber (pressure of $< 10^{-10}$ mbar), such as the UHV fabrication suite developed here at the University of Manchester by Prof Roman Gorbachev, would be the next logical step in the optimisation of this materials system. Fabricating in UHV would be very beneficial because the current state-of-the art, utilising gloveboxes with an inert (argon or nitrogen) environment, does not solve the issue of hydrocarbons present in the air. Additionally, sample annealing (a common method of reducing contamination) of TMDs is limited to $\sim 200^{\circ}$ to prevent damage. This means that some residual surface contamination is left behind during conventional fabrication processes. This new method of UHV fabrication has the potential to provide an environment to prepare devices in a polymer-free (silicon nitride aided with metal adhesion layers are used instead of polymer and tape) and hydrocarbon-free environment. This would be the best way to minimise possible macroscopic pinning as well as provide ultra clean interfaces which currently limit the reproducibility of our ferroelectric switches. It is expected that the UHV fabrication method would also help to minimise twist-angle disorder commonly observed in moiré superlattices.

Finally, it would be particularly interesting to explore other possible device applications that can exploit both the optical and electronic properties of reconstructed lattices of TMDs. For example, there is great potential for semiconducting devices with multi-functionalities such as strain/photo sensing and energy harvesting/photovoltaic s which can be combined with the memory functionality demonstrated in this work.

Bibliography

1. Novoselov, K. S., Geim, A. K., Morozov, S. V., Jiang, D., Zhang, Y., Dubonos, S. V., Grigorieva, I. V. & Firsov, A. A. Electric Field Effect in Atomically Thin Carbon Films. *Science* **306,** 666–669 (2004).

2. Peierls, R. Quelques propriétés typiques des corps solides. fre. *Annales de l'institut Henri Poincaré* **5,** 177–222 (1935).

3. Landau, L. D. On the theory of phase transitions. II. *Zh. Eksp. Teor. Fiz.* **11,** 627 (1937).

4. Meyer, J. C., Geim, A. K., Katsnelson, M. I., Novoselov, K. S., Booth, T. J. & Roth, S. The structure of suspended graphene sheets. *Nature* **446,** 60–63 (2007).

5. Dirac, P. A. M. & Bohr, N. H. D. The quantum theory of the emission and absorption of radiation. *Proceedings of the Royal Society of London. Series A, Containing Papers of a Mathematical and Physical Character* **114,** 243–265 (1927).

6. Fermi, E. Quantum Theory of Radiation. *Rev. Mod. Phys.* **4,** 87–132 (1932).

7. Splendiani, A., Sun, L., Zhang, Y., Li, T., Kim, J., Chim, C. Y., Galli, G. & Wang, F. Emerging photoluminescence in monolayer MoS2. *Nano Letters* **10,** 1271–1275 (2010).

8. Mak, K. F., Lee, C., Hone, J., Shan, J. & Heinz, T. F. Atomically thin MoS2: A new direct-gap semiconductor. *Physical Review Letters* **105,** 2–5 (2010).

9. Radisavljevic, B., Radenovic, A., Brivio, J., Giacometti, V. & Kis, A. Single layer MoS2 transistors. *Nature Nanotechnology* **6,** 147–150 (2011).

10. Britnell, L., Ribeiro, R. M., Eckmann, A., Jalil, R., Belle, B. D., Mishchenko, A., Kim, Y. J., Gorbachev, R. V., Georgiou, T., Morozov, S. V., Grigorenko, A. N., Geim, A. K., Casiraghi, C., Neto, A. H. C. & Novoselov, K. S. Strong Light-Matter Interactions Thin Films. *Science* **340,** 1311–1314 (2013).

11. Kappera, R., Voiry, D., Yalcin, S. E., Branch, B., Gupta, G., Mohite, A. D. & Chhowalla, M. Phase-engineered low-resistance contacts for ultrathin MoS2 transistors. *Nature Materials* **13,** 1128–1134 (2014).

12. Yoo, H., Engelke, R., Carr, S., Fang, S., Zhang, K., Cazeaux, P., Sung, S. H., Hovden, R., Tsen, A. W., Taniguchi, T., Watanabe, K., Yi, G. C., Kim, M., Luskin, M., Tadmor, E. B., Kaxiras, E. & Kim, P. Atomic and electronic reconstruction at the van der Waals interface in twisted bilayer graphene. *Nature Materials* **18,** 448–453 (2019).

13. Das, S., Chen, H. Y., Penumatcha, A. V. & Appenzeller, J. High performance multilayer MoS2 transistors with scandium contacts. *Nano Letters* **13,** 100–105 (2013).

14. Fang, H., Chuang, S., Chang, T. C., Takei, K., Takahashi, T. & Javey, A. High-performance single layered WSe 2 p-FETs with chemically doped contacts. *Nano Letters* **12,** 3788–3792 (2012).

15. Kittel, C. *Introduction to Solid State Physics* **12,** 3299 (1957).

16. Katsnelson, M. I. & Katsnelson, M. I. The electronic structure of ideal graphene. *Graphene* **0,** 1–22 (2012).

17. Charlier, J. C., Gonze, X. & Michenaud, J. P. Graphite interplanar bonding: Electronic delocalization and van der waals interaction. *Epl* **28,** 403–408 (1994).

18. Castro Neto, A. H., Guinea, F., Peres, N. M. R., Novoselov, K. S. & Geim, A. K. The electronic properties of graphene. *Rev. Mod. Phys.* **81,** 109–162 (2009).

19. Novoselov, K. S., Jiang, D., Schedin, F., Booth, T. J., Khotkevich, V. V., Morozov, S. V. & Geim, A. K. Two-dimensional atomic crystals. *Proceedings of the National Academy of Sciences* **102,** 10451–10453 (2005).

20. Zhang, Y., Brar, V. W., Girit, C., Zettl, A. & Crommie, M. F. Origin of spatial charge inhomogeneity in graphene. *Nature Physics* **5,** 722–726 (2009).

21. Martin, J., Akerman, N., Ulbricht, G., Lohmann, T., Smet, J. H., Von Klitzing, K. & Yacoby, A. Observation of electron-hole puddles in graphene using a scanning single-electron transistor. *Nature Physics* **4,** 144–148 (2008).

22. Chen, J. H., Jang, C., Adam, S., Fuhrer, M. S., Williams, E. D. & Ishigami, M. Charged-impurity scattering in graphene. *Nature Physics* **4,** 377–381 (2008).

23. Watanabe, K., Taniguchi, T. & Kanda, H. Direct-bandgap properties and evidence for ultraviolet lasing of hexagonal boron nitride single crystal. *Nature Materials* **3,** 404–409 (2004).

24. Dean, C. R., Young, A. F., Meric, I., Lee, C., Wang, L., Sorgenfrei, S., Watanabe, K., Taniguchi, T., Kim, P., Shepard, K. L. & Hone, J. Boron nitride substrates for high-quality graphene electronics. *Nature Nanotechnology,* 1–5 (2010).

25. Xue, J., Sanchez-Yamagishi, J., Bulmash, D., Jacquod, P., Deshpande, A., Watanabe, K., Taniguchi, T., Jarillo-Herrero, P. & Leroy, B. J. Scanning tunnelling microscopy and spectroscopy of ultra-flat graphene on hexagonal boron nitride. *Nature Materials* **10,** 282–285 (2011).

26. Britnell, L., Gorbachev, R. V., Jalil, R., Belle, B. D., Schedin, F., Katsnelson, M. I., Eaves, L., Morozov, S. V., Mayorov, A. S., Peres, N. M., Castro Neto, A. H., Leist, J., Geim, A. K., Ponomarenko, L. A. & Novoselov, K. S. Electron tunneling through ultrathin boron nitride crystalline barriers. *Nano Letters* **12,** 1707–1710 (2012).

27. PEASE, R. S. Crystal Structure of Boron Nitride. *Nature* **165,** 722–723 (1950).

28. Constantinescu, G., Kuc, A. & Heine, T. Stacking in bulk and bilayer hexagonal boron nitride. *Physical Review Letters* **111,** 1–5 (2013).

29. Wilson, J. A. & Yoffe, A. D. The transition metal dichalcogenides discussion and interpretation of the observed optical, electrical and structural properties. *Advances in Physics* **18,** 193–335 (1969).

30. Sipos, B., Kusmartseva, A. F., Akrap, A., Berger, H., Forró, L. & Tutǐ, E. From Mott state to superconductivity in-1T-TaS2. *Nature Materials* **7,** 960–965 (2008).

31. Tsen, A. W., Hovden, R., Wang, D., Kim, Y. D., Spoth, K. A., Liu, Y., Lu, W., Sun, Y., Hone, J. C., Kourkoutis, L. F., Kim, P. & Pasupathy, A. N. Structure and control of charge density waves in two-dimensional 1T-TaS2. *Proceedings of the National Academy of Sciences of the United States of America* **112,** 15054–15059 (2015).

32. Chhowalla, M., Shin, H. S., Eda, G., Li, L. J., Loh, K. P. & Zhang, H. The chemistry of two-dimensional layered transition metal dichalcogenide nanosheets. *Nature Chemistry* **5,** 263–275 (2013).

33. Moser, J. & Lévy, F. Random stacking in MoS2-x sputtered thin films. *Thin Solid Films* **240,** 56–59 (1994).

34. Zhao, W., Ribeiro, R. M. & Eda, G. Electronic structure and optical signatures of semiconducting transition metal dichalcogenide nanosheets. *Accounts of Chemical Research* **48,** 91–99 (2015).

35. Chu, R. L., Liu, G. B., Yao, W., Xu, X., Xiao, D. & Zhang, C. Spin-orbit-coupled quantum wires and Majorana fermions on zigzag edges of monolayer transition-metal dichalcogenides. *Physical Review B - Condensed Matter and Materials Physics* **89** (2014).

36. Britnell, L., Ribeiro, R. M., Eckmann, A., Jalil, R., Belle, B. D., Mishchenko, A., Kim, Y., Gorbachev, R. V., Georgiou, T., Morozov, S. V., Grigorenko, A. N., Geim, A. K., Casiraghi, C., Neto, A. H. C. & Novoselov, K. S. Strong Light-Matter Interactions Thin Films. **340,** 1311–1315 (2013).

37. Wu, Z., Xu, S., Lu, H., Khamoshi, A., Liu, G. B., Han, T., Wu, Y., Lin, J., Long, G., He, Y., Cai, Y., Yao, Y., Zhang, F. & Wang, N. Even-odd layer-dependent magnetotransport of high-mobility Q-valley electrons in transition metal disulfides. *Nature Communications* **7,** 1–8 (2016).

38. Roy, T., Tosun, M., Kang, J. S., Sachid, A. B., Desai, S. B., Hettick, M., Hu, C. C. & Javey, A. Field-effect transistors built from all two-dimensional material components. *ACS Nano* **8,** 6259–6264 (2014).

39. Chuang, H. J., Chamlagain, B., Koehler, M., Perera, M. M., Yan, J., Mandrus, D., Tománek, D. & Zhou, Z. Low-Resistance 2D/2D Ohmic Contacts: A Universal Approach to High-Performance WSe2, MoS2, and MoSe2 Transistors. *Nano Letters* **16,** 1896–1902 (2016).

40. Hill, H. M., Rigosi, A. F., Rim, K. T., Flynn, G. W. & Heinz, T. F. Band Alignment in MoS2/WS2 Transition Metal Dichalcogenide Heterostructures Probed by Scanning Tunneling Microscopy and Spectroscopy. *Nano Letters* **16,** 4831–4837 (2016).

41. Kang, J., Tongay, S., Zhou, J., Li, J. & Wu, J. Band offsets and heterostructures of two-dimensional semiconductors. *Applied Physics Letters* **102** (2013).

42. Rigosi, A. F., Hill, H. M., Li, Y., Chernikov, A. & Heinz, T. F. Probing Interlayer Interactions in Transition Metal Dichalcogenide Heterostructures by Optical Spectroscopy: MoS2/WS2 and MoSe2/WSe2. *Nano Letters* **15,** 5033–5038 (2015).

43. Rivera, P., Schaibley, J. R., Jones, A. M., Ross, J. S., Wu, S., Aivazian, G., Klement, P., Seyler, K., Clark, G., Ghimire, N. J., Yan, J., Mandrus, D. G., Yao, W. & Xu, X. Observation of long-lived interlayer excitons in monolayer MoSe 2-WSe 2 heterostructures. *Nature Communications* **6,** 4–9 (2015).

44. Cao, Y., Fatemi, V., Demir, A., Fang, S., Tomarken, S. L., Luo, J. Y., Sanchez-Yamagishi, J. D., Watanabe, K., Taniguchi, T., Kaxiras, E., Ashoori, R. C. & Jarillo-Herrero, P. Correlated insulator behaviour at half-filling in magic-angle graphene superlattices. *Nature* **556,** 80–84 (2018).

45. Cao, Y., Fatemi, V., Fang, S., Watanabe, K., Taniguchi, T., Kaxiras, E. & Jarillo-Herrero, P. Unconventional superconductivity in magic-angle graphene superlattices. *Nature* **556,** 43–50 (2018).

46. Chen, G., Jiang, L., Wu, S., Lyu, B., Li, H., Chittari, B. L., Watanabe, K., Taniguchi, T., Shi, Z., Jung, J., Zhang, Y. & Wang, F. Evidence of a gate-tunable Mott insulator in a trilayer graphene moiré superlattice. *Nature Physics* **15,** 237–241 (2019).

47. Xhie, J., Sattler, K., Ge, M. & Venkateswaran, N. Giant and supergiant lattices on graphite. *Physical Review B* **47,** 15835–15841 (1993).

48. Beyer, H., Muller, M. & Schimmel, T. Monolayers of graphite rotated by a defined angle, Hexagonal superstructures by STM. *Applied Physics A: Materials Science and Processing* **68,** 163–166 (1999).

49. Yankowitz, M., Xue, J., Cormode, D., Sanchez-Yamagishi, J. D., Watanabe, K., Taniguchi, T., Jarillo-Herrero, P., Jacquod, P. & Leroy, B. J. Emergence of superlattice Dirac points in graphene on hexagonal boron nitride. *Nature Physics* **8,** 382–386 (2012).

50. Bronsema, K. D., De Boer, J. L. & Jellinek, F. On the structure of molybdenum diselenide and disulfide. *ZAAC - Journal of Inorganic and General Chemistry* **540,** 15–17 (1986).

51. Schutte, W. J., De Boer, J. L. & Jellinek, F. Crystal structures of tungsten disulfide and diselenide. *Journal of Solid State Chemistry* **70,** 207–209 (1987).

52. Baskin, Y. & Meyer, L. Lattice Constants of Graphite at Low Temperatures. *Phys. Rev.* **100,** 544 (1955).

53. Paszkowicz, W., Pelka, J. B., Knapp, M., Szyszko, T. & Podsiadlo, S. Lattice parameters and anisotropic thermal expansion of hexagonal boron nitride in the 10-297.5 K temperature range. *Applied Physics A: Materials Science and Processing* **75,** 431–435 (2002).

54. Davies, A., Albar, J. D., Summerfield, A., Thomas, J. C., Cheng, T. S., Korolkov, V. V., Stapleton, E., Wrigley, J., Goodey, N. L., Mellor, C. J., Khlobystov, A. N., Watanabe, K., Taniguchi, T., Foxon, C. T., Eaves, L., Novikov, S. V. & Beton, P. H. Lattice-Matched Epitaxial Graphene Grown on Boron Nitride. *Nano Letters* **18,** 498–504 (2018).

55. Zhu, M., Ghazaryan, D., Son, S. K., Woods, C. R., Misra, A., He, L., Taniguchi, T., Watanabe, K., Novoselov, K. S., Cao, Y. & Mishchenko, A. Stacking transition in bilayer graphene caused by thermally activated rotation. *2D Materials* **4** (2017).

56. Ribeiro-Palau, R., Zhang, C., Watanabe, K., Taniguchi, T., Hone, J. & Dean, C. R. Twistable electronics with dynamically rotatable heterostructures. *Science* **361,** 690–693 (2018).

57. Ponomarenko, L. A., Gorbachev, R. V., Yu, G. L., Elias, D. C., Jalil, R., Patel, A. A., Mishchenko, A., Mayorov, A. S., Woods, C. R., Wallbank, J. R., Mucha-Kruczynski, M., Piot, B. A., Potemski, M., Grigorieva, I. V., Novoselov, K. S., Guinea, F., Fal'Ko, V. I. & Geim, A. K. Cloning of Dirac fermions in graphene superlattices. *Nature* **497,** 594–597 (2013).

58. Dean, C. R., Wang, L., Maher, P., Forsythe, C., Ghahari, F., Gao, Y., Katoch, J., Ishigami, M., Moon, P., Koshino, M., Taniguchi, T., Watanabe, K., Shepard, K. L., Hone, J. & Kim, P. Hofstadter's butterfly in moire superlattices: A fractal quantum Hall effect. *Nature,* 1–10 (2012).

59. Hunt, B., Sanchez-Yamagishi, J. D., Young, A. F., Yankowitz, M., LeRoy, B. J., Watanabe, K., Taniguchi, T., Moon, P., Koshino, M., Jarillo-Herrero, P. & Ashoori, R. C. Massive dirac fermions and hofstadter butterfly in a van der Waals heterostructure. *Science* **340,** 1427–1430 (2013).

60. Woods, C. R., Britnell, L., Eckmann, A., Ma, R. S., Lu, J. C., Guo, H. M., Lin, X., Yu, G. L., Cao, Y., Gorbachev, R. V., Kretinin, A. V., Park, J., Ponomarenko, L. A., Katsnelson, M. I., Gornostyrev, Y. N., Watanabe, K., Taniguchi, T., Casiraghi, C., Gao, H. J., Geim, A. K. & Novoselov, K. S. Commensurate-incommensurate transition in graphene on hexagonal boron nitride. *Nature Physics* **10,** 451–456 (2014).

61. Braun, O. M. & Kivshar, Y. *The Frenkel Kontorova Model* 1 **edition**, 472 (Springer-Verlag Berlin Heidelberg, 2004).

62. Dos Santos, J. M. B., Peres, N. M. R. & Castro Neto, A. H. Graphene Bilayer with a Twist: Electronic Structure. *Phys. Rev. Lett.* **99,** 256802 (2007).

63. Brihuega, I., Mallet, P., Gonzalez-Herrero, H., Trambly De Laissardiere, G., Ugeda, M. M., Magaud, L., Gomez-Rodriuez, J. M., Yndurain, F. & Veuillen, J. Y. Unraveling the intrinsic and robust nature of van hove singularities in twisted bilayer graphene by scanning tunneling microscopy and theoretical analysis. *Physical Review Letters* **109,** 1–5 (2012).

64. Bistritzer, R. & MacDonald, A. H. Moire bands in twisted double-layer graphene. *PNAS* **108,** 12233–12237 (2010).

65. Po, H. C., Zou, L., Vishwanath, A. & Senthil, T. Origin of Mott Insulating Behavior and Superconductivity in Twisted Bilayer Graphene. *Physical Review X* **8,** 1–33 (2018).

66. Pizarro, J. M., Calderón, M. J. & Bascones, E. The nature of correlations in the insulating states of twisted bilayer graphene. *Journal of Physics Communications* **3,** 35024 (2019).

67. Padhi, B., Setty, C. & Phillips, P. W. Doped Twisted Bilayer Graphene near Magic Angles : Proximity to Wigner Crystallisation, Not Mott Insulation. *Nano Letters* **18,** 6175–6180 (2018).

68. Peltonen, T. J., Ojajarvi, R. & Heikkila, T. T. Mean-field theory for superconductivity in twisted bilayer graphene. *Phys. Rev. B* **98,** 220504 (2018).

69. Kerelsky, A., McGilly, L. J., Kennes, D. M., Xian, L., Yankowitz, M., Chen, S., Watanabe, K., Taniguchi, T., Hone, J., Dean, C., Rubio, A. & Pasupathy, A. N. Maximized electron interactions at the magic angle in twisted bilayer graphene. *Nature* **572,** 95–100 (2019).

70. Xie, Y., Lian, B., Jäck, B., Liu, X., Chiu, C. L., Watanabe, K., Taniguchi, T., Bernevig, B. A. & Yazdani, A. Spectroscopic signatures of many-body correlations in magic-angle twisted bilayer graphene. *Nature* **572,** 101–105 (2019).

71. Jiang, Y., Lai, X., Watanabe, K., Taniguchi, T., Haule, K., Mao, J. & Andrei, E. Y. Charge order and broken rotational symmetry in magic-angle twisted bilayer graphene. *Nature* **573,** 91–95 (2019).

72. Choi, Y., Kemmer, J., Peng, Y., Thomson, A., Arora, H., Polski, R., Zhang, Y., Ren, H., Alicea, J., Refael, G., von Oppen, F., Watanabe, K., Taniguchi, T. & Nadj-Perge, S. Electronic correlations in twisted bilayer graphene near the magic angle. *Nature Physics* **15,** 1174–1180 (2019).

73. Huang, S., Kim, K., Efimkin, D. K., Lovorn, T., Taniguchi, T., Watanabe, K., Macdonald, A. H., Tutuc, E. & Leroy, B. J. Topologically Protected Helical States in Minimally Twisted Bilayer Graphene. *Physical Review Letters* **121,** 37702 (2018).

74. Nam, N. N. T. & Koshino, M. Lattice relaxation and energy band modulation in twisted bilayer graphene. *Phys. Rev. B* **96,** 75311 (2017).

75. Van Wijk, M. M., Schuring, A., Katsnelson, M. I. & Fasolino, A. Relaxation of moiré patterns for slightly misaligned identical lattices: Graphene on graphite. *2D Materials* **2** (2015).

76. Alden, J. S., Tsen, A. W., Huang, P. Y., Hovden, R., Brown, L., Park, J., Muller, D. A. & McEuen, P. L. Strain solitons and topological defects in bilayer graphene. *Proceedings of the National Academy of Sciences* **110,** 11256–11260 (2013).

77. San-Jose, P., Gorbachev, R. V., Geim, A. K., Novoselov, K. S. & Guinea, F. Stacking boundaries and transport in bilayer graphene. *Nano Letters* **14,** 2052–2057 (2014).

78. Huang, J., Akselrod, G. M., Ming, T., Kong, J. & Mikkelsen, M. H. Tailored Emission Spectrum of 2D Semiconductors Using Plasmonic Nanocavities. *ACS Photonics,* acsphotonics.7b01085 (2017).

79. Yuan, L., Zheng, B., Kunstmann, J., Brumme, T., Kuc, A. B., Ma, C., Deng, S., Blach, D., Pan, A. & Huang, L. Twist-angle-dependent interlayer exciton diffusion in WS2–WSe2 heterobilayers. *Nature Materials* (2020).

80. Yao, W., Xu, X., Liu, G.-B., Tang, J. & Yu, H. Moiré excitons: From programmable quantum emitter arrays to spin-orbit–coupled artificial lattices. *Science Advances* **3,** e1701696 (2017).

81. Van der Zande, A. M., Kunstmann, J., Hone, J. C., Chernikov, A., Huang, P. Y., Wang, L., Chenet, D. A., Berkelbach, T. C., Zhang, F., Hybertsen, M. S., You, Y., Reichman, D. R., Heinz, T. F., Zhang, X., Muller, D. A. & van der Zande, A. M. Tailoring the Electronic Structure in Bilayer Molybdenum Disulfide via Interlayer Twist. *Nano Letters* **14,** 3869–3875 (2014).

82. Hsu, W. T., Zhao, Z. A., Li, L. J., Chen, C. H., Chiu, M. H., Chang, P. S., Chou, Y. C. & Chang, W. H. Second harmonic generation from artificially stacked transition metal dichalcogenide twisted bilayers. *ACS Nano* **8,** 2951–2958 (2014).

83. Puretzky, A. A., Liang, L., Li, X., Xiao, K., Sumpter, B. G., Meunier, V. & Geohegan, D. B. Twisted MoSe2 Bilayers with Variable Local Stacking and Interlayer Coupling Revealed by Low-Frequency Raman Spectroscopy. *ACS Nano* **10,** 2736–2744 (2016).

84. Lee, J. U., Kim, K., Han, S., Ryu, G. H., Lee, Z. & Cheong, H. Raman Signatures of Polytypism in Molybdenum Disulfide. *ACS Nano* **10,** 1948–1953 (2016).

85. Enaldiev, V. V., Zólyomi, V., Yelgel, C., Magorrian, S. J. & Fal'ko, V. I. Stacking Domains and Dislocation Networks in Marginally Twisted Bilayers of Transition Metal Dichalcogenides. *Physical Review Letters* **124,** 206101 (2020).

86. Naik, M. H., Maity, I., Maiti, P. K. & Jain, M. Kolmogorov–Crespi Potential For Multilayer Transition-Metal Dichalcogenides: Capturing Structural Transformations in Moiré Superlattices. *The Journal of Physical Chemistry C* **123,** 9770–9778 (2019).

87. Carr, S., Massatt, D., Torrisi, S. B., Cazeaux, P., Luskin, M. & Kaxiras, E. Relaxation and domain formation in incommensurate two-dimensional heterostructures. *Physical Review B* **98,** 1–7 (2018).

88. Maity, I., Maiti, P. K., Krishnamurthy, H. R. & Jain, M. Reconstruction of moiré lattices in twisted transition metal dichalcogenide bilayers. *Physical Review B* **103,** 1–14 (2021).

89. Zhang, C., Chuu, C. P., Ren, X., Li, M. Y., Li, L. J., Jin, C., Chou, M. Y. & Shih, C. K. Interlayer couplings, Moiré patterns, and 2D electronic superlattices in MoS2/WSe2 hetero-bilayers. *Science Advances* **3,** e1601459 (2017).

90. Pan, Y., Fölsch, S., Nie, Y., Waters, D., Lin, Y. C., Jariwala, B., Zhang, K., Cho, K., Robinson, J. A. & Feenstra, R. M. Quantum-Confined Electronic States Arising from the Moiré Pattern of MoS 2 -WSe 2 Heterobilayers. *Nano Letters* **18,** 1849–1855 (2018).

91. Regan, E. C., Wang, D., Jin, C., Bakti Utama, M. I., Gao, B., Wei, X., Zhao, S., Zhao, W., Zhang, Z., Yumigeta, K., Blei, M., Carlström, J. D., Watanabe, K., Taniguchi, T., Tongay, S., Crommie, M., Zettl, A. & Wang, F. Mott and generalized Wigner crystal states in WSe2/WS2 moiré superlattices. *Nature* **579,** 359–363 (2020).

92. Wang, L., Shih, E. M., Ghiotto, A., Xian, L., Rhodes, D. A., Tan, C., Claassen, M., Kennes, D. M., Bai, Y., Kim, B., Watanabe, K., Taniguchi, T., Zhu, X., Hone, J., Rubio, A., Pasupathy, A. N. & Dean, C. R. Correlated electronic phases in twisted bilayer transition metal dichalcogenides. *Nature Materials* **19,** 861–866 (2020).

93. Zhang, Z., Wang, Y., Watanabe, K., Taniguchi, T., Ueno, K., Tutuc, E. & LeRoy, B. J. Flat bands in twisted bilayer transition metal dichalcogenides. *Nature Physics* **16,** 1093–1096 (2020).

94. Mikolajick, T., Slesazeck, S., Mulaosmanovic, H., Park, M. H., Fichtner, S., Lomenzo, P. D., Hoffmann, M. & Schroeder, U. Next generation ferroelectric materials for semiconductor process integration and their applications. *Journal of Applied Physics* **129,** 1–21 (2021).

95. Mitsui, T. *Springer Handbook of Condensed Matter and Materials Data* (**editors** Martienssen, W. & Warlimont, H.) 903–938 (Springer Berlin Heidelberg, Berlin, Heidelberg, 2005).

96. Bertolazzi, S., Bondavalli, P., Roche, S., San, T., Choi, S. Y., Colombo, L., Bonaccorso, F. & Samorì, P. Nonvolatile Memories Based on Graphene and Related 2D Materials. *Advanced Materials* **31,** 1–35 (2019).

97. Kim, Y. S., Kim, D. H., Kim, J. D., Chang, Y. J., Noh, T. W., Kong, J. H., Char, K., Park, Y. D., Bu, S. D., Yoon, J. G. & Chung, J. S. Critical thickness of ultrathin ferroelectric BaTi O3 films. *Applied Physics Letters* **86,** 1–3 (2005).

98. Junquera, J. & Ghosez, P. Critical thickness for ferroelectricity in perovskite ultrathin films. *Nature* **422,** 506–509 (2003).

99. Chang, K., Liu, J., Lin, H., Wang, N., Zhao, K., Zhang, A., Jin, F., Zhong, Y., Hu, X., Duan, W., Zhang, Q., Fu, L., Xue, Q.-K., Chen, X., Ji, S.-H., Oltmans, S. J., Lelieveld, J., Tost, H., Glatthor, N., Bhartia, P. K., Haffner, D., Labow, G. L., Flynn, L., Weber, M., Burrows, J. P., Pan, L. L., Konopka, P., Kinnison, D. E., Tilmes, S., Kinnison, D. E., Bandoro, J., Garcia, R. R., Nash, E. R., Kawa, S. R., Montzka, S. A., Schauffler, S. M., Freckleton, R. S., Shine, K. P., Bodeker, G. E., Solomon, S., Young, P. J., Drdla, K., Schoeberl, M. R., Hamill, P., Toon, O. B., Abalichin, J., Langematz, U., Austin, J., Wilson, J. & Shepherd, T. G. Discovery of robust in-plane ferroelectricity in atomic-thick SnTe. *Science* **353,** 274–278 (2016).

100. Zheng, C., Yu, L., Zhu, L., Collins, J. L., Kim, D., Lou, Y., Xu, C., Li, M., Wei, Z., Zhang, Y., Edmonds, M. T., Li, S., Seidel, J., Zhu, Y., Liu, J. Z., Tang, W. X. & Fuhrer, M. S. Room temperature in-plane ferroelectricity in van der Waals In2Se3. *Science Advances* **4,** 1–8 (2018).

101. Zhou, Y., Wu, D., Zhu, Y., Cho, Y., He, Q., Yang, X., Herrera, K., Chu, Z., Han, Y., Downer, M. C., Peng, H. & Lai, K. Out-of-Plane Piezoelectricity and Ferroelectricity in Layered α-In2Se3 Nanoflakes. *Nano Letters* **17,** 5508–5513 (2017).

102. Fei, Z., Zhao, W., Palomaki, T. A., Sun, B., Miller, M. K., Zhao, Z., Yan, J., Xu, X. & Cobden, D. H. Ferroelectric switching of a two-dimensional metal. *Nature* **560,** 336–339 (2018).

103. Belianinov, A., He, Q., Dziaugys, A., Maksymovych, P., Eliseev, E., Borisevich, A., Morozovska, A., Banys, J., Vysochanskii, Y. & Kalinin, S. V. CuInP2S6 Room Temperature Layered Ferroelectric. *Nano Letters* **15,** 3808–3814 (2015).

104. Wu, M. & Jena, P. The rise of two-dimensional van der Waals ferroelectrics. *Wiley Interdisciplinary Reviews: Computational Molecular Science* **8,** 1–12 (2018).

105. Yasuda, K., Wang, X., Watanabe, K., Taniguchi, T. & Jarillo-Herrero, P. Stacking-engineered ferroelectricity in bilayer boron nitride. *Science* **372,** 1458 LP –1462 (2021).

106. Vizner Stern, M., Waschitz, Y., Cao, W., Nevo, I., Watanabe, K., Taniguchi, T., Sela, E., Urbakh, M., Hod, O. & Ben Shalom, M. Interfacial ferroelectricity by van der Waals sliding. *Science* **372,** 142–1466 (2021).

107. Woods, C. R., Ares, P., Nevison-Andrews, H., Holwill, M. J., Fabregas, R., Guinea, F., Geim, A. K., Novoselov, K. S., Walet, N. R. & Fumagalli, L. Charge-polarized interfacial superlattices in marginally twisted hexagonal boron nitride. *Nature Communications* **12,** 1–7 (2021).

108. Ferreira, F., Enaldiev, V. V., Fal'ko, V. I. & Magorrian, S. J. Weak ferroelectric charge transfer in layer-asymmetric bilayers of 2D semiconductors. *Scientific Reports* **11,** 1–10 (2021).

109. Ferreira, F., Magorrian, S. J., Enaldiev, V. V., Ruiz-Tijerina, D. A. & Fal'ko, V. I. Band energy landscapes in twisted homobilayers of transition metal dichalcogenides. *Applied Physics Letters* **118,** 1–21 (2021).

110. Zomer, P. J., Guimarães, M. H., Brant, J. C., Tombros, N. & Van Wees, B. J. Fast pick up technique for high quality heterostructures of bilayer graphene and hexagonal boron nitride. *Applied Physics Letters* **105** (2014).

111. Frisenda, R., Navarro-Moratalla, E., Gant, P., Perez De Lara, D., Jarillo-Herrero, P., Gorbachev, R. V. & Castellanos-Gomez, A. Recent progress in the assembly of nanodevices and van der Waals heterostructures by deterministic placement of 2D materials. *Chemical Society Reviews* **47,** 53–68 (2018).

112. Blake, P., Hill, E. W., Castro Neto, A. H., Novoselov, K. S., Jiang, D., Yang, R., Booth, T. J. & Geim, A. K. Making graphene visible. *Applied Physics Letters* **91,** 2007–2009 (2007).

113. Gorbachev, R. V., Riaz, I., Nair, R. R., Jalil, R., Britnell, L., Belle, B. D., Hill, E. W., Novoselov, K. S., Watanabe, K., Taniguchi, T., Geim, A. K. & Blake, P. Hunting for monolayer boron nitride: Optical and raman signatures. *Small* **7,** 465–468 (2011).

114. Benameur, M. M., Radisavljevic, B., Héron, J. S., Sahoo, S., Berger, H. & Kis, A. Visibility of dichalcogenide nanolayers. *Nanotechnology* **22** (2011).

115. Neubeck, S., You, Y. M., Ni, Z. H., Blake, P., Shen, Z. X., Geim, A. K. & Novoselov, K. S. Direct determination of the crystallographic orientation of graphene edges by atomic resolution imaging. *Applied Physics Letters* **97,** 95–98 (2010).

116. Kim, K., Yankowitz, M., Fallahazad, B., Kang, S., Movva, H. C., Huang, S., Larentis, S., Corbet, C. M., Taniguchi, T., Watanabe, K., Banerjee, S. K., Leroy, B. J. & Tutuc, E. Van der Waals Heterostructures with High Accuracy Rotational Alignment. *Nano Letters* **16,** 1989–1995 (2016).

117. Chen, X. D., Xin, W., Jiang, W. S., Liu, Z. B., Chen, Y. S. & Tian, J. G. High-Precision Twist-Controlled Bilayer and Trilayer Graphene. *Advanced Materials* **28,** 2563–2570 (2016).

118. Ross, S. & Sussman, A. Surface Oxidation of Molybdenum Disulfide. *The Journal of Physical Chemistry* **59,** 889–892 (1955).

119. Mirabelli, G., McGeough, C., Schmidt, M., McCarthy, E. K., Monaghan, S., Povey, I. M., McCarthy, M., Gity, F., Nagle, R., Hughes, G., Cafolla, A., Hurley, P. K. & Duffy, R. Air sensitivity of MoS2, MoSe2, MoTe2, HfS2, and HfSe2. *Journal of Applied Physics* **120** (2016).

120. Haigh, S. J., Gholinia, A., Jalil, R., Romani, S., Britnell, L., Elias, D. C., Novoselov, K. S., Ponomarenko, L. A., Geim, A. K. & Gorbachev, R. Cross-sectional imaging of individual layers and buried interfaces of graphene-based heterostructures and superlattices. *Nature Materials* **11,** 764–767 (2012).

121. Kretinin, A. V., Cao, Y., Tu, J. S., Yu, G. L., Jalil, R., Novoselov, K. S., Haigh, S. J., Gholinia, A., Mishchenko, A., Lozada, M., Georgiou, T., Woods, C. R., Withers, F., Blake, P., Eda, G., Wirsig, A., Hucho, C., Watanabe, K., Taniguchi, T., Geim, A. K. & Gorbachev, R. V. Electronic properties of graphene encapsulated with different two-dimensional atomic crystals. *Nano Letters* **14,** 3270–3276 (2014).

122. Woods, C. R., Withers, F., Zhu, M. J., Cao, Y., Yu, G. L., Kozikov, A., Ben Shaliom, M., Morozov, S. V., Wijk, M. M. V., Fasolino, A., Katsnelson, M. I., Watanabe, K., Taniguchi, T., Geim, A. K. & Mishchenko, A. Macroscopic self-reorientation of interacting two-dimensional crystals. *Nature Communications,* 1–5 (2016).

123. Pizzocchero, F., Gammelgaard, L., Jessen, B. S., Caridad, J. M., Wang, L., Hone, J., Bøggild, P. & Booth, T. J. The hot pick-up technique for batch assembly of van der Waals heterostructures. *Nature Communications* **7** (2016).

124. Rosenberger, M. R., Chuang, H. J., McCreary, K. M., Hanbicki, A. T., Sivaram, S. V. & Jonker, B. T. Nano-"Squeegee" for the Creation of Clean 2D Material Interfaces. *ACS Applied Materials and Interfaces* **10,** 10379–10387 (2018).

125. Cadiz, F., Courtade, E., Robert, C., Wang, G., Shen, Y., Cai, H., Taniguchi, T., Watanabe, K., Carrere, H., Lagarde, D., Manca, M., Amand, T., Renucci, P., Tongay, S., Marie, X. & Urbaszek, B. Excitonic linewidth approaching the homogeneous limit in MoS2-based van der Waals heterostructures. *Physical Review X* **7,** 1–12 (2017).

126. Lin, Y. C., Lu, C. C., Yeh, C. H., Jin, C., Suenaga, K. & Chiu, P. W. Graphene annealing: How clean can it be? *Nano Letters* **12,** 414–419 (2012).

127. Pease, R. F. Electron beam ilthography. *Contemporary Physics* **22,** 265–290 (1981).

128. Giubileo, F. & Di Bartolomeo, A. The role of contact resistance in graphene field-effect devices. *Progress in Surface Science* **92,** 143–175 (2017).

129. Binnig, G., Quate, C. F. & Gerber, C. Atomic force microscope. *Physical Review Letters* **56,** 930–933 (1986).

130. Glatzel, T., Lux-Steiner, M. C., Strassburg, E., Boag, A. & Rosenwaks, Y. Principles of kelvin probe force microscopy. *Scanning Probe Microscopy* **2,** 113–131 (2007).

131. Car, R., Ertl, G. & Freund, H.-J. *Kelvin Probe Force microscopy:From single charge detection to device characterization* 530 (Springer, 2018).

132. Voigtlaender, B. *Scanning Probe Microscopy* 1 **edition**, 382 (Springer-Verlag Berlin Heidelberg, 2015).

133. Kang, S., Lee, B.-Y., Lee, S.-H. & Lee, S.-D. *Surface Tension in Microsystems* **1,** 13066 (2013).

134. Jones, J. E. On the Determination of Molecular Fields. II. From The Equation of State of a Gas. *Mathematical Proceedings of the Cambridge Philosophical Society* **22,** 105–112 (1924).

135. Duman, M., Neundlinger, I., Zhu, R., Preiner, J., Lamprecht, C., Chtcheglova, L. A., Rankl, C., Puntheeranurak, T., Ebner, A. & Hinterdorfer, P. *Atomic force microscopy* 111–143 (2012).

136. Pang, G. K., Baba-Kishi, K. Z. & Patel, A. Topographic and phase-contrast imaging in atomic force microscopy. *Ultramicroscopy* **81,** 35–40 (2000).

137. Celano, U. *Electrical Atomic Force Microscopy for Nanoelectornics* (**editor** Celano, U.) 231–265 (Springer, Cham, 2019).

138. Harnagea, C., Alexe, M., Hesse, D. & Pignolet, A. Contact resonances in voltage-modulated force microscopy. *Applied Physics Letters* **83,** 338–340 (2003).

139. McGilly, L. J., Kerelsky, A., Finney, N. R., Shapovalov, K., Shih, E. M., Ghiotto, A., Zeng, Y., Moore, S. L., Wu, W., Bai, Y., Watanabe, K., Taniguchi, T., Stengel, M., Zhou, L., Hone, J., Zhu, X., Basov, D. N., Dean, C., Dreyer, C. E. & Pasupathy, A. N. Visualization of moiré superlattices. *Nature Nanotechnology* (2020).

140. Pandey, M., Soni, R., Mathur, A., Singh, A., Singh, A. K., Raghavan, S. & Chandni, U. Noninvasive Subsurface Electrical Probe for Encapsulated Layers in van der Waals Heterostructures. *Physical Review Applied* **12,** 1 (2019).

141. Altvater, M. A., Wu, S., Zhang, Z., Zhu, T., Li, G., Watanabe, K., Taniguchi, T. & Andrei, E. Y. Electrostatic imaging of encapsulated graphene. *2D Materials* **6** (2019).

142. Ares, P., Cea, T., Holwill, M., Wang, Y. B., Roldán, R., Guinea, F., Andreeva, D. V., Fumagalli, L., Novoselov, K. S. & Woods, C. R. Piezoelectricity in Monolayer Hexagonal Boron Nitride. *Advanced Materials* **32** (2020).

143. Wang, W., Zhou, L., Hu, S., Novoselov, K. S. & Cao, Y. Visualizing Piezoelectricity on 2D Crystals Nanobubbles. *Advanced Functional Materials* **31,** 1–7 (2021).

144. Lei, C. H., Das, A., Elliott, M. & Macdonald, J. E. Quantitative electrostatic force microscopy-phase measurements. *Nanotechnology* **15,** 627–634 (2004).

145. Magonov, S. N. *NT-MDT Application note: SINGLE-PASS MEASUREMENTS IN ATOMIC FORCE MICROSCOPY: KELVIN PROBE FORCE MICROSCOPY AND LOCAL DIELECTRIC STUDIES* 2017.

146. Necas, D. & Klapetek, P. Gwyddion: An open-source software for SPM data analysis. *Central European Journal of Physics* **10,** 181–188 (2012).

147. Kohl, H. & Reimer, L. *Transmission Electron Microscopy* Springer S, 1–586 (Springer, New York, NY, New York, 2008).

148. Lu, N., Wang, J., Oviedo, J. P., Lian, G. & Kim, M. J. Atomic Resolution Scanning Transmission Electron Microscopy of Two-Dimensional Layered Transition Metal Dichalcogenides. *Applied Microscopy* **45,** 225–229 (2015).

149. Van Aert, S., Verbeeck, J., Erni, R., Bals, S., Luysberg, M., Dyck, D. V. & Tendeloo, G. V. Quantitative atomic resolution mapping using high-angle annular dark field scanning transmission electron microscopy. *Ultramicroscopy* **109,** 1236–1244 (2009).

150. Krivanek, O. L., Chisholm, M. F., Nicolosi, V., Pennycook, T. J., Corbin, G. J., Dellby, N., Murfitt, M. F., Own, C. S., Szilagyi, Z. S., Oxley, M. P., Pantelides, S. T. & Pennycook, S. J. Atom-by-atom structural and chemical analysis by annular dark-field electron microscopy. *Nature* **464,** 571–574 (2010).

151. Williams, D. B. & Carter, C. B. *Transmission electron microscopy: A textbook for materials science* 1–760 (2009).

152. Egerton, R. F. *Physical principles of electron microscopy: An introduction to TEM, SEM, and AEM, second edition* 1–196 (2016).

153. Ashida, K., Kajino, T., Kutsuma, Y., Ohtani, N. & Kaneko, T. Crystallographic orientation dependence of SEM contrast revealed by SiC polytypes. *Journal of Vacuum Science & Technology B, Nanotechnology and Microelectronics: Materials, Processing, Measurement, and Phenomena* **33,** 04E104 (2015).

154. Andersen, T. I., Scuri, G., Sushko, A., De Greve, K., Sung, J., Zhou, Y., Wild, D. S., Gelly, R. J., Heo, H., Bérubé, D., Joe, A. Y., Jauregui, L. A., Watanabe, K., Taniguchi, T., Kim, P., Park, H. & Lukin, M. D. Excitons in a reconstructed moiré potential in twisted WSe2/WSe2 homobilayers. *Nature Materials* **20,** 480–487 (2021).

155. Orieux, F., Giovannelli, J.-F. & Rodet, T. Bayesian estimation of regularization and point spread function parameters for Wiener–Hunt deconvolution. *Journal of the Optical Society of America A* **27,** 1593–1607 (2010).

156. Hunt, B. A matrix theory proof of the discrete convolution theorem. *IEEE Transactions on Audio and Electroacoustics* **19,** 285–288 (1971).

157. De la Peña, F., Ostasevicius, T., Fauske, V. T., Burdet, P., Jokubauskas, P., Nord, M., Prestat, E., Sarahan, M., MacArthur, K. E., Johnstone, D. N., Taillon, J., Caron, J., Furnival, T., Eljarrat, A., Mazzucco, S., Migunov, V., Aarholt, T., Walls, M., Winkler, F., Martineau, B., Donval, G., Hoglund, E. R., Alxneit, I., Hjorth, I., Zagonel, L. F., Garmannslund, A., Gohlke, C., Iyengar, I. & Chang, H.-W. *Hyperspy/Hyperspy: Hyperspy 1.3* 2017.

158. *Nanocharacterisation* (**editors** Hutchison, J. & Kirkland, A.) P001–304 (The Royal Society of Chemistry, 2007).

159. Scherzer, O. Über einige Fehler von Elektronenlinsen. *Zeitschrift für Physik* **101,** 593–603 (1936).

160. Kirkland, E. J. Computation in electron microscopy. *Acta Crystallographica Section A: Foundations and Advances* **72,** 1–27 (2016).

161. Brydson, R. *Aberration-Corrected Analytical Transmission Electron Microscopy* (2011).

162. Cowley, J. M. IMAGE CONTRAST IN A TRANSMISSION SCANNING ELECTRON MICROSCOPE. *Applied Physics Letters* **15,** 58–59 (1969).

163. Nellist, P. D. & Pennycook, S. J. *The principles and interpretation of annular dark-field Z-contrast imaging* **C,** 147–203 (2000).

164. Phillips, P. J., De Graef, M., Kovarik, L., Agrawal, A., Windl, W. & Mills, M. J. Atomic-resolution defect contrast in low angle annular dark-field STEM. *Ultramicroscopy* **116,** 47–55 (2012).

165. Nellist, P. D. *Springer Handbook of Microscopy* (**editors** Hawkes, P. W. & Spence, J. C. H.) 49–99 (Springer, 2019).

166. Ishikawa, R., Lugg, N. R., Inoue, K., Sawada, H. & Taniguchi, T. Interfacial Atomic Structure of Twisted Few-Layer Graphene. *Nature Publishing Group,* 1–9 (2016).

167. Treacy, M. M. Z dependence of electron scattering by single atoms into annular dark-field detectors. *Microscopy and Microanalysis* **17,** 847–858 (2011).

168. Van Dyck, D. Persistent misconceptions about incoherence in electron microscopy. *Ultramicroscopy* **111,** 894–900 (2011).

169. Somnath, S., Smith, C. R., Kalinin, S. V., Chi, M., Borisevich, A., Cross, N., Duscher, G. & Jesse, S. Feature extraction via similarity search: application to atom finding and denoising in electron and scanning probe microscopy imaging. *Advanced Structural and Chemical Imaging* **4** (2018).

170. Egerton, R. F., Li, P. & Malac, M. Radiation damage in the TEM and SEM. *Micron* **35,** 399–409 (2004).

171. Egerton, R. F., McLeod, R., Wang, F. & Malac, M. Basic questions related to electron-induced sputtering in the TEM. *Ultramicroscopy* **110,** 991–997 (2010).

172. Egerton, R. F. Control of radiation damage in the TEM. *Ultramicroscopy* **127,** 100–108 (2013).

173. Mitchell, D. R. Contamination mitigation strategies for scanning transmission electron microscopy. *Micron* **73,** 36–46 (2015).

174. Naik, M. H. & Jain, M. Ultraflatbands and Shear Solitons in Moiré Patterns of Twisted Bilayer Transition Metal Dichalcogenides. *Physical Review Letters* **121,** 266401 (2018).

175. Carr, S., Fang, S., Jarillo-Herrero, P. & Kaxiras, E. Pressure dependence of the magic twist angle in graphene superlattices. *Physical Review B* **98,** 1–6 (2018).

176. Cazeaux, P., Luskin, M. & Massatt, D. Energy Minimization of Two Dimensional Incommensurate Heterostructures. *Archive for Rational Mechanics and Analysis* **235,** 1289–1325 (2020).

177. Jiang, L., Wang, S., Shi, Z., Jin, C., Utama, M. I. B., Zhao, S., Shen, Y.-r., Gao, H.-j., Zhang, G. & Wang, F. Manipulation of domain-wall solitons in bi- and trilayer graphene. *Nature Nanotechnology* **13** (2018).

178. Weston, A., Zou, Y., Enaldiev, V., Summerfield, A., Clark, N., Zólyomi, V., Graham, A., Yelgel, C., Magorrian, S., Zhou, M., Zultak, J., Hopkinson, D., Barinov, A., Bointon, T. H., Kretinin, A., Wilson, N. R., Beton, P. H., Fal'ko, V. I., Haigh, S. J. & Gorbachev, R. Atomic reconstruction in twisted bilayers of transition metal dichalcogenides. *Nature Nanotechnology* (2020).

179. Hamer, M. J., Hopkinson, D. G., Clark, N., Zhou, M., Wang, W., Zou, Y., Kelly, D. J., Bointon, T. H., Haigh, S. J. & Gorbachev, R. V. Atomic Resolution Imaging of CrBr3Using Adhesion-Enhanced Grids. *Nano Letters* **20,** 6582–6589 (2020).

180. Tran, K., Moody, G., Wu, F., Lu, X., Choi, J., Kim, K., Rai, A., Sanchez, D. A., Quan, J., Singh, A., Embley, J., Zepeda, A., Campbell, M., Autry, T., Taniguchi, T., Watanabe, K., Lu, N., Banerjee, S. K., Silverman, K. L., Kim, S., Tutuc, E., Yang, L., MacDonald, A. H. & Li, X. Evidence for moiré excitons in van der Waals heterostructures. *Nature* **567,** 71–75 (2019).

181. Zhao, X., Ning, S., Fu, W., Pennycook, S. J. & Loh, K. P. Differentiating Polymorphs in Molybdenum Disulfide via Electron Microscopy. *Advanced Materials* **30,** 1–11 (2018).

182. Yan, A., Chen, W., Ophus, C., Ciston, J., Lin, Y., Persson, K. & Zettl, A. Identifying different stacking sequences in few-layer CVD-grown Mo S2 by low-energy atomic-resolution scanning transmission electron microscopy. *Physical Review B* **93,** 1–5 (2016).

183. Weston, A., Castanon, E. G., Enaldiev, V., Ferreira, F., Bhattacharjee, S., Xu, S., Corte-Leon, H., Wu, Z., Clark, N., Summerfield, A., Hashimoto, T., Gao, Y., Wang, W., Hamer, M., Read, H., Fumagalli, L., Kretinin, A. V., Haigh, S. J., Kazakova, O., Geim, A. K., Fal'ko, V. I. & Gorbachev, R. Interfacial ferroelectricity in marginally twisted 2D semiconductors. *arXiv* (2021).

184. Kim, T., Fan, S., Lee, S., Joo, M. K. & Lee, Y. H. High-mobility junction field-effect transistor via graphene/MoS2 heterointerface. *Scientific Reports* **10,** 1–8 (2020).

185. Romanov, R. I., Slavich, A. S., Kozodaev, M. G., Myakota, D. I., Lebedinskii, Y. Y., Novikov, S. M. & Markeev, A. M. Band Alignment in As-Transferred and Annealed Graphene/MoS2 Heterostructures. *Physica Status Solidi - Rapid Research Letters* **14,** 1–6 (2020).

186. Zhu, H., Wang, Y., Xiao, J., Liu, M., Xiong, S., Wong, Z. J., Ye, Z., Ye, Y., Yin, X. & Zhang, X. Observation of piezoelectricity in free-standing monolayer MoS2. *Nature Nanotechnology* **10,** 151–155 (2015).

187. Castanon, E., Fernández Scarioni, A., Schumacher, H. W., Spencer, S., Perry, R., Vicary, J. A., Clifford, C. A. & Corte-León, H. Calibrated Kelvin-probe force microscopy of 2D materials using Pt-coated probes. *Journal of Physics Communications* **4,** 042001 (2020).

188. Giannozzi, P., Baseggio, O., Bonfà, P., Brunato, D., Car, R., Carnimeo, I., Cavazzoni, C., De Gironcoli, S., Delugas, P., Ferrari Ruffino, F., Ferretti, A., Marzari, N., Timrov, I., Urru, A. & Baroni, S. Quantum ESPRESSO toward the exascale. *Journal of Chemical Physics* **152** (2020).

189. Enaldiev, V. V., Ferreira, F., Magorrian, S. J. & Falko, V. I. Piezoelectric networks and ferroelectric domains in twistronic superlattices in WS2/MoS2 and WSe2/MoSe2 bilayers. *2D Materials* **8** (2021).

190. Halbertal, D., Finney, N. R., Sunku, S. S., Kerelsky, A., Rubio-Verdú, C., Shabani, S., Xian, L., Carr, S., Chen, S., Zhang, C., Wang, L., Gonzalez-Acevedo, D., McLeod, A. S., Rhodes, D., Watanabe, K., Taniguchi, T., Kaxiras, E., Dean, C. R., Hone, J. C., Pasupathy, A. N., Kennes, D. M., Rubio, A. & Basov, D. N. Moiré metrology of energy landscapes in van der Waals heterostructures. *Nature Communications* **12,** 1–8 (2021).

191. Hattori, Y., Taniguchi, T., Watanabe, K. & Nagashio, K. Layer-by-layer dielectric breakdown of hexagonal boron nitride. *ACS Nano* **9,** 916–921 (2015).

192. Kaushik, N., Mackenzie, D. M., Thakar, K., Goyal, N., Mukherjee, B., Boggild, P., Petersen, D. H. & Lodha, S. Reversible hysteresis inversion in MoS2 field effect transistors. *npj 2D Materials and Applications* **1,** 1–9 (2017).

193. Illarionov, Y. Y., Waltl, M., Bartolomeo, A. D., Genovese, L., Illarionov, Y. Y., Rzepa, G., Waltl, M., Knobloch, T. & Grill, A. The role of charge trapping in MoS2/SiO2 and MoS2/hBN field-effect transistors The role of charge trapping in MoS2/SiO2 and MoS2/hBN field-effect transistors. *2D Materials* **3,** 1–10 (2016).

194. Zheng, Y. & Ando, T. Hall conductivity of a two-dimensional graphite system. *Physical Review B - Condensed Matter and Materials Physics* **65,** 2454201–24542011 (2002).

195. Laturia, A., Van de Put, M. L. & Vandenberghe, W. G. Dielectric properties of hexagonal boron nitride and transition metal dichalcogenides: from monolayer to bulk. *npj 2D Materials and Applications* **2** (2018).

196. Cho, K., Park, W., Park, J., Jeong, H., Jang, J., Kim, T.-Y., Hong, W.-K., Hong, S. & Lee, T. Electric Stress-Induced Threshold Voltage Instability of Multilayer MoS2 Field Effect Transistors. *ACS Nano* **7,** 7751–7758 (2013).

197. Shu, J., Wu, G., Guo, Y., Liu, B., Wei, X. & Chen, Q. The intrinsic origin of hysteresis in MoS2 field effect transistors. *Nanoscale* **8,** 3049–3056 (2016).

198. Ramasubramaniam, A., Naveh, D. & Towe, E. Tunable band gaps in bilayer transition-metal dichalcogenides. *Physical Review B - Condensed Matter and Materials Physics* **84,** 1–10 (2011).

Appendices

Chapter A

Rights and Permissions

SPRINGER NATURE LICENSE
TERMS AND CONDITIONS

Sep 15, 2021

This Agreement between University of Manchester -- Astrid Weston ("You") and Springer Nature ("Springer Nature") consists of your license details and the terms and conditions provided by Springer Nature and Copyright Clearance Center.

License Number	5150170857234
License date	Sep 15, 2021
Licensed Content Publisher	Springer Nature
Licensed Content Publication	Nature
Licensed Content Title	Maximized electron interactions at the magic angle in twisted bilayer graphene
Licensed Content Author	Alexander Kerelsky et al
Licensed Content Date	Jul 31, 2019
Type of Use	Thesis/Dissertation
Requestor type	academic/university or research institute
Format	print and electronic
Portion	figures/tables/illustrations
Number of figures/tables/illustrations	2
High-res required	no
Will you be translating?	no

Circulation/distribution	1 - 29
Author of this Springer Nature content	no
Title	PhD student
Institution name	University of Manchester
Expected presentation date	Sep 2021
Portions	Fig 1.f , Fig2.f
Requestor Location	University of Manchester flat 15 Sawmill Court, 3 Murray street, Manchester, England M4 6HS United Kingdom Attn: University of Manchester
Total	0.00 GBP

Terms and Conditions

Springer Nature Customer Service Centre GmbH
Terms and Conditions

This agreement sets out the terms and conditions of the licence (the **Licence**) between you and **Springer Nature Customer Service Centre GmbH** (the **Licensor**). By clicking 'accept' and completing the transaction for the material (**Licensed Material**), you also confirm your acceptance of these terms and conditions.

1. Grant of License

1. 1. The Licensor grants you a personal, non-exclusive, non-transferable, world-wide licence to reproduce the Licensed Material for the purpose specified in your order only. Licences are granted for the specific use requested in the order and for no other use, subject to the conditions below.

1. 2. The Licensor warrants that it has, to the best of its knowledge, the rights to license reuse of the Licensed Material. However, you should ensure that the material you are requesting is original to the Licensor and does not carry the copyright of another entity (as credited in the published version).

1. 3. If the credit line on any part of the material you have requested indicates that it was reprinted or adapted with permission from another source, then you should also

seek permission from that source to reuse the material.

2. Scope of Licence

2. 1. You may only use the Licensed Content in the manner and to the extent permitted by these Ts&Cs and any applicable laws.

2. 2. A separate licence may be required for any additional use of the Licensed Material, e.g. where a licence has been purchased for print only use, separate permission must be obtained for electronic re-use. Similarly, a licence is only valid in the language selected and does not apply for editions in other languages unless additional translation rights have been granted separately in the licence. Any content owned by third parties are expressly excluded from the licence.

2. 3. Similarly, rights for additional components such as custom editions and derivatives require additional permission and may be subject to an additional fee. Please apply to Journalpermissions@springernature.com/bookpermissions@springernature.com for these rights.

2. 4. Where permission has been granted **free of charge** for material in print, permission may also be granted for any electronic version of that work, provided that the material is incidental to your work as a whole and that the electronic version is essentially equivalent to, or substitutes for, the print version.

2. 5. An alternative scope of licence may apply to signatories of the STM Permissions Guidelines, as amended from time to time.

3. Duration of Licence

3. 1. A licence for is valid from the date of purchase ('Licence Date') at the end of the relevant period in the below table:

Scope of Licence	Duration of Licence
Post on a website	12 months
Presentations	12 months
Books and journals	Lifetime of the edition in the language purchased

4. Acknowledgement

4. 1. The Licensor's permission must be acknowledged next to the Licenced Material in print. In electronic form, this acknowledgement must be visible at the same time as the figures/tables/illustrations or abstract, and must be hyperlinked to the journal/book's homepage. Our required acknowledgement format is in the Appendix below.

5. Restrictions on use

5. 1. Use of the Licensed Material may be permitted for incidental promotional use and minor editing privileges e.g. minor adaptations of single figures, changes of format, colour and/or style where the adaptation is credited as set out in Appendix 1 below. Any other changes including but not limited to, cropping, adapting, omitting material that

affect the meaning, intention or moral rights of the author are strictly prohibited.

5. 2. You must not use any Licensed Material as part of any design or trademark.

5. 3. Licensed Material may be used in Open Access Publications (OAP) before publication by Springer Nature, but any Licensed Material must be removed from OAP sites prior to final publication.

6. Ownership of Rights

6. 1. Licensed Material remains the property of either Licensor or the relevant third party and any rights not explicitly granted herein are expressly reserved.

7. Warranty

IN NO EVENT SHALL LICENSOR BE LIABLE TO YOU OR ANY OTHER PARTY OR ANY OTHER PERSON OR FOR ANY SPECIAL, CONSEQUENTIAL, INCIDENTAL OR INDIRECT DAMAGES, HOWEVER CAUSED, ARISING OUT OF OR IN CONNECTION WITH THE DOWNLOADING, VIEWING OR USE OF THE MATERIALS REGARDLESS OF THE FORM OF ACTION, WHETHER FOR BREACH OF CONTRACT, BREACH OF WARRANTY, TORT, NEGLIGENCE, INFRINGEMENT OR OTHERWISE (INCLUDING, WITHOUT LIMITATION, DAMAGES BASED ON LOSS OF PROFITS, DATA, FILES, USE, BUSINESS OPPORTUNITY OR CLAIMS OF THIRD PARTIES), AND
WHETHER OR NOT THE PARTY HAS BEEN ADVISED OF THE POSSIBILITY OF SUCH DAMAGES. THIS LIMITATION SHALL APPLY NOTWITHSTANDING ANY FAILURE OF ESSENTIAL PURPOSE OF ANY LIMITED REMEDY PROVIDED HEREIN.

8. Limitations

8. 1. ***BOOKS ONLY:*** Where **'reuse in a dissertation/thesis'** has been selected the following terms apply: Print rights of the final author's accepted manuscript (for clarity, NOT the published version) for up to 100 copies, electronic rights for use only on a personal website or institutional repository as defined by the Sherpa guideline (www.sherpa.ac.uk/romeo/).

8. 2. For content reuse requests that qualify for permission under the STM Permissions Guidelines, which may be updated from time to time, the STM Permissions Guidelines supersede the terms and conditions contained in this licence.

9. Termination and Cancellation

9. 1. Licences will expire after the period shown in Clause 3 (above).

9. 2. Licensee reserves the right to terminate the Licence in the event that payment is not received in full or if there has been a breach of this agreement by you.

Appendix 1 — Acknowledgements:

For Journal Content:
Reprinted by permission from [**the Licensor**]: [**Journal Publisher** (e.g. Nature/Springer/Palgrave)] [**JOURNAL NAME**] [**REFERENCE CITATION** (Article name, Author(s) Name), [**COPYRIGHT**] (year of publication)

For **Advance Online Publication papers:**
Reprinted by permission from [**the Licensor**]: [**Journal Publisher** (e.g. Nature/Springer/Palgrave)] [**JOURNAL NAME**] [**REFERENCE CITATION** (Article name, Author(s) Name), [**COPYRIGHT**] (year of publication), advance online publication, day month year (doi: 10.1038/sj.[JOURNAL ACRONYM].)

For Adaptations/Translations:
Adapted/Translated by permission from [**the Licensor**]: [**Journal Publisher** (e.g. Nature/Springer/Palgrave)] [**JOURNAL NAME**] [**REFERENCE CITATION** (Article name, Author(s) Name), [**COPYRIGHT**] (year of publication)

Note: For any republication from the British Journal of Cancer, the following credit line style applies:

Reprinted/adapted/translated by permission from [**the Licensor**]: on behalf of Cancer Research UK: : [**Journal Publisher** (e.g. Nature/Springer/Palgrave)] [**JOURNAL NAME**] [**REFERENCE CITATION** (Article name, Author(s) Name), [**COPYRIGHT**] (year of publication)

For **Advance Online Publication** papers:
Reprinted by permission from The [**the Licensor**]: on behalf of Cancer Research UK: [**Journal Publisher** (e.g. Nature/Springer/Palgrave)] [**JOURNAL NAME**] [**REFERENCE CITATION** (Article name, Author(s) Name), [**COPYRIGHT**] (year of publication), advance online publication, day month year (doi: 10.1038/sj.[JOURNAL ACRONYM])

For Book content:
Reprinted/adapted by permission from [**the Licensor**]: [**Book Publisher** (e.g. Palgrave Macmillan, Springer etc) [**Book Title**] by [**Book author**(s)] [**COPYRIGHT**] (year of publication)

Other Conditions:

Version 1.3

Questions? customercare@copyright.com or +1-855-239-3415 (toll free in the US) or +1-978-646-2777.

SPRINGER NATURE LICENSE
TERMS AND CONDITIONS

Sep 15, 2021

This Agreement between University of Manchester -- Astrid Weston ("You") and Springer Nature ("Springer Nature") consists of your license details and the terms and conditions provided by Springer Nature and Copyright Clearance Center.

License Number	5150180357460
License date	Sep 15, 2021
Licensed Content Publisher	Springer Nature
Licensed Content Publication	Nature
Licensed Content Title	Spectroscopic signatures of many-body correlations in magic-angle twisted bilayer graphene
Licensed Content Author	Yonglong Xie et al
Licensed Content Date	Jul 31, 2019
Type of Use	Thesis/Dissertation
Requestor type	academic/university or research institute
Format	print and electronic
Portion	figures/tables/illustrations
Number of figures/tables/illustrations	1
High-res required	no

Will you be translating?	no
Circulation/distribution	1 - 29
Author of this Springer Nature content	no
Title	PhD student
Institution name	University of Manchester
Expected presentation date	Sep 2021
Portions	Figure 3
Requestor Location	University of Manchester flat 15 Sawmill Court, 3 Murray street, Manchester, England M4 6HS United Kingdom Attn: University of Manchester
Total	0.00 GBP

Terms and Conditions

Springer Nature Customer Service Centre GmbH
Terms and Conditions

This agreement sets out the terms and conditions of the licence (the **Licence**) between you and **Springer Nature Customer Service Centre GmbH** (the **Licensor**). By clicking 'accept' and completing the transaction for the material (**Licensed Material**), you also confirm your acceptance of these terms and conditions.

1. Grant of License

1. 1. The Licensor grants you a personal, non-exclusive, non-transferable, world-wide licence to reproduce the Licensed Material for the purpose specified in your order only. Licences are granted for the specific use requested in the order and for no other use, subject to the conditions below.

1. 2. The Licensor warrants that it has, to the best of its knowledge, the rights to license reuse of the Licensed Material. However, you should ensure that the material you are requesting is original to the Licensor and does not carry the copyright of another entity (as credited in the published version).

1. 3. If the credit line on any part of the material you have requested indicates that it was reprinted or adapted with permission from another source, then you should also seek permission from that source to reuse the material.

2. Scope of Licence

2. 1. You may only use the Licensed Content in the manner and to the extent permitted by these Ts&Cs and any applicable laws.

2. 2. A separate licence may be required for any additional use of the Licensed Material, e.g. where a licence has been purchased for print only use, separate permission must be obtained for electronic re-use. Similarly, a licence is only valid in the language selected and does not apply for editions in other languages unless additional translation rights have been granted separately in the licence. Any content owned by third parties are expressly excluded from the licence.

2. 3. Similarly, rights for additional components such as custom editions and derivatives require additional permission and may be subject to an additional fee. Please apply to Journalpermissions@springernature.com/bookpermissions@springernature.com for these rights.

2. 4. Where permission has been granted **free of charge** for material in print, permission may also be granted for any electronic version of that work, provided that the material is incidental to your work as a whole and that the electronic version is essentially equivalent to, or substitutes for, the print version.

2. 5. An alternative scope of licence may apply to signatories of the STM Permissions Guidelines, as amended from time to time.

3. Duration of Licence

3. 1. A licence for is valid from the date of purchase ('Licence Date') at the end of the relevant period in the below table:

Scope of Licence	Duration of Licence
Post on a website	12 months
Presentations	12 months
Books and journals	Lifetime of the edition in the language purchased

4. Acknowledgement

4. 1. The Licensor's permission must be acknowledged next to the Licenced Material in print. In electronic form, this acknowledgement must be visible at the same time as the figures/tables/illustrations or abstract, and must be hyperlinked to the journal/book's homepage. Our required acknowledgement format is in the Appendix below.

5. Restrictions on use

5. 1. Use of the Licensed Material may be permitted for incidental promotional use and minor editing privileges e.g. minor adaptations of single figures, changes of format, colour and/or style where the adaptation is credited as set out in Appendix 1 below. Any

other changes including but not limited to, cropping, adapting, omitting material that affect the meaning, intention or moral rights of the author are strictly prohibited.

5. 2. You must not use any Licensed Material as part of any design or trademark.

5. 3. Licensed Material may be used in Open Access Publications (OAP) before publication by Springer Nature, but any Licensed Material must be removed from OAP sites prior to final publication.

6. Ownership of Rights

6. 1. Licensed Material remains the property of either Licensor or the relevant third party and any rights not explicitly granted herein are expressly reserved.

7. Warranty

IN NO EVENT SHALL LICENSOR BE LIABLE TO YOU OR ANY OTHER PARTY OR ANY OTHER PERSON OR FOR ANY SPECIAL, CONSEQUENTIAL, INCIDENTAL OR INDIRECT DAMAGES, HOWEVER CAUSED, ARISING OUT OF OR IN CONNECTION WITH THE DOWNLOADING, VIEWING OR USE OF THE MATERIALS REGARDLESS OF THE FORM OF ACTION, WHETHER FOR BREACH OF CONTRACT, BREACH OF WARRANTY, TORT, NEGLIGENCE, INFRINGEMENT OR OTHERWISE (INCLUDING, WITHOUT LIMITATION, DAMAGES BASED ON LOSS OF PROFITS, DATA, FILES, USE, BUSINESS OPPORTUNITY OR CLAIMS OF THIRD PARTIES), AND
WHETHER OR NOT THE PARTY HAS BEEN ADVISED OF THE POSSIBILITY OF SUCH DAMAGES. THIS LIMITATION SHALL APPLY NOTWITHSTANDING ANY FAILURE OF ESSENTIAL PURPOSE OF ANY LIMITED REMEDY PROVIDED HEREIN.

8. Limitations

8. 1. ***BOOKS ONLY:***Where **'reuse in a dissertation/thesis'** has been selected the following terms apply: Print rights of the final author's accepted manuscript (for clarity, NOT the published version) for up to 100 copies, electronic rights for use only on a personal website or institutional repository as defined by the Sherpa guideline (www.sherpa.ac.uk/romeo/).

8. 2. For content reuse requests that qualify for permission under the STM Permissions Guidelines, which may be updated from time to time, the STM Permissions Guidelines supersede the terms and conditions contained in this licence.

9. Termination and Cancellation

9. 1. Licences will expire after the period shown in Clause 3 (above).

9. 2. Licensee reserves the right to terminate the Licence in the event that payment is not received in full or if there has been a breach of this agreement by you.

Appendix 1 — Acknowledgements:

For Journal Content:
Reprinted by permission from [**the Licensor**]: [**Journal Publisher** (e.g. Nature/Springer/Palgrave)] [**JOURNAL NAME**] [**REFERENCE CITATION** (Article name, Author(s) Name), [**COPYRIGHT**] (year of publication)

For **Advance Online Publication papers:**
Reprinted by permission from [**the Licensor**]: [**Journal Publisher** (e.g. Nature/Springer/Palgrave)] [**JOURNAL NAME**] [**REFERENCE CITATION** (Article name, Author(s) Name), [**COPYRIGHT**] (year of publication), advance online publication, day month year (doi: 10.1038/sj.[JOURNAL ACRONYM].)

For Adaptations/Translations:
Adapted/Translated by permission from [**the Licensor**]: [**Journal Publisher** (e.g. Nature/Springer/Palgrave)] [**JOURNAL NAME**] [**REFERENCE CITATION** (Article name, Author(s) Name), [**COPYRIGHT**] (year of publication)

Note: For any republication from the British Journal of Cancer, the following credit line style applies:

Reprinted/adapted/translated by permission from [**the Licensor**]: on behalf of Cancer Research UK: : [**Journal Publisher** (e.g. Nature/Springer/Palgrave)] [**JOURNAL NAME**] [**REFERENCE CITATION** (Article name, Author(s) Name), [**COPYRIGHT]** (year of publication)

For **Advance Online Publication** papers:
Reprinted by permission from The [**the Licensor**]: on behalf of Cancer Research UK: [**Journal Publisher** (e.g. Nature/Springer/Palgrave)] [**JOURNAL NAME**] [**REFERENCE CITATION** (Article name, Author(s) Name), [**COPYRIGHT**] (year of publication), advance online publication, day month year (doi: 10.1038/sj.[JOURNAL ACRONYM])

For Book content:
Reprinted/adapted by permission from [**the Licensor**]: [**Book Publisher** (e.g. Palgrave Macmillan, Springer etc) [**Book Title**] by [**Book author**(s)] [**COPYRIGHT**] (year of publication)

Other Conditions:

Version 1.3

Questions? customercare@copyright.com or +1-855-239-3415 (toll free in the US) or +1-978-646-2777.

ACS Publications
Most Trusted. Most Cited. Most Read.

Electronic Structure and Optical Signatures of Semiconducting Transition Metal Dichalcogenide Nanosheets

Author: Weijie Zhao, Ricardo Mendes Ribeiro, Goki Eda
Publication: Accounts of Chemical Research
Publisher: American Chemical Society
Date: Jan 1, 2015

PERMISSION/LICENSE IS GRANTED FOR YOUR ORDER AT NO CHARGE

This type of permission/license, instead of the standard Terms and Conditions, is sent to you because no fee is being charged for your order. Please note the following:

- Permission is granted for your request in both print and electronic formats, and translations.
- If figures and/or tables were requested, they may be adapted or used in part.
- Please print this page for your records and send a copy of it to your publisher/graduate school.
- Appropriate credit for the requested material should be given as follows: "Reprinted (adapted) with permission from {COMPLETE REFERENCE CITATION}. Copyright {YEAR} American Chemical Society." Insert appropriate information in place of the capitalized words.
- One-time permission is granted only for the use specified in your RightsLink request. No additional uses are granted (such as derivative works or other editions). For any uses, please submit a new request.

If credit is given to another source for the material you requested from RightsLink, permission must be obtained from that source.

BACK CLOSE WINDOW

Emerging Photoluminescence in Monolayer MoS2

Author: Andrea Splendiani, Liang Sun, Yuanbo Zhang, et al
Publication: Nano Letters
Publisher: American Chemical Society
Date: Apr 1, 2010

PERMISSION/LICENSE IS GRANTED FOR YOUR ORDER AT NO CHARGE

This type of permission/license, instead of the standard Terms and Conditions, is sent to you because no fee is being charged for your order. Please note the following:

- Permission is granted for your request in both print and electronic formats, and translations.
- If figures and/or tables were requested, they may be adapted or used in part.
- Please print this page for your records and send a copy of it to your publisher/graduate school.
- Appropriate credit for the requested material should be given as follows: "Reprinted (adapted) with permission from {COMPLETE REFERENCE CITATION}. Copyright {YEAR} American Chemical Society." Insert appropriate information in place of the capitalized words.
- One-time permission is granted only for the use specified in your RightsLink request. No additional uses are granted (such as derivative works or other editions). For any uses, please submit a new request.

If credit is given to another source for the material you requested from RightsLink, permission must be obtained from that source.

BACK CLOSE WINDOW

Quantum-Confined Electronic States Arising from the Moiré Pattern of MoS2–WSe2 Heterobilayers

Author: Yi Pan, Stefan Fölsch, Yifan Nie, et al

Publication: Nano Letters

Publisher: American Chemical Society

Date: Mar 1, 2018

PERMISSION/LICENSE IS GRANTED FOR YOUR ORDER AT NO CHARGE

This type of permission/license, instead of the standard Terms and Conditions, is sent to you because no fee is being charged for your order. Please note the following:

- Permission is granted for your request in both print and electronic formats, and translations.
- If figures and/or tables were requested, they may be adapted or used in part.
- Please print this page for your records and send a copy of it to your publisher/graduate school.
- Appropriate credit for the requested material should be given as follows: "Reprinted (adapted) with permission from {COMPLETE REFERENCE CITATION}. Copyright {YEAR} American Chemical Society." Insert appropriate information in place of the capitalized words.
- One-time permission is granted only for the use specified in your RightsLink request. No additional uses are granted (such as derivative works or other editions). For any uses, please submit a new request.

If credit is given to another source for the material you requested from RightsLink, permission must be obtained from that source.

BACK CLOSE WINDOW

American Physical Society
Reuse and Permissions License

15-Sep-2021

This license agreement between the American Physical Society ("APS") and Astrid Weston ("You") consists of your license details and the terms and conditions provided by the American Physical Society and SciPris.

Licensed Content Information

License Number:	**RNP/21/SEP/044537**
License date:	15-Sep-2021
DOI:	10.1103/RevModPhys.81.109
Title:	The electronic properties of graphene
Author:	A. H. Castro Neto et al.
Publication:	Reviews of Modern Physics
Publisher:	American Physical Society
Cost:	USD $ 0.00

Request Details

Does your reuse require significant modifications: No

Specify intended distribution locations:	UK & Commonwealth (excluding Canada)
Reuse Category:	Reuse in a thesis/dissertation
Requestor Type:	Student
Items for Reuse:	Figures/Tables
Number of Figure/Tables:	1
Figure/Tables Details:	Fig. 3
Format for Reuse:	Electronic and Print
Total number of print copies:	Up to 1000

Information about New Publication:

University/Publisher:	University of Manchester
Title of dissertation/thesis:	Atomic and electronic properties of 2D moiré interfaces
Author(s):	Astrid Marie Weston
Expected completion date:	Sep. 2021

License Requestor Information

Name:	Astrid Weston
Affiliation:	Individual
Email Id:	astrid.weston204@gmail.com
Country:	United Kingdom

American Physical Society
Reuse and Permissions License

TERMS AND CONDITIONS

The American Physical Society (APS) is pleased to grant the Requestor of this license a non-exclusive, non-transferable permission, limited to Electronic and Print format, provided all criteria outlined below are followed.

1. You must also obtain permission from at least one of the lead authors for each separate work, if you haven't done so already. The author's name and affiliation can be found on the first page of the published Article.

2. For electronic format permissions, Requestor agrees to provide a hyperlink from the reprinted APS material using the source material's DOI on the web page where the work appears. The hyperlink should use the standard DOI resolution URL, http://dx.doi.org/{DOI}. The hyperlink may be embedded in the copyright credit line.

3. For print format permissions, Requestor agrees to print the required copyright credit line on the first page where the material appears: "Reprinted (abstract/excerpt/figure) with permission from [(FULL REFERENCE CITATION) as follows: Author's Names, APS Journal Title, Volume Number, Page Number and Year of Publication.] Copyright (YEAR) by the American Physical Society."

4. Permission granted in this license is for a one-time use and does not include permission for any future editions, updates, databases, formats or other matters. Permission must be sought for any additional use.

5. Use of the material does not and must not imply any endorsement by APS.

6. APS does not imply, purport or intend to grant permission to reuse materials to which it does not hold copyright. It is the requestor's sole responsibility to ensure the licensed material is original to APS and does not contain the copyright of another entity, and that the copyright notice of the figure, photograph, cover or table does not indicate it was reprinted by APS with permission from another source.

7. The permission granted herein is personal to the Requestor for the use specified and is not transferable or assignable without express written permission of APS. This license may not be amended except in writing by APS.

8. You may not alter, edit or modify the material in any manner.

9. You may translate the materials only when translation rights have been granted.

10. APS is not responsible for any errors or omissions due to translation.

11. You may not use the material for promotional, sales, advertising or marketing purposes.

12. The foregoing license shall not take effect unless and until APS or its agent, Aptara, receives payment in full in accordance with Aptara Billing and Payment Terms and Conditions, which are incorporated herein by reference.

13. Should the terms of this license be violated at any time, APS or Aptara may revoke the license with no refund to you and seek relief to the fullest extent of the laws of the USA. Official written notice will be made using the contact information provided with the permission request. Failure to receive such notice will not nullify revocation of the permission.

14. APS reserves all rights not specifically granted herein.

15. This document, including the Aptara Billing and Payment Terms and Conditions, shall be the entire agreement between the parties relating to the subject matter hereof.

American Physical Society
Reuse and Permissions License

15-Sep-2021

This license agreement between the American Physical Society ("APS") and Astrid Weston ("You") consists of your license details and the terms and conditions provided by the American Physical Society and SciPris.

Licensed Content Information

License Number:	**RNP/21/SEP/044539**
License date:	15-Sep-2021
DOI:	10.1103/PhysRevLett.105.136805
Title:	Atomically Thin ${\mathrm{MoS}}_{2}$: A New Direct-Gap Semiconductor
Author:	Kin Fai Mak et al.
Publication:	Physical Review Letters
Publisher:	American Physical Society
Cost:	USD $ 0.00

Request Details

Does your reuse require significant modifications: No

Specify intended distribution locations:	UK & Commonwealth (excluding Canada)
Reuse Category:	Reuse in a thesis/dissertation
Requestor Type:	Student
Items for Reuse:	Figures/Tables
Number of Figure/Tables:	1
Figure/Tables Details:	Fig 3
Format for Reuse:	Print and Electronic
Total number of print copies:	Up to 1000

Information about New Publication:

University/Publisher:	University of Manchester
Title of dissertation/thesis:	Atomic and electronic properties of moiré interfaces
Author(s):	Astrid Marie Weston
Expected completion date:	Sep. 2021

License Requestor Information

Name:	Astrid Weston
Affiliation:	Individual
Email Id:	astrid.weston204@gmail.com
Country:	United Kingdom

American Physical Society
Reuse and Permissions License

TERMS AND CONDITIONS

The American Physical Society (APS) is pleased to grant the Requestor of this license a non-exclusive, non-transferable permission, limited to Print and Electronic format, provided all criteria outlined below are followed.

1. You must also obtain permission from at least one of the lead authors for each separate work, if you haven't done so already. The author's name and affiliation can be found on the first page of the published Article.
2. For electronic format permissions, Requestor agrees to provide a hyperlink from the reprinted APS material using the source material's DOI on the web page where the work appears. The hyperlink should use the standard DOI resolution URL, http://dx.doi.org/{DOI}. The hyperlink may be embedded in the copyright credit line.
3. For print format permissions, Requestor agrees to print the required copyright credit line on the first page where the material appears: "Reprinted (abstract/excerpt/figure) with permission from [(FULL REFERENCE CITATION) as follows: Author's Names, APS Journal Title, Volume Number, Page Number and Year of Publication.] Copyright (YEAR) by the American Physical Society."
4. Permission granted in this license is for a one-time use and does not include permission for any future editions, updates, databases, formats or other matters. Permission must be sought for any additional use.
5. Use of the material does not and must not imply any endorsement by APS.
6. APS does not imply, purport or intend to grant permission to reuse materials to which it does not hold copyright. It is the requestor's sole responsibility to ensure the licensed material is original to APS and does not contain the copyright of another entity, and that the copyright notice of the figure, photograph, cover or table does not indicate it was reprinted by APS with permission from another source.
7. The permission granted herein is personal to the Requestor for the use specified and is not transferable or assignable without express written permission of APS. This license may not be amended except in writing by APS.
8. You may not alter, edit or modify the material in any manner.
9. You may translate the materials only when translation rights have been granted.
10. APS is not responsible for any errors or omissions due to translation.
11. You may not use the material for promotional, sales, advertising or marketing purposes.
12. The foregoing license shall not take effect unless and until APS or its agent, Aptara, receives payment in full in accordance with Aptara Billing and Payment Terms and Conditions, which are incorporated herein by reference.
13. Should the terms of this license be violated at any time, APS or Aptara may revoke the license with no refund to you and seek relief to the fullest extent of the laws of the USA. Official written notice will be made using the contact information provided with the permission request. Failure to receive such notice will not nullify revocation of the permission.
14. APS reserves all rights not specifically granted herein.
15. This document, including the Aptara Billing and Payment Terms and Conditions, shall be the entire agreement between the parties relating to the subject matter hereof.

American Physical Society
Reuse and Permissions License

15-Sep-2021

This license agreement between the American Physical Society ("APS") and Astrid Weston ("You") consists of your license details and the terms and conditions provided by the American Physical Society and SciPris.

Licensed Content Information

License Number:	**RNP/21/SEP/044540**
License date:	15-Sep-2021
DOI:	10.1103/PhysRevLett.109.196802
Title:	Unraveling the Intrinsic and Robust Nature of van Hove Singularities in Twisted Bilayer Graphene by Scanning Tunneling Microscopy and Theoretical Analysis
Author:	I. Brihuega et al.
Publication:	Physical Review Letters
Publisher:	American Physical Society
Cost:	USD $ 0.00

Request Details

Does your reuse require significant modifications: No

Specify intended distribution locations:	UK & Commonwealth (excluding Canada)
Reuse Category:	Reuse in a thesis/dissertation
Requestor Type:	Student
Items for Reuse:	Figures/Tables
Number of Figure/Tables:	1
Figure/Tables Details:	Fig 1
Format for Reuse:	Print and Electronic
Total number of print copies:	Up to 1000

Information about New Publication:

University/Publisher:	University of Manchester
Title of dissertation/thesis:	Atomic and electronic properties of moiré interfaces
Author(s):	Astrid Marie Weston
Expected completion date:	Sep. 2021

License Requestor Information

Name:	Astrid Weston
Affiliation:	Individual
Email Id:	astrid.weston204@gmail.com
Country:	United Kingdom

American Physical Society
Reuse and Permissions License

TERMS AND CONDITIONS

The American Physical Society (APS) is pleased to grant the Requestor of this license a non-exclusive, non-transferable permission, limited to Print and Electronic format, provided all criteria outlined below are followed.

1. You must also obtain permission from at least one of the lead authors for each separate work, if you haven't done so already. The author's name and affiliation can be found on the first page of the published Article.

2. For electronic format permissions, Requestor agrees to provide a hyperlink from the reprinted APS material using the source material's DOI on the web page where the work appears. The hyperlink should use the standard DOI resolution URL, http://dx.doi.org/{DOI}. The hyperlink may be embedded in the copyright credit line.

3. For print format permissions, Requestor agrees to print the required copyright credit line on the first page where the material appears: "Reprinted (abstract/excerpt/figure) with permission from [(FULL REFERENCE CITATION) as follows: Author's Names, APS Journal Title, Volume Number, Page Number and Year of Publication.] Copyright (YEAR) by the American Physical Society."

4. Permission granted in this license is for a one-time use and does not include permission for any future editions, updates, databases, formats or other matters. Permission must be sought for any additional use.

5. Use of the material does not and must not imply any endorsement by APS.

6. APS does not imply, purport or intend to grant permission to reuse materials to which it does not hold copyright. It is the requestor's sole responsibility to ensure the licensed material is original to APS and does not contain the copyright of another entity, and that the copyright notice of the figure, photograph, cover or table does not indicate it was reprinted by APS with permission from another source.

7. The permission granted herein is personal to the Requestor for the use specified and is not transferable or assignable without express written permission of APS. This license may not be amended except in writing by APS.

8. You may not alter, edit or modify the material in any manner.

9. You may translate the materials only when translation rights have been granted.

10. APS is not responsible for any errors or omissions due to translation.

11. You may not use the material for promotional, sales, advertising or marketing purposes.

12. The foregoing license shall not take effect unless and until APS or its agent, Aptara, receives payment in full in accordance with Aptara Billing and Payment Terms and Conditions, which are incorporated herein by reference.

13. Should the terms of this license be violated at any time, APS or Aptara may revoke the license with no refund to you and seek relief to the fullest extent of the laws of the USA. Official written notice will be made using the contact information provided with the permission request. Failure to receive such notice will not nullify revocation of the permission.

14. APS reserves all rights not specifically granted herein.

15. This document, including the Aptara Billing and Payment Terms and Conditions, shall be the entire agreement between the parties relating to the subject matter hereof.

American Physical Society
Reuse and Permissions License

15-Sep-2021

This license agreement between the American Physical Society ("APS") and Astrid Weston ("You") consists of your license details and the terms and conditions provided by the American Physical Society and SciPris.

Licensed Content Information

License Number:	**RNP/21/SEP/044542**
License date:	15-Sep-2021
DOI:	10.1103/PhysRevLett.121.037702
Title:	Topologically Protected Helical States in Minimally Twisted Bilayer Graphene
Author:	Shengqiang Huang et al.
Publication:	Physical Review Letters
Publisher:	American Physical Society
Cost:	USD $ 0.00

Request Details

Does your reuse require significant modifications: No

Specify intended distribution locations:	UK & Commonwealth (excluding Canada)
Reuse Category:	Reuse in a thesis/dissertation
Requestor Type:	Student
Items for Reuse:	Figures/Tables
Number of Figure/Tables:	1
Figure/Tables Details:	figure 1c-d and figure 2
Format for Reuse:	Print and Electronic
Total number of print copies:	Up to 1000

Information about New Publication:

University/Publisher:	University of Manchester
Title of dissertation/thesis:	Atomic and electronic properties of moiré interfaces
Author(s):	Astrid Weston
Expected completion date:	Sep. 2021

License Requestor Information

Name:	Astrid Weston
Affiliation:	Individual
Email Id:	astrid.weston204@gmail.com
Country:	United Kingdom

American Physical Society
Reuse and Permissions License

TERMS AND CONDITIONS

The American Physical Society (APS) is pleased to grant the Requestor of this license a non-exclusive, non-transferable permission, limited to Print and Electronic format, provided all criteria outlined below are followed.

1. You must also obtain permission from at least one of the lead authors for each separate work, if you haven't done so already. The author's name and affiliation can be found on the first page of the published Article.

2. For electronic format permissions, Requestor agrees to provide a hyperlink from the reprinted APS material using the source material's DOI on the web page where the work appears. The hyperlink should use the standard DOI resolution URL, http://dx.doi.org/{DOI}. The hyperlink may be embedded in the copyright credit line.

3. For print format permissions, Requestor agrees to print the required copyright credit line on the first page where the material appears: "Reprinted (abstract/excerpt/figure) with permission from [(FULL REFERENCE CITATION) as follows: Author's Names, APS Journal Title, Volume Number, Page Number and Year of Publication.] Copyright (YEAR) by the American Physical Society."

4. Permission granted in this license is for a one-time use and does not include permission for any future editions, updates, databases, formats or other matters. Permission must be sought for any additional use.

5. Use of the material does not and must not imply any endorsement by APS.

6. APS does not imply, purport or intend to grant permission to reuse materials to which it does not hold copyright. It is the requestor's sole responsibility to ensure the licensed material is original to APS and does not contain the copyright of another entity, and that the copyright notice of the figure, photograph, cover or table does not indicate it was reprinted by APS with permission from another source.

7. The permission granted herein is personal to the Requestor for the use specified and is not transferable or assignable without express written permission of APS. This license may not be amended except in writing by APS.

8. You may not alter, edit or modify the material in any manner.

9. You may translate the materials only when translation rights have been granted.

10. APS is not responsible for any errors or omissions due to translation.

11. You may not use the material for promotional, sales, advertising or marketing purposes.

12. The foregoing license shall not take effect unless and until APS or its agent, Aptara, receives payment in full in accordance with Aptara Billing and Payment Terms and Conditions, which are incorporated herein by reference.

13. Should the terms of this license be violated at any time, APS or Aptara may revoke the license with no refund to you and seek relief to the fullest extent of the laws of the USA. Official written notice will be made using the contact information provided with the permission request. Failure to receive such notice will not nullify revocation of the permission.

14. APS reserves all rights not specifically granted herein.

15. This document, including the Aptara Billing and Payment Terms and Conditions, shall be the entire agreement between the parties relating to the subject matter hereof.